The Structural Evolution of an Ancient Accretionary Prism in the Damara Belt, Namibia

Michael Ian Hay Hartnady

University of Cape Town

a dissertation submitted in fulfilment of the degree of

Master of Science

in the Department of Geological Sciences, University of Cape Town,

South Africa.

September 2014

The copyright of this thesis vests in the author. No quotation from it or information derived from it is to be published without full acknowledgement of the source. The thesis is to be used for private study or non-commercial research purposes only.

Published by the University of Cape Town (UCT) in terms of the non-exclusive license granted to UCT by the author.

University of Cape Town

Abstract

The Southern Marginal Zone (SMZ) of the Damara Belt, exposed in the Gaub Canyon in central Namibia, consists of fourteen lithotectonic units of high strain amphibolite facies rock with pelagic, hemi-pelagic and clastic sedimentary protoliths. These rocks are intercalated with lenses of metabasite. Regional high-pressure - low-temperature metamorphic conditions ($\sim$10 kbar and $\sim$600°C) dominate the Southern and Southern Marginal Zones of the Damara Belt, leading to the interpretation that these tectonostratigraphic terranes formed in an accretionary prism along an ancient subduction margin.

The structures in the SMZ are the result of progressive deformation, inferred to have initiated under low-grade metamorphic conditions (D_1) and evolved through prograde to peak metamorphism (D_2), ending in relatively low-temperature retrograde conditions (D_3). Each of the deformation phases is characterised by a foliation. D_1 is associated with pure shear dominated layer-parallel extension characterised by disrupted lithological layering and bedding-parallel foliation S_{0+1}. D_2 is defined as deformation related to the formation of an axial-planar S_2 caused by folding of S_{0+1} around F_2 hinge lines. Widespread isoclinal recumbent folding resulted in transposition of these fabrics and the general foliation is thus termed S_{0+1+2}. This composite foliation contains a down-dip stretching lineation L_2. Folding was contemporaneous with top-to-the-SE directed thrusting in D_2 faults and shear zones that are seen to displace D_1 fabric. Fold hinge lines parallel to L_2 suggest D_2 is characterised by non-ideal simple shear. D_3 is defined by a crenulation cleavage S_3, at near right angles to S_{0+1+2} foliation resulting from NW-SE pure shear shortening. This phase of deformation is also associated with retrograde, reverse faulting that is localised along some of the D_2 shear zones. The presence, in places, of a sub-horizontal stretching lineation (L_3) on a few fault surfaces is attributed to a component of strike-slip during D_3 deformation.

This deformation sequence is related to the deformation processes observed in modern accretionary prisms. In this model, D_1 deformation is associated with underthrusting of marine and trench-fill sediments beneath the accretionary prism. D_2 deformation is attributed to disruption of the underthrust sediment by imbricate thrusting. This is believed to have occurred in the brittle regime during early D_2 deformation. During progressive burial and heating through the brittle-viscous transition, ductile shear zones localised on these precursor brittle structures. Isoclinal recumbent folding during bulk non-coaxial shear of the accreted thrust packages generated axial planar S_2 which was transposed with S_{0+1} through progressive deformation. During this time strain was concentrated in weaker pelitic rock types. D_1 and early brittle D_2 structures are therefore still preserved in more competent quartzitic rock types. D_3 structures are interpreted to record the change from the accretionary to the collisional phase in the Damara Orogeny. If this is true, then exhumation-related deformation and retrogression of the Khomas accretionary prism was concentrated on discrete D_2 structures, as continental crust entered the subduction zone. As a result, the individual lithotectonic units that make up the SMZ show very little evidence for the (probably short-lived) collision between the Kalahari and Congo Cratons, and deformation features related to the accretionary phases are remarkably well preserved.

The rocks in the Gaub Canyon are therefore an impressive natural laboratory for studying subduction zone fault-processes below the brittle-viscous transition at scale unmatched by other exhumed accretionary analogues. It is shown that dislocation creep is the dominant deformation mechanism operating at temperatures $>500°C$. Dissolution-precipitation creep is also believed to be an important deformation mechanism; however, its occurrence appears to be limited to the larger shear zones. Both of these deformation mechanisms are also aseismic and these observations therefore generally agree with the observed decrease in seismic coupling below active seismogenic zones. There is nevertheless a predominance of mixed-mode, brittle-viscous deformation, with localised brittle deformation evident at micro- and meso-scales. This type of deformation regime has been suggested to account for the phenomenona of slow slip and episodic non-volcanic tremor observed at depths and temperatures spanning (and below) the seismic-to-aseismic transition in many contemporary subduction zones.

Acknowledgements

Completing this thesis would not have been possible without the support of a number of people.

I owe a great deal of thanks to my two supervisors, Dr. Åke Fagereng and Dr. Johann Diener. Your support, guidance, advice and critisism have been invaluable, and your enthusiasm for this research has inspired me to do my best. The National Research Foundation (NRF) is acknowledged for financial support throughout the past year. I would like to thank Dr. Roy Miller and the rest of the Namibian Geological Survey for leading an inspiring field trip across the Damara Belt in August which opened my eyes to the beauty and complexities of Namibian Precambrian geology. Dr. Reiner Klemd is also thanked for interesting discussions on subduction.

Thanks to Graeme Hillary for his help in the field and for keeping the thieving jackal at bay; and my office mates, Greg, Sukey, Tebz, Chelsea and Paiva for the daily distractions. Thanks also to Byron Coetsee for helping out when Python was not cooperating. Thanks also to Lesley Jennings for reading and commenting on an early draft of this thesis.

None of this would have been possible without the support of my parents whose constant encouragement gave me the motivation I needed to get this done. Thanks for proof reading and making this thesis as good as possible!

Contents

List of Tables

List of Figures

Chapter 1

Introduction

At subduction zones, cold oceanic lithosphere is subducted beneath an overriding lithospheric plate. Subduction zones are therefore characterised by relatively low geothermal gradients (Peacock, 1996; Brown, 2006) and the subduction plate-boundary fault is characterised by a much broader seismogenic zone than in other crustal faults. The seismogenic zone is defined as the part of the fault capable of generating earthquakes, and is generally confined to a portion of the plate interface above and below which aseismic deformation predominates (Hyndman *et al.*, 1997; Hyndman, 2007). As earthquake moment release is related to rupture area (Aki, 1967; Kanamori & Anderson, 1975), some of the largest and most devasting earthquakes in recorded history have occurred along these faults, such as the M_w 9.1 Sumatra-Andaman earthquake in December 2004 (Lay *et al.*, 2005) or the M_w 9.0 Tohoku-Oki earthquake of March 2011 (Ide *et al.*, 2011). The seismic behaviour of the subduction fault zone, and the inherent natural hazard, is controlled by the combination of fault processes occurring within it (Sibson, 1986; Fagereng, 2011a); and understanding the processes of rock deformation in these environments is a fundamental step towards mitigating the risks associated with these natural hazards.

Accretionary prisms form at subduction zones where sea-floor sediment is scraped off the down-going lithospheric plate to form a wedge of highly sheared, marine and trench-fill sediment, along with fragments of oceanic crust (e.g. Sample & Fisher, 1986; Kimura & Mukai, 1991; Kimura *et al.*, 1996). They overlie the megathrust, and therefore the internal structures form part of the plate-boundary fault system (Davis *et al.*, 1983). The structures preserved in these complexes thus contain a record of the deformation processes occurring within the subduction megathrust (Moore *et al.*, 2007). Accretionary prisms are often characterised by occurrences of highly disrupted mixed-rock assemblages called a mélange (e.g. Cowan, 1985; Needham, 1995; Kimura *et al.*, 2012). The chaotic nature of these mélanges and association with shavings of oceanic crust lead to the interpretation that they formed in the subduction plate-boundary fault (Cowan, 1985). The processes of mélange formation are therefore a good indication of the processes occurring in the subduction megathrust (Fagereng, 2011a;

Kimura *et al.*, 2012).

Because of this, Phanerozoic accretionary complexes have been the focus of many detailed studies since the 1980s (Davis *et al.*, 1983; Moore & Byrne, 1987; Byrne & Fisher, 1990; Kimura *et al.*, 1996; Kusky & Bradley, 1999; Ujiie, 2002; Meneghini & Moore, 2007; Fagereng, 2011a), with the aim of identifying the deformation processes occurring in and around the earthquake source region. Regional-scale seismic imaging (e.g. Westbrook *et al.*, 1988; Strasser *et al.*, 2009) has been invaluable in characterising the large-scale geometry of accretionary prisms and describing how relative plate motion is accommodated by the accretionary wedge (Davis *et al.*, 1983). However, the hectometre- to kilometre-scale wavelengths of the seismic radiation mean that resolution is low, and cannot provide any information on smaller, grain- to outcrop-scale processes such as the physical mechanisms of rock deformation (e.g. Sibson, 1986). Such mechanistic information is gathered through studies of exhumed accretionary analogues. These studies have been commonly limited to exposed portions of actively forming accretionary prisms, where peak metamorphism does not typically exceed greenschist facies (e.g. Shimanto Belt and Chrystalls Beach Complex: Ujiie, 2002; Fagereng, 2011a), or older exhumed accretionary terranes where outcrop is limited (e.g. Kodiak Island and the Franciscan Complex: Kimura & Mukai, 1991; Kusky & Bradley, 1999; Meneghini & Moore, 2007). Such work has provided a great deal of information on the deformation processes occurring on the 1-100 m length scales. However, the broader context for these studies is often inferred or lacking and is usually limited to depths <15 km and temperature <300°C. There is therefore a distinct lack of knowledge of the hectometre- to kilometre-scale deformation processes operating below these depth and temperature conditions on actively accreting margins.

Speculation on the behaviour of the subduction megathrust at temperatures and depths greater than 300°C and 15 km is generated through observation of changes in seismic style from dominantly seismic to aseismic slip, and rupture limits during large earthquakes (Hyndman *et al.*, 1995; Oleskevich *et al.*, 1999; Hyndman, 2013). These changes, at the down-dip limit of seismogenic zone, are believed to be thermally controlled, occurring over the temperature range of 350-450°C and therefore over the brittle-viscous transition (Hyndman & Wang, 1993). The brittle-viscous transition is a mechanical boundary in crustal faults (Scholz, 1988). It is not a sharp boundary but rather a diffuse zone over which there is a change in the dominant deformation mechanism and mechanical behaviour (Chapter 2): from dominantly localised frictional sliding to distributed aseismic viscous creep (Sibson, 1986). However, within this transition zone, both modes of deformation are possible. Monitoring of extensive geodetic and seismic networks has indirectly constrained the depths at which this transition occurs along active subduction margins (e.g. 30-to-40 km along the Cascadia margin: Hyndman, 2013). A physical basis for these observations, and the precise changes in the nature of the rocks in the megathrust at these depth and temperature conditions, are not well understood (Schwartz & Rokosky, 2007). Part of the reason for this is a lack of well

exposed natural analogues exhumed from these depth and temperature conditions.

The deeper parts of accretionary prisms are not exposed on actively accreting margins and more deeply buried exhumed analogues are often found in collisional orogenic belts where mélanges are often preserved in palaeo-sutures (e.g. The Apennines and European Alps Vannucchi & Bettelli, 2002; Bachmann *et al.*, 2009). In these places, the geometry of the original subduction fabrics are, however, often strongly overprinted by structures related to post-subduction shortening (Bachmann *et al.*, 2009). One notable exception to this is the Pan-African Damara Belt (Figure 1.1) which preserves a 100-km wide section of deeply eroded rocks that formed as a Neoproterozoic accretionary prism, and has experienced very little post-subduction shortening (Meneghini *et al.*, 2014).

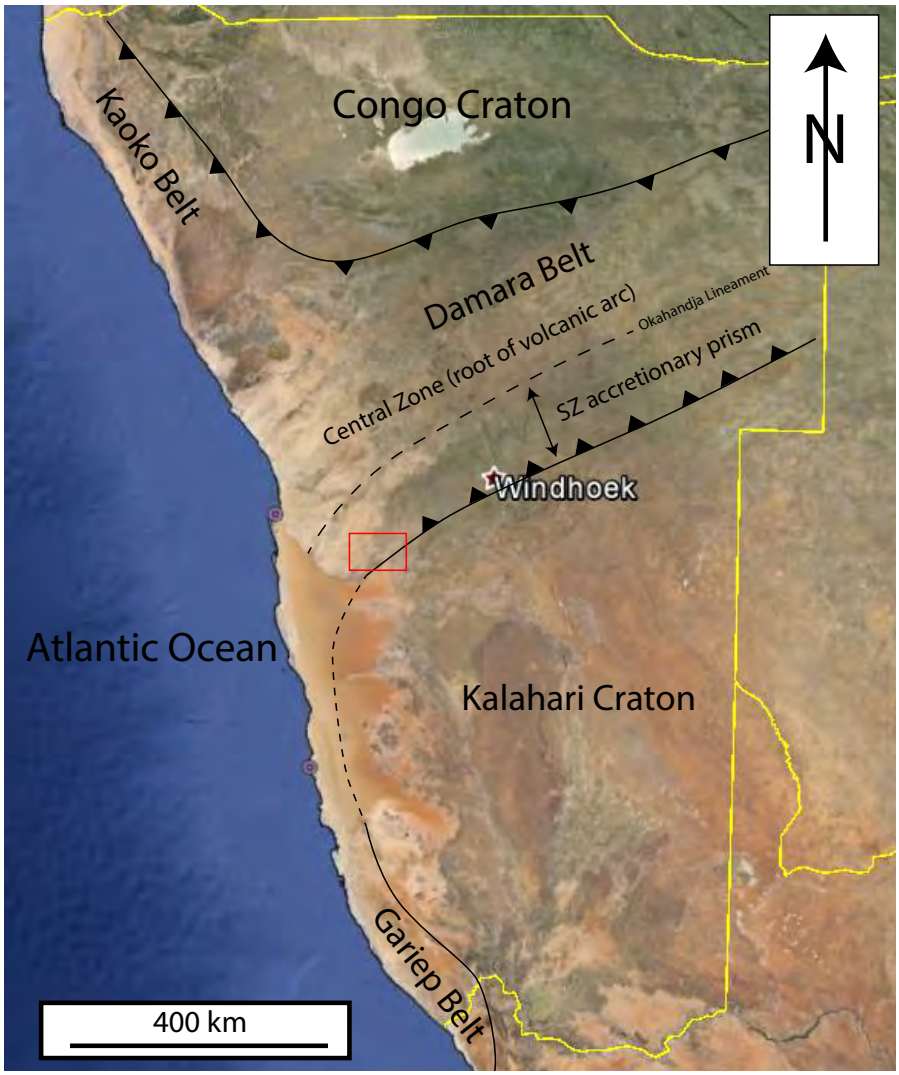

Figure 1.1: The location of the Damara Belt. Annonated image from Google Earth showing the position and orientation of the Damara Belt between the Kalahari and Congo Cratons. Red box marks the position of the study area shown in Figure 1.2.

1.1 Study Area: The Gaub Canyon

The rocks of the Southern Zone (SZ) of the Damara Belt in central Namibia (Figure 1.1) have been reported as one of the best preserved Precambrian accretionary prims (Khomas-Hochland accretionary prism; Kukla & Stanistreet, 1991) which formed during convergence of the Kalahari and Congo Cratons (Figure 1.1; Kukla & Stanistreet, 1991; Gray *et al.*, 2007; Cross, 2013; Meneghini *et al.*, 2014). The SMZ forms the boundary between the SZ accretionary prism (upper plate) and the Kalahari basement (lower plate)(Figure 1.2) and may therefore contain the remnants of the Neoproterozoic plate-boundary fault. Regional high-pressure low-temperature (HP/LT) metamorphism dominates the Southern Zone (SZ) and the Southern Marginal Zone (SMZ) (Chapter 4) with an apparent geothermal gradient of $\sim 18°C.km^{-1}$ and an apparent depth of ~30 km (Kasch, 1983b; Cross, 2013) indicative of subduction environments (Miyashiro, 1973; Brown, 2006). As yet, however, no characteristic mélange deposits have been documented in SZ and SMZ. If the SMZ does indeed contain the mélange related subduction phase of the Damara Orogeny, then these may be one of the best exposed and deeply exhumed subduction mélanges on Earth.

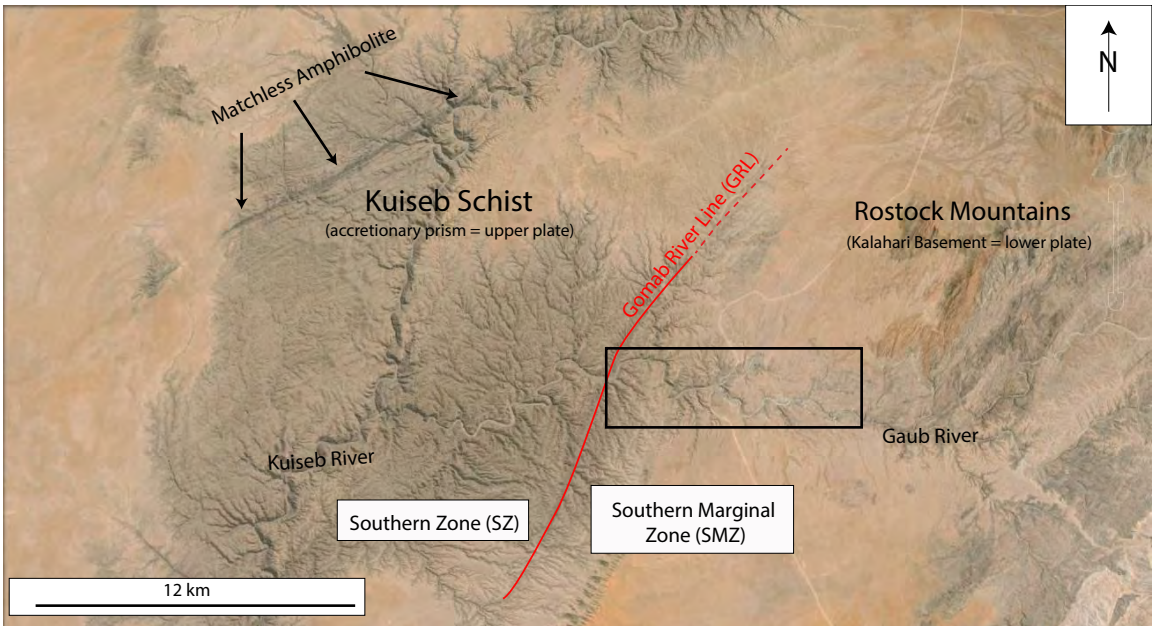

Figure 1.2: Images modified from Google Earth showing the location of the Gaub River Canyon from a regional perspective along with the position of a number of important geographic and geological features. The field area in the box is located approximately 50 km as the crow flies NW of Solitaire (just out of the image).

The Gaub River runs from east to west across central Namibia, joining the Kuiseb River at the confluence near the northern margin of the Namib dune desert (Figures 1.1 and 1.2). Along its course, the Gaub River carves out a canyon through the entire SMZ, exposing a sequence of rocks from the Kalahari Craton basement through to the SZ accretionary prism.

The study area (Figure 1.2) is located approximately 50 km northwest of the town of Solitaire in central Namibia, straddling the boundary between the Khomas and Erongo Provinces. In this area the Gaub Canyon intersects 8 km of the SMZ, between the Rostock Mountains inlier (Kalahari Craton) and its boundary with the Kuiseb Schist of the SZ (marked by the Gomab River line; Figure 1.2). The location and orientation of the canyon is such that it cuts through a near complete section of the SMZ approximately perpendicular to the main structural grain of the rocks in the area. With 8 km of continuous exposure, the Gaub Canyon provides an ideal transect for investigating the structural geology of the rocks of the SMZ. Given the depth of burial and metamorphic grade of thes rocks, they are an ideal natural analogue for examining the deformation processes occurring at depth in modern accretionary margins, at a scale and resolution that cannot be retrieved in most modern and ancient accretionary terranes.

1.2 Aims for this Thesis

Based on the aforementioned context, the main aims of this study are to compile a detailed structural map of the rocks of the Gaub Canyon between the Rostock mountain inlier and the Gomab River Line (GRL). It will focus on the distribution of various rock types and the geometry of planar and linear rock fabrics as well as distribution of strain within the SMZ, as gauged by the spatial relationships and relative intensity of these fabrics. This information will be used to determine regional shortening and/or extension directions and the kinematic history of the rocks in this area. These observations will then be compared and contrasted with rock fabrics developed in other known modern and ancient accretionary mélanges. Given the medium- to high-grade nature of these rocks (Chapter 4; Kasch, 1983b; Cross, 2013), the map and structural data gathered will be used to draw conclusions and implications on the nature and mechanical behaviour of the subduction megathrust at depths and temperatures below the brittle-viscous transition. Specific questions that will be addressed are:

1. What are the deformation mechanisms operating at depths and temperatures below the brittle-viscous transition along active subduction zones?

2. How is the change from frictional to viscous regimes accommodated on earlier formed structures, and what changes occur in the plate boundary fault over this transition?

3. How is this deformation accommodated by different rock types, and what implications does this have for the array of seismic signals observed at active subduction zones?

The Damara Belt is also widely regarded as the root zone of a Proterozoic orogen (Figure 1.1; Gray *et al.*, 2007; Miller, 2008) and the exhumation history is not well constrained. This study therefore also aims to assess the effect that continental collision has had on the preservation of accretion-related fabrics in the SMZ. Some further questions that will be addressed are:

1. Which fabrics are related to subduction and collision-exhumation phases, and how do the collisional fabrics overprint the earlier ones?

2. Under what conditions did exhumation occur?

In addressing the issues and questions raised above, this study aims to extend the current knowledge on accretionary deformation processes below the brittle-viscous transition, as well as the tectonic evolution of this part of the Damara Belt.

Chapter 2

Fault Rocks and Deformation Mechanisms

Before the data are presented it is necessary to review some key concepts that will be drawn on in the discussions that follow. The work is focused on rock deformation and the resultant structures. This chapter reviews general concepts related to the mechanisms by which deformation is accommodated in rocks and the structures that are left behind. The focus of Chapter 3 is more specific to accretionary prisms and will relate many of the concepts discussed in this chapter to these environments.

The deformation mechanisms active within a rock produce characteristic structures/microstructures that form in response to tectonic stress, and vary with a number of physical and envronmental factors including mineralogy, grain-size, temperature, pressure, fluid pressure, differential stress and strain rate. Mineral deformation mechanisms generally fall into three categories (Engelder, 1974; McClay, 1977; Knipe, 1989; Passchier & Trouw, 2005):

1. Cataclastic flow - deformation involving microcracking, fracturing and frictional sliding;
2. Diffusive mass transfer (DMT) - accommodates strain through the redistribution of material along stress-induced chemical potential gradients;
3. Crystal plasticity - internal deformation of crystals through the movement of lattice line defects and twinning.

2.1 Brittle Deformation

Brittle deformation is defined as a permanent change in a solid material (rock) by growth of fractures or frictional sliding (Van der Pluijm & Marshak, 2004), and is therefore discontinuous by nature. When separation of originally joined bodies occurs it is termed "fracturing"; and "faulting" when there is shear displacement (slip) across the discontinuity.

2.1.1 Stress

Stress is defined as a force per unit area (Van der Pluijm & Marshak, 2004) and is fundamental in dynamic analysis and the interpretation of brittle structures in rock. Stress on a plane is a vector and therefore has both a magnitude and an orientation. Stress at a point is defined by all the stress vectors associated with an infinite number of planes of different orientations passing through that point (Jaeger & Cook, 1979; Twiss & Moores, 1992; Marrett & Peacock, 1999; Gudmundsson, 2011). For any given stress state there will then be three mutually perpendicular planes which have zero resolved shear stress. These planes are termed the principal planes of stress, the normals to which represent the principal stress components σ_1, σ_2 and σ_3, where σ_1 is the greatest principal compressive stress, σ_2 is the intermediate principal stress and σ_3 is the minimum principal stress, so that $\sigma_1 \geq \sigma_2 \geq \sigma_3$. Stress at a point is therefore a second-order tensor quantity and is fully described in terms of a nine-component matrix in three dimensions, or a four-component matrix in two dimensions (Twiss & Moores, 1992; Gudmundsson, 2011), as shown in Figure 2.1.

For geological purposes it is useful to simplify problems down to two dimensions as it is rare that one has enough information to solve for the full three-dimensional stress state. A common simplifying assumption in the interpretation of brittle structures, such as fractures and veins, is that they contain the intermediate principal stress (σ_2) and thus these structures can be analysed solely in terms of the orientations of σ_1 and σ_3 (e.g. Anderson, 1951; Sibson, 1998). However, further estimations have to be made to calculate magnitudes, as these may vary depending on the physical properties of the rock in which the structures occur, as well as other environmental variables such as temperature, pressure and fluid pressure. Experimental deformation experiments and rock mechanics have been invaluable in this regard.

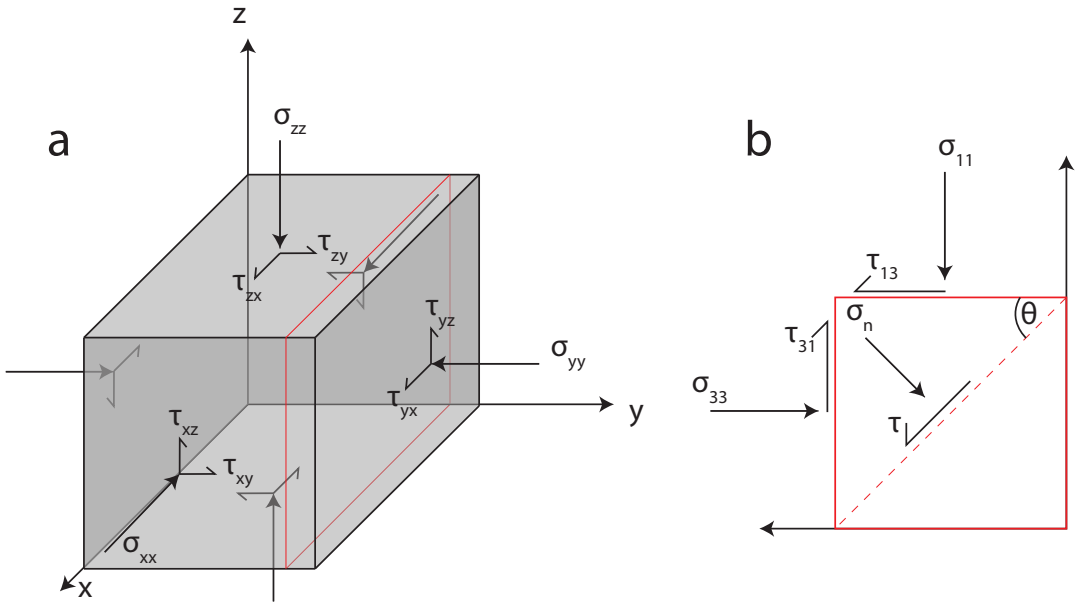

Figure 2.1: a) Three-dimensional stress state at a point in Cartesian coordinates, x,y,z. b) Two-dimensional stress on a plane at angle θ to the principal stresses. Note that this projection assumes that the plane under consideration (dashed red line) contains the intermediate principal stress.

2.1.2 Fracture Mechanics

Rock mechanics and structural geology have focused historically on providing methods for predicting the failure strength of any rock, and the geometry of structures that form within it under certain stress and physical conditions (Jaeger & Cook, 1979; Lockner, 1995). Many of these methods are commonly employed in dynamic analysis (Twiss & Moores, 1992; Marrett & Peacock, 1999). Theories developed experimentally by rock mechanics on laboratory scale tests have been applied successfully to geological scale stress sytems (Anderson, 1951; Hubbert & Rubey, 1959; Brace, 1960; Sibson, 1985, 1998). The simplest and most effective of these is the empirical Griffth-Coulomb failure criterion, which is widely applied to explain the formation of macroscopic brittle structures such as extension veins, dilational-shears and faults (and combinations of these); it is also extended to account for reshear on existing fault planes (e.g. Sibson, 1985, 2012).

Griffith-Coulomb failure criterion and the Mohr Diagram

The three macroscopic modes of brittle failure recognised for intact isotropic rocks are: (1) tensile fracture, (2) hybrid tensile-shear fractures and (3) Coulomb shear fractures or faults (Figure 2.2). All these failure modes are fluid pressure dependent, therefore emprical relationships describing the stress conditions required for failure are combined with the law of effective stress to define the failure conditions (Sibson, 2003). The law of effective stress states that, for a fluid saturated rock mass with interconnected pore space, normal stresses are reduced to effective values (Rice & Cleary, 1976):

$$\sigma'_n = (\sigma_n - \alpha P_f), \tag{2.1}$$

where α represents a poroelastic parameter usually taken as unity, and P_f is the fluid pressure (Hubbert & Rubey, 1959). The effective principle compressive stresses then become:

$$\sigma'_1 = (\sigma_1 - P_f) \geq \sigma'_2 = (\sigma_2 - P_f) \geq \sigma'_3 = (\sigma_3 - P_f). \tag{2.2}$$

The failure envelope of the Mohr diagram is constructed by combining the parabolic Griffith criterion and the linear Coulomb failure criterion. The Griffith failure criterion accounts for tensile-shear failure ($\sigma'_n < 0$), where T is the tensile strength:

$$\tau^2 = 4\sigma'_n T + 4T^2. \tag{2.3}$$

The Coulomb failure criterion accounts for compressional-shear failure ($\sigma'_n > 0$):

$$\tau = C_0 + \mu_i(\sigma'_n), \tag{2.4}$$

where τ is the shear stress on fault at failure, C_0 is a constant representing the cohesive strength of the rock ($\sim 2T$), σ'_n is the effective normal stress on the fault, and μ_i is a constant representing the internal coefficient of friction. Rock failure is therefore dependent on the physical stress conditions as well as the physical properties of the given rock mass.

A rock will fail when the applied compressive shear or tensile stress exceeds the strength of the rock; when the edge of the Mohr circle touches the failure envelope (Jaeger & Cook, 1979). Failure of intact isotropic rock therefore depends on the size of the Mohr circle (differential stress = $\sigma_1 - \sigma_3$) and the fluid pressure, because increased fluid pressure decreases the magnitude of all principal stresses (Equations 2.1 and 2.2), pushing the Mohr circle towards the tensile field of the diagram.

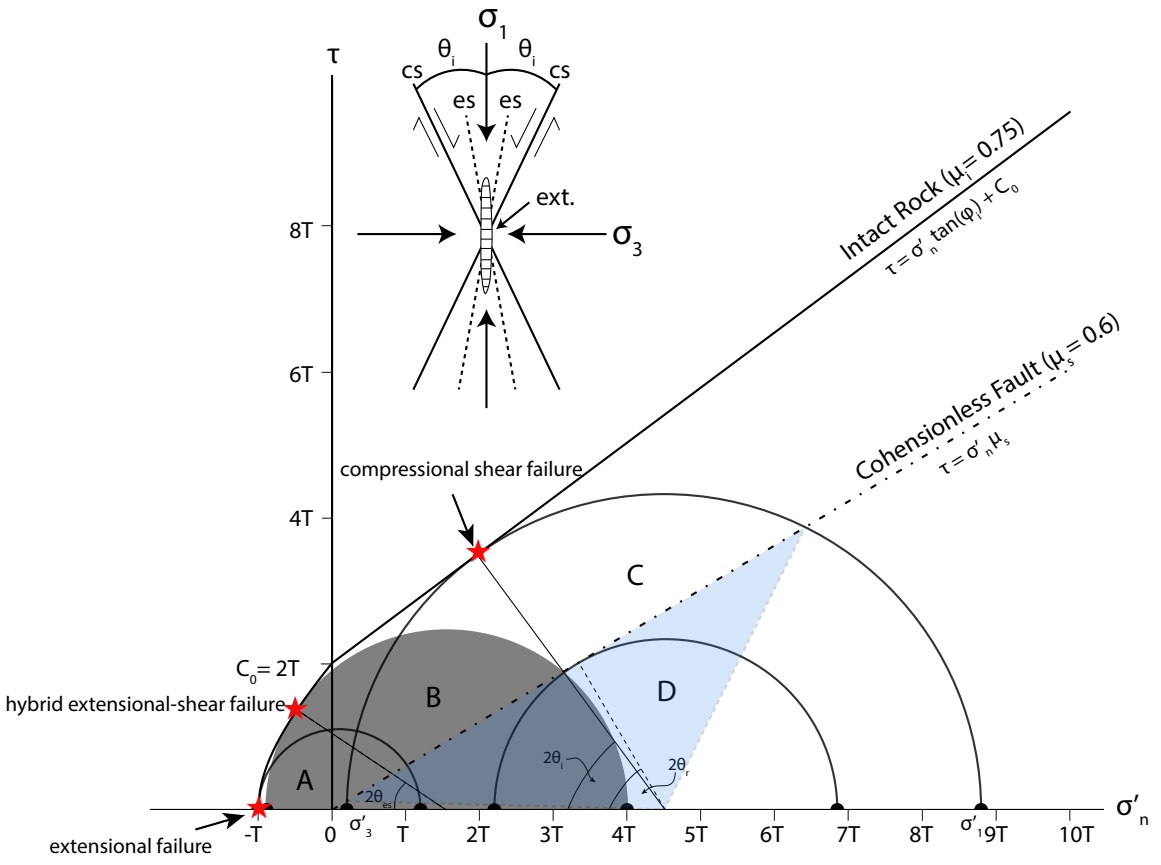

Figure 2.2: Mohr diagram containing the composite Griffith-Coulomb failure envelope for intact isotropic rock with internal coefficient of friction (μ_i) and a pre-existing fracture with static coefficient of friction (μ_s) after Sibson (1998) and Scholz (2002). Circles A, B and C show the neccessary relationship between shear stress (τ) and effective normal stress (σ'_n) required to promote the various modes of brittle failure (red stars), while D shows the conditions required for reshear of a pre-existing fault. Note that, for the stress state depicted in C, pre-existing faults with 2θ orientations lying in the range defined by the shaded blue area will be re-activated prior to the formation of new fractures.

Formation of new fractures and faults

Pure tensile failure or hydraulic extension failure occurs if $\sigma_3 = -T$ or, if $\sigma_3 > -T$, $P_f = \sigma_3 + T$ (Jaeger & Cook, 1979; Sibson, 1998). As shown by stress state A in Figure 2.2, these fractures form planes of zero shear stress ($\tau = 0$) at right angles to σ_3 and therefore usually contain both σ_1 and σ_2. The widespread occurrence of extension fractures in the crust suggests that, at least locally and transiently, these stress and fluid pressure conditions are met (Sibson, 1998, 2003; Bons *et al.*, 2012). Hybrid tensile-shear failure still requires that $\sigma_3' < 0$ although here, the conditions $\tau \neq 0$ and $\sigma_3' > -T$ must also be satisfied. They therefore form under mixed compressive-tensile stress states and are considered an intermediate between pure extension and shear fractures (Stress state B in Figure 2.2; Ramsey & Chester, 2004).

When shear failure takes place according to the Coulomb failure criterion in intact isotropic rock, it will create two conjugate planes containing σ_2 at an angle θ_i to the maximum principle compressive stress (σ_1). The value of θ_i depends on the slope of the Coulomb failure envelope (Jaeger & Cook, 1979; Scholz, 2002) and is therefore a function of μ_i:

$$\theta_i = 45^\circ - \frac{tan^{-1}(\mu_i)}{2}. \tag{2.5}$$

On the Mohr diagram this is shown as an angle $2\theta_i$ (stress state C), which represents the angle between two conjugate faults that are bisected by the greatest principle compressive stress, σ_1 (Figure 2.2).

Anderson (1951) proposed a theory of faulting in terms of the Coulomb failure criterion, with the underlying assumption that the Earth's surface (approximated as a flat geometrical plane with no topography) is a plane of zero shear stress and therefore a principal plane of stress. In this scenario one of the principal compressive stresses must be orientated perpendicular to the Earth's surface which will therefore contain the other two;, although this may not always be the case (e.g. Blenkinsop, 2008). However, following Anderson (1951), one recognises three possible fault systems corresponding to which of the principal compressive stresses is vertical: thrust faults if σ_1 is vertical, normal faults if σ_3 is vertical, and strike-slip faults if σ_2 is vertical (Figure 2.3).

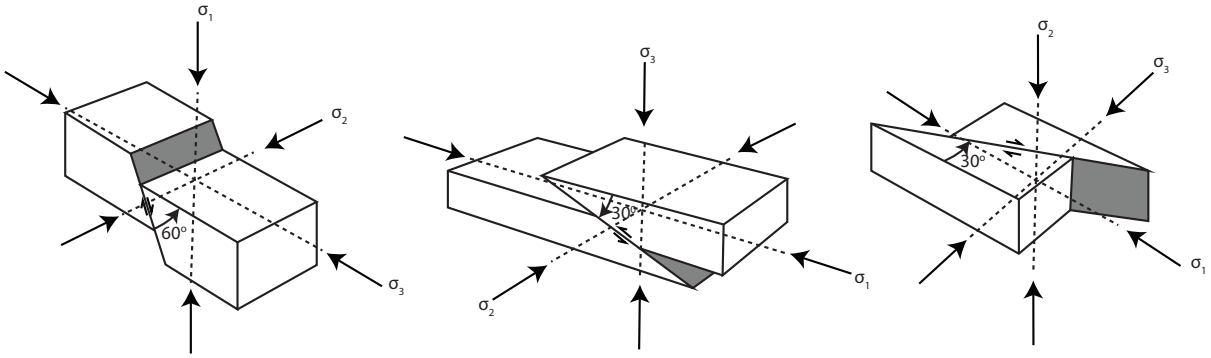

Figure 2.3: Three faulting regimes shown with their respective Andersonian stress fields after Twiss & Moores (1992). Note that in all cases the intermediate principle stress, σ_2, lies in the plane of the fault.

Reactivation of pre-existing planes of weakness

It is common in areas that have experienced multiple deformation episodes for there to be pre-existing structures that are reactivated during later deformation events. Departure from Andersonian fault orientations is evident from the presence of high angle reverse faults and low angle normal faults (e.g. Wernicke, 1995) and are generally interpreted to occur as a result of fault reactivation (Sibson, 1985, and references therein). The criterion for frictional reactivation of a pre-existing fault lacking cohesive strength (Sibson, 1985; Scholz, 2002; Sibson, 2009, 2012) is:

$$\tau = \mu_s \sigma'_n = \mu_s(\sigma_n - P_f), \tag{2.6}$$

where τ and σ'_n are again the shear and effective normal stresses acting on the fault, and μ_s is the static coefficient of friction. μ_s is generally taken at the lower end of the Byerlee (1978) range of $0.6 < \mu_s < 0.8$. Pre-existing structures are also likely to have less cohesion than the surrounding intact rock (Figure 2.2). The consequence of this is that the differential stress required for reactivation of pre-existing faults (stress state D in Figure 2.2) is less than that required for formation of new faults (stress state C in Figure 2.2), as the shear strength of the pre-existing faults is less than that of the surrounding intact rock (Figure 2.2). Therefore pre-existing faults will become reactivated before failure of the surrounding intact rock, provided that these structures are suitably orientated for reshear in the prevailing stress field (Sibson, 1985).

To assess whether a fault is optimally orientated for reactivation, it is useful to re-define the previous equation in terms of the principle stresses. Doing so, Sibson (1985) shows that the stress ratio R, required for reactivation of a cohesionless fault that contains σ_2, is a function of μ_s and reactivation angle θ_r:

$$R = \frac{\sigma_1'}{\sigma_3'} = \frac{(1 + \mu_s cot\theta_r)}{(1 - \mu_s tan\theta_r)}. \tag{2.7}$$

R obtains a minimum value at $R^* = (\sqrt{1 + \mu_s^2} + \mu_s)^2$ which occurs at the optimal angle for reactivation $\theta_r^* = 0.5tan^{-1}(\frac{1}{\mu_s})$, and tends to infinity as θ_r approaches 0 and $2\theta_r^*$. The minimum stress ratio and optimal angle of reactivation therefore vary as a function of μ_s; $R^* \sim 3$ and $\theta^* \sim 29.5$ when $\mu_s = 0.6$.

If a compressional Andersonian stress regime is assumed ($\sigma_v = \sigma_3$), then Equation 2.6 can be reformulated in terms of differential stress and the fluid pressure state, given by the pore fluid factor $\lambda_v = P_f/\sigma_v$, thus allowing for assessment of the effect of fluid pressure and the reactivation angle on the differential stress required for reactivation at a given depth (Sibson, 2009, 2012):

$$\sigma_1 - \sigma_3 = \mu_s(\frac{tan\theta_r + cot\theta_r}{1 - \mu_s tan\theta_r})\rho g z(1 - \lambda_v). \tag{2.8}$$

Equations 2.7 and 2.8 above show that differential stresses required for reactivation attain a minimum value when: (1) faults are optimally orientated for reshear in the prevailing stress field, (2) fluid pressures are high, and (3) μ_s is low, owing to the presence of weak minerals for instance (e.g. Niemeijer & Spiers, 2005). The potential for reactivation is therefore significantly increased when these conditions are met. The latter two are also generally cited as reasons for the presence of 'weak' faults that are severely misorientated for shear in the prevailing stress field (e.g. Sibson, 1985; Zoback *et al.*, 1987; Collettini *et al.*, 2009; Fagereng *et al.*, 2010)

2.2 Ductile Deformation

Ductile deformation is here defined as deformation that is macroscopically continuous at the scale of observation. Shear zones are therefore included as ductile structures even though they may represent major regional scale discontinuities that have accommodated kilometers of displacement.

2.2.1 Strain

Strain is a change in shape. If all parts of an object of some initial dimensions experienced the same strain, it is termed homogeneous strain. If different parts of an object experience different strains, it is termed heterogenous strain (Ramsay, 1980; Van der Pluijm & Marshak, 2004). In a geological context strain is rarely homogenous (due to strain localisation etc.); however, heterogenous deformation can still be analysed by separating a heterogenously deformed body into homogenously deformed regions. The degree to which the strain of a given area can be described in terms of homogenous deformation therefore depends on the scale of strain localisation and the scale of observation. At a fundamental level, the strain experienced by an object is defined by the change in length of lines within that object. For the purpose of this study it is not neccesary to go into too much detail on these precise methods. Of more relevance is the concept of the strain ellipsoid.

The strain ellipsoid is a graphical representation of the distortion experience by any entity, such as a body of rock, undergoing homogeneous strain. Consider the 2-dimensional case of a unit circle, such as the one depicted in Figure 2.4 below, undergoing homogeneous simple shear. During progressive shearing of the unit circle into an ellipse one can see that there are a set of lines that remain perpendicular to one another after straining. These lines define the axes of the ellipse and are termed the principal strain axes. The lengths of these axes define the strain magnitude and, in three dimensions, are defined as $X \geq Y \geq Z$ where X represents the line of greatest extension, Z is the line of greatest shortening, and Y is the intermediate strain axis (not shown). The final ellipse at time (2) represents the total accumulated strain and is termed the finite strain ellipse. Superimposing this onto the unstrained unit circle, one sees that there is a pair of lines that experiences zero length change. These lines of zero finite extension separate the regions of finite shortening and finite extension in strain ellipse. Other material lines are depicted as dashed lines. In the simple shear case, the incremental strain (X_1 and Z_1; Figure 2.4) axes rotate relative to the finite strain axes (X_2 and Z_2; Figure 2.4). Because of this rotation of incremental strain axes, lines initially at high angles to the XY plane will experience shortening followed by extension, while lines at low angles to the XY plane will experience extension followed by shortening. Structures reflecting different strain states may therefore develop in non-coaxial shearing.
For the case of pure shear, the incremental strain axes remain parallel to the finite strain

axes and there is therefore no rotation of these lines. This is also termed coaxial shear. However, lines at angles to the axis of greatest shortening or extension are progressively rotated towards the XY plane of the strain ellipsoid. In the case of vertical loading, lines at high angles to the XY plane of the strain ellipsoid will initially experience shortening, but with progressive deformation these lines will be progressively rotated into parallelism with the XY plane, resulting in increasing extension.

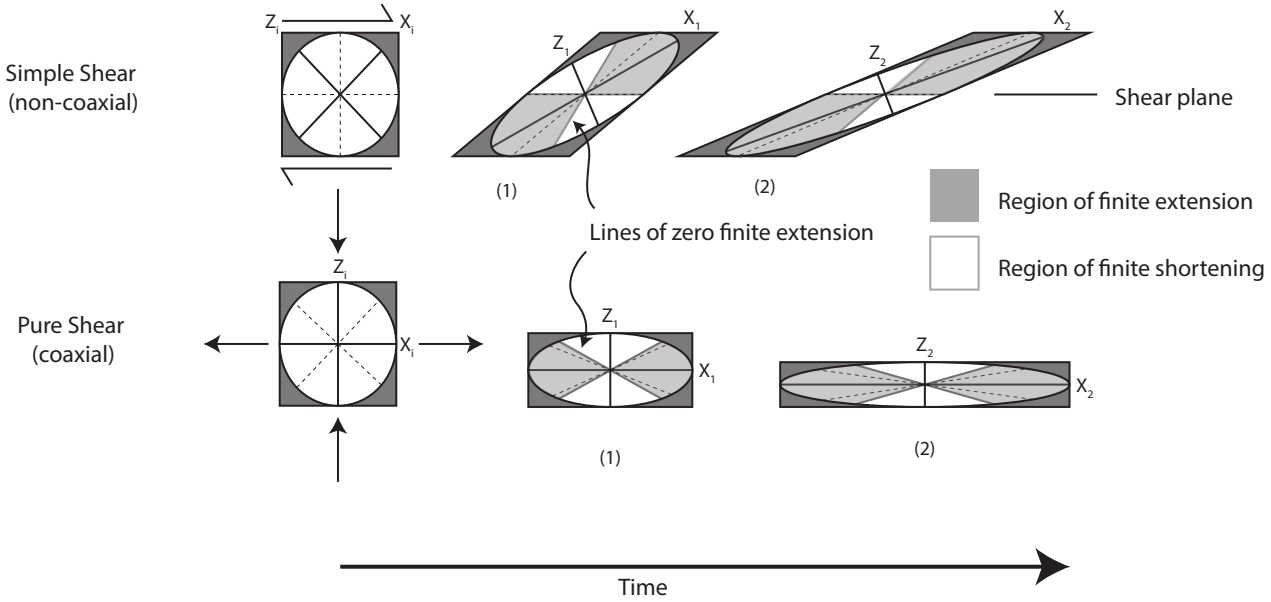

Figure 2.4: 2D diagram from Van der Pluijm & Marshak (2004) showing the different effects of pure and simple shear on the orientations of the principal axes of the finite strain ellipse (solid lines) and other material lines (dashed lines). Note in this 2D illustration the Y axis of the strain ellipsoid is not shown but is perpendicular to both X and Z and therefore trends into the plane of page.

2.2.2 Ductile Shear Zones

Ductile shear zones are tabular zones of macroscopically continuous rock deforming between two subparallel shear zone walls outside of which relatively little or no deformation occurs (Ramsay, 1980; White *et al.*, 1980; Fagereng, 2013). They are common features of regional metamorphic terranes of greenschist facies or higher.

Shear zone geometry

The geometry of a shear zone, away from its end-points is idealised in the following manner; (1) the shear zone walls are parallel; (2) deformation is continuous throughout the shear zone; and (3) the displacement and finite strain profiles in any cross-section through the shear zone

are identical (Ramsay, 1980). From these boundary conditions, assuming homogeneous simple shear, the structural elements observed in ductile shear zones can be related to displacement and finite strain, given that the Y axis of the finite strain ellipsoid lies in a plane parallel to the shear zone walls (Ramsay, 1980; Fagereng, 2013). It then follows that during simple shear parallel to the shear zone walls, shear strain (γ), distributed homogeneously over a shear zone of width w, will be related to the displacement s by;

$$\gamma = s/w. \tag{2.9}$$

In intact isotropic rock a shear zone will form at 45° to σ_1 (Figure 2.5) and should therefore develop an intial foliation perpendicular to σ_1 at 45° to the shear zone wall. During progressive simple shear the planar fabric within the shear zone would then track finite strain and rotate with the orientation of the X axis of the finite strain ellipse. The orientation of the planar fabric within the shear zone would then approximate the orientation of the XY plane of the finite strain ellipse. The angle it makes with the shear zone boundary θ' is therefore a function of finite shear strain:

$$tan2\theta' = 2/\gamma, \tag{2.10}$$

and if volume change occurs (Ramsay, 1980):

$$tan2\theta' = \frac{2\gamma(1+\Delta_v)}{1+\gamma^2-(1+\Delta_v)^2}. \tag{2.11}$$

From the equations above one can see that, as shear strain increases, the angle between the direction of finite stretching (X) and the shear zone margins (θ') decreases (Figure 2.6). Therefore with progressive deformation the foliation will be rotated into parallelism with the shear zone margins. The rate at which this occurs will depend on the strain rate and will therefore vary with the shear zone thickness as well as the far field displacement rate that is being acccommodated. However, it will also be accelerated if the deformation contains a component of pure shear (flattening) or if volume loss occurs (Figure 2.6c).

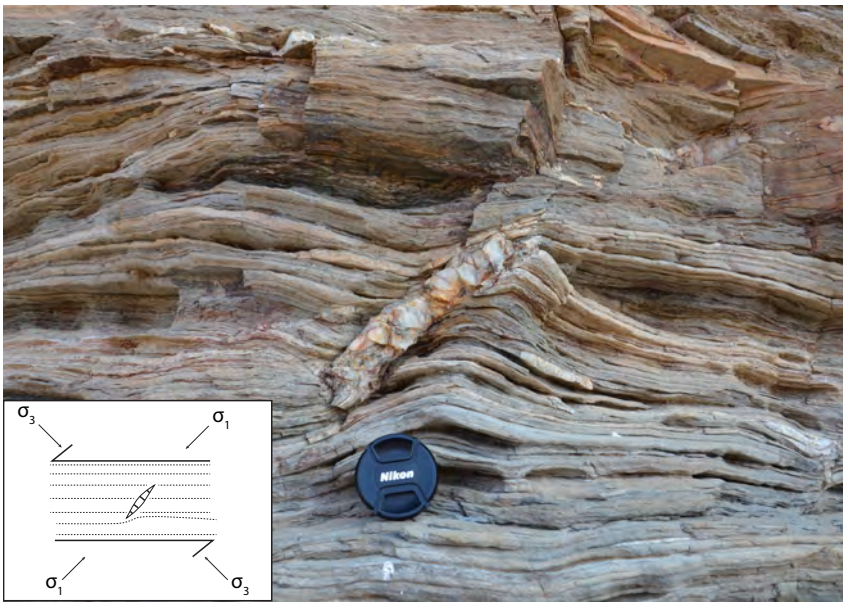

Figure 2.5: Tabular low angle reverse ductile shear zone from the Gaub Canyon. Inset highlights the geometry of the major structural features with respect to the principal stresses and shear directions. Quartz vein (extension fracture) orientated at approximately 45° to the shear zone walls. Note that the foliation inside the shear zone is approximately parallel to the margins indicating very high strain and/or volume loss.

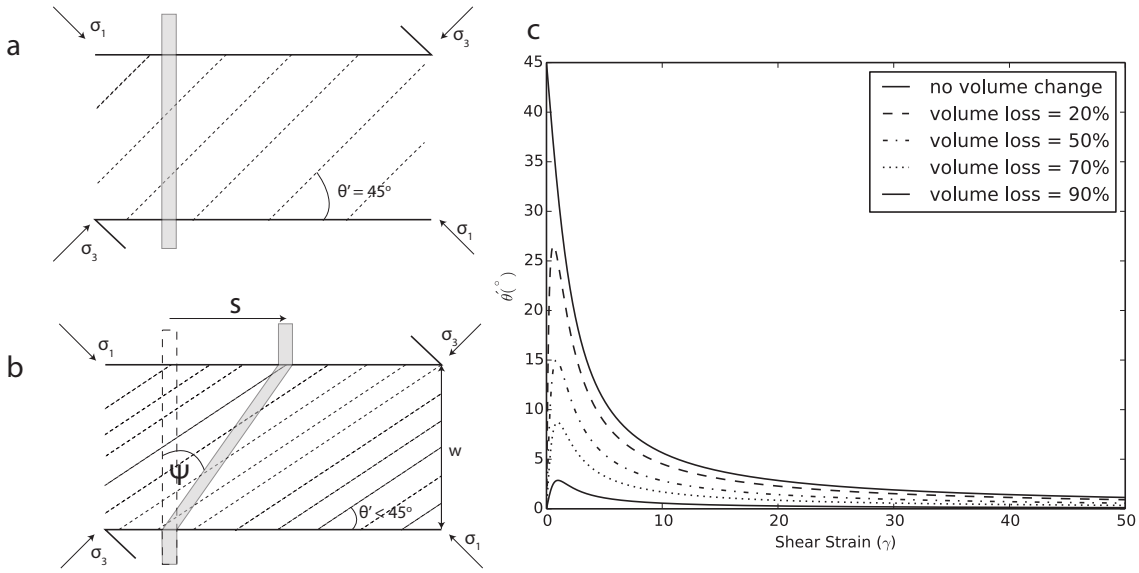

Figure 2.6: Idealised shear zone geometry (after Fagereng, 2013). a) Shear zone initially forms at time t_0 at 45° to σ_1 with foliation 45° to shear zone walls. b) At time $t > t_0$ a marker is displace by distance s, equating to angular shear Ψ. Foliation is now at <45° to shear zone walls. c) Graph of θ' vs γ at various values of Δ_v showing the effect of volume loss on θ'.

2.3 Fault-Zone Deformation Mechanisms

2.3.1 Independent particulate flow

Independent particulate flow or granular flow is a ductile flow mechanism which involves the frictional sliding of particles past one another while individual grains undergo rigid body rotation and remain undeformed (Borradaile, 1981; Fagereng & Toy, 2011). It will initiate when the friction between adjacent grains is overcome by an applied shear stress. Granular flow requires dilation and is therefore favoured under conditions of low confining pressure (low σ_n) and high fluid pressure; commonly occurring in unconsolidated or partially lithified, fluid saturated sediment at shallow depths (Knipe, 1989). It will therefore be suppressed at greater depth as σ_n increases, and compaction, dewatering, and diagenetic chemical reactions cause cementation and lithification, which act to increase cohesion and rigidity promoting elastic behaviour (Moore & Saffer, 2001; Fagereng & Toy, 2011).

2.3.2 Fracture processes

Fracturing requires nucleation, propagation and diplacement along newly formed surfaces during deformation and is associated with grain refinement through rigid-body rotation and fragmentation (Engelder, 1974; Knipe, 1989). Cataclastic flow occurs through progressive brittle fracturing along with frictional grain boundary sliding and rotation (Engelder, 1974; Sibson, 1986). This mechanism is mainly pressure dependent and is inhibited by high confining pressures (Sibson, 1986), although it may be assisted by raised fluid pressures through reduction of effective normal stress. This can occur rapidly during repeated transient high velocity (possibly seismic) events or by relatively slow fracturing of individual grains (Sibson, 1986). The finite intensity of cataclasis is generally gauged using the mean grain size (Engelder, 1974) or the proportion of clast to matrix material (Sibson, 1977) as both decrease with progressive deformation.

2.3.3 Diffusive Mass Transfer

The term diffusive mass transfer refers to ductile deformation mechanisms whereby material is transported along chemical potential gradients induced by differences in intergranular normal stress (McClay, 1977; Knipe, 1989). This is seen in deformed rock by the presence of dissolution structures such as truncated mineral grains and fossils, and stylolites, or sites of precipitation such as mineral overgrowths in boudin necks, fold hinges or pressure shadows and veins (McClay, 1977; Rutter, 1983; Knipe, 1989). A number of different mechanisms are recognised based on variation in the mode of material transfer (Knipe, 1989). If diffusion occurs through mineral grains it is called lattice diffusion or Nabarro-Herring Creep, whereas if diffusion occurs largely on grain boundaries it is termed grain-boundary diffusion or Coble Creep (McClay, 1977). These are thought to be important mechanisms at high temperature where solid-state diffusion rates are high; however, they are too slow at low temperature (200-

350°C). This is at odds with the strains observed in low grade metamorphic rocks (McClay, 1977). Fluid-assisted grain-boundary diffusion or dissolution-precipitation creep is therefore thought be an important mechanism in upper crustal fine-grained fault rocks where fluids are abundant and ambient temperatures are relatively low (McClay, 1977; Rutter, 1983; Passchier & Trouw, 2005).

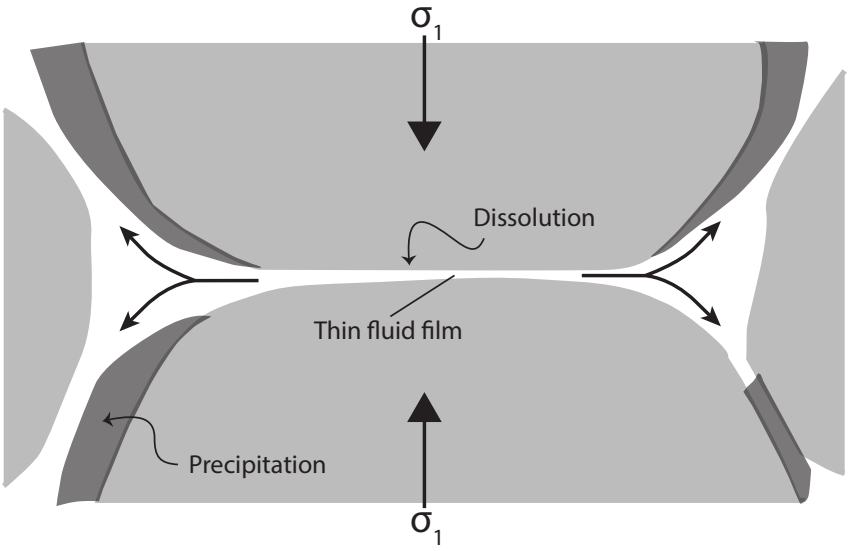

Figure 2.7: Grain-scale cartoon showing basic concepts of dissolution-precipitation creep after McClay (1977). Material is dissolved at sites of high normal stress (grain boundaries perpendicular to σ_1) where it is transported and deposited in areas of relatively low stress (grain boundaries at low angle to σ_1).

Dissolution-precipitation creep can be divided up into three phases: (1) Dissolution mechanisms control how material enters the diffusion path; (2) diffusion occurs where material migrates along a pathway; and (3) precipitation occurs where material is deposited (Figure 2.7 Rutter, 1983; Knipe, 1989; Shimizu, 1995; Gratier & Gueydan, 2007; Fagereng & Toy, 2011). The slowest of these mechanisms will be the rate limiting step and will therefore determine the kinetics of the whole process through one of the following constitutive creep laws (Gratier & Gueydan, 2007):

If the rate of dissolution or precipitation is the rate-limiting step:

$$\dot{\varepsilon} = \alpha k c V_s (\Delta\sigma_n)^n / RTd, \tag{2.12}$$

and if the rate of diffusion through the liquid phase is rate-limiting:

$$\dot{\varepsilon} = \beta D w c V_s (\Delta\sigma_n)^n / RTd^3, \tag{2.13}$$

where $\dot{\varepsilon}$ is the axial strain rate, α and β are constants that describe the geometry of the interface, and k is the kinetics constant for the dissolution/precipitation reaction (mol.m^{-2}.s^{-1}). c is the solubilty of the diffusing solid (mol.m^{-3}), V_s is the molar volume of the solid (m^3.mol^{-1}), D is the diffusion constant along the interface (m^2.s^{-1}), and w is the thickness of the fluid interface (m) along which diffusion occurs. R is the universal gas constant (8.32 m^3.Pa.mol^{-1}.K^{-1}), and T is the absolute temperature in (K). d is the size of the closed system of diffusion (m) which is commonly approximated by the grain size (e.g. Shimizu, 1995), although fracture spacing may be equally important (Gratier & Gueydan, 2007; Gratier *et al.*, 2009). The stress exponent n is usually taken as unity although Gratier & Gueydan (2007) point out that this is only a first approximation. Nevertheless, from the equations one can see that these diffusion-aided processes have an inverse proportionality to grain size (or d^3) and are therefore likely to be enhanced by grain-size reduction during catacalsis (fracturing) or viscous flow (Scholz, 2002). Consequently dissolution-precipitation creep is believed to be an important mechanism operating in fine-grained, fractured, fluid-saturated rocks (Gratier & Gueydan, 2007; Fagereng & Toy, 2011).

These deformation mechanisms are also commonly grouped under the term grain-size sensitive creep (e.g. Fagereng & Toy, 2011). However, minerals such as calcite and dolomite have been shown, under experimental conditions, to exhibit a strong grain-size sensitivity during high-temperature viscous (crystal-plastic) flow (Table 2.1), and this is interpreted to represent competition between different mechanims operating simultaneously (Walker *et al.*, 1990; Delle Piane *et al.*, 2008). In this thesis, to avoid confusion, solid-state diffusion mechanisms will be referred to as diffusion creep, while fluid-assisted diffusion mechanisms will be referred to as dissolution-precipitation creep. Other grain-size sensitive plastic mechanisms are considered to operate under the dislocation creep regime.

2.3.4 Dislocation Creep

Dislocation creep is a crystal plastic deformation mechanism in which strain is accumulated through the migration of line defects (dislocations) through a crystal lattice (Nicolas & Poirier, 1976; Knipe, 1989; Blenkinsop, 2000; Passchier & Trouw, 2005; Fossen, 2010). At low temperature this occurs through dislocation glide where dislocations move within a specific crystallographic (glide/slip) plane. When dislocations encounter immobile obstacles such as impurites in the crystal lattice or grain boundaries, they 'pile-up' forming dislocation tangles. These dislocation tangles restrict further motion in the slip plane making the crystal more resistant to further deformation (strain-hardening). Build-up of strain in these areas can result in stress concentrations that, if the stress exceeds the elastic strength of the crystal, can cause brittle failure. At higher temperature, dislocations may move out of the slip planes through dislocation climb or cross-slip (Nicolas & Poirier, 1976). This prevents the build-up of dislocation tangles and counteracts the strain hardening process, therefore allowing for further crystal plastic strain accumulation (strain-weakening). Processes such as dislocation

climb reduce the internal strain energy of a crystal and are also termed recovery processess. If a sufficient number of dislocations line up and form a dislocation wall, then there is likely to be a small difference in orientation of the crystal lattice on either side of the wall. This leads to the formation of deformation bands which are tabular zones of a crystal with an extinction angle different from that of other parts of the mineral grain. If this continues until the dislocation walls form an interconnecting network, they can isolate patches of the crystal that then become misorientated relative to the neighbouring patches or host grain. These misorientated patches form subgrains (Figure 2.8) showing variable extinction orientations under crossed polarised light (Blenkinsop, 2000; Fossen, 2010).

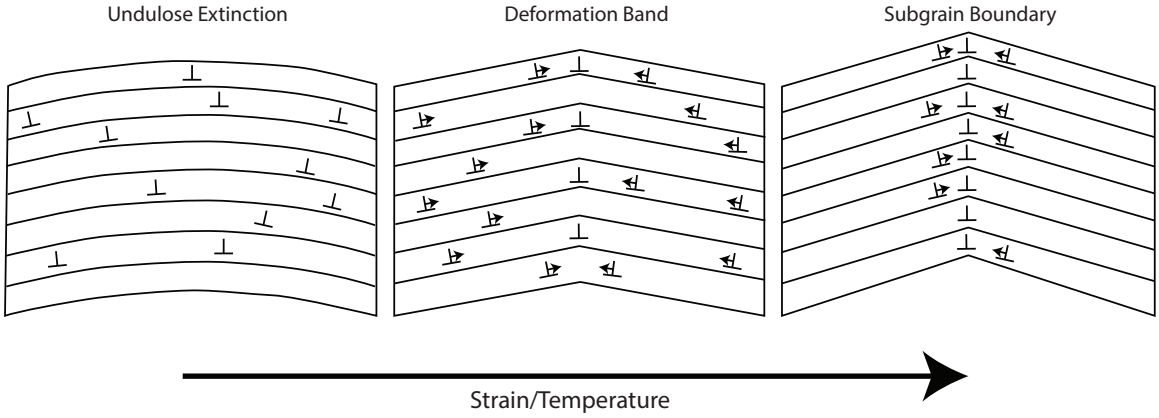

Figure 2.8: Formation of deformation bands and subgrains through dislocation creep (after Blenkinsop, 2000). At low strains dislocations form in a crystal producing undulose extinction. As strain accumulates and/or temperature increases, dislocations migrate to form dislocation walls and deformation bands. Further strain results in more accumulation of dislocations and misorientation of the crystal lattice on either side of the wall, forming a subgrain boundary.

As recovery continues, further incorporation of dislocations into the subgrain boundaries (walls) causes rotation of the subgrains and ultimately segregation of 'new', relatively strain-free, recrystallised grains (Blenkinsop, 2000; Passchier & Trouw, 2005; Fossen, 2010). If this process occurs under an applied differential stress it is called dynamic recrystallisation (Fossen, 2010). Dynamic recrystallisation can occur via a number of mechanisms (Urai *et al.*, 1986; Passchier & Trouw, 2005; Fossen, 2010):

1. **Grain boundary bulging (BLG)** occurs at low temperatures, when dislocation climb is difficult and the rate of dislocation production is greater than the rate of climb. Under these conditions, grain boundaries may locally migrate into areas of high dislocation density in neighbouring grains.

2. **Subgrain rotation (SGR)** occurs at higher temperatures, where dislocation climb allows for progressive migration of dislocations into subgrain boundaries, resulting in subgrain rotation. Subgrains are defined when the angle of rotation is $>10^{\circ}$ from the original grain.

3. **Grain boundary migration (GBM)** occurs at even higher temperature, where the rate of dislocation climb is high enough that grain boundaries may rapidly migrate into neighbouring grains.

Each of these mechanisms also produces a characteristic microstructure. It is important to note, however, that these mechanisms do not operate independently (Stipp *et al.*, 2002). This is discussed later, in Section 2.4.1.

The movement of dislocations requires breaking of atomic bonds in the crystal lattice. It therefore depends not only on temperature (T) but also the applied stress (σ) and the activation energy (Q). These variables are related to the strain rate ($\dot{\varepsilon}$) by means of an empirically-determined flow law of the form (Evans & Kohlstedt, 1995):

$$\dot{\varepsilon} = A\sigma^{n} exp(\frac{-Q}{RT})d^{m}, \tag{2.14}$$

where A, Q and n are material specific parameters (Table 2.1) and R is the universal gas constant. If one rearranges the previous equation to be in terms of differential stress, it is clear that there is a strong inverse exponential relationship with temperature:

$$\sigma_1 - \sigma_3 = (\frac{\dot{\varepsilon}}{A})^{1/n} exp(\frac{-Q}{nRT}). \tag{2.15}$$

Therefore, for a given strain rate, the sustainable differential stress of a given lithology (i.e. constant A, Q and n) decreases rapidly as temperature increases.

Mineral	$\log A(\mathrm{MPa}^{-n}\mathrm{s}^{-1})$	$Q(\mathrm{kJ.mol}^{-1})$	n	m	References
Quartz	-5	163	2.4	0	Jaoul *et al.* (1984)
Calcite	2	190	3.3	-1.3	Walker *et al.* (1990)
Dolomite	15±0.4	368	1.3	-2.6	Delle Piane *et al.* (2008)
Biotite	-29.9	18	51	0	Kronenberg *et al.* (1990)

Table 2.1: Material parameters for dislocation creep flow laws of various minerals. A is the pre-exponential factor, Q is the activation energy, n is the stress exponent. Note that carbonate mineral flow laws also contain a grain-size parameter, where m is the grain-size exponent.

2.4 Crustal Fault-Zone Model

The fabrics and assemblages preserved in exhumed fault rocks and shear zones reflect the mechanical processes by which faults accommodate deformation and the physical conditions under which deformation occurred (Sibson, 1977, 1986; Knipe, 1989). This is conceptualised in the crustal fault zone model (Figure 2.9).

2.4.1 Fault-rock fabrics

Sibson (1977) proposed a textural classification scheme for naturally-formed fault rocks based on outcrops in the Moine thrust belt of NW Scotland. The main division is between random and foliated fabrics in incohesive and cohesive rocks (Table 2.2). In the incohesive rocks, breccias and gouges are distinguished based on grain size. The cohesive fault rocks are subdivided based on the amount of tectonic grain size reduction from the host rock. This is gauged from the proportion of fine grained matrix relative to coarse fragments/porhyroclasts (Sibson, 1977; Scholz, 2002). A broad distinction between the foliated and non-foliated fault rocks is that foliated rocks form by dominantly ductile processes, while the non-foliated rocks form in the brittle regime. This is not necessarily always true as the rheology of the rocks in the fault is also a governing factor; however, it provides a useful platform for genetic interpretations of rock fabrics preserved in ancient fault zones.

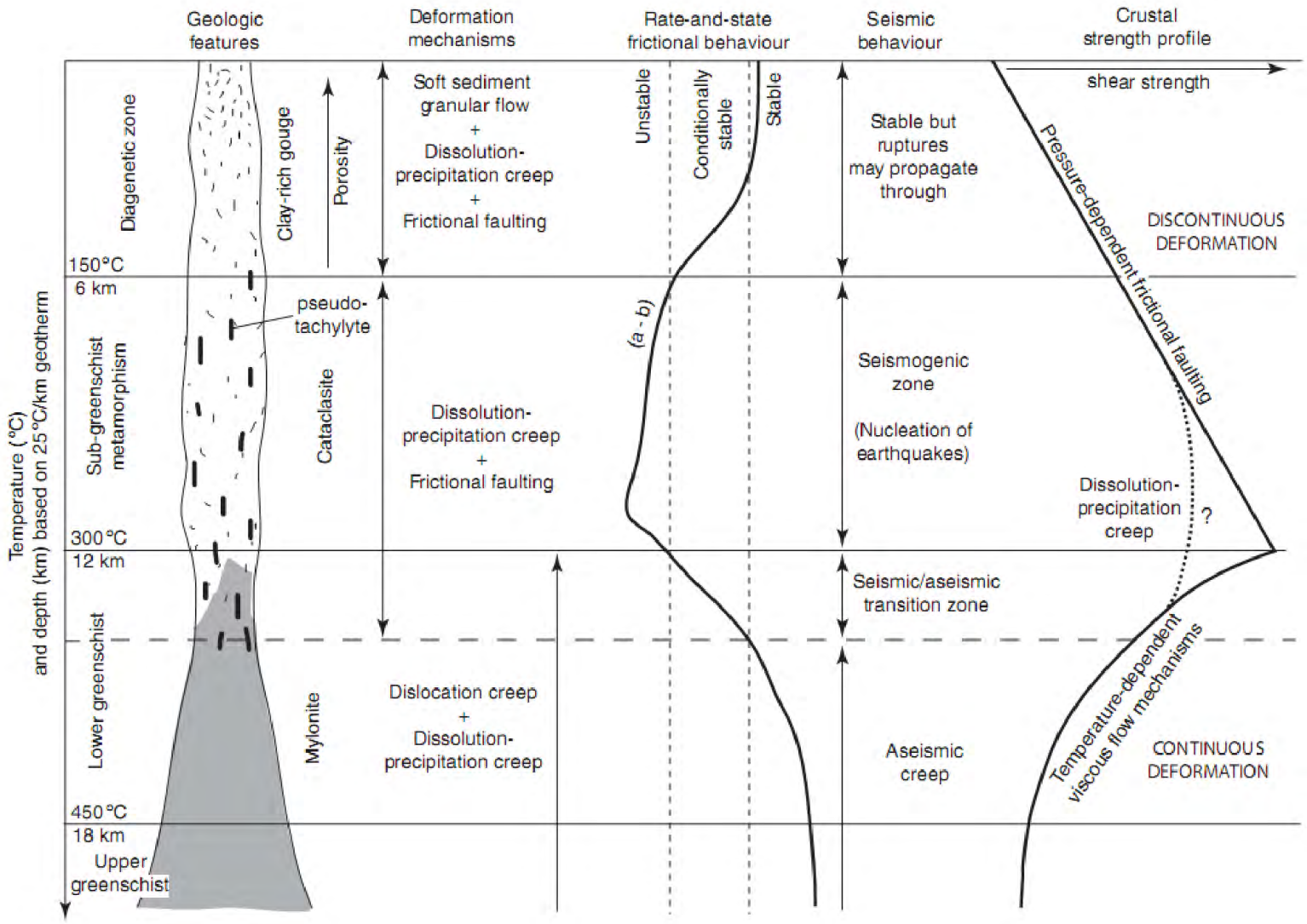

Figure 2.9: Crustal shear zone model taken from Fagereng & Toy (2011) showing the changes in fault rock fabric, deformation mechanism, seismic behaviour and mode of deformation with increasing depth.

Table 2.2: Textural classification table of fault rocks (after Sibson, 1977; Scholz, 2002).

<table>
<tr><th></th><th colspan="4">Random (non-foliated) fabric</th><th colspan="5">Foliated</th></tr>
<tr><td rowspan="2">Incohesive</td><td colspan="4">Fault breccia (visible fragments > 30% of rock mass)</td><td colspan="5">?</td></tr>
<tr><td colspan="4">Fault gouge (visible fragments < 30% of rock mass)</td><td colspan="5">Foliated gouge</td></tr>
<tr><td rowspan="7">Cohesive</td><td colspan="2">Glass -devitrified glass</td><td colspan="2">Psuedotachyle</td><td colspan="5">?</td></tr>
<tr><td rowspan="6">Tectonic reduction in grain size dominates growth</td><td colspan="4">Crush breccia (fragments >0.5 cm)</td><td rowspan="3">0-10</td><td rowspan="6">Percent of matrix</td></tr>
<tr><td colspan="4">Fine crush breccia (0.1 <fragments <0.5 cm)</td></tr>
<tr><td colspan="4">Crush microbreccia (fragments <0.1 cm)</td></tr>
<tr><td rowspan="3">Cataclasite series</td><td>Protocataclasite</td><td rowspan="3">Mylonite series</td><td colspan="2">Protomylonite</td><td>10-50</td></tr>
<tr><td>Cataclasite</td><td>Mylonite</td><td rowspan="2">Phyllonite series</td><td>50-90</td></tr>
<tr><td>Ultracataclasite</td><td>Ultramylonite</td><td>90-100</td></tr>
<tr><td colspan="2">Grain growth pronounced</td><td colspan="2">?</td><td colspan="5">Blastomylonite</td></tr>
</table>

Fault rocks formed in the brittle regime

Naturally formed brittle fault rocks include incohesive gouges and breccias, and cohesive cataclasites (Sibson, 1977, 1986). These form at low temperature and confining pressure in the upper crust, as a result of pressure sensitive mechanisms such as fracture and cataclasis (Engelder, 1974; Sibson, 1977, 1986; Knipe, 1989). The cohesive rocks are generally considered to form at slightly higher temperature and pressure (deeper). This is because of the increased role of fluids and diffusive mass tranfer that aids cementation through precipitation of quartz, calcite, epidote (etc.) in pore spaces and veins (Knipe, 1989; Passchier & Trouw, 2005). The formation of Riedel shear fractures is common in many brittle fault zones and is recognised on regional and meso-to microscales (e.g. Petit, 1987; Chester & Chester, 1998). The geometry of these structures is characterised by localised deformation on subsidiary R shear fractures which form at acute angles to the main shear direction (Figure 2.10), with the acute angle pointing in the direction of relative motion. P shears also form symmetrically with respect to the shear plane from the R shears showing the same sense of shear. Antihetic R' shears also form at high angles to the shear plane, and have an opposite sense of shear to the other subsidiary fractures (Figure 2.10). These subsidiary fractures therefore provide a useful criterion for the kinematic analysis of brittle structures in rocks (Twiss & Moores, 1992; Fossen, 2010)

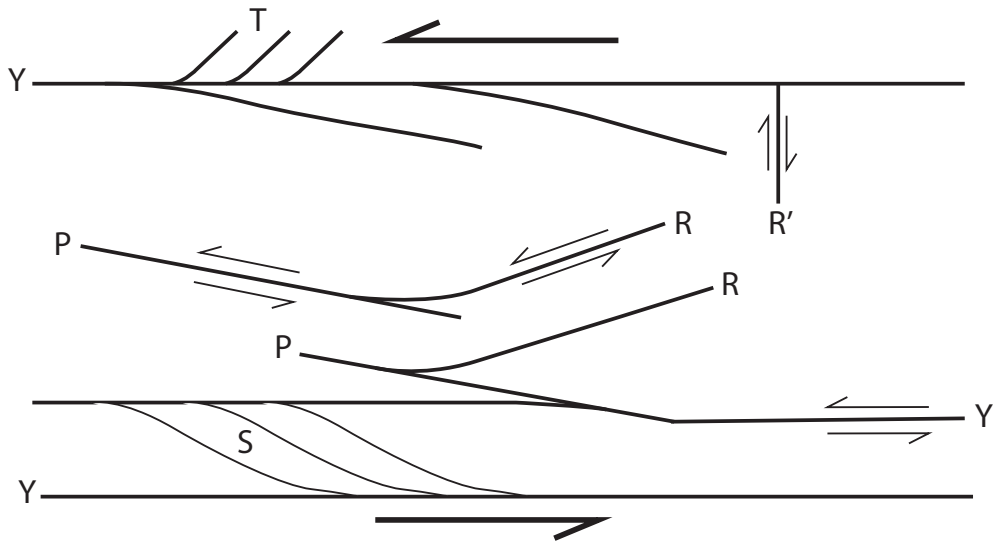

Figure 2.10: Sketch showing the geometry and kinematics of a Riedel shear network formed in the brittle regime during sinistral simple shear (Passchier & Trouw, 2005). S surface shear bands are shown for comparison.

Fault rocks formed in the ductile regime

The rocks of the mylonite series are the most common products of ductile shear zones and form by the action of thermally activated crystal plastic deformation mechanisms such as dislocation creep (Sibson, 1977; White *et al.*, 1980; Sibson, 1986). Dynamic recrystallisation is an important grain refinement mechanism in ductile shear zones (White *et al.*, 1980) and plays an important role in fabric development and strain localisation in these structures (Sibson, 1977; Stipp & Tullis, 2003; Platt & Behr, 2011). A common characteristic of shear zones is the formation of lenticular bodies or lozenges of relatively less deformed rock separated by zones of more intense deformation. On a microscale, this may be observed as porhyroclasts or ribbons surrounded by a finer grained deforming matrix (Figure 2.11b), while on meso- and regional scales it may be seen by anastamosing networks of shear zones separating larger lenticular bodies of rock (Sibson, 1977; Fusseis *et al.*, 2006; Ponce *et al.*, 2013). Mylonitic rocks are therefore usually characterised by anastamosing shape fabrics with a single lineation and foliation defined by the preferential alignment of mineral grains (e.g. S-C-C' structure and grain shape fabrics; Figure 2.11c). These fabrics reflect the geometry of the strain field or kinematic framework within the deforming body of rock and are not necessarily indicative of a particular deformation mechanism (Scholz, 2002). The development of mylonitic fabrics in quartz dominated ductile shear zones is well documented and is shown to change with the mechanisms of dynamic recrystallisation that vary as a function of strain and temperature (c.f. Hirth & Tullis, 1992; Stipp *et al.*, 2002; Stipp & Kunze, 2008). Low temperature bulging recrystallisation (BLG) produces new grains through the segregaton of bulges from the original grain (Hirth & Tullis, 1992). This produces a fabric where the original grain is surrounded by a halo of finer recrystallised grains and is referred to as core-and-mantle structure (White *et al.*, 1980; Passchier & Trouw, 2005). During subgrain rotation recrystallisation (SGR) a new grain is formed by progressive rotation of subgrains and formation of a high angle grain boundary (Hirth & Tullis, 1992). It is therefore characterised by a core-and-mantle type fabric, where the recrystallised grains are of similar size to the subgrains in the original ribbon grain. During high temperature grain boundary migration (GBM) recrystallisation grain boundaries migrate easily through neighbouring crystals (Passchier & Trouw, 2005). This produces a texture of highly irregular grain boundaries, as well as variable grain size which is typically greater than the size of subgrains in the adjacent grains (Hirth & Tullis, 1992).

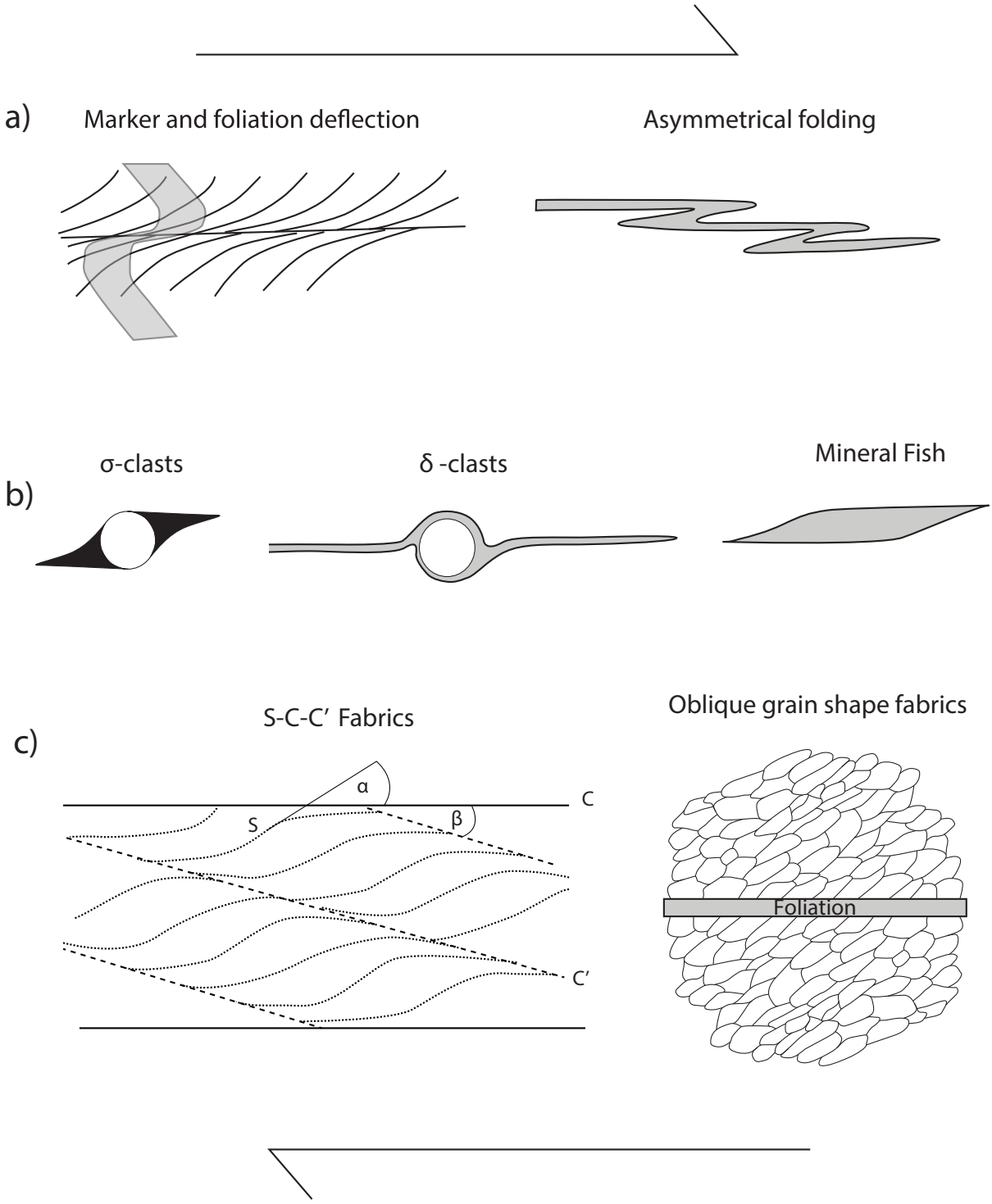

Figure 2.11: Shear sense indicators formed in natural ductile shear zones. a) Deflection of markers, foliations and asymmetric folding. b) Porhyroclast systems (after Passchier & Trouw, 2005). c) Grain geometry and shape fabrics. S-C-C' fabric with α and β angles used for classification (after Blenkinsop & Treloar, 1995). Note that, while the S-C-C' nomenclature originally referred to shear bands, in this thesis it is also adopted for grain shape fabrics.

2.4.2 The Brittle-Viscous Transition

In general, deformation in the upper crust is governed by pressure-dependent frictional flow involving discontinuous brittle fracture and dilatancy and frictional sliding. At greater depth, increased normal stresses restrict dilatancy (Scholz, 2002), thus there is a change from this brittle regime to a viscous regime. In this regime, deformation is accommodated by non-frictional, continuous, viscous flow; which is governed by thermally-activated mechanisms such as crystal plasticity and dissolution-precipitation creep (Sibson, 1977, 1986; Scholz, 2002; Stewart *et al.*, 2000; Fagereng & Toy, 2011). The pressure (depth) of the brittle-viscous transition is predicted by the intersection of the dislocation creep flow law (Equation 2.14) with the Byerlee (1978) friction law (Equation 2.6). In reality, however, this transition is not abrupt and the major change-over between pressure- and temperature-dependent deformation is likely to occur over a range of pressures and temperatures; typically 350°-450°C for quartzofeldspathic crust (Scholz, 1988, 1989; Fagereng & Toy, 2011), although it may fluctuate with varying lithology and strain rate. In this broad and complex transition zone both discontinuous (brittle fracture) and continuous (plastic flow) modes of deformation may occur (Figure 2.9). Cataclastic fabrics will also give way to mylonitic fabrics over this zone. The brittle-viscous transition is therefore considered to impose a lower limit on seismic faulting, as indicated by the focal depth distributions of continental earthquakes (Sibson, 1982).

The model depicted in Figure 2.9 is one of a purely strike-slip continental (quartzofeldspathic) fault zone. While this model still applies to dip-slip faults, in these circumstances there is added complexity as material will be transported through different pressure-temperature conditions if movement continues through the exhumation of the fault zone (Scholz, 2002). For the case of a reverse fault, material will be transported from deeper to shallower levels in the crust. There will therefore be a variety of fault rocks formed under different conditions; for a reverse fault zone being exhumed along a stable geothermal gradient, earlier high temperature fabrics will be progressively destroyed and overprinted by those developed at lower temperatures.

Chapter 3

Accretionary Prisms

Considered the marine analogue of fold-and-thrust belts, accretionary prisms are found on active convergent plate boundaries (Figure 3.1). Shear between the two plates produces a wedge consisting of deformed upper plate turbidites, pelagic sediment and oceanic basalt that is scraped off the down-going plate as it is subducted, and added/accreted to the overriding plate. Originally these highly deformed, mixed rock complexes were structural conundrums because of the intricate relationship between hydrological and deformational processes but, over the last few decades, marine geophysical work (Westbrook *et al.*, 1988; **?**; Strasser *et al.*, 2009), deep-sea drilling programs (Moore *et al.*, 2001), analyses of subaerially exposed exhumed accretionary complexes (Ujiie, 2002; Moore *et al.*, 2007; Fagereng, 2011a) and theoretical advances (Davis *et al.*, 1983; Dahlen, 1990; Wang & Hu, 2006) have produced major breakthroughs in characterising and understanding their geometry as well as the deformation processes at work.

3.1 Geometry: Critical Taper Theory

The common characteristics of all accretionary prisms are (1) a basal decollement dipping toward the arc, which forms the actual plate boundary and below which little or no deformation occurs; and (2) a wedge shape which tapers toward the margin of the prism and terminates at the trench (Davis *et al.*, 1983). Deformation within the wedge is dominated by imbricate thrusts that dip away from the toe and fault-bend folding (Dahlen, 1990). The wedge itself is further subdivided into the outer wedge with a steep surface slope containing most of the deformation, and a more stable inner wedge that has a gentler slope and is often overlain by fore-arc basin sediment (Figure 3.2 Wang & Hu, 2006; Raimbourg *et al.*, 2009). The mechanics and morphology of an accretionary prism are inherently linked, and are conceptualised by the Critical Taper or Coulomb Wedge theory which draws parallels between actively-deforming accretionary prism and wedges of sand or snow formed in front of a bulldozer or snow plough. In short, critical taper theory describes the evolution of a fold-and-thrust belt/accretionary wedge by a dynamic equilibrium between (1) addition of new mate-

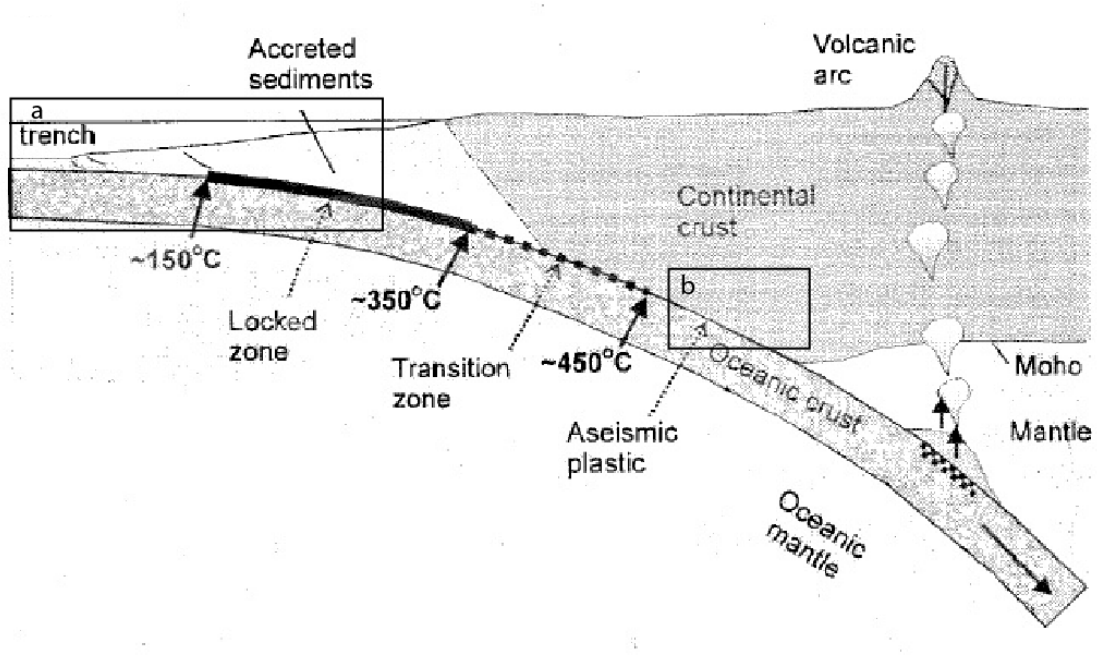

Figure 3.1: Schematic cross section through a subduction margin showing the tapered geometry of the accretionary prisms along with the thermal constraints on seismogenesis of the plate boundary fault (Hyndman *et al.*, 1997). Inset (a) shows the approximate position of Figure 3.2, and inset (b) shows the approximate depth of rocks from the Gaub Canyon.

rial at the toe of the wedge that decreases the surface slope; (2) internal deformation within the prism that causes thickening of the wedge and increases surface slope; and (3) extensional collapse (normal faulting) and slumping that causes thinning of the wedge (Davis *et al.*, 1983; Dahlen, 1990). These processes act to maintain a critical wedge taper angle defined as the dip of the wedge slope plus the dip of the basal décollement. The magnitude of the wedge taper depends on the ratio between décollement strength and the strength of the wedge material (Davis *et al.*, 1983). If frictional strength on the décollement is increased, the wedge will deform internally (and thicken) to accommodate plate motion. If the wedge material is strong relative to the décollement, it will be able to slide stably along the décollement and can thus maintain a low taper (Dahlen, 1990).

This qualitative description is simplified and assumes steady slip on the décollement. It nevertheless highlights the important processes occurring at accretionary margins. In reality, wedge taper varies with difference in pore fluid pressure in the wedge and the basal décollement as well as the frictional properties of the material in the plate boundary fault (e.g. Fagereng, 2011b), all of which may vary over the course of a seismic cycle (Wang & Hu, 2006). Wang & Hu (2006) overcome the steady state approximation in their dynamic Coulomb wedge model that relates deformation in the wedge to the variations in strength of the décollement over the earthquake cycle. They state that, during coseismic slip on the décollement, the outer

wedge deforms elastically as a result of the velocity-strengthening[1]behaviour on this portion of the basal thrust. If the earthquake is large enough, the outer wedge may be pushed into its critical state and will deform internally, otherwise the built-up elastic strain may be released by distributed aseismic creep to bring the wedge back to a stable state.

The frictional properties and fluid pressures are physical parameters that govern the geometry, and consequently the distribution of deformation in an accretionary prism. They are ultimately controlled by the nature of the rocks in the plate boundary fault, and therefore the rocks that make up the décollement zone exert significant control on deformation in the wedge. However, they also exert significant control on deformation in the plate boundary fault itself.

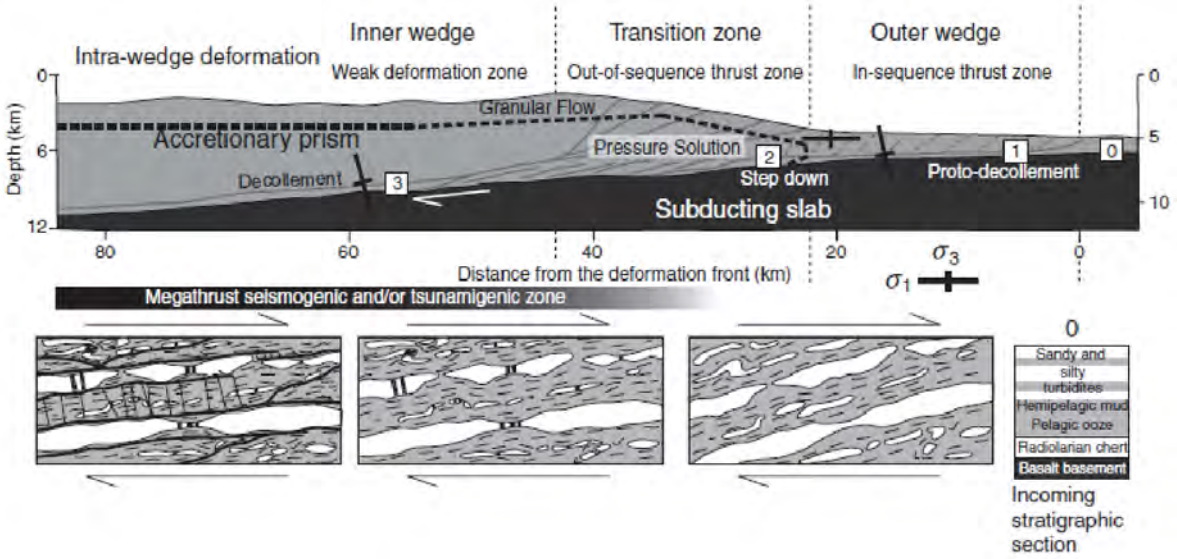

Figure 3.2: Diagram showing the conceptualised geometry of an accretionary prism along with stress states and the change in mode of deformation of underthrust sediment from the toe towards the inner prism (from (Fagereng, 2011a)).

[1]The terms velocity-strengthening and velocity-weakening refer to the dynamic frictional behaviour of faults during earthquake rupture and are defined in the Rate-and-State friction laws outlined by Scholz (1998). In the velocity-weakening field frictional resistance is lower when there is movement on the fault; this behaviour is fundamentally unstable and facilitates stick-slip sliding (seismic rupture). Velocity-strengthening behaviour thus describes the situation where fault friction increases to resist the slip. Whether a fault exhibits velocity-strengthening or velocity-weakening behaviour is a function of the material in the fault, temperature, strain rate, fluid pressure and normal stress.

3.2 Tectonic Processes and Mélange Formation

The Shimanto complex of Southwest Japan (Kimura & Mukai, 1991; Ujiie, 2002; Kimura *et al.*, 2012), the Apennines and European Alps (Vannucchi & Bettelli, 2002; Bachmann *et al.*, 2009), the McHugh Complex (Kusky & Bradley, 1999) and Kodiak Island of Alaska (Sample & Fisher, 1986), and the Franciscan Complex (Kimura *et al.*, 1996) are some of the most well-studied ancient accretionary terranes. Significant components of these terranes are tectonic mélanges. Characterised by a block-in-matrix appearance, these rock assemblages contain a chaotic mixture of rock types including turbiditic sandstone, chert, limestone and oceanic basalt, produced by a variety of stratal disruption and mixing processes (Cowan, 1985; Needham, 1995; Festa *et al.*, 2012). Study of these formations in actively deforming prisms is difficult because they form at depths too deep for drilling, and small scale structure cannot be resolved by geophysical methods. Therefore study of these features is limited to ancient and exhumed accretionary prims with the hope of understanding their geometry and the implications for deformation processes. The large scale geometry of accretionary prisms is a reflection of the relative strength between the material in the wedge and the décollement (Section 3.1), and these same processes are responsible for rock deformation in the plate boundary fault. These processes can be distinguished as:

Frontal Accretion/Offscraping

The outer wedge is characterised by distinct, trench-verging thrust faults and folds, formed under horizontal compression and fault-bend folding (Suppe, 1983). The toe of the Nankai accretionary complex is a typical example of this, showing imbricate thrust packages and hanging wall anticlines (Moore *et al.*, 2001) that form by propogation of the décollement into the incoming sediment pile, usually on discrete horizons. The deformation history of sediment offscraped at the toe of an accretionary prism is therefore one of progressive horizontal shortening, dewatering, compaction and lithification, with a general increase in the degree of deformation landward of the deformation front. These rocks will therefore only record shallow deformation processes.

Underthrusting

Sediment that is not offscraped at the toe is buried underneath the outer wedge with the subducting slab. Rocks interpreted to have formed during this process show structural evidence for a variety of deformation processes associated with progressive burial and consolidation. Boudinaged sandstone blocks set in a scaly-fabric mud matrix are observed in the Mugi mélange of the Shimanto complex (Kimura & Mukai, 1991; Ujiie, 2002) and the Chrystals Beach Complex in New Zealand (Fagereng, 2011a). These early-stage deformation structures could be representative of gravity slumps on the wedge slope (sedimentary mélanges

or olistostromes) but also of shearing or loading of poorly consolidated underthrust sediment (tectonic melanges; Kimura & Mukai, 1991), where independent particulate flow is the dominant deformation mechanism (Fagereng, 2011a). After further consolidation, dewatering and lithification, brittle shear failure becomes the dominant process responsible for stratal disruption (Figure 3.2) and mélange formation, with dissolution-precipitation creep being the dominant mechanism of ductile deformation (Byrne & Fisher, 1990; Fagereng & Toy, 2011). Rocks that are underthrust may even be taken into the mantle with the subducting slab; however, at some depth they are usually added to the bottom of the accretionary prism.

Underplating

Early workers on accretionary margins proposed underplating as a mode of accretion, to account for uplift observed as some accretionary prisms and the mass-balance of sediment entering the subduction zone (Platt *et al.*, 1985, and references therein). Geophysical evidence confirmed that a thin layer of sediment can be underthrust for several kilometres along the décollement (Westbrook *et al.*, 1988). Field studies on exhumed mélanges recognised that the large- and small-scale structure and incremental strain histories were consistent with a model of underthrusting and underplating by formation of duplex structures at the base of the accretionary prism (Sample & Fisher, 1986; Byrne & Fisher, 1990; Kimura & Mukai, 1991; Kimura *et al.*, 1996; Kusky & Bradley, 1999). In this duplex accretion model the décollement propagates into flat lying sediments on the subducting slab, and isolates a thrust slice that is coupled to the overriding prism. The thrust slice then undergoes bulk shear which progressively rotates it landward and results in the development of asymmetric fabrics that verge towards the trench. This process continues as more thrust slices are added to form a duplex structure (Sample & Fisher, 1986). This means that each slice represents the décollement zone at some point in time (e.g. Meneghini & Moore, 2007).

The processes of underthrusting and underplating are sequential. Therefore an exhumed accretionary prism should show a record of both processes, where the structural fabrics associated with underthrusting are overprinted or cross-cut by those associated with underplating, and later by exhumation. In an accretionary prism exhumed from amphibolite facies depths, the change from brittle to viscous regimes may also play a crucial role in deformation and fabric development.

3.3 Stress and Strain in Accretionary Prisms

The early taper theories proposed by Davis *et al.* (1983) and Dahlen (1990) stated that a critically-tapered, non-cohesive wedge at Coulomb failure would be under horizontal compression throughout. More recent theories (Wang & Hu, 2006) show that the earlier models approximate the time-average state, and that the stress state not only varies between the inner and outer wedges but, for both parts of the prism, varies over the course of a seismic cycle as a result of the changes in frictional strength along the décollement. It is not relevant to discuss these variations in detail as, for the purposes of this study, the earlier model suffices; exhumed rocks show a record of the long-term, time-average state.

Of more relevance are the stress states in the décollement itself, as the structural fabrics observed in many ancient and exhumed mélanges are interpreted to record deformation in the plate boundary fault (Sample & Fisher, 1986; Kimura & Mukai, 1991; Kimura *et al.*, 1996; Kusky & Bradley, 1999; Ujiie, 2002; Fagereng, 2011a). Therefore the stress states have to be inferred by analysing the incremental strain histories from structural fabrics in exhumed mélanges. Since sediment that is offscraped at the toe never makes it into the décollement, only underthrusting and underplating are considered.

Structures associated with underthrusting are characterised by layer-parallel extension. This may occur due to flattening of unconsolidated sediment (Kusky & Bradley, 1999; Ujiie, 2002; Fagereng, 2011a) or, as Fagereng (2013) points out, simple shear and volume loss. Either way suggests that maximum compressive stress (σ_1) is vertical as a result of the weight of the overlying prism. The asymmetric fabrics associated with underplating (Sample & Fisher, 1986; Kusky & Bradley, 1999) indicate that simple shear is the dominant mode of strain in this environment. Progressive deformation in this environment causes rotation of material lines into the extension field of the finite strain ellipsoid, resulting in further layer-parallel extension and disruption. Sub-vertical extension veins and contemporaneous asymmetric fabrics (Figure 3.2) are found in the Chrystalls Beach Mélange in New Zealand (Fagereng, 2013, 2011a) indicating that, even though the mode of strain may change, the stress state remains the same down the décollement (Figure 3.2). Exhumed accretionary prisms therefore record the progressive strain history experienced by rocks in the décollement, including shallow disruption, layer parallel shear and extension, and bulk shear during underplating.

3.4 Strain Localisation in Accretionary Prisms

Small scale strain localisation in accretionary prisms is fairly well studied (Moore *et al.*, 2007; Fagereng & Sibson, 2010; Fagereng, 2011a) and, in partially- to fully-lithified sediment at least, appears to result from material heterogeneity and the resulting rheological contrasts (Fagereng & Sibson, 2010). Initially, when underthurst sediment is still unconsolidated, strain is accommodated by ductile particulate flow of rock, and early faulting is characterised by broad deformation zones of sheared mudstone with lenticular boudinage of competent lithologies (e.g. chert and sandstone; Moore *et al.*, 2007; Fagereng, 2011a). During progressive burial, dewatering, cementation and lithification, there is a greater partitioning of strain, and thus strain rate, between competent and incompetent rock types, and strain is increasingly localised along the boundaries of different lithological domains where there are high strain-rate gradients (Goodwin & Tikoff, 2002; Fagereng & Sibson, 2010). This manifests in the appearance of an anastomosing network of discrete brittle shear surfaces along which most of the displacement is accommodated (Fagereng, 2011a; Rowe *et al.*, 2013). Small scale strain localisation is not the main focus of this study, but it is important to understand because the processes that affect the small scale can provide insight into the large-scale behaviour of these systems.

Unfortunately, large-scale strain localisation in accretionary prisms is not well understood. Moore *et al.* (2007) and Kimura *et al.* (2007) note that the appearance of large-scale strain localisation in the form of out-of-sequence thrust and duplexes appears to coincide with the upper transition from the aseismic to the seismic portion of the basal décollement, where the seismic portion is the segment of the plate interface that is capable of producing earthquakes by stick-slip sliding (Hyndman, 2007). It therefore appears to result largely from the consolidation and lithification (strengthening) of hanging wall sediment that enables it to deform as large, relatively rigid blocks separated by discrete faults/shear zones along which shear strain is concentrated (Moore & Saffer, 2001). A major area of uncertainty is the change in behaviour of the rocks at depths around the change from brittle to viscous regimes.

Chapter 4

Regional Geology

This chapter describes the regional geology and history of the Damara Belt in order to provide context for the study that was undertaken. For the large part the summary is quite general, but particular attention is given to descriptions of the Khomas Subprovince/Southern and Southern Marginal Zones, as the geology in these terranes is of particular interest for the study.

4.1 Background: The Damara Belt

The Damara Orogen is a Neoproterozoic-to-Cambrian continent-continent collisional belt that is part of a network of Pan-African orogenic systems formed during amalgamation of Gondwana (Figure 1.1). It consists of three belts, the NE-SW-trending Damara Belt and NNW-trending coastal branches comprised of the Kaoko and Gariep Belts that lie to the north and south of the Damara Belt respectively (Miller, 1983; Kukla & Stanistreet, 1991; Gray *et al.*, 2007). The Damara Belt (Figure 4.1A), also referred to as the Inland Branch (Miller, 1983), covers a large portion of central and northern Namibia. It is approximately 400 km wide and consists of Archean-to-Proterozoic basement granites and gneisses, syn- and post-tectonic igneous rocks as well as Neoproterozoic metasedimentary rock.

4.1.1 Tectonostratigraphic Subdivisions

A tectonostratigraphic terrane is a fault-bounded geological entity of regional extent that is characterised by a geological history different from that of neighbouring terranes (Coney *et al.*, 1980; Schermer *et al.*, 1984). The zones described by Miller (1983), subdivided based on lithology, structure and airborne geophysical data, resemble such terranes. The Northern Zone (NZ) and Central Zone (CZ) are characterised by an abundance of granitic rocks with ages ranging from 560 Ma to 460 Ma (Gray *et al.* (2007) and references therein) and display a different sedimentary facies (see Section 4.1.2) from the rocks in the Southern Zone (SZ) and Southern Marginal Zone (SMZ). The SZ is also known as the Khomas Trough/Subprovince, and is separated from the CZ by a prominent NE-trending feature called the Okahandja

Lineament. This lineament serves as a boundary separating zones of different sedimentary facies, structural style and metamorphic character. It also marks the southern-most extent of granite magmatism in the Damara Belt, with the exception of the post-tectonic Donkerhoek, Dachsberg and Omakuara granites that intrude along this lineament (Kasch, 1983b). The Gomab River Line (GRL) separates the SZ and SMZ (Figures 1.2 & 4.1A).

4.1.2 Lithostratigraphic Subdivisions

Rocks of the Swakop Group make up most of the outcrop in the NZ, CZ, SZ and SMZ. This is characterised by metasedimentary rocks with shelf and turbiditic sedimentary protoliths. The Khomas Region of the Damara Belt (SZ) is interpreted by Martin & Porada (1977) and Miller (1983) as a major site of deposition due to the progression of carbonate and terrigenous shelf sediment in the NZ and CZ, to metagreywackes, pelites and calc-silicates that have been metamorphosed to form the Kuiseb Schist. This is a garnet-mica schist and metapelite with minor marble, calc-silicate and amphibolite which completely dominates the SZ with an overall thickness of approximately 100 km (Miller, 1983; Kukla & Stanistreet, 1991; Miller, 2008). Overlying the Kuiseb Formation schists are the almost identical schists of the Hureb Formation. Consisting largely of metapsammite and sub-aluminous metapelite with calc-silicate lenses, it is only recognisable as a separate geological entity by the fact that they show evidence for only two phases of deformation (D_2 and D_3; Section 4.1.3). A prominent marker in the southern zone is the Matchless Amphibolite. It is approximately 350 km long, occurring as 200-300 m thick shear-zone hosted lenses of deformed basalt and gabbro with a tholeiitic chemical affinity, displaying remnant igneous features such as flattened pillow structures (Miller, 1983). It is thus believed to be an obducted remnant of the Khomas oceanic crust (Kukla & Stanistreet, 1991; Foster & Goscombe, 2013), although Meneghini *et al.* (2014) point out that it may be an ancient relic of a ridge-trench interaction.

The SMZ has been previously interpreted as a conjugate passive margin to the shelf environment inferred for the NZ and CZ citing the presence in both regions, of the Chuos Formation(s), a pebbly schist/diamictite, and lack of a clear suture, as evidence for geosynclinals/aulacogen models for the Damara Belt (Martin & Porada, 1977). Kasch (1983a) later proposed that the asymmetry of both structure and metamorphism in the Damara Belt (sections 4.1.3 and 4.1.4) refuted this model, and proposed a plate tectonic model involving continental collision instead. This agrees with later interpretations of the SMZ as a tectonic mixture of quartzitic turbidite, passive margin sediment and granitic basement, which form the Hakos-Aus and Naukluft Nappes, and granite inliers that are found along the length of the SMZ. The rocks in this region, however, show a remarkable similarity to the Kuiseb Schist. Just south of the GRL, in the structure referred to by Miller (2008) as the Naos Nappe, the SMZ is made up of metapsammitic, metapelitic schist, intercalated with calc-silicate and metamafic amphibolite bodies. More importantly, the fabric elements and metamorphic conditions in this zone closely resemble those recorded by the rocks of the Kuiseb Formation

(Kasch, 1983b; Miller, 1983, 2008).

4.1.3 Geometry and Deformation

The large scale structure of the Damara Belt is highly asymmetric, with doubly vergent fold and thrust structures that verge north in the northern zones and southeast in the central and southern zones (Miller, 1983). In general the southern zones show more intense deformation with recumbent folding and overthrust structures, while deformation in the north is less intense and is dominated by upright structures (Figure 4.1C; Coward (1983)). Overall, four phases of deformation are recognised in the large-scale structure and fabric elements in the Southern and Southern Marginal Zones:

1. D_1 is attributed to the formation of fold and thrust structures in the Kuiseb Formation that are only rarely exposed in the region of the Okahandja Lineament (Miller, 1983) and have largely been overprinted by D_2 and D_3 deformation events (Miller, 2008);

2. D_2 resulted in the large-scale SE-vergent folding and formation of an axial planar S_2 cleavage, and SE directed thrusting as observed by NW trending, L_2 stretching lineations in metapelites of the Kuiseb Schist (Miller, 1983, 2008);

3. D_3 is characterised by open upright folds in the Okahandja Lineament region, and become isoclinal recumbent SE-verging folds as one moves south across the SZ, increasing in intensity. In the southernmost part of the SZ, D_3 completely overprints D_1 and D_2 structures, and is recognised by a composite $S_{0+1+2+3}$ penetrative fabric (Miller, 2008). In this region it is associated with a second NW-dipping stretching lineation that indicates SE directed tectonic transport (Miller, 1983, 2008);

4. D_4 is characterised by a steeply westerly-dipping crenulation cleavage that is present throughout the southern SZ and SMZ. This late stage of NW-SE compressional is believed to be responsible for the domal structures in which pre-Damara basement of the Kalahari Craton is exposed (Miller, 2008).

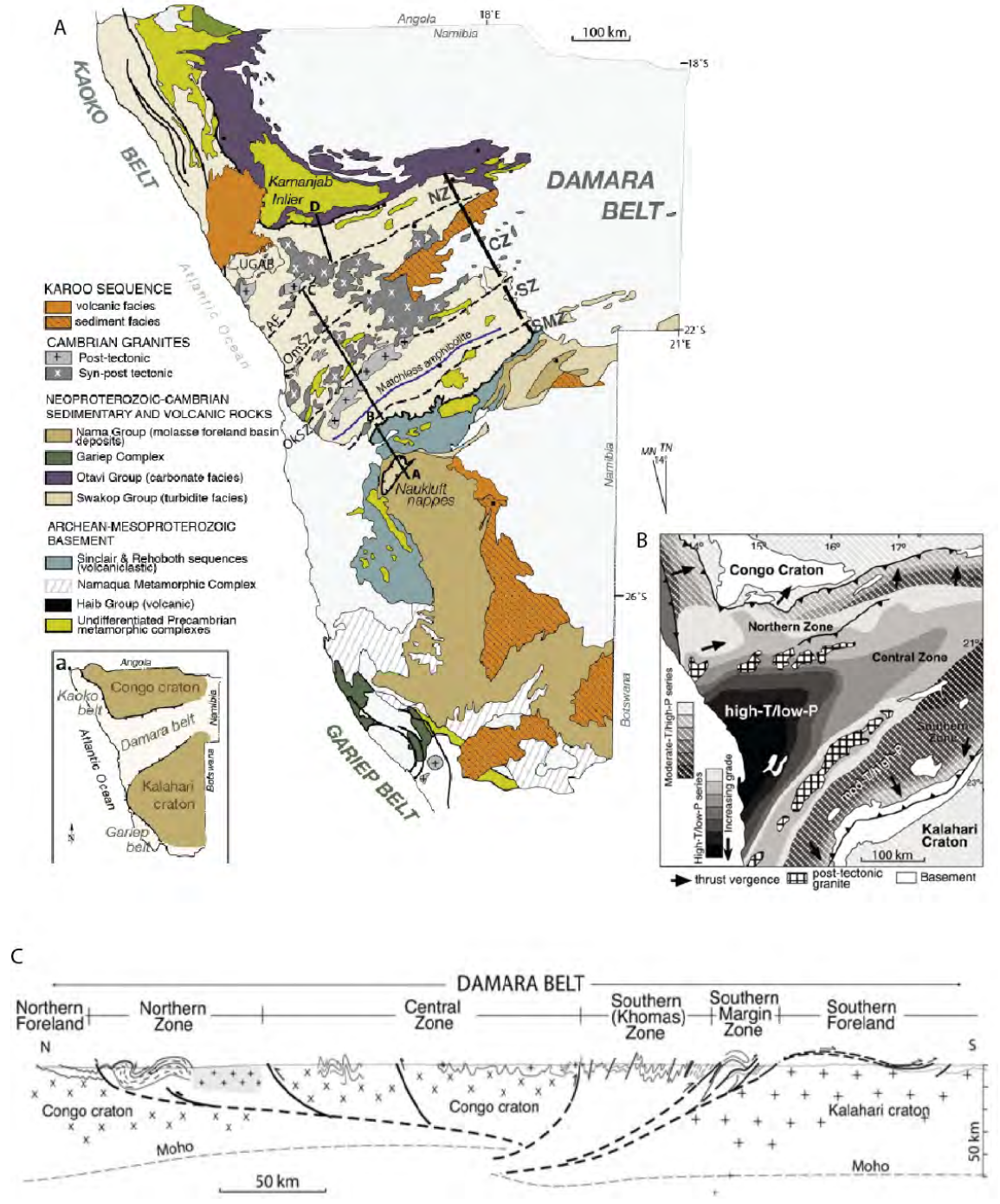

Figure 4.1: A) Map of the Damara Orogen showing the tectonic divisions, distribution of sedimentary facies and position of the cross-section profile A-D (Figure 4.1C). NZ = Northern Zone; CZ = Central Zone; SZ = Southern Zone; SMZ = Southern Marginal Zone; OkSZ = Okahandja Shear Zone; OmSZ = Omaruru Shear Zone. B) Metamorphism in the Damara Orogen (From Foster & Goscombe (2013)).

4.1.4 Metamorphism

Kasch (1983a,b) noted that, like the large scale structure of the Damara Belt, metamorphism is also fairly asymmetric, with an increase in apparent geothermal gradient from both the north and the south towards the Central Zone which displays an abundance of igneous rock (Figure 4.1B and C). The Southern Zone and Southern Marginal Zone are characterised by intermediate-T/intermediate-P Barrovian-style metamorphism with metapelitic assemblages of kyanite + staurolite + garnet + biotite + chlorite + muscovite + quartz indicating maximum temperatures of 588±50°C and pressures in the range 8.8-11.2 kbar (Kasch, 1983b). In contrast, the Central Zone of the Damara Belt has undergone moderate-P/high-T metamorphism with maximum temperatures of 652°± 50°C, and pressures of 4.3±0.2 kbar obtained for an area approximately 30 km west of Swakopmund as determined by garnet-cordierite exchange thermometry (Kasch, 1983b, and references therein). Alternatively, more recent estimates place temperature conditions at ∼750°C and ∼5 kbar (Masberg *et al.*, 1992; Jung & Mezger, 2003; Ward *et al.*, 2008).

Kasch (1983a) recognises two metamorphic events M1 and M2 for the SZ and SMZ. Peak pressures were attained in M1, whereas M2 was purely a thermal event occurring after a decrease in both pressure and temperature during the final phases of deformation. Cross (2013) did pseudosection modelling on samples taken from the Kuiseb and Gaub Rivers, thereby showing M2 as a near isobaric heating event following peak pressure (end of M1), placing the preserved peak at approximately 550°-605°C and 9.2-10.8 kbar. This was interpreted as a record of subduction of a spreading centre during the final phases of accretion in the Damara Orogeny (Cross, 2013; Meneghini *et al.*, 2014).

4.2 Tectonic evolution of the Damara Belt

The current theory for the tectonic evolution (Figure 4.2) of the Damara Belt is neatly summarised by Gray *et al.* (2007). Initially rifting occurred along two NE-trending intracontinental rifts dated between 1000 Ma and 750 Ma from silicic and acid volcanic deposits found in the northern and central Nosib Group deposits. Further extension in the southern-most rift led to the development of a mid-ocean ridge and creation of oceanic crust in the Khomas Trough at approximately 700 Ma (Miller, 1983), whereas complete opening of the northern graben never occurred (Kasch, 1983a). This spreading phase was followed by closure of the Khomas Sea between 570 and 540 Ma, in which NW-directed subduction of oceanic crust occurred beneath the Congo Craton and hemipelagic, pelagic and turbiditic trench sediment of the Khomas ocean basin were accreted onto the continental margin (Kasch, 1983a), and formed what is now known as the Khomas-Hochland accretionary prism (Kukla & Stanistreet, 1991). In this model, the Matchless Amphibolite can be interpreted as an obducted remnant of oceanic crust or a sliver that was thrust into the prism during the accretionary phase, although more recent work suggests otherwise (Meneghini *et al.*, 2014). The Okahandja

Lineament thus forms the steep backstop to the prism. The main phases of deformation resulting in the shallow SE-directed folding and overthrusting are believed to be related to the continental collision of the Kalahari and Congo Cratons. Subduction of Kalahari basement resulted in the exposure of granitic basement with turbiditic and passive margin material along the southern margin of the orogen (Miller, 1983; Kukla & Stanistreet, 1991).

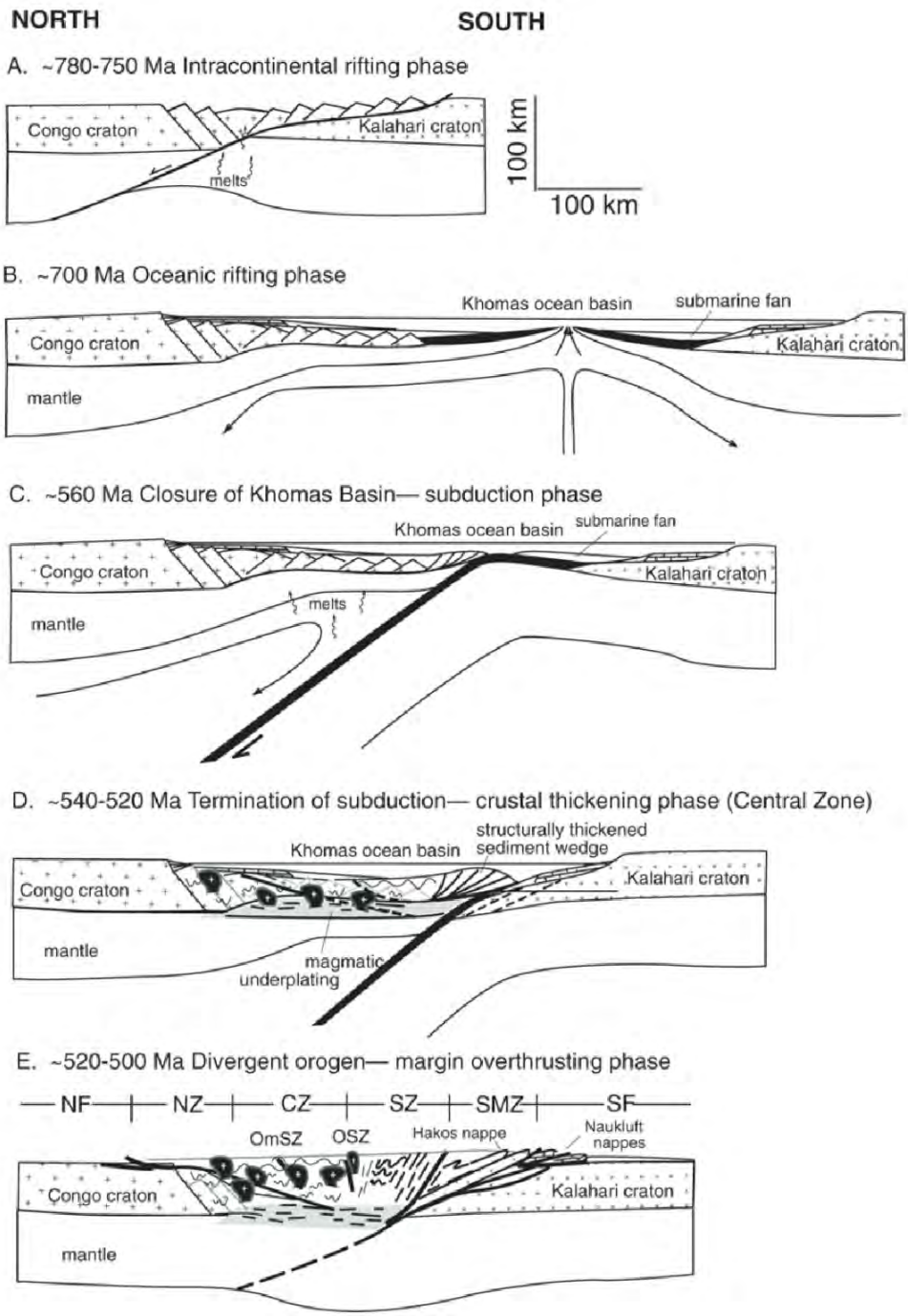

Figure 4.2: Tectonic evolution diagram for the Damara Belt from Gray *et al.* (2007)

Chapter 5

Geology and Deformation Fabrics of the SMZ

This chapter describes the field observations made in the Gaub Canyon. Seven main lithological units are recognised (Section 5.1, Figure 5.1 and Appendix A). Mapping was done by lithological assemblages, where rock types commonly occurring together were grouped together into lithological assemblages. These lithological assemblages also form the major fault-bounded lithotectonic units or thrust sheets (TS1, etc.; Figure 5.1 and Figure 5.2). It is important to note that, while there is repetition of rock types in the map area, it does not necessarily indicate repetition of the same tectonostratigraphic unit.

The section of the SMZ in the Gaub Canyon consists of a tectonically-layered sequence of metapelite and metapsammite along with quartzite, metaconglomerate and metamafic rock (Figure 5.1 and Figure 5.2). This sequence contains layered packages of metapelite and quartzite that are interpreted to have turbiditic protoliths, although no complete bouma sequences are preserved. These packages are hereafter referred to as metaturbidite. Metapsammitic assemblages are more dominant in the eastern region of the study area and metapelites are more abundant in the western regions. Quartzitic and turbiditic sequences occur in the eastern and western regions of the study area, respectively, whereas metaconglomerate is found only in the eastern regions (Figure 5.1). The following lithological/thrust sheets units are described in their approximate tectonostratigraphic order (from bottom to top) with exceptions where the same lithological assemblage is repeated in the stratigraphy. This is not necessarily a reflection of their age order.

Figure 5.1: A) Mosaic of Google Earth images of the SMZ in the Gaub Canyon used during field work. B) Summary Map of the study area in the Gaub Canyon showing the distribution of the main tectonostratigraphic units and major thrust fault discontinuities. Inset showing the different lithotectonic units numbered from bottom to top.

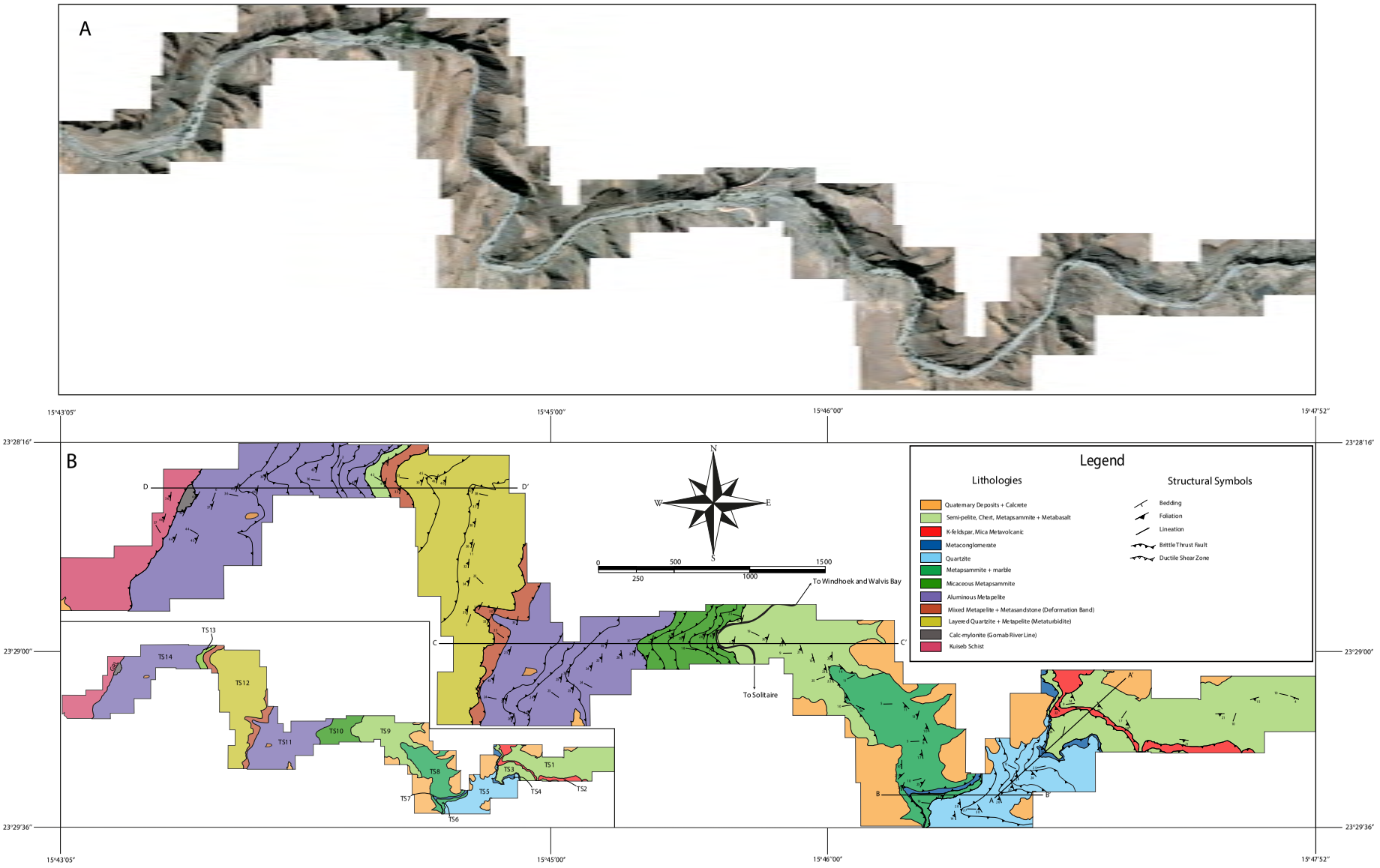

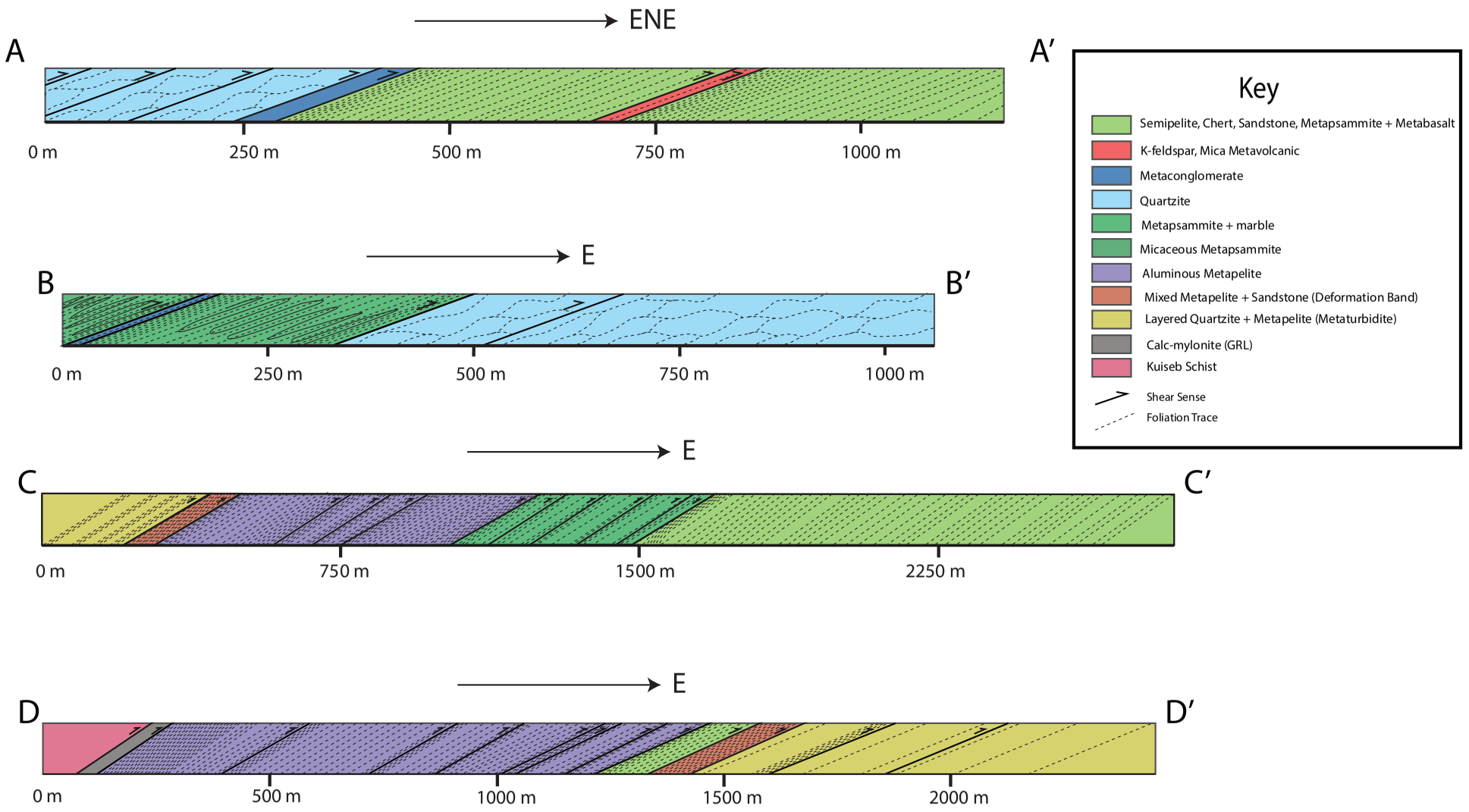

Figure 5.2: Cross sections (A-to-D) drawn roughly perpendicular to strike showing the imbricate nature of the tectonic stratigraphy and the gradual steepening of the approximately foliation parallel faults and shear zones from east to west.

5.1 Lithological Units of the SMZ

5.1.1 Semipelite with metamafic lenses

This rock assemblage is found across the study area as four distinct thrust sheets (TS1, TS3, TS9 and TS13) with thicknesses generally greater than 500 m. It dominates the eastern regions of the map area and occurs only as a thin (100 m thick) thrust slice near the western end of the map area (TS13). It is characterised by the occurrence of blocks/lenses of different rock types in a metapeltitic/semipeltic matrix. This semipelitic matrix occurs as intercalated 1-15 m thick layers of chlorite-biotite-muscovite-quartz metapelite and a biotite-quartz metapsammite, both containing minor amounts of epidote. These semipelitic rocks exhibit small-scale banding defined by layering of mica-rich and relatively mica-free bands, each approximately 1 cm thick. Semipeltic rocks have a strong foliation defined by the aligment of muscovite, chlorite and biotite whereas the metapsammitic rock have a weaker schistosity defined by the alignment of biotite. Very fine-grained epidote also defines the foliation in the metapsammitic rock types. Metabasalt and metagabbro lenses account for approximately 15% of exposed rock, are also characteristic of this assemblage (Figure 5.3A and B). These lenses are typically less that 10 m thick with lengths in the order of metres to hundereds of metres. Metabasalts have a fine-grained metamorphic assemblage composed predominantly of hornblende (90%) with quartz and minor amounts of sphene, epidote, chlorite and biotite. Hornblende defines the foliation in the metabasalt. Lenses of metagabrro are often found within thicker metabasalt lenses (Figure 5.3C). Metagabbros are composed predominantly of approximately equal proportions of plagioclase and hornblende. Chert lenses also make up a minor component of this rock assemblage (Figure 5.3B). These rocks are composed almost completely of quartz and have a fine-grained granular texture with no platy minerals to define a foliation. These chert lenses range in thick from 20 cm to 1 m (Figure 5.3B) with a 10-30 cm tabular bedding sporadically preserved in the thicker lenses.

5.1.2 Quartz-K-Feldspar-Mica Rock

This well-foliated coarse-grained rock assemblage occurs as a thin (∼30-50 m) thrust sheet separating two sheets of semipelite with mafic lenses in the eastern corner of the study area (TS2). It is composed mainly of quartz, biotite, muscovite and K-feldspar. Variations in the amount of mica define a composition layering. The mineralogy and appearence of this rock is, at face value, similar to granite. The composition layering, however, suggests that it may be derived from some kind of volcaniclastic protolith.

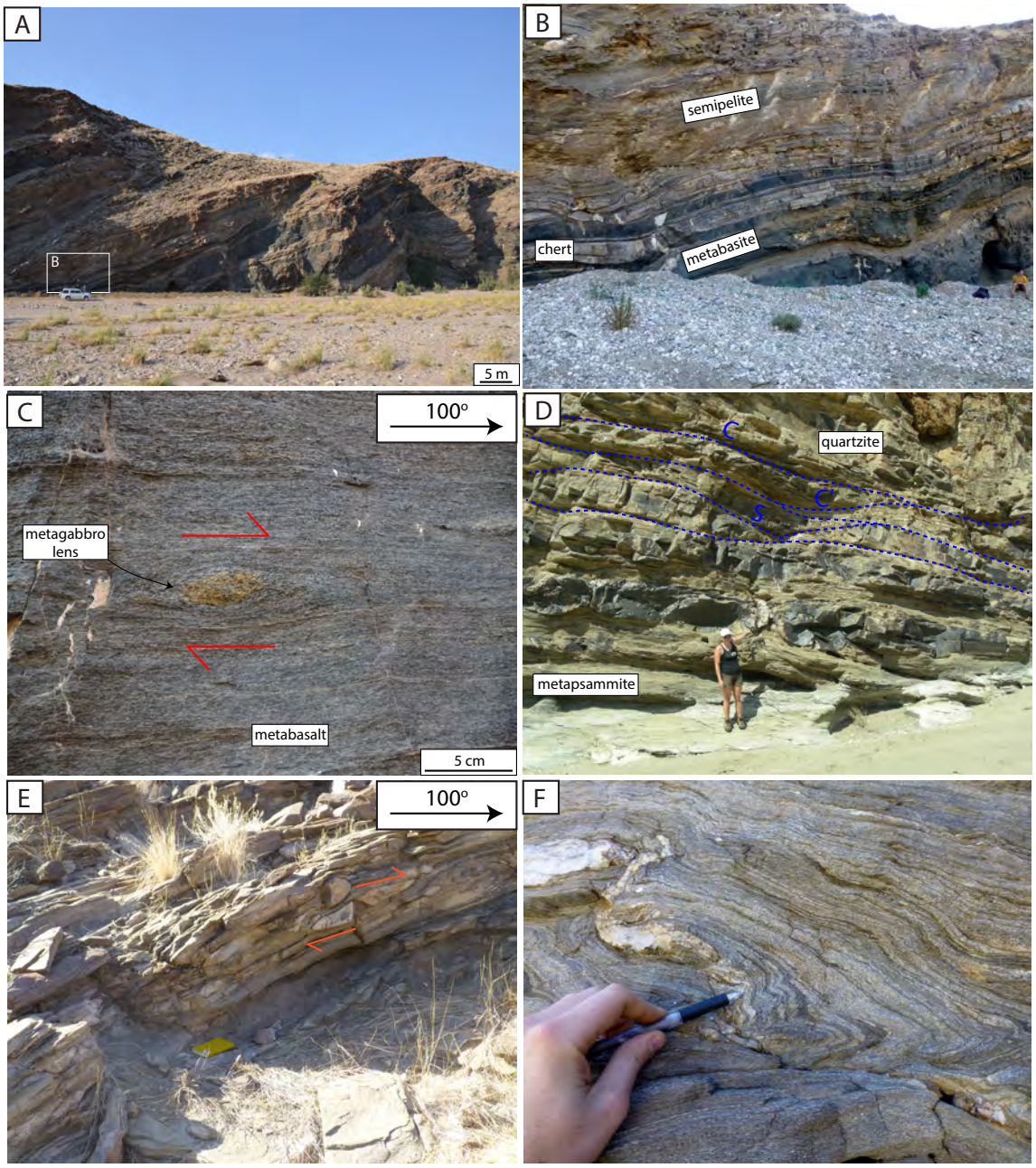

Figure 5.3: Rock types of the SMZ. A) and B) Cliff in the central map area (TS9) showing the block-in-matrix assemblage of semipelite, metapsammite and chert with metamafic lenses. White box in A) marks the position of B). Car for scale. C) Sigmoidal lens of metagabbro within metabasalt. D) Quartzitic unit TS3 with disjunctive phacoidal cleavage (blue lines) and boudinaged layer of quartzite surround by foliated metapsammite. E) Metaconglomerate (TS7) with sigmoidal clast indicating top-to-east shear sense. F) Metapsammitic unit (TS8) showing compositional banding.

5.1.3 Metaconglomerate

Two sheets of 5-10 m thick metaconglomerate are found in the eastern region of the study area. The first (TS4) occurs along a fault zone separating a sheet of metamafic-bearing semipelite from an overlying sheet of quartzite (TS5), and is highly strained. In places elongate pebbles define a down dip lineation.

The second conglomerate (TS7) is a thin sheet separating two sheet of internally folded metapsammite. It is relatively less strained than the first, and is thus identifiable as a polymictic paraconglomerate with deformed clasts in a dark fine-grained matrix. Pebbles in this unit are largely oblate, and elongation direction again defines a down dip lineation (Figure 5.3E). Fold hinge lines, parallel to the down dip lineation, are seen from folded pebbles on surfaces that cut across the foliation.

5.1.4 Quartzite

A ∼750 m thick thrust-sheet of quartzite is found in the eastern region of the study area (TS5). It is composed predominantly of medium-grained quartz in the lower regions, although near the top of this unit there are higher proportions of phyllosilicate-rich metapsammite, with metapsammite:quartzite ratios of approximately 2:3. These metapsammitic layer are 1-2 m thick in places. Generally quartzitic layers show disrupted layering that forms an anastomosing fabric, and generates phacoidal blocks of quartzite (Figure 5.3D) with no pervasive planar fabric. These phyllosilicate-rich layers, still composed predominantly of medium-grained quartz, contain approximately 10-15% combined modal biotite and muscovite which define the foliation. More psammitic layers therefore show a well-developed foliation. In the quartzitic regions, brittle thrust faults cut the disjunctive fabric at shallow angles, while in the upper part of this thrust sheet, large pinch-and-swell structures are seen in disrupted quartzite layers between layers of relatively phyllosilicate-rich metapsammite (Figure 5.3B).

5.1.5 Metapsammite

Two types of metapsammite are found in the study area and are distinguished by minor differences in mineral composition. A more distinct difference, however, is their mode of strain accommodation. The lowermost unit is a 500-600 m thick homogenous unit that overlies the quartzite sheet in the central to eastern region of the map (TS8). It consists of predominantly quartz-biotite schist, with a minor muscovite component, and contains thin (<50 cm thick) metapsammite layers. This unit exhibits a closely-spaced planar fabric defined by the alignment of micaceous minerals and, in places, shows a compositional layering (Figure 5.3E) with light and dark bands indicating relatively biotite rich and poor layers respectively. The second, stratigraphically higher, metapsammite unit (TS10) crops out in the central region of the map and is separated from the first by a thrust sheet of the metamafic-bearing semipelitic assemblage. The unit is ∼500 m thick and consists of a fairly

homogenous quartz-mica schist although it has considerably higher muscovite content and no apparent compositional layering. Quartz veining is abundant in this unit. Veins have a sigmoidal shape and commonly occur as lenses that taper up and down dip in the foliation.

5.1.6 Metapelite

The most abundant metapelite is an aluminous garnet-staurolite-chlorite-quartz-mica schist, which occurs as two 1000-1200 m thick thrust sheets in the central and western regions of the map (TS11 and TS14 respectively). This rock has a strong schistosity defined by the alignment of fine- to very fine-grained chlorite and muscovite. Quartz and biotite make up a minor component of this rock and commonly define the lineation that trends down dip in the foliation plane, although on particularly mica-rich surfaces, a second sub-horizontal lineation may also be weakly defined by biotite. This fabric is overprinted, in places, by reddish-brown circular pophyroblasts of garnet $\sim$ 1 cm in diameter, and black staurolite lathes $\sim$0.5 cm in length that show no preferred orientation (Figure 5.3G and H). Thin calc-silicate layers also occur within these metapelitic units. Calc-silicates contain dark brown-to-black needles of hornblende and biotite within an off white matrix of calcite. Fine circular grains of garnet also occur sporadically within these layers. The calc-silicate layers are generally no more than 50 cm thick and hornblende defines the foliation and down dip lineation in these layers.

Quartz veins are abundant in this unit. These are commonly 1-3 cm thick and and occur as lenses through the rock, typically tapering out up and down dip on the foliation (Figure 5.3G). Ductile shear zones occur in this metapelite, usually close to lithological contacts with calc-silicate layers, and are characterised by an increase in foliation intensity and, in places, show boudinaged layers of metabasalt in the hanging wall. These metabasalt are of similar composition to those described for the metamafic-bearing semipelitic unit and are composed predominantly of hornblende which defines a strong shistosity.

5.1.7 Metaturbidite

Resembling the quartzite and graphitic schist described on the 1:500 000 Geological map of the Damara Orogen by (Miller, 1983), this $\sim$750 m thick unit is present in the central-western to western regions of the study area (TS12). It is bounded on either side by two 10-20 m thick zones of a deformed mix of metapelite and quartzite. In the lower parts of this unit, it appears as a layered sequence of intensely foliated metapelite and well-bedded quartzite with a metapelite-quartzite ratio of approximately 1:3 (Figure 5.3G). Metapelitic layers are 1-2 m thick whereas quartzitic layers are typically 3-4 m thick, although thin (<1 m thick) lenticular layers of quartzite are, in place, visible in the metapelitic layers. Metapelitic layers have a strong schistose appearance with a fabric defined by the alignment of fine-grained quartz, muscovite and biotite. Coarser grains of biotite and staurolite (0.5-1 cm in length) sporadically overprints this fabric (Figure 5.3J). Quartzitic layers do not show

a structural foliation and preserve a tabular bedding with a bedding thickness of ∼50 cm. Foliation parallel quartz veins are again common in the metapelitic layers but are absent in the quartzitic layers. At higher structural levels in this unit, the amount of metapelite decreases, becoming almost completely quartzitic at the top. This reduction in the metapelite-quartzite ratio is accompanied by an increase in the disruption of bedding in the quartzite and the appearance of discrete faulting, as illustrated by pinching of bedding layers.

5.1.8 SMZ-SZ Boundary Shear Zone

The boundary between the SMZ and the SZ, and the western limit of the study area, is marked by a 5-10 m thick regional-scale shear zone, the Gomab River Line (GRL; Figure 5.3K). This contains a fault rock exposed in an elliptical-shaped out-crop in the western region of the map area (Figure 5.1). It is composed largely of reddish-brown, fine-grained calcite which forms the groundmass, and contains disaggregated veins of quartz up to 10 cm thick in places. Quartz veins define the foliation in this rock (Figure 5.3L). These veins are also locally displaced by a array of subsidiary fractures that displace the quartz veins up to a few centimetres in place. Carbonate is found along only three other faults in the study area and is limited to large unit-bounding faults. These are described in detail later in Section 5.4 whereas a more detailed petrographic analysis of the GRL is given in Chapter 6.

5.1.9 Kuiseb Schist

The Kuiseb Schist is separated from the rocks of the SMZ by the Gomab River Line (GRL; Figure 5.3K). In the western corner of the map area it is composed predominantly of a garnet-muscvoite-biotite-quartz metapelitic schist. Fine-grained staurolite is also locally present. Minor metapsammitic layers with relatively less mica and cal-silicate are also present but amount to approximately one third of the volume of metapelite. The fabric of the Kuiseb Schist is defined by the aligment of muscovite and biotite with staurolite and garnet overprinting this fabric.

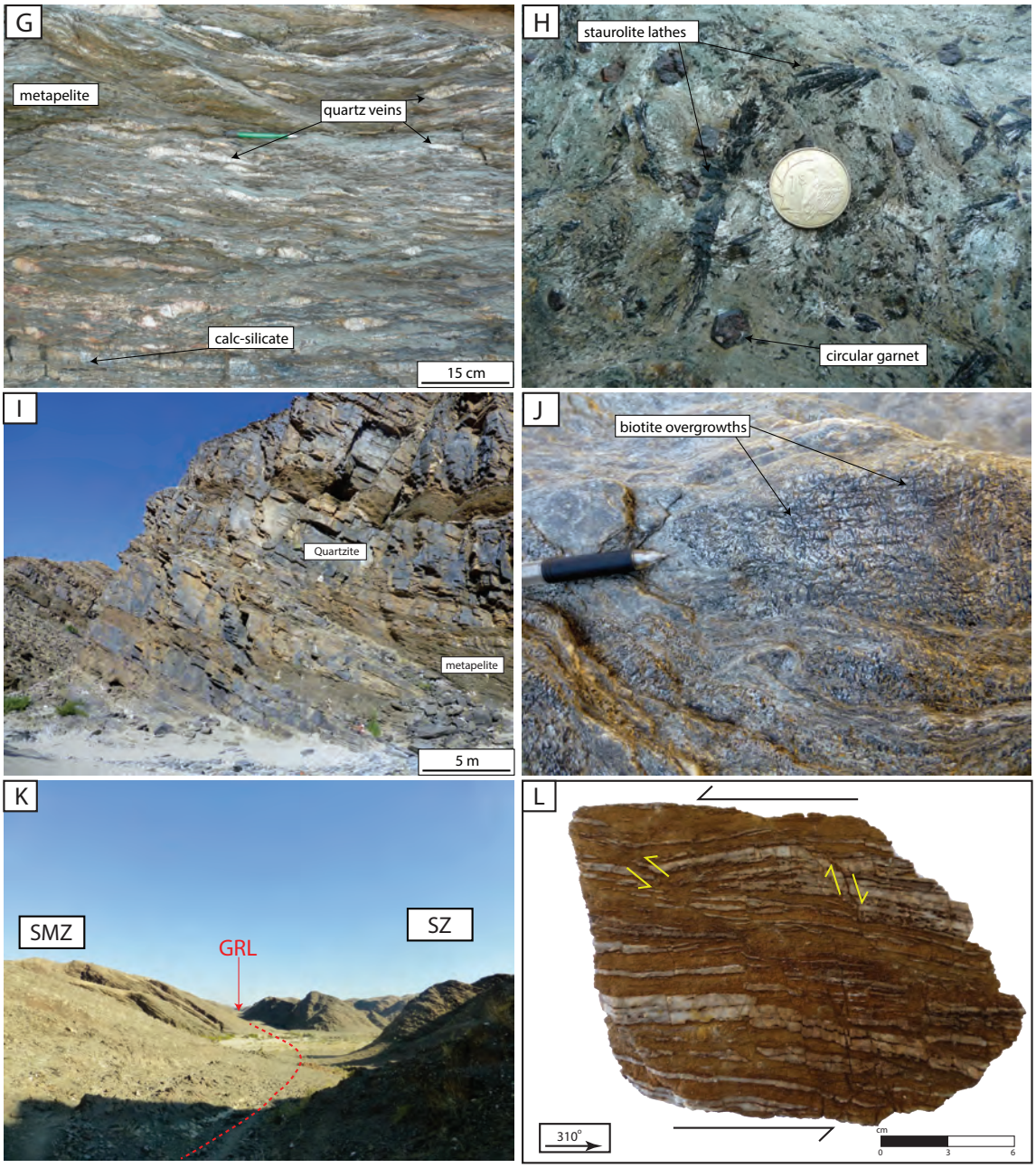

Figure 5.3: Rock types of the SMZ continued: G) Metapelite with calc-silicate. Photo shows the abundance of quartz veins in this unit. H) Metapelite with laths of staurolite showing no preferred orientation and large garnet porphyroblasts. I) Lower regions of the metaturbidite (TS12) with sheared metapelitic layers and relatively undisrupted layers of quartzite. J) Phyllosilicate-rich surface in the upper regions of metaturbidite showing biotite overgrowths defining the down dip lineation. A weak sub-horizontal lineation is also present. K) Terrane boundary shear zone. The boundary between the SMZ and the SZ is marked by a large gulley. L) Calc-mylonite in large shear zone separating the SMZ from the Kuiseb Schist with fabric-defining quartz veins displaced by subsidiary fracture.

5.2 Deformation Fabrics

The following section details the geometry and nature of the planar (S_x) and linear (L_x) deformation fabrics preserved in the rocks of the SMZ. These fabrics are attributed to distinct deformation events (D_x) based on the cross-cutting relationships between the various fabric elements.

5.2.1 Foliations

S_0 is the primary rock fabric defined by lithological contact between rocks that are interpreted to have the same sedimentary origin; i.e. are likely to have been deposited on top of one another. For example, in the metaturbidite, pelitic layers in this unit display a higher strain fabric than those of the adjacent quartzitic layers. These layers are likely to have accommodated more strain, for reasons discussed later, and therefore effectively act as shear zones separating quartzite layers. The boundaries of the pelitic shear zone are parallel to the sedimentary bedding observed in the quartzite (Figure 5.3J); therefore, it is assumed that, as a result, the shear zone edges lie along sedimentary contacts and that the shear zone boundaries reactivate primary bedding.

The D_1 fabric is defined by S_1 (Figure 5.4A) which is pervasive throughout the study area. In metapelitic and metapsammitic rock types it is typically defined by the alignment of mica (biotite, muscovite and/or chlorite). It is bedding parallel and mostly indistinguishable from S_0 (Figure 5.4C). However, in quartzite unit (TS5), it is developed as a disjuctive S-C fracture cleavage. C surface run along beding planes whereas S surfaces transect bedding, dividing beds up into phacoidal blocks (Figure 5.3D). It has an average strike of 187° and an average dip of 24°W. In the eastern regions of the study area it has an average orientation of 113°/15° S, gradually changing orientation and steepening to attain a strike of approximately 202° and dip of 33° W in the western regions (Figures 5.1).

The D_2 foliation S_2 is parallel to S_0 and S_1, and is only rarely distinguishable in the hinges of folds where the S_{0+1} fabric is cross-cut (Figures 5.6B, C and D). It has an average strike of 158° and ranges from 146° to 220° with an average dip of 17°±10° W. Although S_2 is observed locally, the overall fabric in the SMZ is a composite fabric and will hereinafter be referred to as S_{0+1+2} except where it is distinguishable from S_{0+1}.

S_3 is a crenulation cleavage and is recognised by slight buckling of S_{0+1+2} (Figure 5.6E and F). The crenulation axial plane is steeply-dipping with orientation 234°/72° NW, while crenulation hinge lines on average trend 234° and plunge 17°. It is thus approximately perpendicular to S_{0+1+2} (Figure 5.6F).

There is a distinct difference between the relative intensity of the foliation for each unit. The nature of the dominant fabric varies significantly with rock type as well. In metapelitic and metapsammitic assemblages, the S_{0+1+2} is well developed with a fine spacing of approximately 0.5 mm. In quartzitic rock types, the penetrative foliation is poorly developed, and these preserved anastomosing discontinuous shear fabrics instead (Figure 5.3D and Figure 5.5). The lower regions of the metaturbidite unit highlight this contrast; metapsammitic and metapeltic layers show a well-developed S_{0+1+2} whereas the quartzitic layers are relatively intact and still appear to preserve a sedimentary layering (S_0).

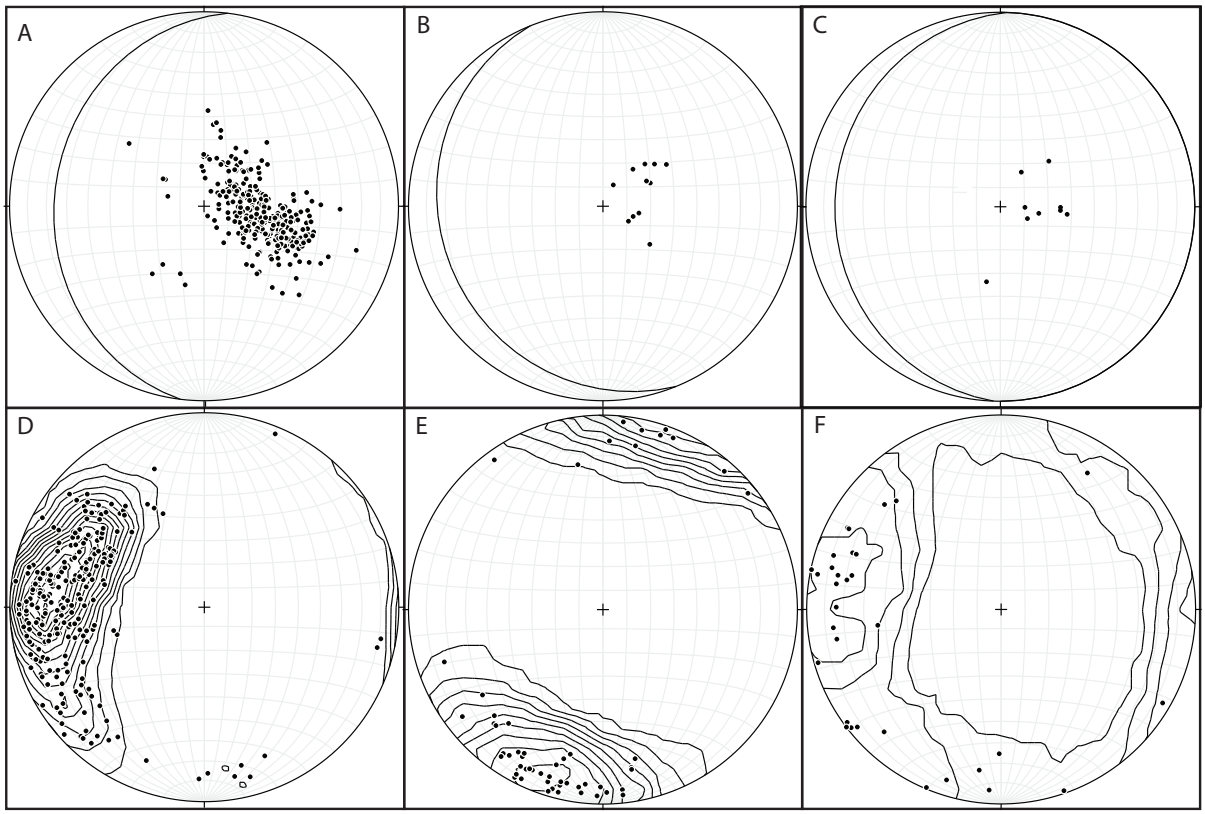

Figure 5.4: Equal area lower hemisphere stereographic projections of structural data collected in the Gaub Canyon plotted using Stereonet 8 (Allmendinger *et al.*, 2012). A) Poles to S_1 with mean S_1 surface. B) Poles to S_2 with mean S_2 surface. C) Poles to S_0 with mean S_0 surface. D) Down dip L_2 stretching lineation. E) Subhorizontal L_3 stretching lineation. F) Fold hinge lines.

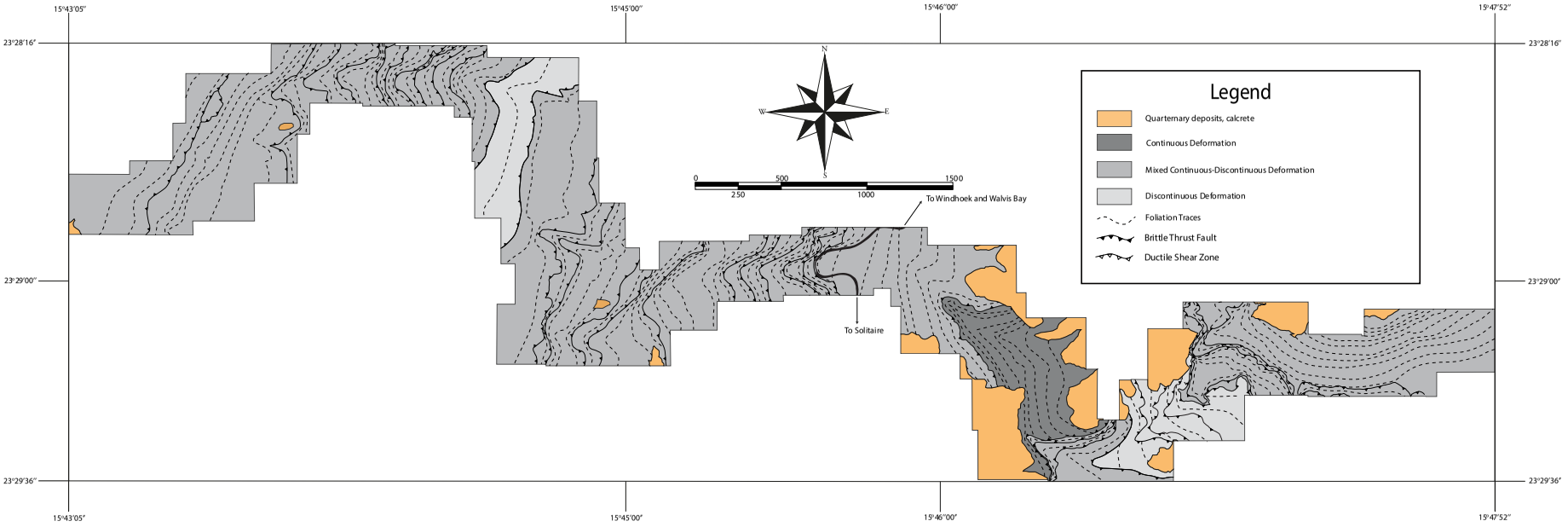

Figure 5.5: Map of the study area in the Gaub Canyon showing zones of continuous, discontinuous and mixed continuous-discontinuous deformation as well as foliation traces that show the variation in strike across the study area. The different spacing of the foliation traces represents the variation in foliation intensity.

5.2.2 Lineations

S_{0+1+2} contains two lineations. The down dip lineation has been termed L_2 and the sub-horizontal lineation is termed L_3 as it is found cross-cutting L_2 in places. S_1 is preserved only very locally in unit TS5 and elsewhere has been overprinted by S_2. There is no apparent structural lineation associated with S_1.

L_2 is roughly down dip on S_{0+1+2} with an average trend of 274° and plunge of 28° (Figure 5.4D). Its spatial variation follows that of S_1 with trends ranging from 158° to 340° and plunge between 2° and 46°. It is defined by stretched quartz in more psammitic assemblages, biotite and muscovite in metapelitic rocks and horneblende in metamafics and calc-silicates.

L_3 is less ubiquitous and has an average trend of 204° and plunge of 19° (Figure 5.4E). It is found to plunge in both SW and NE directions with trends in two clusters of 168° to 252° and 002° to 51°, respectively, and plunges between 03° and 24°. There is no indication that L_3 varies significantly over the study area and is more easily identifiable on more micaceous surfaces.

On micaceous surface in the quartzite and in the metapelite generally, fabric forming quartz and biotite define a down dip lineation, whereas the shallow plunging sub-horizontal lineation trending approximately 200° is defined predominantly by coarser biotite and locally staurolite overgrowths, although the latter is usually not well developed (Figure 5.3J). This sub-horizontal stretching lineation (L_3) is also found sporadically on large brittle fault zones separating a few of the major litho-tectonic units.

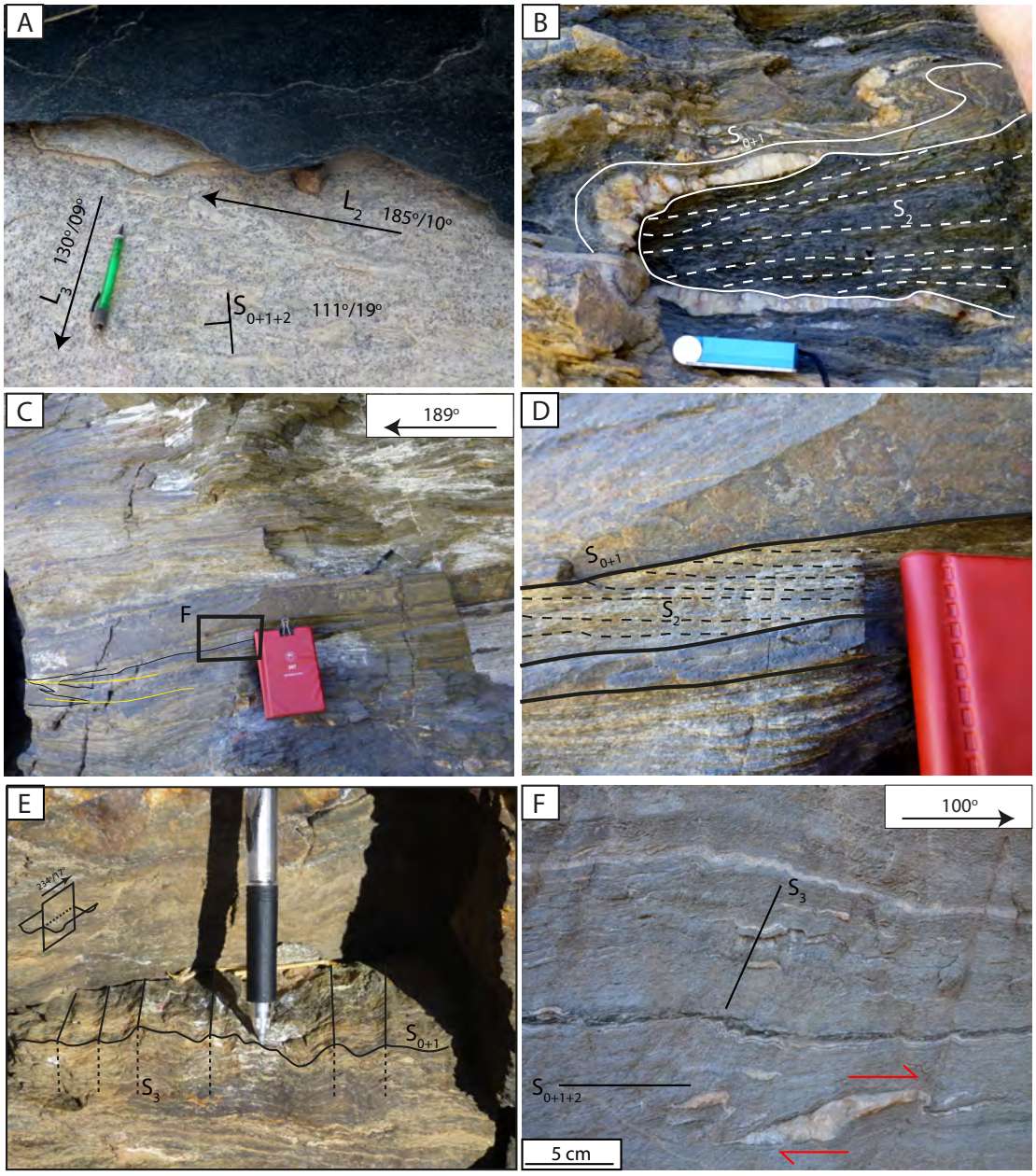

Figure 5.6: Relationships between D_1, D_2 and D_3 structures. A) Relationship between L_1 and L_2 seen on a foliation surface in the mixed semipelite and metamafic unit. B) S_2 (dashed lines) cross-cutting folded quartz vein. C) Isolclinally recumbently folded quartz-rich layers in mica-poor metapsammite (TS8). Dashed lines show S_{0+1+2} warping around boudinaged fold limbs. D) Cross cutting of S_{0+1} and S_2 near hinge zone of folded metasandstone layers. E) and F) S_3 cross-cutting S_{0+1+2}. Note in F) how weak the S_3 fabric is compared to S_{0+1+2}.

5.3 Ductile Structures

5.3.1 Folding

Both primary bedding and the S_{0+1} foliation are tightly folded in asymmetric isoclinal recumbent folds with gently SW-to-NW dipping axial planes parallel to the S_{0+1+2} foliation (Figure 5.4F and Figures 5.7A and B). Hinge line trends vary between 161° and 316° with plunges in the range of 0° to 26° with an average orientation of 258°/16°. In places, fold hinges are observed to trend parallel to the down dip stretching lineation L_2 (Figures 5.7C and E and Figure 5.8) and accordingly, the variation of fold hinge lines shows a similar trend to L_2 with a progressive systematic rotation and steepening from east to west (Figure 5.4F). Bedding parallel quartz veins are also folded in a similar manner, and are used to identify folding in lithologically homogeneous units. These quartz veins have also been disrupted by boudiange and occur as sigmoidal/phacoidal lenses in ductilely deformed matrix (Figures 5.7D). The degree of folding as a mode of strain accommodation varies for each unit: quartzitic rock types do not show folding, whereas the metapsammitic and metapeltic rock types do show it although with varying scale. In the lower metapsammitic unit (TS8), metasandstone layers and compositional layering aid the identification of isoclinal recumbent folding (Figures 5.6D and E) as the dominant mode of strain accommodation; providing an explanation for the appreciable thickness of this unit. Biotite defines a lineation in this unit that trends down dip on the main foliation and is sub-parallel to the hinge line trend (Figure 5.7C and E, and Figure 5.8). A less dominant axial planar foliation (S_2) is also identifiable in the hinges of folds where it cross-cuts the main foliation while, due to the isoclinal recumbent style of folding, it is sub-parallel to it away from the fold hinges.

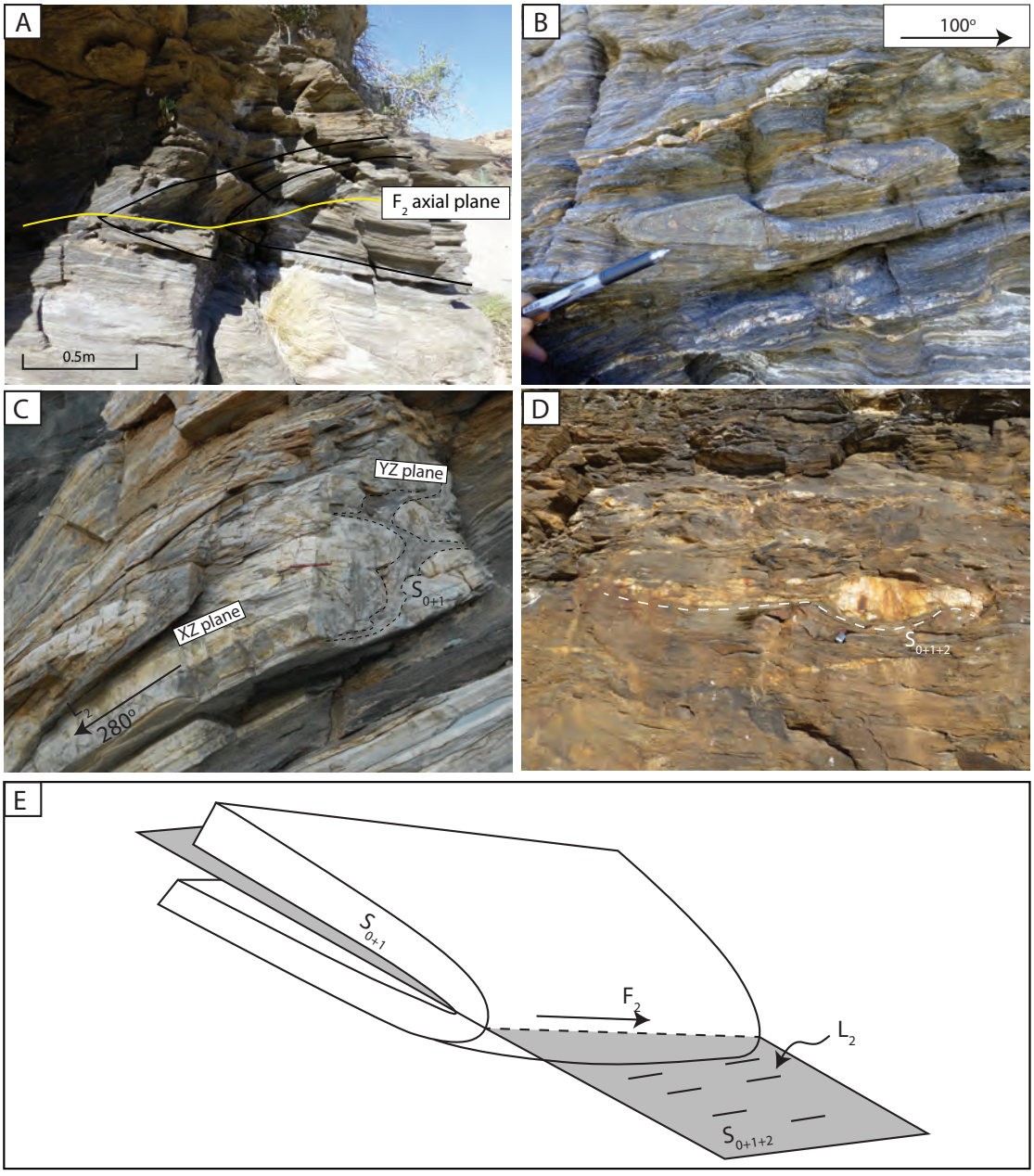

Figure 5.7: Folding in the SMZ. A) and B) Isoclinal recumbent folds in mica-poor metapsammite (TS8) with axial plane parallel to S_{0+1+2}. Note in B) that folds verge towards the SE. C) Outcrop showing the geometry of folds with fold hinge lines best exposed on YZ planes. Black dashed lines show folded S_{0+1}. D) Dismembered isoclinally recumbently folded quartz vein in metapsammite (TS5). E) Simplified sketch showing the geometrical relationship between F_2 folds and the main penetrative foliation (S_{0+1+2}). Fold axial planes are parallel to S_{0+1+2} whereas fold hinge lines are roughly down dip on S_{0+1+2}, parallel to the stretching lineation L_2.

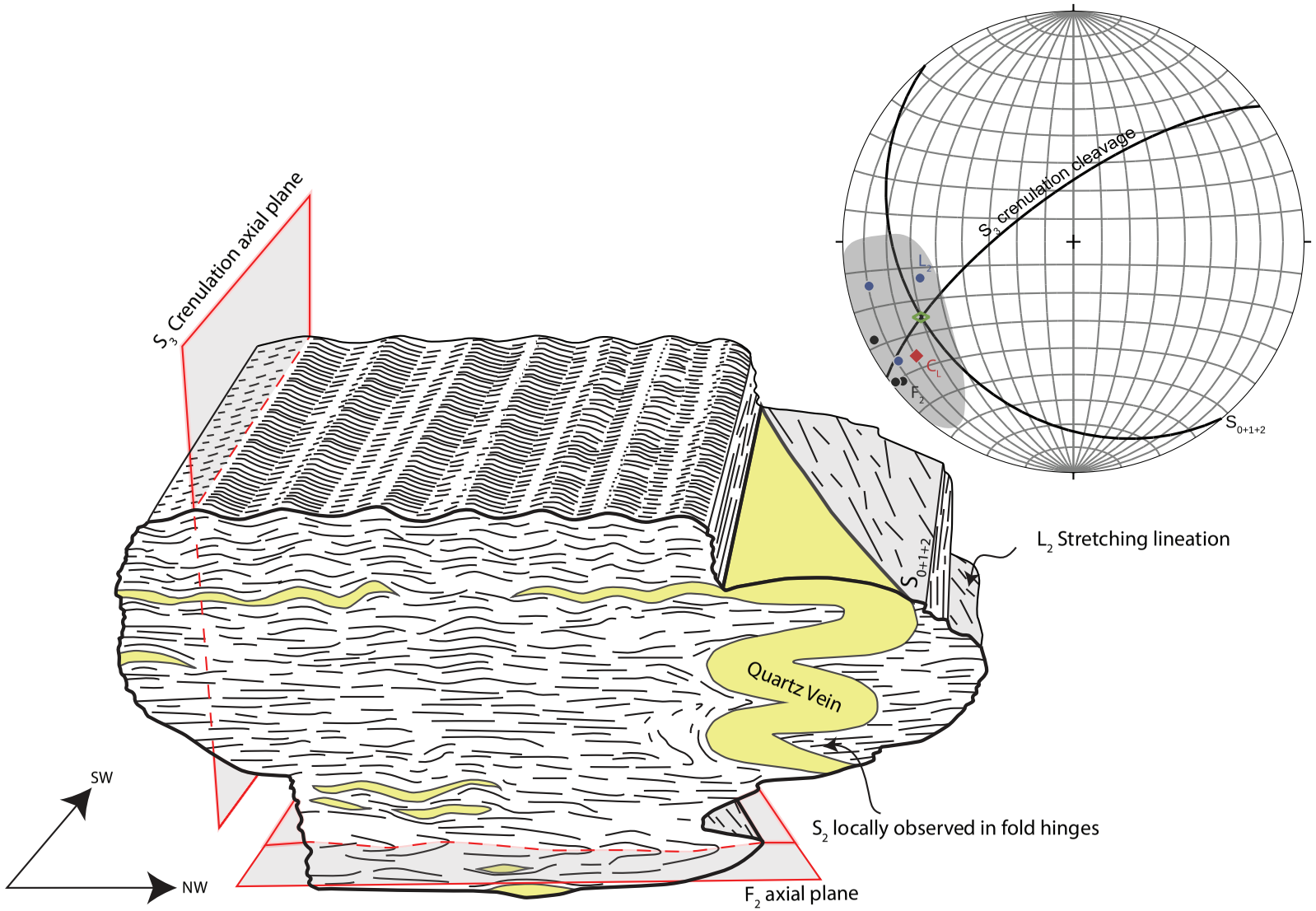

Figure 5.8: Cartoon (modified from Kasch, 1983b) based on outcrops of metapsammitic schist (TS8; Figure 5.6G&H) and stereonet showing the geometrical relationship between D_2 and D_3 structures. F_2 fold axial planes are parallel to S_{0+1+2} with hinge lines roughly parallel to stretching lineation L_2. Both are down dip on S_{0+1+2}. S_3 crenulation cleavage has axial plane sub-perpendicular to S_{0+1+2}. Crenulation hinge lines (red diamond), defined by the intersection of S_{0+1+2} and S_3 (green diamond), are approximately parallel to L_2 and F_2 hinge lines, as indicated by the shaded region on the stereonet.

5.3.2 Shear Zones

Shear zones are found to bound the major lithotectonic units and are often present within the more metapelitic units. Both unit-bounding and intra-unit shear zones occur as 1-2 m thick shear zones that are characterised by increase in intensity of foliation, which is usually sub-parallel to the shear zone boundaries and general fabric away from these zones (Figure 5.9A,B and D). Solution cleavages with a spacing of 0.5-1 cm are also found in unit-bounding structures which also commonly contain lenticular quartz veins. This is best seen in the shear zone separating TS8 and TS9 (Figure 5.9B). Intra-unit shear zones within metapelitic and metapsammitic thrust sheets are characterised by increase in foliation intensity, and reduced grain sizes relative to the surrounding wall rock (Figure 5.9D). Shortening was accommodated via these shear zones with a top-to-the-east sense of movement, as indicated by slight deflection of foliation away from the shear plane in the footwall as well as the shape and orientation of quartz veins within these structures (Figure 5.9B and D). This is consistent with other kinematic indicators (See Section 5.5).

The shear zones themselves are largely parallel to the composite S_{0+1+2} fabric with an average orientation of 155°/15° W, and vary spatially with this; in the east they strike at approximately 82° and dip 20° S, whereas in the west they have strikes of approximately 196° and dip between 28° and 35° (Figure 5.9E). Lineations in the shear zones trend down dip and show a similar clustering to the L_2 lineation with an average trend of 266° and plunge of 25° (Figure 5.9F).

Shear zones are recognised at all scales throughout the SMZ. Large shear zones bound the major thrust sheets which have a fairly constant thickness ranging between 750-1000 m. Shear zones are also generally present within mica-rich metapsammitic and metapelitic thrust sheets. These 1-2 m thick, mappable intra-unit shear zones show a spacing of 100-200 m. Shear zones are also locally present on 20-30 m scales in metapelitic thrust sheets. Smaller scale shear zones of thickness 1 m or less are also found 5-10 m apart in imbricate arrays (Figure 5.9C) are also found locally within these units. There also appears to be a general increase in the amount of localised deformation towards the western end of the map area as 1-2 m thick imbricate shear zones with a spacing of 10-15 m are recognised in metapelite (TS14). Gauging offsets on these shear zones is difficult due to the limited outcrop exposure, which equates to the height of the canyon walls (100-200 m), as well as a lack of any distinct markers that are displaced across the shear zones. One can speculate that offsets are likely on the order of hectometres to kilometres due to the highly strained nature of the rocks, as indicated by the near zero angle between shear zone foliation and shear zone boundaries (Chapter 2 and Figures 5.9B and D) as well as the fact that these shear zones juxtapose rock types of different sedimentary origin.

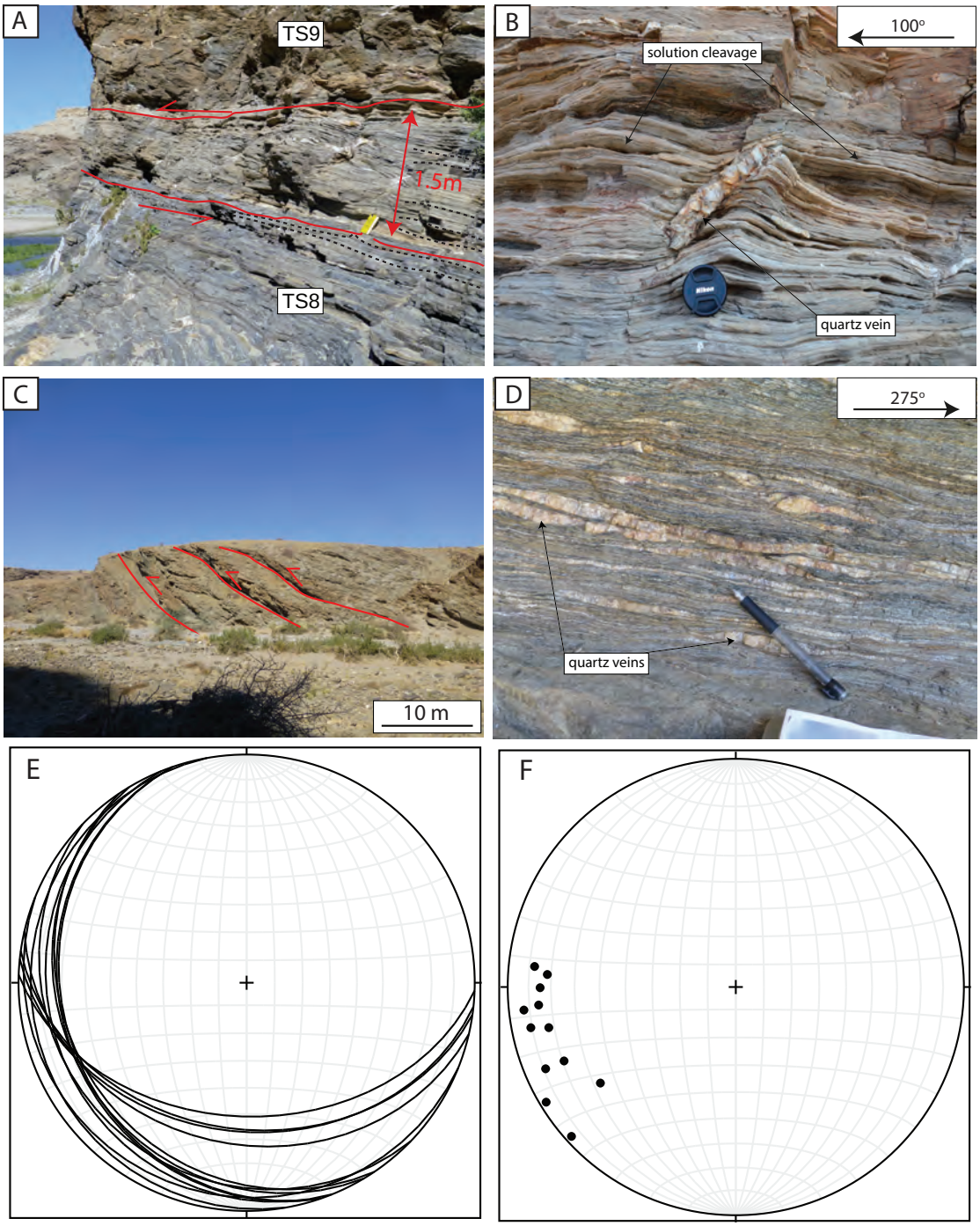

Figure 5.9: Unit-bounding and intra-unit shear zones of the SMZ. A) Large unit-bounding shear zone separating TS8 and TS9. B) Close up on the TS8-TS9 shear zone highlighting the geometry of the main structural features. Foliation is approximately parallel to the shear zone boundaries and typically contains quartz veins orientated at 45° to the shear zone boundary. C) Imbricate shear zones within the central metapelitic unit (TS11). D) Close up of an internal shear zone showing the strong mylonitic foliation and occurrence of foliation parallel, and often lenticular, quartz veins. E) D_2 shear zone boundaries and foliations. F) D_2 shear zone lineations.

5.4 Brittle Structures

5.4.1 Pinch-and-Swell/Boudinage

Pinch-and-swell and boudinage structure are well-developed where metpsammites or metamafics are enveloped by less competent rock types. Boudinage is observed to occur via both brittle and viscous mechanisms. It is, however, most readily observed as vein filled fracture boudins in quartzitic and metamafic lenses. In the quartzitic unit (TS5) boudinage structures are symmetrical with apparent shortening directions approximately perpendicular to S_{0+1}, although the foliation is warped inwards towards the boudin necks which typically contain quartz veins (Figure 5.10A and B). Symmetrical boudinage is also visible in metamafic lenses in the hanging walls of a number of the ductile shear zones occurring within the metapelitic units (TS11 and TS14; Figure 5.10B). Asymmetrical boudinage structures are also present

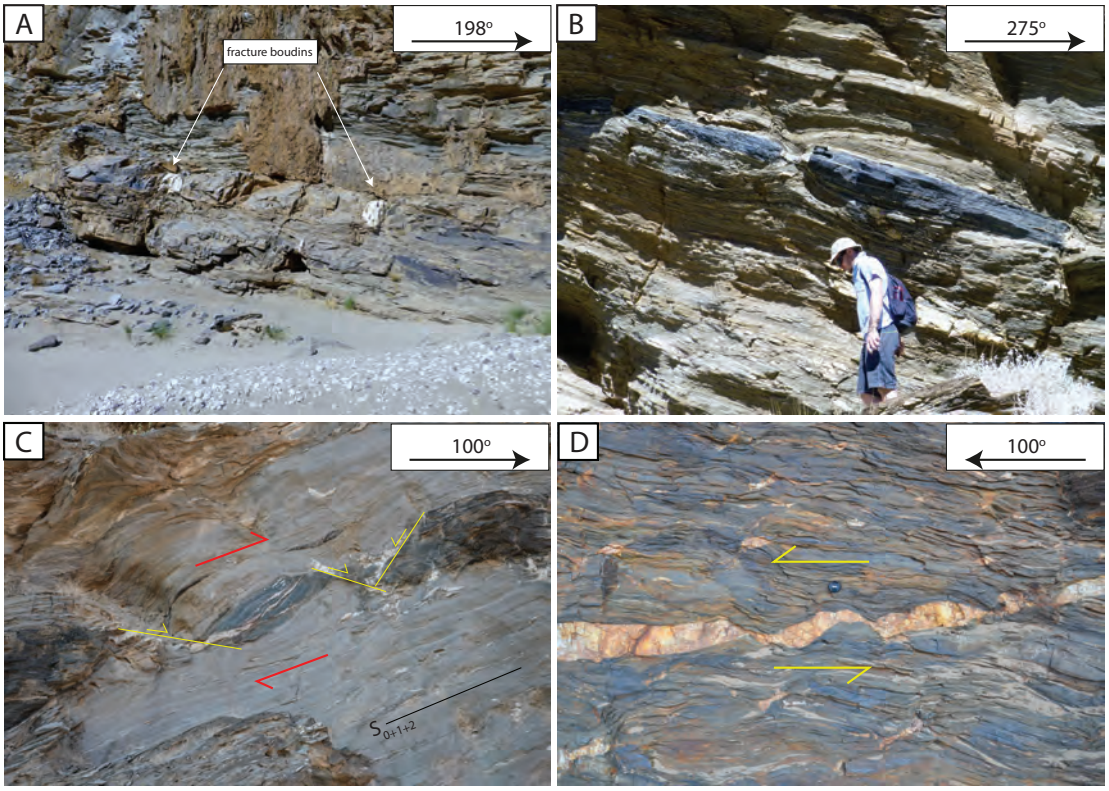

Figure 5.10: Boudinage structures in the SMZ. A) Symmetrical fracture boudins in quartzite layer surrounded by viscously deformed metapsammite in TS5. B) Boundin of metamafic rock in the hanging wall above a reverse shear zone in the central metapelite (TS11). C) Asymmetrical boudinage of metamafic lenses in mélange unit (TS9) in the centre of the map area. Extension of metamafic lenses is accomodated by normal shear fracture while surrounding matrix is viscously deformed. D) Asymmetrical boudinage of quartz vein in metapsammitic unit (TS8). Note that, in this case extension is accommodated by viscous shearing.

(Figure 5.10C and D). In the block-in-matrix unit in the centre of the map area (TS9), metamafic slices have, in places, been extended via formation of normal-sense shear fractures (5.10C). In the mica-poor metapsammite (TS8), quartz veins also show asymmetrical boudinage, although in this case it appears to have been accommodated entirely by viscous processes (5.10D). In both instances the foliation is observed to wrap around the boudinage lozenges.

Large-scale brittle deformation is largely restricted to more competent units such as the quartzite (Figure 5.11A) and the upper metapelite-poor part of the metaturbidite, where faults are identified by distinct breaks in the rock and pinching of bedding in the sandstone (Figure 5.11D). Metamafic lenses are also visible in places along these surfaces (Figure 5.11A) in the quartzite (TS5). These faults show spacing similar to ductile shear zone of 100-200 m, and have similar orientations (Figure 5.11E and F). Most of the major brittle structures, however, appear as tabular fault zones (Figure 5.11C and Figures 5.12A and C). The geometry of these structures is similar to the more discrete brittle faults and shear zones, and a sub-horizontal stretching lineation (L_3) is found on foliation surfaces in a few of the major fault zones (Figure 5.11F).

The major brittle structures occur along the boundaries of the major lithostratigraphic units. Two of these occur in the eastern region of the map area separating tectonostratigraphic units TS1 and TS2, and TS5 and TS6 respectively. The third occurs in the western region and separates units TS12 and TS13. Their brittle nature is indicated by the presence of carbonate-bearing cataclasites, breccias and fault gouges, and retrogression of either hanging wall or footwall rock (or both) to greenschist and subgreenshict facies assemblages that are usually dominated by chlorite or amphibole. Each of these faults is unique, as they have different macroscopic appearances, texture and mineralogy. In all cases, however, the brittle structures appear to overprint ealier ductile deformation features. Outcrop-scale observations are presented below, while more detailed petrographic and microstructural data are presented in Chapter 6.

5.4.2 TS1-TS2 Fault

The main fault zone in this structure is a 1 m thick zone of well-foliated fault gouge that lies between the high strain footwall of TS1 and retrogressed hanging wall of TS2 (Figure 5.12A). The gouge is composed mainly of fine-grained clay and carbonate minerals. It is well-foliated by a closely-spaced pressure solution cleavage and contains 5-15 cm thick lenses of less-foliated quartzitic material (Figure 5.12B). The planar fabric in the fault is parallel to the fault orientation with strike of 087° and dip of 21°. It also contains sub-horizontal lineation with trends 092° and 251°, with plunges of 04° and 07° respectively (Figure 5.11E and F).

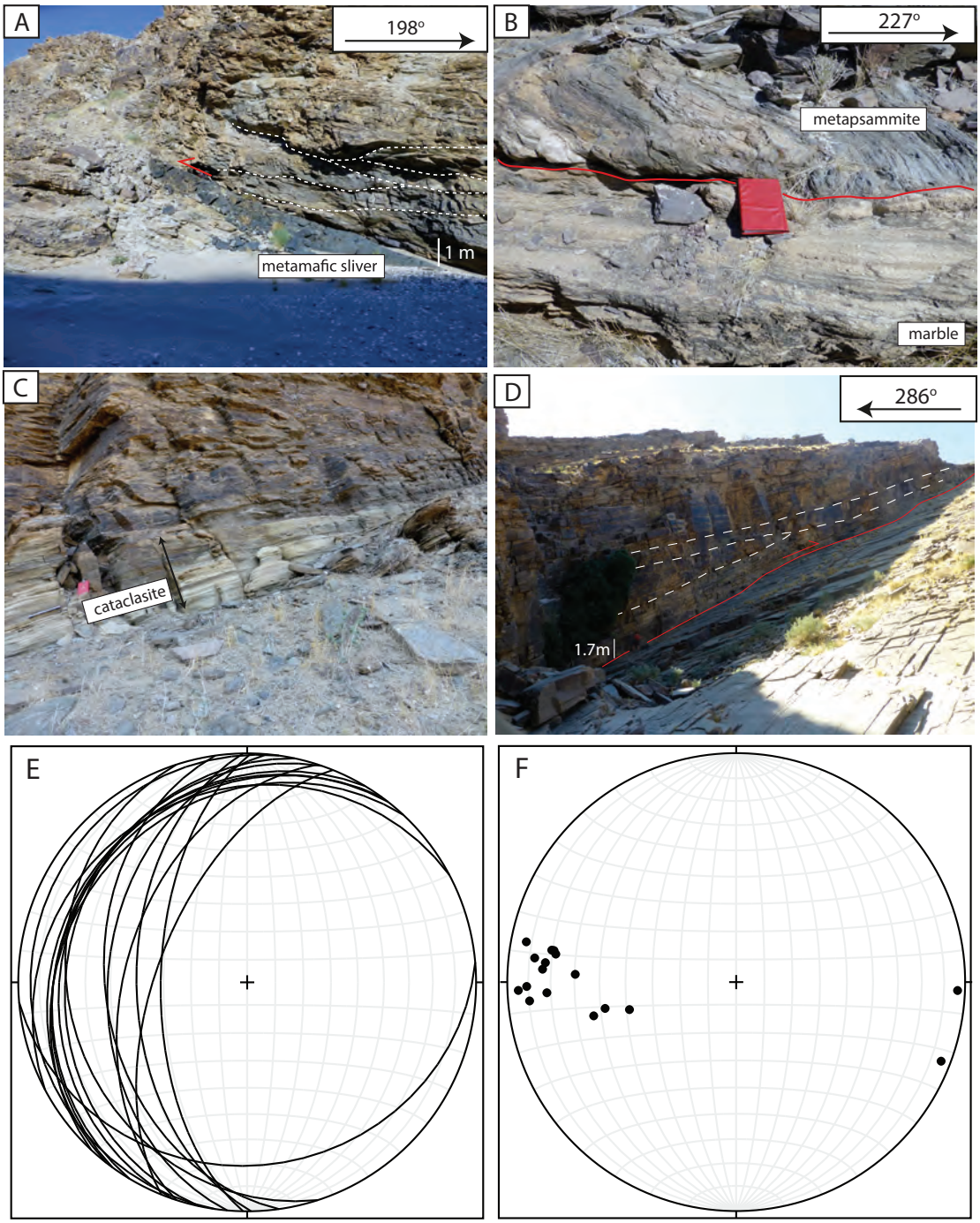

Figure 5.11: Faults in the Gaub Canyon. A) Brittle thrust fault with metamafic lens in quartzite (TS5) cross cutting the disjunctive shear fabric (dashed white lines). B) Marble-bearing fault cutting foliation in metapsammitic unit (TS6). C) Cataclastic fault zone at the base of the metaturbidite (TS12). D) Large brittle thrust in upper metaturbidite with slight pinching of hanging wall bedding (dashed white lines). E) Fault zone orientation and foliations. F) Fault zone lineations. Note that the sub-horizontal fault lineation is only found on D_3 fault planes.

5.4.3 TS5-TS6 Fault

This fault zone is a 1-2 m thick fault zone that separates the quartzitic unit (TS5) from an overriding metapsammitic unit (TS6)(Figure 5.12D). It contains a 50 cm thick, dark red, fine-grained quartz, feldspar, carbonate breccia that directly overlies the quartzite of unit TS5 (Figure 5.12E). This massive fault breccia appears to be largely recrystallised although fine-grained clasts appear to have an elongation direction parallel to dip on the fault. Moving higher up the fault gouge gives way to high strain hanging wall metapsammitic rock assemblage in which boudinaged sandstone layers and metamafic slivers are present. Quartz and calcite veining is also abundant near the base of unit TS6. The hanging wall rock has a well-developed ductile foliation which wraps around sandstone lenses and is warped in towards the quartz and calcite veins. There is a strong down dip lineation in this zone that is defined by quartz, hornblende and biotite.

5.4.4 TS12-TS13 Fault

This fault is different from the previous two, as it does not occur as a fault zone but rather a discrete surface at the top of a highly deformed mix of metapelite and quartzite. Across this surface there is a noticeable discordance of foliation orientation, with steeply dipping foliation in the footwall and relatively shallow dipping foliation in the hanging wall. The foootwall rock is high strain metapelite whereas the hanging wall is mostly composed of semipelite with 50 cm thick metapsammitic layers and metamafic lenses. The fault surface itself appears to run along the contact of the pelite/semipelite and one of the metapsammitic layers (Figure 5.12E). The hanging wall rock appears does not appear to be retrogressed, whereas the footwall rock is retrogressed and composed largely of a variety amphibole minerals (tremolite and actinolite) with a fibrous fan-shaped habit.

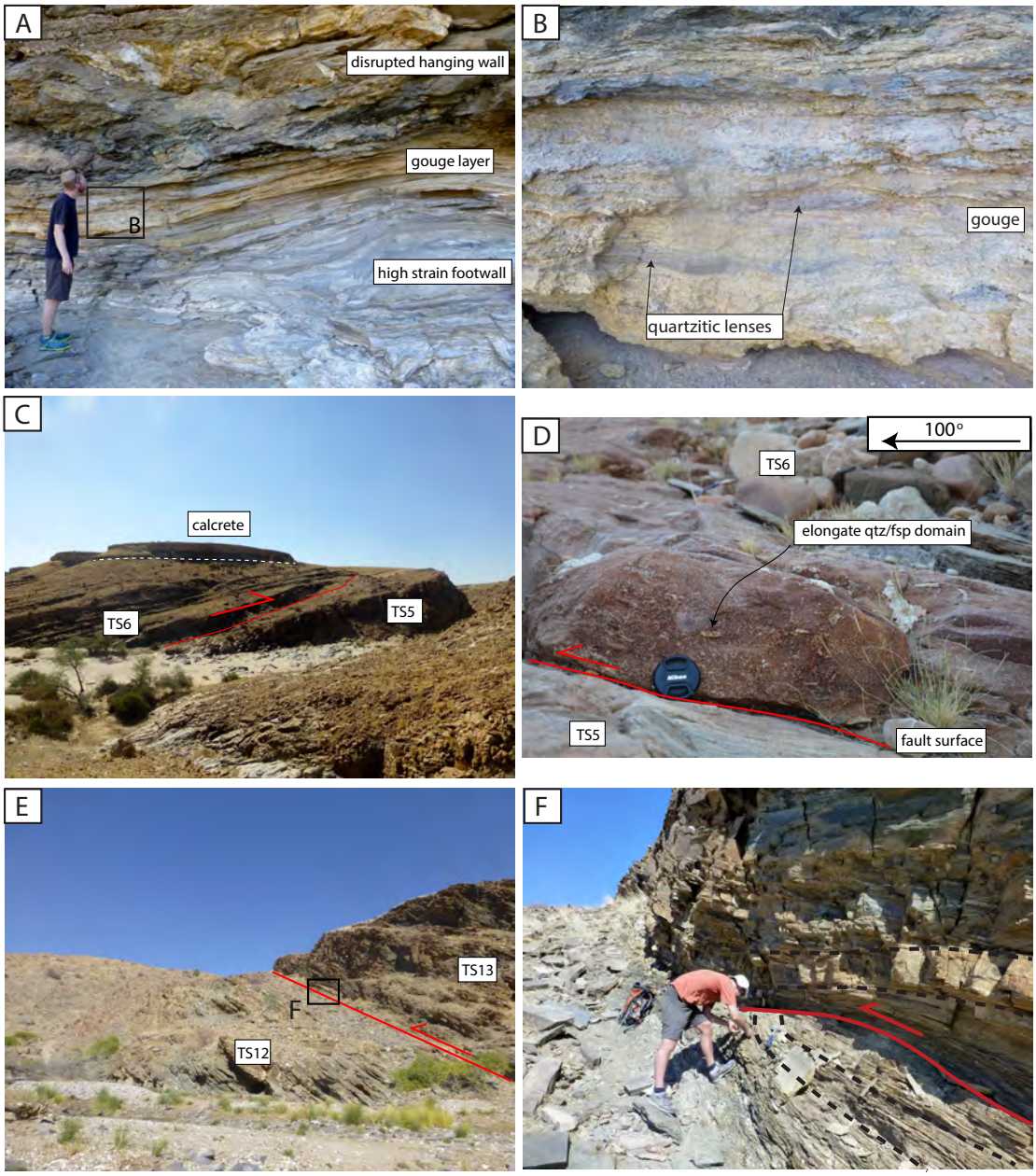

Figure 5.12: D_3 faults. A) Large brittle fault showing between units TS1 and TS2 with carbonate fault gouge underlying a fairly thick zone of retrogressed hanging wall. B) Gouge layer in A) showing quartzitic lenses within fine grained carbonate-clay gouge. C) Large brittle fault separating units TS5 and TS6. D) Red carbonate breccia overlying quarzite on the TS5-TS6 fault. Lighter elongate fragments are composed of quartz and feldspar. E) Large brittle fault separating units TS12 and TS13 identified by a distinct break in slope. F) Close up on E) showing the discordance of foliation between the footwall and hanging wall.

5.5 Summary of Outcrop-Scale Observations

Shear sense can be seen on map scale by the gradual steepening of the foliation towards the large fault separating the SMZ from rocks of the Kuiseb Schist in the west (Figure 5.2). This is also seen on a smaller scale, as disjunctive fabrics in the quartzite are cut by brittle thrust faults at acute angles that point up-dip (Figure 5.11A). Other kinematic indicators include: sigmoidal clasts in the metaconglomerate and sigmoidal quartz veins in metapelite (Figure 5.13A) that taper both up and down dip (Figure 5.3D); flow perturbation folds that form on lithological boundaries between metapelite and metamafic with a SE vergence (Figure 5.13B). All shear sense indicators therefore suggest that the dominant transport direction is top to the southeast.

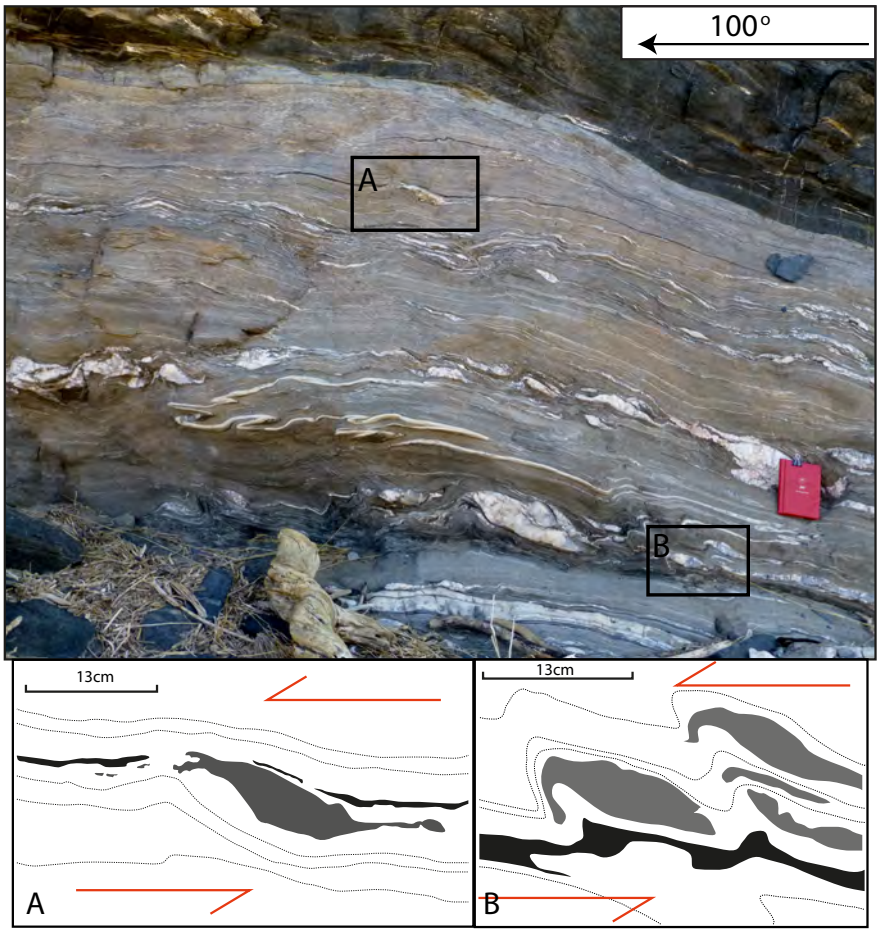

Figure 5.13: Shear sense indicators from an outcrop of semipelitic rock with mafic slices Insets A and B show the positions of the sketches below. A) Sigmoidal quartz clast (grey) with disaggregated metamafic sliver (black). B) Transposed fabric. Note that, while the fabric of the semi-pelite is displaced by folding, metamafic slivers are not, and appear to be stretched out rather than folded.

This shear sense is observed in both D_2 and D_3, although locally the sub-horizontal lineation

L_3 points to a component of NE-SW movement. L_3 trends in the strike direction of the crenulation cleavage (S_3) which cross-cuts S_{0+1+2}. L_3 is also found, very locally, on dicrete brittle fault zones.

The deformation features preserved in the rocks of the SMZ are summarised in Figure 5.14. The overall fabric of rocks in the SMZ is the penetrative ductile foliation S_{0+1+2} which is, throughout the region, defined by prograde-to-peak platy metamorphic minerals such as chlorite, biotite and muscovite in metapelites and metapsammites, as well as hornblende in metamafic rock types. There is nevertheless a heterogeneous distribution of deformation and each lithogical assemblage is charaterised by a distinct structural style. Pervasive ductile deformation dominates the metapelitic and micaceous metapsammitic units which are often internally thickened through folding and the action of reverse shear zones (TS10, TS11 and TS14), whereas in the mica-poor metapsammitic units (TS8) no reverse shear zones are present and internal thickening has been accommodated exclusively by folding. Evidence of localised brittle deformation is, however, present in the form of quartz veins that are abundant in both these rock types. In quarzitic units (TS5 and TS12) brittle thrusting is the dominant mode of deformation although ductile shearing is locally present within these units, where it is concentrated in metapelitic or metapsammitic rocks. The block-in-matrix semipeltite and metamafic assemblage is characterised by mixed-mode deformation. Semipelitic rock types are typically ductily deformed and show a strong, closely-spaced penetrative foliation, although locally quartz veins are again present. Metamafic and chert lenses are commonly boudinaged with quartz veins in the boudin necks, although in places, extension in metamafics is also accommodated by normal-sense shear fractures.

Intense brittle deformation is found overprinting earlier D_2 ductile deformation on a few of the major unit-bounding shear zones (e.g.TS1-TS2, TS5-TS6 and TS12-TS13 faults and the GRL). The cores of these fault zones are characterised by gouges, breccias, cataclasites or distinct fractures, and the hanging wall and footwall rock surrouding these fault zones is often retrogressed to greenschist or sub-greenschist facies mineral assemblage dominate by tremolite, actinolite and chlorite with other fine-grained clay minerals. Such deformation features are not found within the interleaving units between these faults zones and this phase of deformation appears to be highly localised on a few of the unit-bouding fault structures (Figure 5.14).

The macro-scale structures preserved in the SMZ thus record a two-stage deformation history. The first stage of deformation is associated with progressive development major penetrative fabrics during distributed ductile deformation along the prograde-to-peak metamorphic path (D_1 and D_2). A later stage of brittle deformation occurred during retrogression and exhumation of the SMZ (D_3). It was, however, highly localised on a few unit-bounding structures and S_{0+1+2} is only weakly overprinted by S_3 within the interleaving thrust sheets.

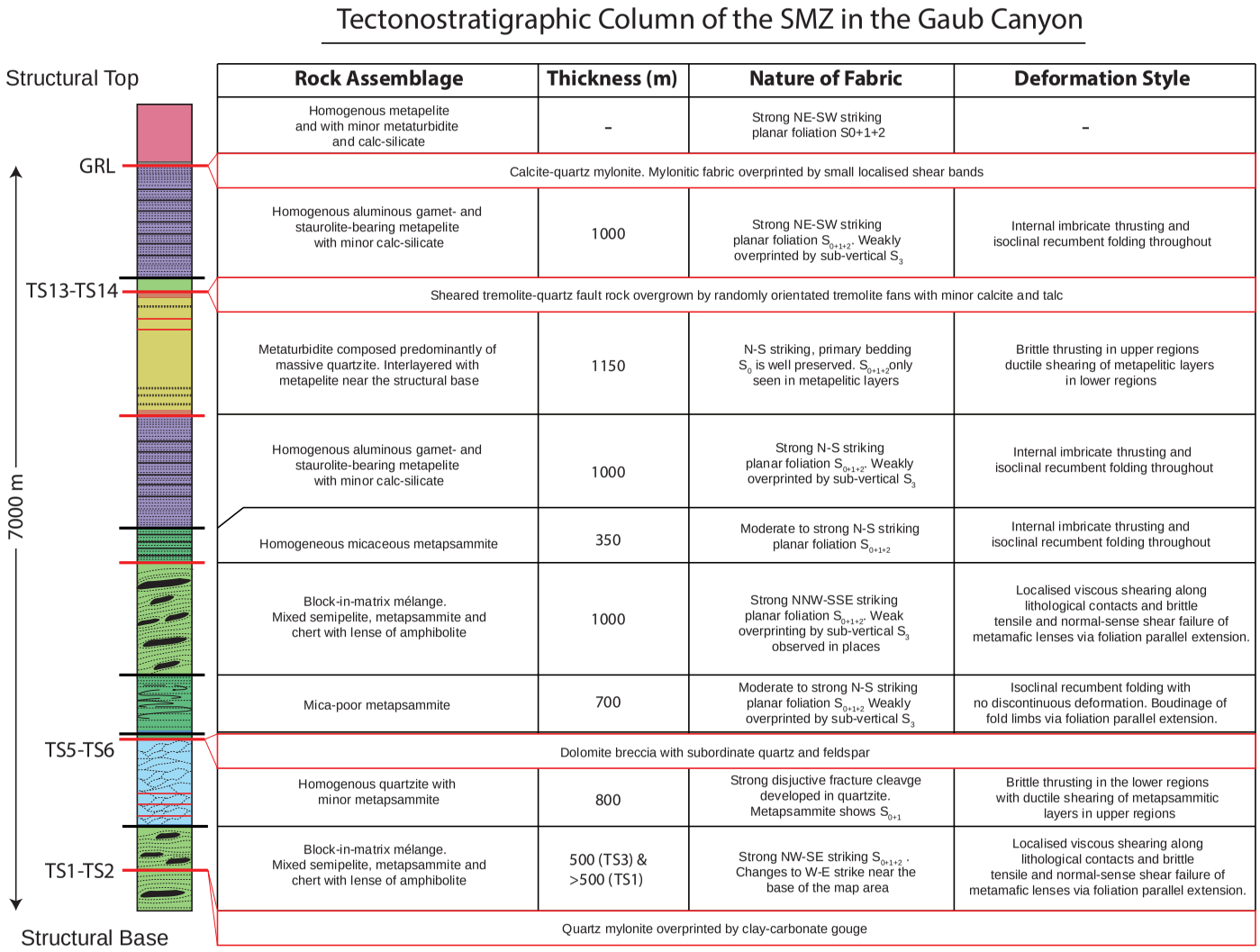

Figure 5.14: Representative tectonostratigraphic column of the SMZ drawn approximately to scale. Table summarises the important lithological, fabric and deformation characteristics of the various thrust sheets as well as the major brittle unit-bounding fault structures. Note that, in the column, black lines represent ductile shear zones, red lines brittle faults while dashed black lines represent the foliation.

Chapter 6

Fault Rock Petrography

The faults and shear zones in the SMZ can be distinguished based on their position with respect to the major litho-tectonic units (Table 6.1). Faults internal to the lithotectonic units are grouped together, and faults that bound lithotectonic units are grouped together. This classification scheme is used for the reason that retrograde (D_3) brittle deformation in the SMZ is localised solely on unit-bouding shear zones, while earlier prograde-to-peak ductile deformation (D_2) is preserved in the internal shear zones (Chapter 5). This classification scheme therefore also allows for easy separation of the prograde-to-peak (D_2) and the overprinting retrograde (D_3) events, and allows discussion of microstructures and deformation mechanisms relating to each deformation event separately.

	Fault Rock	**Samples**
Internal (D_2; prograde-to-peak; mostly ductile)	Quartzitic Mylonites	GB17, GB18 (TS5);
	Micaceous Mylonites	GB27, GB28 (TS12);
Unit Bounding (D_3; retrograde; ductile-to-brittle)	Fault Gouge	GB14, GB15, GB16 (TS1-TS2);
	Fine Crush Breccia	GB19, GB20 (TS5-TS6);
	Calc-mylonite/cataclasite	GB32, GB33, GB34, GB35 (GRL);
	Mylonite	GB29, GB30, GB31 (TS12-TS13);

Table 6.1: Classification table for sampled fault rocks in the SMZ. Samples are classified based on the fault rock textures (after Sibson, 1977) and position relative to the major lithotectonic units. Ductile Shear zone rocks are termed mylonites and are classified according to their mineralogy. Samples from the same fault zone are separated by commas.

6.1 Structures internal to litho-tectonic units

Ductile shear zones internal to lithotectonic units fall into two broad groups: those that are predominently quartzitic with subsidiary mica (both bioite and muscovite) depending on the host protolith; and those that are predominently micaceous with quartz lenses and ribbons. Other accessory phases may also include Fe-Mg oxides, epidote, feldspar and amphibole (actinolite and hornblende), although these are usually not present in proportions high enough to control the rheological behaviour. The textures and microstructures that develop in these mylonitic rocks change with this varying composition.

6.1.1 Quartz-dominated mylonites

Quartz mylonites and mica-bearing S-C mylonites are found mostly in 1-2 m wide ductile shear zones in the upper portion of the major quartzitic unit (TS5). These shear zones show a decimetre-scale layering with mica-rich and mica-poor domains. Samples GB17 and GB18 are representative of the mica-poor and mica-rich domains of a shear zone in the centre of unit TS5 and approximate other shear zones in this unit.

Mica-poor mylonites have a fine-grained matrix composed of 85% quartz (Figure 6.1A and Figure 6.2A). The remainder is composed of roughly 10% in equal proportions of biotite and actinolite, and 5% magnetite and epidote. Rare plagioclase feldspars are also found within the quartz matrix. Quartz grain size ranges between 0.01 and 0.4 mm with a fairly continuous gradation from the finer to coarser grains within this range, although there appears to be weakly bimodal grain-size distribution (Figure 6.3). The finer quartz grains are anhedral to subhedral and exhibit a very weak grain-shape preferred orientation (GSPO) in grains with more elliptical shapes. This defines a weak continuous foliation. No evidence for intra-crystalline deformation is observed in these grains. The coarser quartz grains occur as lens-shaped domains with an aggregate-shape preferred orientation (ASPO) that is generally parallel to the main fabric. Quartz veins also locally transect this fabric at 45° or less (Figure 6.1A). The coarser quartz grains in the ribbons and veins are generally more angular. A weak undulatory extinction and subgrains may be found in grains >0.05 mm (Figure 6.2A), but this is not common. Qualitative examination of crystallographic preferred orientation (CPO) in quartz using a gypsum tint-plate revealed that quartz grains have seemingly random crystal orientations.

Biotites and actinolites form coarse-grained porphyroclasts within the quartz matrix and are fairly randomly distributed throughout the rock giving it a patchy texture. The porphyroclast grain size ranges between 1.0 and 3.0 mm, typically with highly irregular grain boundaries resulting from the encroachment of the quartz matrix (Figure 6.1C). Actinolite grains commonly have inclusions of quartz whereas biotite grains are relatively inclusion free. Both minerals show three preferred orientations, with (010) cleavage parallel to the weak

quartz GSPO or slightly oblique to it (both clockwise and anticlockwise) in sections perpendicular to foliation and parallel to lineation. Actinolite grains that are oblique with respect to the foliation typically show undulose extinction. In places, biotite porphyroclasts show evidence for very localised brittle deformation as micro-breccias that are present along the porphyroclast-matrix contact (Figure 6.2E).

Quartz-Mica mylonites typify the Type-II S-C mylonites of Lister & Snoke (1984). The major mineral phases in these rocks are quartz and mica (3:2 muscovite and biotite) with approximate modal proportions of 65% and 35% respectively. Magnetite constitutes <1% of the rock which also contains trace amounts of epidote along with rare grains of plagioclase feldspar. Quartz grain sizes range between <0.01 and 0.4 mm, with the majority of the grains ranging from 0.1 mm to 0.4 mm. There is an observable bimodal grain size distribution (Figure 6.3). Quartz grain shapes are subhedral to anhedral and coarser grains are generally more angular than the finer grains; however, some quartz grains do exhibit fairly irregular grain boundaries. These grains exhibit weak-to-moderate undulose extinction and subgrains (Figure 6.2B), although in places where mica is present in enough propotions to form an interconnect network subgrains are not developed in quartz (Figure 6.2C). Quartz shows no preferred crystal orientation, although a moderate GSPO is observed trending parallel to the main foliation as defined by the mica C-surfaces.

In sections cut perpendicular to foliation and parallel to down dip stretching lineation, the mica forms an interconnected network (Figure 6.1B). This geometry results from the preferential alignment of mica (010) crystallographic axes along three principal orientations, forming S, C and C' surfaces. C surfaces form the main spaced foliation and, whereas S surfaces are more dominant, mica grains trending along C' surfaces are observed in places. α and β angles (defined as the angles between S and C, and C and C' surfaces respectively; Figure 2.11C) range from 11-25° and 15-20° respectively. This typifies the banded type fabric of Blenkinsop & Treloar (1995). Mica grains also show a strong CPO which is illustrated by simultaneous extinction of most grains under cross-polarised light (Figure 6.1D).

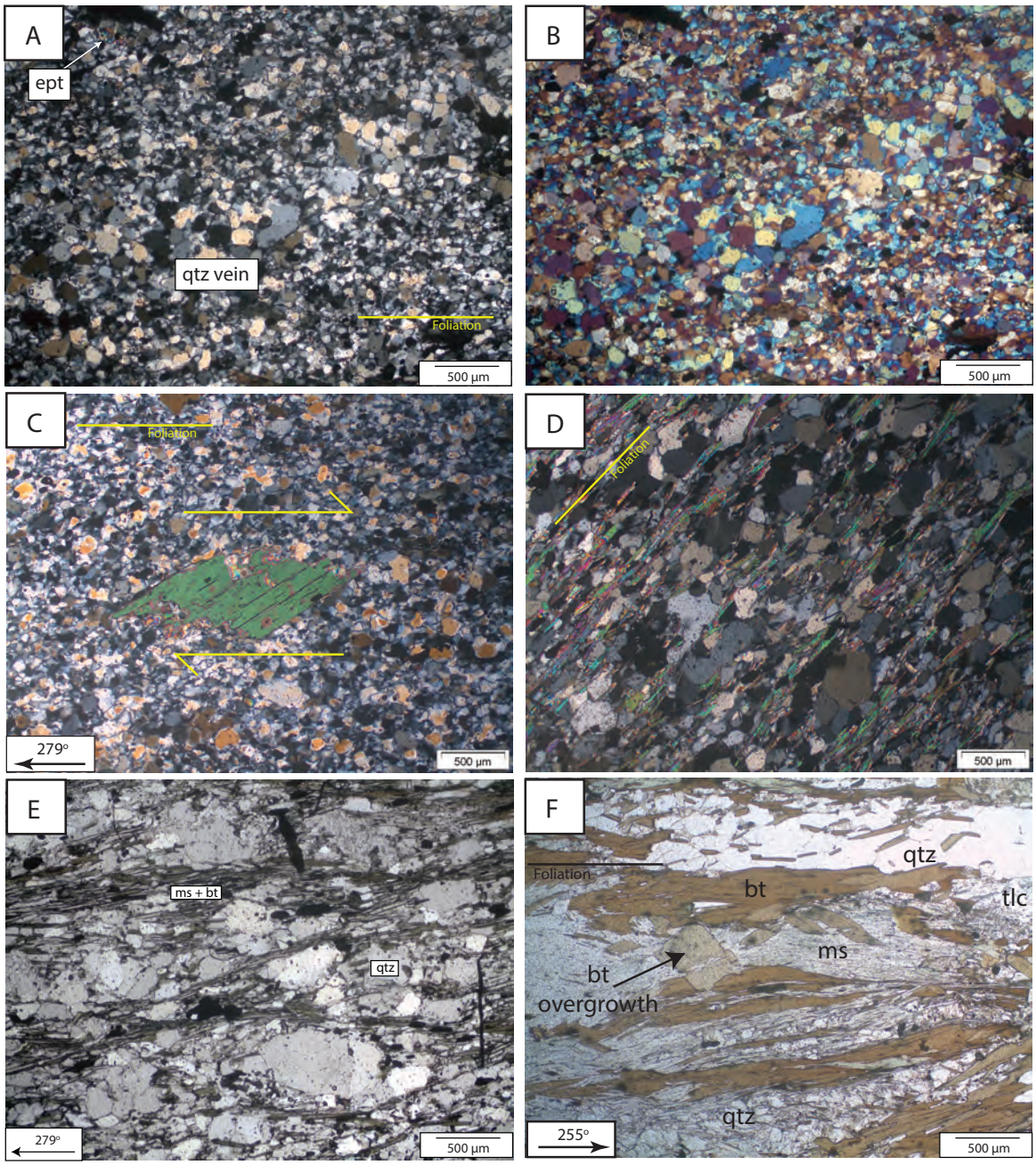

Figure 6.1: Photomicrographs of quartzitic and micaceous mylonites from the SMZ. A) quartz mylonite from unit TS5 with highly recrystallised matrix and coarser grained vein cross-cutting the foliation. B) Quartz mylonite from A) with gypsum tint plate in showing random crystallographic fabric. C) Biotite porphyroclast in quartz mylonite. D) Quartz-mica mylonite from unit TS5 with low mica interconnectivity and a strong mica LPO. E) Quartz mica mylonite with high mica interconnectivity showing C-type S-C structure where C shear bands form a spaced mylonitic foliation. F) Micaceous mylonite from unit TS12. The mylonitic foliation is defined by the alignment of mica and DSPO of quartz ribbons. Biotite overgrowth with long axis into plane of thin section is also present. qtz = quartz, ept = epidote, ms = muscovite and bt = biotite.

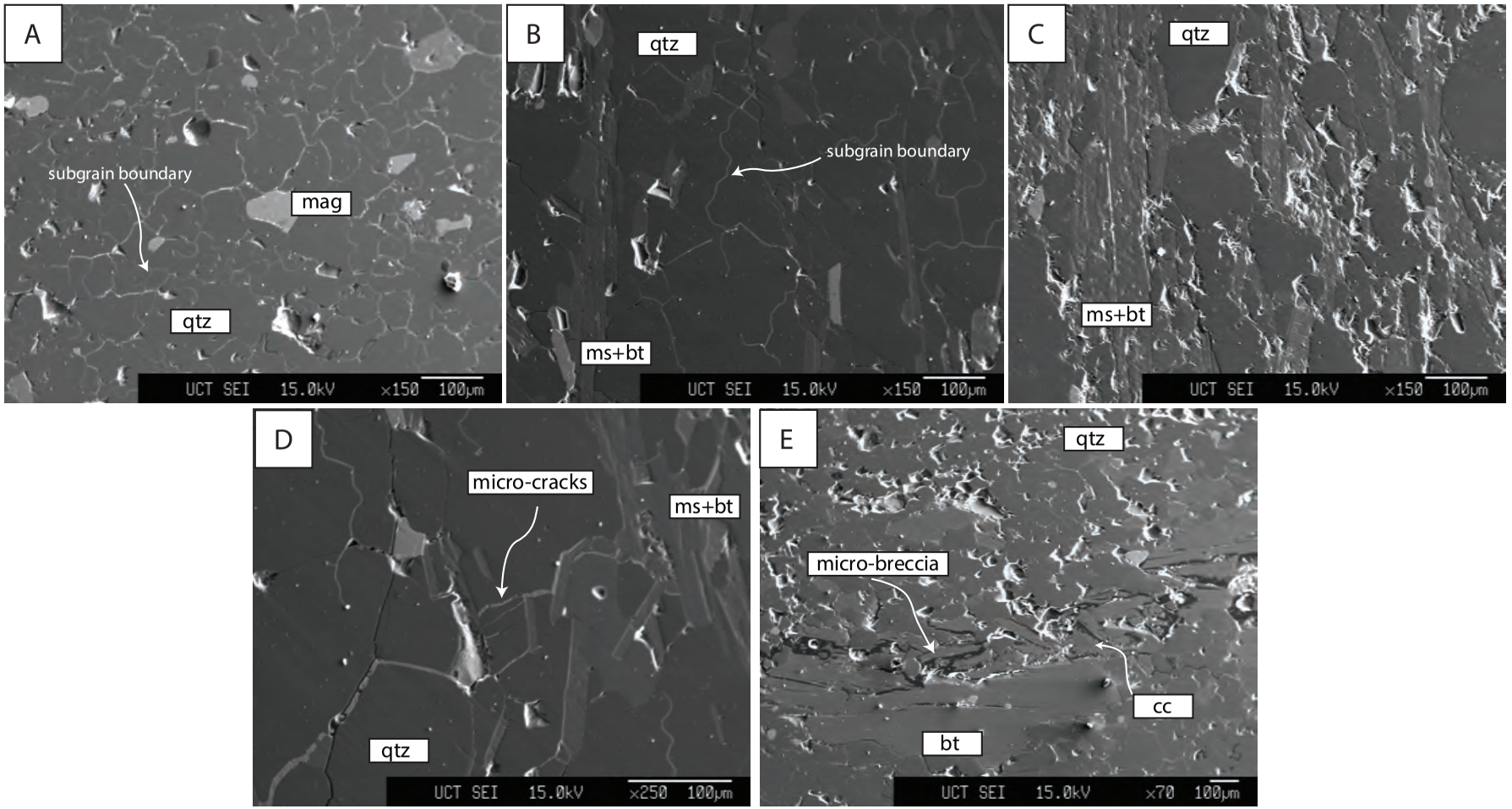

Figure 6.2: Backscatter-electron photomicrographs from quartz and quartz-mica mylonites: A) Subgrains abundant in quartz mylonite matrix; B) Quartz-mica mylonite without through-going mica network; C) Quartz-mica mylonite with through-going mica network. Note that in the latter no subgrains develop in quartz domains. D) and E) Microscopic brittle structures found locally in both quartz and quartz-mica mylonites. These tend to form at quartz-mica grain boundaries. cc = calcite and mag = magnetite.

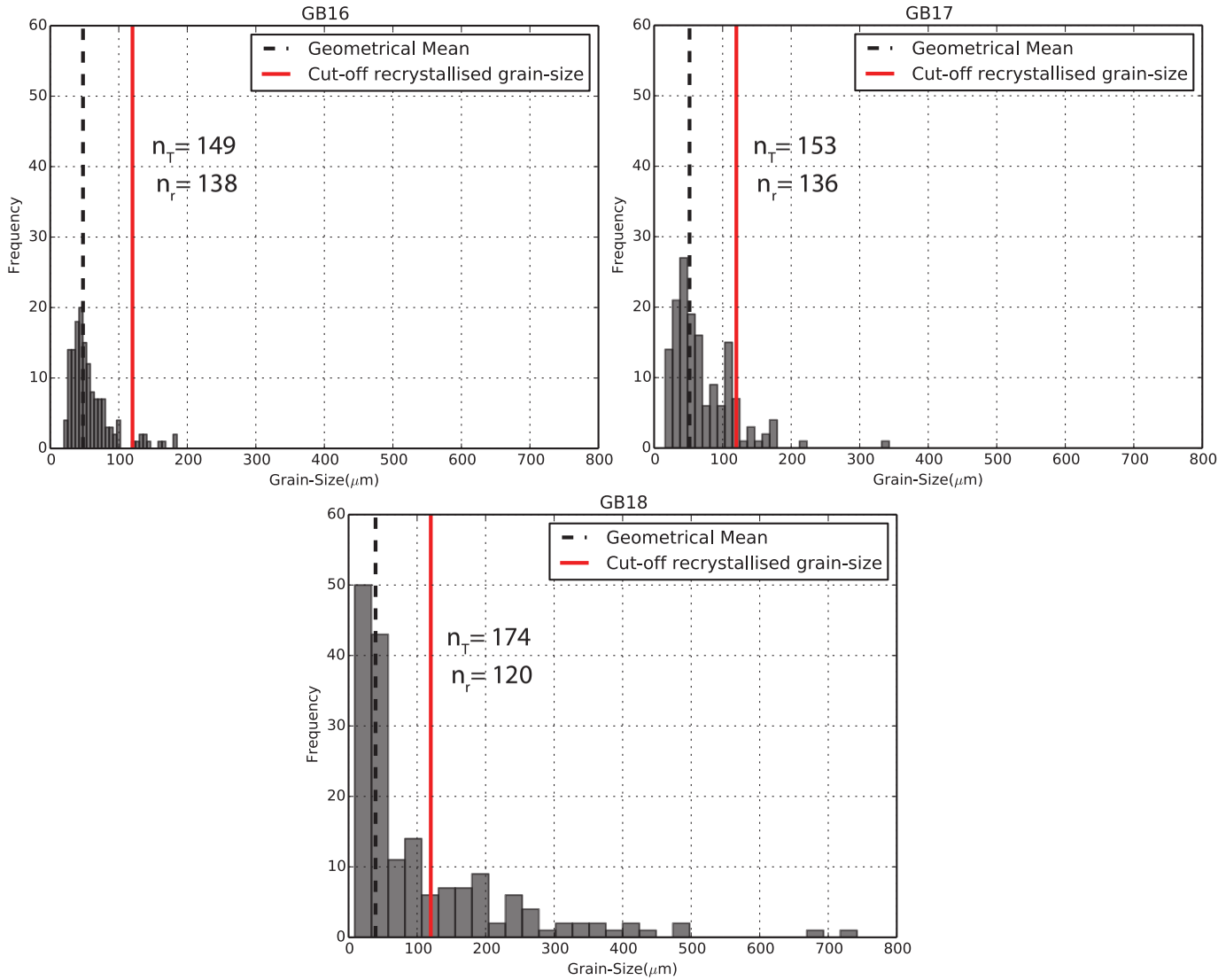

Figure 6.3: Grain size frequency plots for quartz mylonites (GB16 & GB17) and quartz-mica mylonites (GB18). n_T = total measurements taken and n_r = number of measurements below recrystallised grain-size cut-off vlaue. Note that quartz-mica mylonites have a smaller average recrystallised grain-size and a higher proportion of grains >120 μm.

6.1.2 Mica-dominated mylonites

Mica-dominated mylonitic rocks occur as thin (<50-100 cm) micaceous layers within the turbiditic unit (TS12). These intensely foliated metapelitic layers record much higher finite strains than the surrounding metapsammitic and quartzitic layers which still preserve primary bedding structures. The micaceous layers would therefore have acted as bedding parallel shear zones which have accommodated an appreciable amount of strain in this unit (Chapter 5). Samples GB27 and GB28 were taking from two of these shear zones.

Mica-quartz mylonites are composed largely of quartz veins and mica ribbons set in a quartz-mica matrix. The matrix is dominated by fine-grained quartz with biotite forming a dense interconnected network similar to the quartz-mica mylonites described in Section 6.1. Rare grains of partially sericitised plagioclase feldspar are also present. Mica ribbons are mostly quartz-free and are composed of fine-grained muscovite (60%) and medium-grained elongate biotite (40%). Quartz veins contain coarse-grained quartz (> 90%) and flakes of biotite, the amount of which varies between 0-10%. The mylonitic foliation is defined by the preferred orientation of the micas and the ASPO of the quartz veins and mica ribbons (Figure 6.1F). Both the micaceous ribbons and quartz veins have highly oblate shapes with a>b>>c, where a is parallel to the down dip stretching lineation in the foliation plane, b is perpendicular to this lineation in the foliation plane, and c is perpendicular to both the lineation and the foliation plane.

Quartz grains in quartz veins with relatively little mica have grain-sizes approximately 1 mm in diameter, and exhibit microstructures associated with grain boundary migration (GBM) recrystallisation (Figure 6.4A and B). They have highly lobate grain boundaries and typically show subgrains in the grain interior, as well as a sweeping undulose extinction. In veins with higher mica content the average quartz grain size is smaller (< 0.8 mm). These grains also tend to have only slightly wavy or straight grain boundaries. Pinning structure of quartz grain boundaries on biotite is common in these ribbons (Figure 6.1F and Figure 6.4B). Subgrains and undulose extinction are present, although not as commonly as in mica-poor quartz veins.

In the micaceous domains both muscovite and biotite exhibit a strong SPO where grains lie parallel to the main mylonitic foliation. Recrystallised muscovite and biotite also form microfolds (Figure 6.4C) or polygonal arcs (Passchier & Trouw, 2005). They also have a strong LPO showing simultaneous extinction, although this has been modified slightly by crenulations (Figure 6.4D). The folds have a tight isoclinal attitude. An axial planar S_2 cleavage is discernable in the fold hinges (Figure 6.4C) but lies parallel to S_1 (defined by coarser elongate biotite) away from the hinge zones. Shear bands/microfaults are also present in the micaceous domains, and at their steepest point are oriented at approximately 45° to the mylonitic

foliation, roughly parallel to the axial planes of gentle crenulations in muscovite. The cross-cutting relationship with the mylonitic fabric indicates that these structures accommodated reverse slip (Figure 6.4D).

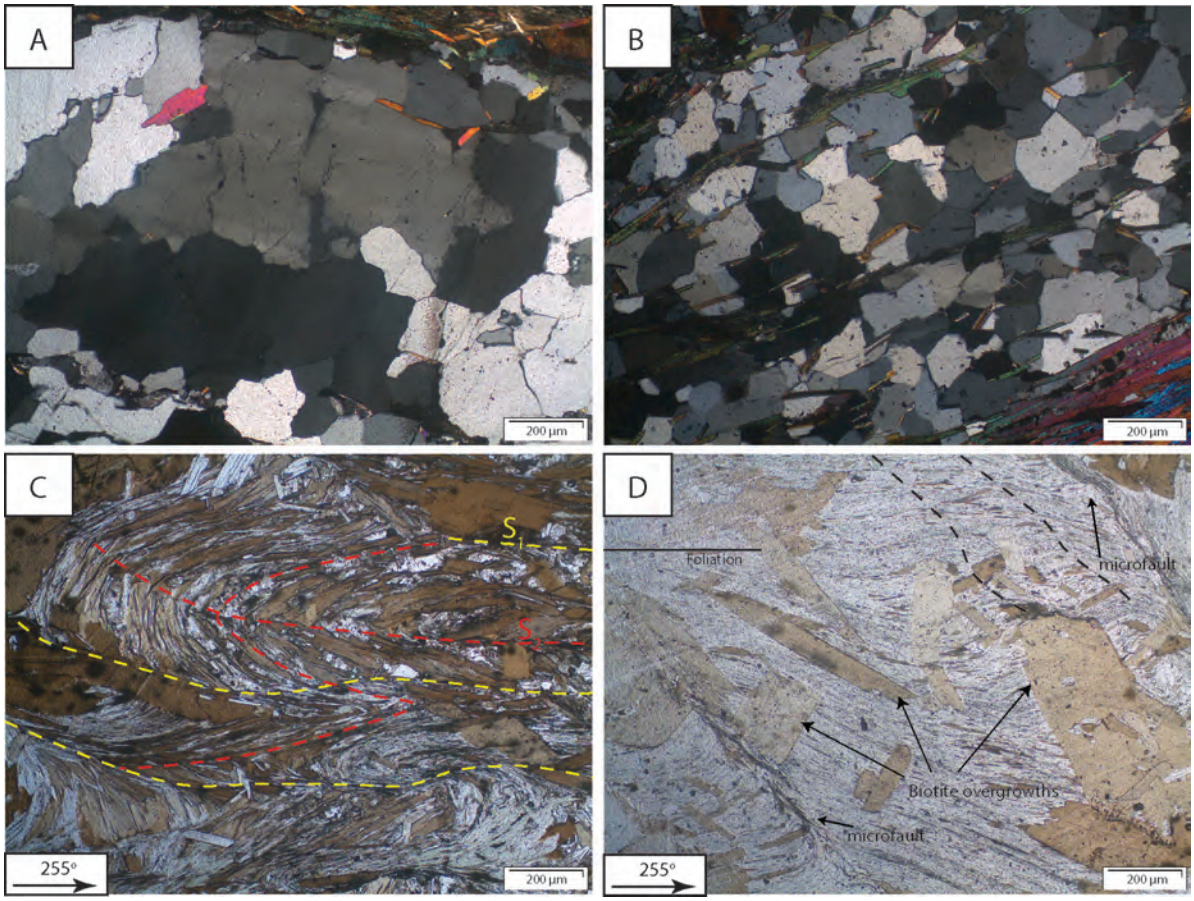

Figure 6.4: Microstructures in micaceous mylonites of unit TS12. A) and B) show microstructure indicative of dynamic recrystallisation by grain-boundary migration (GBM), namely, highly irregular grain boundaries, and grain boundary pinning of biotite. C) Assymetric, isoclinal folding of recrystallised muscovite and biotite produces axial planar S_2 parallel to mylonitic folaition (S_{0+1}). D) Shear bands/microfaults in micaceous domains with syn-to-post tectonic biotite porphyroblasts. Dashed lines show that the orientation of the weak crenulation axial planes is also roughly parallel to the microfaults.

Coarse-grained biotite overgrowths are also present. Commonly occurring in micaceous ribbons, these overgrowths are also found in the quartz-mica matrix; however, never in the quartz veins. These porphyroblasts overprint the mylonitic fabric and contain inclusions of fine-grained muscovite. In other, more micaceous shear zones (GB28), coarse-grained biotite dominates the fabric, suggesting extensive grain growth following earlier recrystallisation and shearing. Some biotite grains also show a preferred orientation with long axes orientated parallel to the shear bands/microfaults; however they are also locally cut by the microfaults (Figure 6.4D). Circular clusters of coarse-grained muscovite and biotite also occur in the mi-

caceous domains. The mineral grains in these clusters show no preferred orientation, and are generally observed to overprint the mylonitic fabric, although recrystallised muscovite can be found to wrap around these features locally.

6.2 Structures bounding litho-tectonic units

Some of the structures that bound the various lithotectonic units are brittle tabular fault zones. They are characterised by highly disrupted layering, fractures and retrograde greenschist (and lower) facies mineral assemblages (Chapter 5). These faults are also characterised by the presence of carbonates as both a major rock forming mineral phase and as vein precipitates. Each of these fault zones has a unique texture and mineralogy, and they are therefore described separately in the sections that follow.

6.2.1 TS1-TS2 Structure

The quartzitic lenses of the fault gouge consist of quartz ribbons set in a fine-grained matrix of quartz (>95%), epidote and magnetite (<5%). In the quartz matrix, grains are generally very fine, ranging between 0.02 and 0.04 mm, and are subhedral with slightly irregular to straight grain boundaries and 120° grain boundary triple junctions. These grains have a moderate GSPO, and a weak undulose extinction is observed in places. The magnetite grains have a similar grain-size to the quartz grains, and show a strong GSPO parallel to that of the quartz (Figure 6.5A). Coarse-grained idiomorphic magnetite is also found to overprint the quartz fabric, and it shows a close spatial relationship with pressure solution seams. Plagioclase grains are also found in places as porphyroclasts in the matrix. These grains usually contain inclusions of quartz, have irregular grain boundaries, and show a strong undulose extinction. These are altered to sericite in places. The quartz ribbons are coarser-grained, with grain sizes in the range 0.2-0.8 mm, and show both serrated and straight grain boundaries. Subgrains and undulose extinction are common in ribbon grains. The ribbons have a clear ASPO that is parallel to the GSPO of the quartz matrix. The preferred orientation of these ribbons and GSPO of the matrix defines a continuous mylonitic foliation. The quartz ribbons also show symmetrical microboudinage that is associated with deflection of the mylonitic foliation toward boudin neck. The boudin necks are also sites for precipitation/deposition of soluble material (Figure 6.5A).

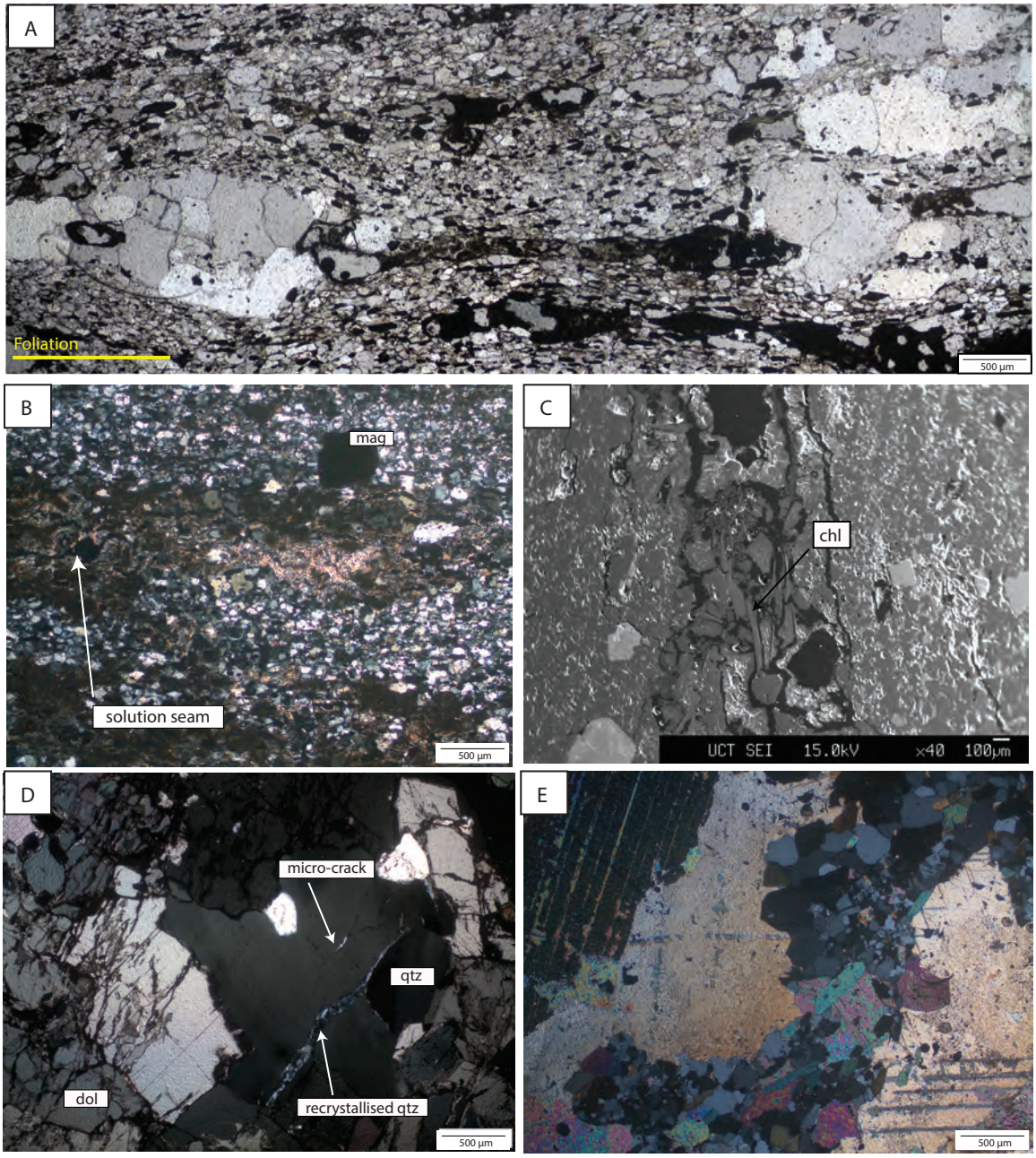

Figure 6.5: Photomicrographs from TS1-TS2 (A,B and C) and TS5-TS6 (D and E) structures. A) Boudinaged ribbon of coarse-grained quartz surrounded by ductile matrix of quartz and magnetite. Note that dark material accumulates in boudin necks. B) Seams of dark material cutting through the mylonitic fabric. Light material comprises of fine-grained clay minerals. Euhedral magnetite also overprint the mylonitic fabric. C) Backscatter-electron image of seam cutting through recrystallised quartz in TS1-TS2 structure. Note that seams contain retrograde hydrothermal chlorite. D) Sub-parallel fractures in blocky dolomite. Note how adjacent quartz grain is relatively undeformed. E) Calcite veins cross-cut and deflect the mylonitic foliation. Both syn- and post-tectonic twin morphologies are found in vein calcite. mag = magnetite, chl = chlorite, dol = dolomite and qtz = quartz.

Structures related to diffusive mass transer (DMT) are abundant in this rock, and are clearly illustrated by the presence of pressure solution seams that cut the mylonitic quartz fabric (Figure 6.5B), as well as the presence of a dark intergranular film that outlines the matrix grain boundaries under plane-polarised light. The seams have a smooth-to-wavy morphology, and generally lie parallel to the mylonitic foliation although they do anastomose. Large seams are spaced between 2-8 mm apart and thus define a spaced pressure solution cleavage. Precipitation of dark fine-grained clay minerals (Figure 6.5B), reddish-brown iron oxide, and fine grains of chlorite and biotite are also associated with the pressure solution cleavage. Reddish-brown iron oxide is also present away from seams as an intergranular film.

6.2.2 TS5-TS6 Structure

A mesoscopic lithological layering is clear in this fault zone with a basal fine-grained quartz-carbonate crush breccia overlain by a fine-grained fault gouge that gives way to the hanging wall mylonite (Chapter 5). There is therefore a recognisable decrease in the dominance of brittle deformation as one moves up through the fault zone, most likely reflecting localisation of deformation towards the basal fault surface during cooling.

The basal breccia contains blocky dolomite groundmass with quartzitic and feldspathic domains (and mixtures of the two), with variable textures. Some domains clearly show a recrystallised mylonitic texture (Figure 6.5C) and contain fine-grained quartz and feldspar (0.08-0.16 mm) along with slightly coarser calcite (0.4 mm). All grains in these domains show a strong GSPO. Domains composed solely of medium-grained feldspar are also present. The domains have an ASPO that trends roughly down dip on the fault, and is parallel to both the weak stretching lineation in the rock and the GSPO of fine-grained quartz, feldspar and calcite in these domains. These domains, however, only make up a small portion of the rock volume and are randomly distributed throughout it (Figure 5.12C).

Most of the rock is made up of blocky dolomite groundmass. The dolomite is fairly coarse with an average grain-size of approximately 1 mm. Dolomite grain boundaries are largely straight, although some grains show irregular and wavy boundaries. Grains of quartz and feldspar may also be found, and in places dolomite appears to overprint these, containing inclusions of quartz that are in optical continuity with surrounding grains. Dolomite grains are also highly fractured (Figure 6.5D). These fractures trend in a common direction and transect dolomite-dolomite grain boundaries. There is no evidence for dynamic recrystallisation in dolomite, and any reduction in grain size is largely a result of brittle fracture. Quartz and feldspar grains show little evidence for brittle fracture; however, intracrystalline deformation is observed by subgrains and undulose extinction in quartz and tapered mechanical twinning in feldspars. No twinning is observed for dolomite. Microcracks and thin recrystallisation bands are also rarely observed between coarse quartz grains (Figure 6.5D). Thin calcite-bearing veins perpendicular to the quartz-feldspar domain ASPO cut through both dolomite,

quartz and feldspar grains.

The hanging wall of this fault zone is composed of 90% quartz and hornblende in the approximate ratio 2:1. The remaining 10% is made up of biotite and patchy calcite veins with <1% epidote. Fine-grained equigranular quartz forms the mylonitic matrix. Biotite and hornblende occur as patches in the quartz matrix. Hornblende grains have an irregular shape while biotite grains exhibit mostly straight grain boundaries. The preferred orientation of these hornblende grains maps out a disconnected S-C fabric. The C-bands of this fabric are parallel to the weak GSPO in the quartz matrix which together form a continuous foliation. The sizes of quartz grains in the matrix range between 0.02-0.24 mm. The finer grains are anhedral to subhedral and have smooth-to-straight grain boundaries, while larger grains tend to have more irregular grain boundaries and show undulose extinction in places. Plagioclase feldspars with irregular grain boundaries also occur in the matrix. These are recognised by their classical tabular albite twinning, but also show tapered mechanical twins.
Calcite is present as highly anhedral grains with irregular grain boundaries that occur randomly throughout the matrix. Large grains of calcite are found in veins (Figure 6.5E). On a hand specimen scale the calcite veins appear as disaggregated patches as well as planar bodies sub-parallel and sub-perpendicular to the foliation. The mylonitic foliation that surrounds the veins is deflected and warped towards them. The vein calcite is subhedral but also has irregular grain boundaries. Twins are also occasionally observed in vein calcite; however, this is rare, and where it is observed, the twin density is low. Some twins are relatively thick, patchy and often composed of tiny grain trails (Figure 6.5E) resembleing the type IV twins of Burkhard (1993). Both thick and thin straight twins are found together in some grains, resembling the type II and type I twins of Burkhard (1993). Thick twins usually occur as one set of parallel twins, while thinner twins occur as two sets orientated at approximately 60° to each other. The latter are concentrated around the edges of the grains and do not transect them entirely.

6.2.3 TS12-TS13 Structure

This fault zone is a 1-2 m wide zone of extremely friable mylonitised mica-metapsammitic schist. A fault surface, recognisable by a slight discordance of foliation, separates retrogressed talc-tremolite-quartz schist footwall from micaceous metapsammitic hanging wall rock (Chapter 5).

The footwall rock sample GB29 is a tremolite-quartz mylonite with 3:2 proportion of tremolite to quartz. The sample shows a rough banding into quartz-rich and tremolite-rich domains. The alignment of tremolite and ASPO of quartz ribbons, that are parallel to one another, defines the mylonitic foliation. In the quartz-rich domains, quartz grain sizes vary between 0.08 and 0.26 mm, and the majority of the grains lie towards the upper end of this range. Quartz grain boundaries are generally slightly lobate, but a number of grains also

show straight grain boundaries. There is a weak quartz GSPO parallel to the mylonitic foliation. Undulose extinction is fairly common while subgrains are also present in a few of the larger grains.

Tremolite grains are also present in these quartz-rich domains. The tremolite grains are elongate, highly fragmented, and lie between quartz ribbons showing very little evidence for intracrystalline deformation, although a weak undulose extinction is observed in places. Some tremolite grains with long axes perpendicular to the plane of the section occur as porphyroclasts in the quartz-tremolite matrix. These porphyroclasts have slightly irregular grain boundaries, and tend to show more intracrystalline deformation through subgrains and undulose extinction. In the tremolite-rich domains, fine tremolite grains are all aligned with long axes (approximately 1 mm) parallel to the mylonitic foliation. Coarser grains with long axes of approximately 4 mm are also present, and these show undulose extinction.

Calcite-filled veins cut through the mylonitic foliation and define a spaced cleavage. Around the margin of these veins the wall rock is highly disrupted and brecciated, with fine truncated fragments of tremolite suspended in a carbonate matrix. Domino structures are also preserved in coarser-grained tremolite (Figure 6.6B). Closer to the centre of the fault zone retrograde alteration is more apparent, and the high temperature mylonitic fabric is preserved only locally in thin section (Figure 6.6C). This is characterised by highly irregular coarse tremolite and quartz grains with a strong unduluse extinction and extensive development of subgrains. This fabric is overprinted by fine-grained tremolite which forms in fan-shaped clusters at random orientations through the sample and is intergrown with talc and calcite (Figure 5.10F). This stage of tremolite growth is also associated with pressure solution seams that cut the sample parallel to the mylonitic foliation. Calcite grains in both samples typically show one set of thick (type II) twins.

The hangingwall of this fault zone is a mica-quartz mylonite composed of coarse-grained quartz ribbons set in a matrix dominated by fine-grained muscovite (40%), biotite (40%) and quartz (20%). The alignment of mica and the ASPO quartz ribbons forms a continuous mylonitic foliation (Figure 6.6F). In the ribbons, quartz grain sizes vary between 0.1 and 0.6 mm, and the grain size appears to be proportional to the size of the ribbon. In the thicker ribbons, quartz grains show strong undulose extinction and subgrains; however, in the finer grains, crystal plastic deformation is not common. The coarser grains are also typically elongate parallel to the ribbon ASPO and the overall rock fabric. Coarse-grained garnets, approximately 6 mm in diameter, are also found to overprint the mylonitic fabric in places and contain inclusion of mica and quartz. Inside the garnets, mica and quartz define a fabric parallel to that outside of the garnet. The mylonitic fabric is cut by pressure-solution seams that contain fragments of mica and quartz suspended in a reddish-brown iron-oxide residue (Figure 6.6E and F). These seams generally lie parallel to the mylonitic fabric but

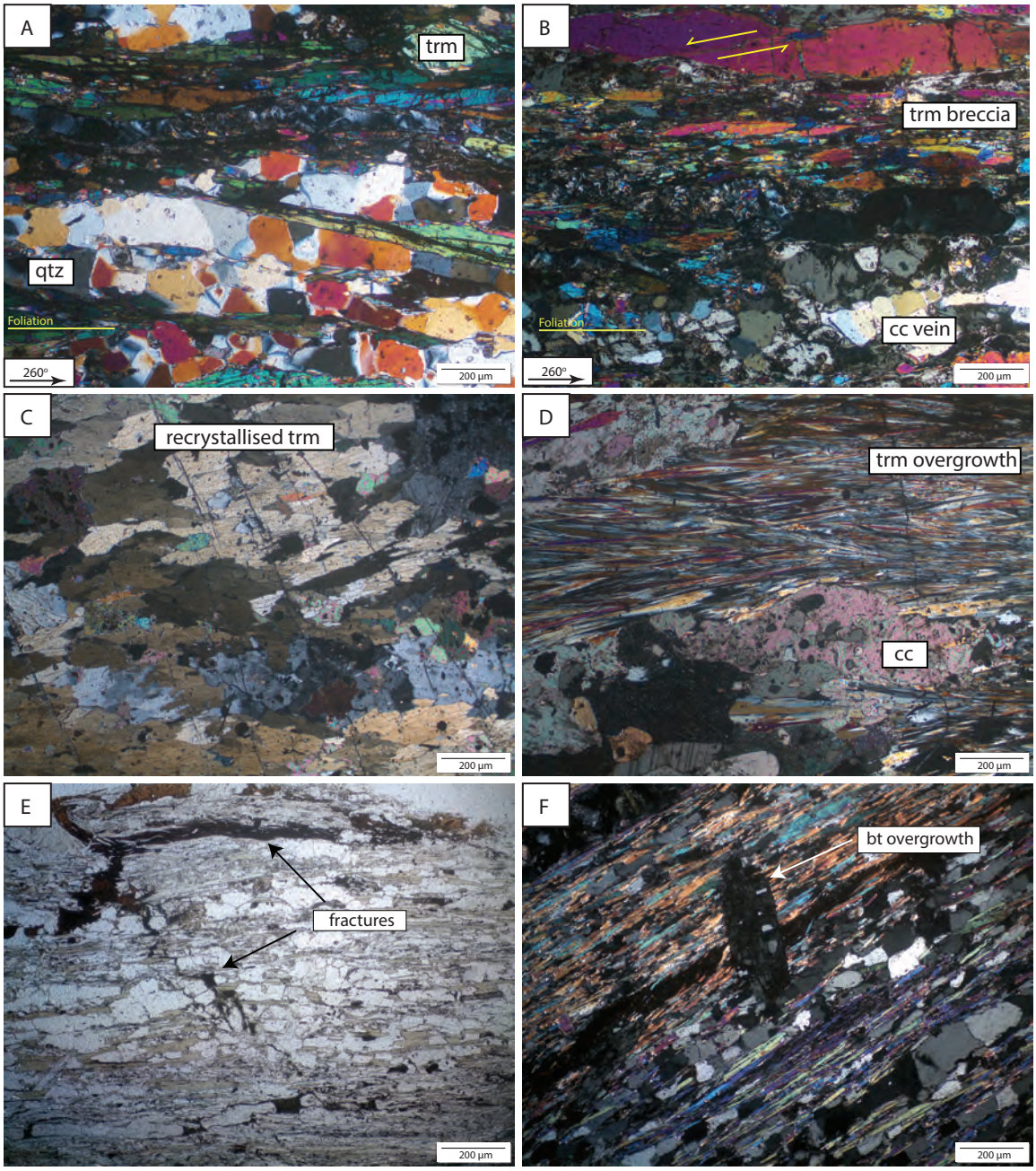

Figure 6.6: Photomicrographs from the fault rock of the TS13-TS14 structure. A) Footwall tremolite-quartz mylonite with quartz ribbons and elongate tremolite (GB29). Pressure solution seams cut mylonitic fabric and are associated with truncation and fracturing of tremolite grains. B) Highly disrupted fine-grained tremolite surrounding a thick calcite-quartz filled pressure solution seam with coarse tremolite showing domino structure. C) High temperature mylonitic fabric locally preserved in GB30 with tremolite and quartz both high temperature crystal plastic deformation. D) Mylonitic fabric in C) is largely overprinted/replaced by fine-grained retrograde tremolite, talc and calcite. E) and F) Fractured hangingwall mica-quartz mylonite. Fractures run largely parallel to the mylonitic foliation but locally transect it at high angles. Fractures are filled with reddish brown residue.

transect it at high angles in places (Figure 6.6E).

6.2.4 The Gomab River Line

Macroscopically, this rock still preserves a mylonitic fabric defined by the orientation of isoclinal recumbently folded quartz veins in a matrix of fine-grained calcite and dolomite. Quartz veins are also boudinaged through extension parallel to the foliation. This mylonitic texture is cut by brittle fractures and cataclastic shear bands that locally displace quartz veins by a few centimetres (Figure 6.7A).

The matrix is dominated by recrystallised calcite, and contains subordinate grains and lenticular ribbons/boudins of quartz (Figure 6.7A). The carbonate grain sizes range between 0.1-0.3 mm, although this may be an underestimate as grains have been extensively truncated by a pressure solution cleavage. There is also evidence that these seams have accommodated small amounts of slip as some grains have been offset relative to one another across the seams. Individual quartz grains in the matrix are all of similar size to the calcite grains. Fine grains of sheet silicate are also present in the matrix (Figure 6.7A). These are rare, and where present, appear to be pinning carbonate and quartz grains, and are aligned parallel to the mylonitic fabric. Quartz grains in the lenticular ribbons are coarser than the matrix calcite with an average size of 0.4 mm. These grains have much more irregular boundaries and, whereas substructures are present only in a few quartz grains, a strong undulose extinction is common. In some coarser quartz domains core-and-mantle structures give evidence for dynamic recrystallisation by grain boundary bulging (BLG). Calcite grains in the matrix are extensively twinned and typically contain closely-spaced sets of both thick (Type II) and thin (Type I) twins (cf. Burkhard, 1993), although the thicker type II twins appear more dominant. Both carbonate and quartz grains in the matrix have a moderate shape fabric that is parallel to the ASPO of quartz ribbons and the overall rock fabric (Figure 6.7A).

The fabric of the matrix is cross-cut by cataclastic bands of fine-to-ultrafine grained carbonates and quartz (Figure 6.7B,C and D). These are recognised by reduced grain sizes from the background matrix as well as a disruption of the shape fabric. For a single cataclastic band, the texture varies laterally and longitudinally. This is clear in Figure 6.7B, where proto-cataclasites and cataclasite/ultra-cataclasite are shown occurring together with a fairly continuous gradation from one to the other. Protocataclastite is recognised by the abundance of relatively coarse angular clasts in a fine matrix, while in cataclasite and ultra-cataclasite the clasts are finer, more rounded and the matrix dominates the texture (Sibson, 1977). The major cataclastic bands display a geometry of Riedel shears, with Y bands trending sub-parallel to the mylonitic fabric. However, thinner R' bands trend subperpendicular to the mylonitic foliation and locally displace the foliation sub-parallel cataclastic bands (Figures 6.7B and C). The orientation of the sub-parallel bands with respect to the foliation varies between 0° and 45°, and smaller bands branch off from larger ones in R and P shears. The

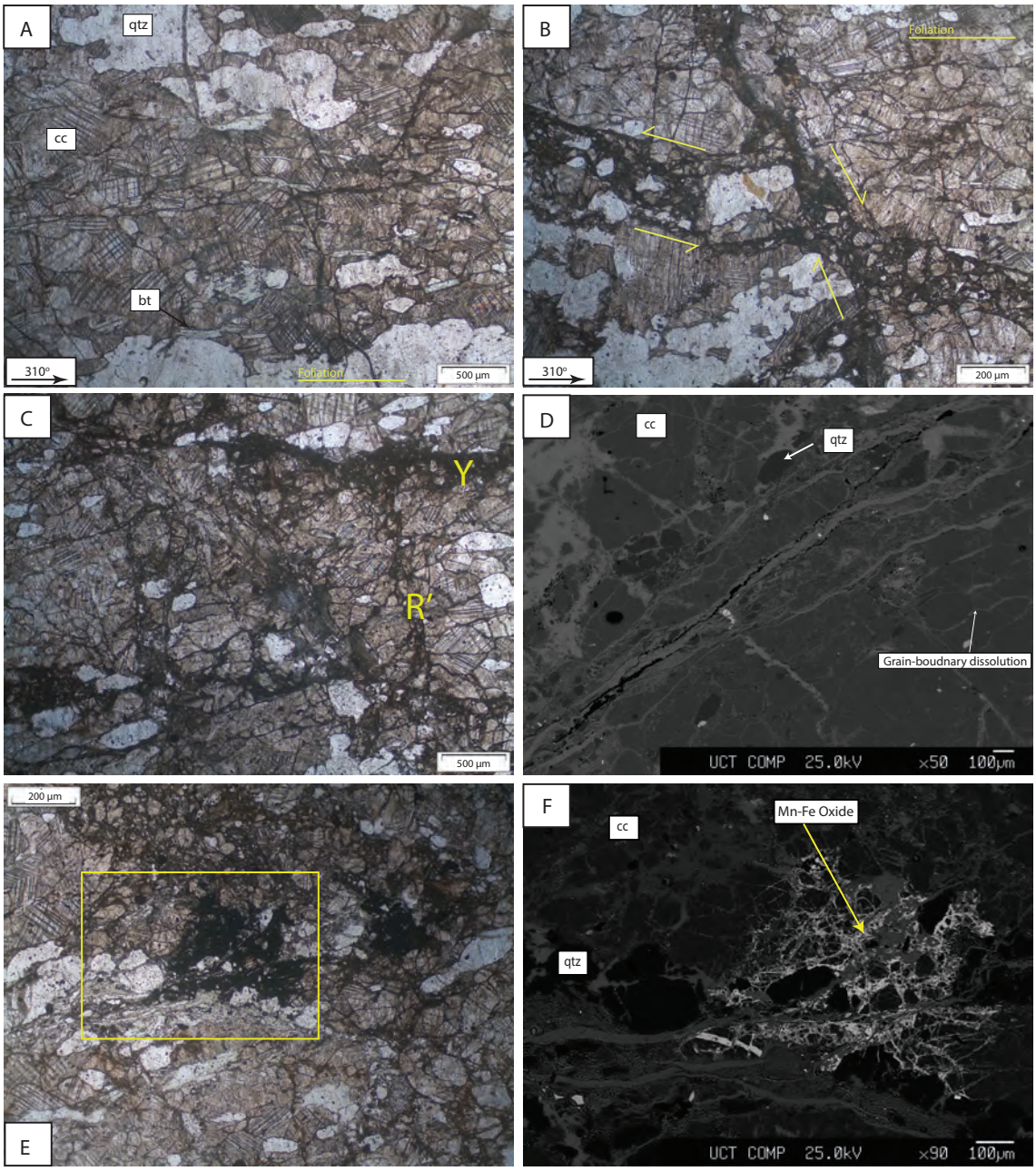

Figure 6.7: The GRL fault rock. A) Photomicrograph of carbonate matrix with shape fabric defined by dolomite, calcite and quartz. Matrix grains are truncated by pressure solution cleavage that is parallel to mylonitic shape fabric. B)Y/R shear band is displace by a later R' shear band. C) Blocks of matrix are isolated by foliation parallel (Y) and foliation perpendicular (R') cataclastic bands. D) Backscatter-electron image of cataclastic fracture surrounded by brecciated wall rock. E)Dark metal-oxide material containing fragments on host rock in cataclastic band. F) Close up on figure 6.7E. Dark material in the previous figure is a Mn-Fe oxide shown here to form the matrix containing broken fragments of quartz and calcite. Note how material is contained within small fractures in the surrounding rock and is distributed around a larger through-going fracture.

cataclastic bands therefore appear to anastomose through the rock. The overall texture is also highly variable on a thin section scale and, in some samples, the rock fabric is dominantly cataclastic and the older mylonitic fabric is preserved only in large multi-grain clasts suspended in the cataclastic matrix.

An opaque metal-oxide is also observed at a microscale in a number of samples from this fault zone and is recognised by the suspension of fine dolomite and quartz particles in the dark matrix. This is most abundant in the major cataclastic bands and is typically found in small fractures surrounding the larger shear surfaces (Figure 6.7F). Quantitative mineral chemistry analyses show this material to be an Fe-Mn oxide. Large calcite- and epidote-filled ataxial veins cut through cataclastic bands and wall rock material. The calcite crystals in these veins are elongate perpendicular to the vein margins and show no evidence for 'tracking' (Passchier & Trouw, 2005).

6.3 Summary of Micro-scale Observations

The observations presented in this Chapter highlight the two-stage deformation history described in Chapter 5. Quartzitic intra-unit shear zones preserve microstructures associated with high-temperature viscous flow. Whereas highly localised brittle deformation may be found in these structures as well, it does not appear to overprint the ductile fabrics and may have occured during high temperature viscous flow (Figure 6.2D and E). In the micaceous intra-unit shear zones there is evidence for brittle overprint in the form of micro-faults, although, this again is highly localised. These shear zones are often characterised by blastomylonitic textures with coarse-grained biotite overgrowths.

A few of the unit-bounding structures are characterised by intense brittle deformation. Viscous deformation micro-fabrics are often preserved in the hanging walls of these structures; however, the mylonitic fabrics in these rocks are often cross-cut by veins and fractures (Figure 6.6E). Dissolution structures are also common in many of these fault zones appearing alongside both viscous and frictional microstructures (Figures 6.5A and 6.6A and B). The most intense brittle deformation is observed in the carbonate fault zones, specifically the Gomab River Line. In this fault zone mylonitic textures are cross-cut by a Riedel shear-fracture system characterised by intense cataclasis of surrounding rock. Diffusive mass transfer structures are also abundant in this fault zone.

In conclusion, the unit-bounding fault structures preserve much lower temperature microstructures than those of the intra-unit shear zones, and therefore appear to have remained active during exhumation of the rocks of the SMZ. The conditions under which exhumation occurred are investigated and discussed in the following Chapter.

Chapter 7

Mineral Chemistry and Thermal History

Quantitative chemical analyses were performed on representative fault rock samples using a JEOL JXA-8100 Electron Microprobe (EMP) in the Department of Geological Sciences at the University of Cape Town. Analyses of silicate minerals were carried out on carbon-coated polished thin sections with an acceleration voltage of 15.0 kV, a beam current of 2 nA, and a beam width of 3 μm with a counting time of 10 s for all elements. Analyses of carbonate minerals were carried out with an acceleration voltage of 25.0 kV. The analyses of phyllosilicates and feldspars were calibrated using natural and synthetic internal standards.

7.1 Mineral Chemistry

The chemical composition of minerals can be a good indicator of the pressure and temperature conditions under which those minerals formed (Walshe, 1986; Kranidiotis & MacLean, 1987; Cathelineau, 1988; Zang & Fyfe, 1995; Frimmel, 1997; Potel *et al.*, 2006). Field observations (Chapter 5) and petrography on sampled fault rocks (Chapter 6) reveal that the rocks in the Gaub Canyon experienced at least a two-stage thermal and mechanical history. Earlier penetrative D_2 deformation occurred under increasing temperature and pressure conditions (Cross, 2013). Later localised D_3 deformation was concentrated on a few fault structures (Chapter 5). The cross-cutting relationship of microstructures from these faults suggests that these structures were active under conditions of decreasing temperature and pressure (Chapter 6). Samples from a few structures were therefore selected for mineral chemistry analysis in order to constrain further the temperature and pressure conditions of retrograde deformation (D_3). These samples were:

- Sample GB14 - a brittle fault gouge from the eastern region of the map area that separates two major litho-tectonic units (TS1-TS2 structure). This contains a prograde mylonitic fabric of recrystallised quartz with minor feldspar, epidote and magnetite which is cross-cut by seams containing fine-grained clay minerals, biotite and chlorite.

- Sample GB17 - a quartz mylonite from a shear zone within the quartzitic unit (TS5) composed of recrystallised quartz and biotite porphyroclasts along with feldspar, epidote and magnetite.
- Sample GB18 - a quartz-mica mylonite from a micaceous layer within the same shear zone as GB17, which contains an interconnected phyllosilicate network of muscovite and biotite.

These samples were chosen because, on a qualitative basis, they appear to have similar mineral assemblages, and therefore differences in mineral chemistry are more likely to reflect the physical conditions of formation. Minerals analysed were biotite, muscovite, plagioclase and chlorite. A table of all the mineral composition data is supplied in Appendix B, while summary tables and relevant geochemical plots are presented in the sections that follow.

7.1.1 Biotite

Three different types of biotite were analysed: (1) Gouge biotite in GB14 which occurs as individual grains in pressure solution seams; (2) biotite occurring as isolated porphyroclasts in a quartz mylonite (GB17) and; (3) biotite occurring with muscovite, forming an interconnected phyllosilicate network in a quartz-mica mylonite (GB18).

Gouge biotite tends to have slightly less Si per formula unit (pfu, based on 22 oxygens), with values in the range 5.63-5.72, while in the mylonitic rocks it ranges from 5.67 to 5.81 pfu (Figure 7.1a). Biotites from the quartz-mica mylonite have Al ranging from 2.62 to 2.72, while the gouge and quartz mylonite biotites have Al between 2.76 and 2.94 pfu. All three biotite types have similar K contents, lying between 1.50 and 1.80, while Ti concentrations appear to be slightly higher in the biotites from the gouge and quartz-mica mylonite (Table 7.1 and Figure 7.1C). Major differences occur in the Mg and Fe contents, as gouge biotites are more annitic having significantly higher X_{Fe} values with an average of 0.33; close to twice those of the biotites in mylonitic rocks with averages of 0.14 and 0.17 for GB17 and GB18 respectively (Table 7.1; Figure 7.1A and B).

Table 7.1: Average compositions of biotite and muscovites from samples GB14. GB17 and GB18. n = number of measurements, and sd = the standard deviation. Formula proportions are calculated on the basis of 22 oxygens and all Fe = Fe^{2+}.

	Biotite						Muscovite	
Sample	GB14		GB17		GB18		GB18	
	n=11	sd	n=11	sd	n=7	sd	n=11	sd
SiO_2	37.86	0.67	40.2	0.31	39.66	0.27	47.49	0.64
Al_2O_3	15.87	0.31	17.01	0.30	15.50	0.25	26.68	0.69
TiO_2	1.29	0.06	0.81	0.05	1.40	0.12	1.31	0.08
K_2O	8.41	0.58	9.49	0.23	9.33	0.52	10.2	0.16
Na_2O	0.11	0.05	0.15	0.03	0.11	0.08	0.15	0.04
MnO	0.13	0.02	0.14	0.04	0.24	0.03	0.05	0.02
CaO	0.09	0.06	0.01	0.02	0.33	0.56	0.01	0.01
MgO	15.67	0.45	20.8	0.31	20.21	0.52	2.96	0.27
Cr_2O_3	0.07	0.03	0.01	0.02	0.01	0.01	0.01	0.02
FeO	13.95	0.42	5.91	0.08	7.47	0.29	5.60	0.36
Total	93.45	1.48	94.53	0.31	94.25	0.93	94.46	0.56
	Formula Proportions							
Si	5.68	0.04	5.74	0.04	5.75	0.05	6.53	0.08
$Al^{(IV)}$	2.32	0.04	2.26	0.04	2.25	0.05	1.47	0.08
$Al^{(VI)}$	0.49	0.04	0.61	0.03	0.39	0.04	2.86	0.03
Ti	0.15	0.01	0.09	0	0.15	0.01	0.14	0.01
K	1.61	0.1	1.73	0.05	1.72	0.09	1.79	0.03
Na	0.03	0.01	0.04	0.01	0.03	0.02	0.04	0.01
Mn	0.02	0	0.02	<0.01	0.03	<0.01	0.01	<0.01
Ca	0.02	0.01	0.00	<0.01	0.05	0.09	0.00	<0.01
Mg	3.51	0.09	4.43	0.06	4.37	0.11	0.61	0.05
Cr	0.01	<0.01	0.00	<0.01	0.00	<0.01	0.00	<0.01
Fe	1.75	0.05	0.71	0.01	0.91	0.04	0.64	0.04
X_{Fe}	0.33	0.01	0.14	<0.01	0.17	0.01	0.52	0.04
X_{mu}	-	-	-	-	-	-	0.98	0.01

7.1.2 Muscovite

Muscovites from the quartz-mica mylonite have an average stoichiometric composition of $(K_{1.79}Na_{0.04})(Al_{2.86}Mg_{0.61}Fe_{0.64}\ Ti_{0.14})(Si_{6.53}Al_{1.47}O_{20})(OH)_4$ and are therefore close to the ideal muscovite compositions with minor substitutions of $Al^{(VI)}$ for Mg, Fe^{2+} and Ti. Mn is not considered because it is present in concentrations close to or below the detection limit of the microprobe. This ideal composition is also reflected in the mean X_{mu} = K/(K+Na) = 0.98, close to unity (Table 7.1).

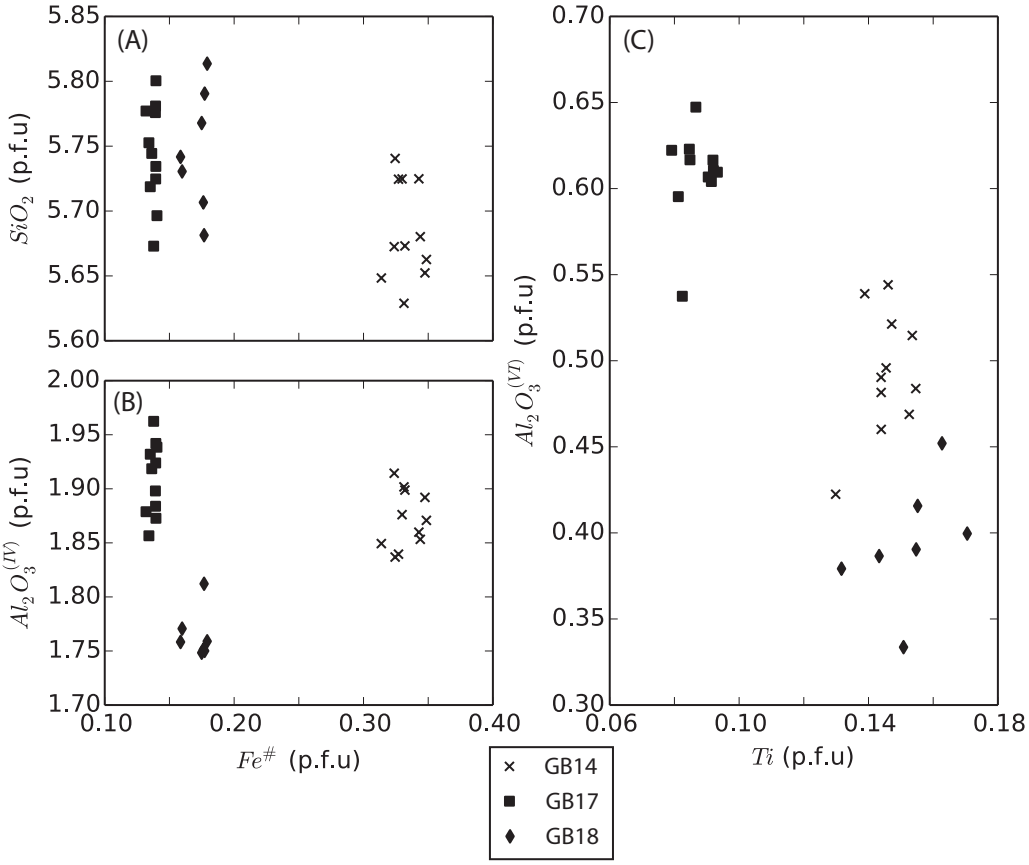

Figure 7.1: Chemical variation in biotites from GB14, GB17 and GB18. (A) SiO_2 vs X_{Fe}. (B) Al $^{(IV)}$ vs X_{Fe}. (C) Al $^{(VI)}$ vs TiO_2. Note the difference in biotite composition between retrograde unit-bounding faults (GB14) and prograde-to-peak internal shear zones (GB17 and GB18) in plots (A) and (B).

7.1.3 Feldspar

Feldspar compositions from both the gouge and quartz mylonite are dominantly albitic with >90% Na when normalised to total alkali elements (Na+Ca+K). Ti, Mn, Mg and K are not present in significant proportions, although trace amounts may be present (Figure 7.2) due to small inclusions of epidote or sericite. A number of the feldspars analysed in the fault gouge plot with orthoclase components in the range Or_{10-30}. This may reflect a slight alteration of earlier metamorphic albite.

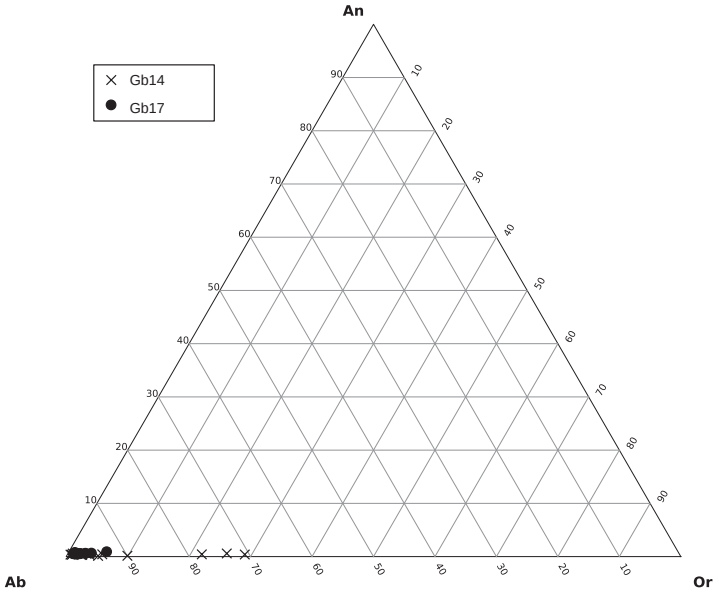

Figure 7.2: Triangular plot of K, Na and Ca in feldspars showing the dominantly albitic composition of plagioclase in samples GB14 and GB17.

7.1.4 Chlorite

Chlorites from the fault gouge GB14 have Fe^{2+} values ranging from 2.53 to 3.07 (pfu) calculated on an anhydrous basis with 28 oxygens. X_{Fe} ranges between 0.24 and 0.33. Total Si contents average 5.51 pfu, and total Al has a mean value of 5.06 pfu (Table 7.2). The majority of chlorites fulfil the requirements for non-contamination, with Σ Ca+Na+K <0.2, with the exception of one (see Appendix B; Table B.1 Gb14f) which is not included in the data analysis. The low average total interlayer charge (t.i.c < 0.2) also indicates that smectite or illite impurities are insignificant (Table 7.2).

The Si-Fe-Mg plot (Figure 7.3A) shows that chlorite compositions lie close to the Fe-Mg solid solution tie line between chamosite and clinochlore with X_{Fe} in the range 0.24 to 0.33. The compositions of fabric-forming chlorites from Cross (2013) are also plotted here for comparison. These are tightly clustered with X_{Fe} in the range 0.42 to 0.48 and are, on average, more aluminous with approximately 3 wt% more Al_2O_3 than gouge chlorites (Table 7.2). They are therefore chemically separate from the chlorites of the fault gouge (Figure 7.3A). This is also seen in Figure 7.3B as chlorites plot close to the clinochlore end-member with total non-interlayer cations ≈20, consistent with a tri-octahedral crystal structure. Chlorites from Cross (2013) also plot close to clinochlore although they are again tightly clustered at slightly higher Al values. The difference in X_{Fe} and Al contents between fabric-forming chlorites and the gouge chlorites analysed in this study may be due to differences in bulk rock composition, as the chlorites from Cross (2013) occur in aluminous metapelitic rocks (Units TS11

and TS14; Chapter 5).

Table 7.2: Average chemical compositions of chlorites from sample GB14 and Cross (2013). Formula proportions are calculated on an anhydrous basis using 28 oxygens and all Fe is taken as Fe^{2+}. Average temperatures from the empirical thermometer of Cathelineau (1988) are also presented.

Chlorite				
Sample	GB14		Cross (2013)	
	n = 12	sd	n = 84	sd
Al_2O_3	21.40	0.78	24.45	0.36
SiO_2	27.52	0.90	25.60	0.31
TiO_2	0.09	0.04	0.08	0.02
K_2O	0.03	0.04	0.03	0.03
MgO	21.72	0.68	17.36	0.69
Cr_2O_3	0.03	0.04	0.02	0.02
CaO	0.05	0.05	0.02	0.01
Na_2O	0.02	0.02	0.05	0.05
MnO	0.23	0.03	0.06	0.03
FeO	16.74	1.49	24.35	1.24
Total	87.83	0.79	92.03	0.82
Formula Proportions				
Si	5.51	0.16	5.09	0.05
$Al^{(IV)}$	2.49	0.16	2.91	0.05
$Al^{(VI)}$	2.57	0.07	2.81	0.06
Ti	0.01	0.01	0.01	0.00
K	0.01	0.01	0.01	0.01
Mg	6.49	0.19	5.14	0.20
Cr	0.00	0.01	0.00	0.00
Ca	0.01	0.01	0.01	0.00
Na	0.01	0.01	0.02	0.02
Mn	0.04	0.01	0.01	0.00
Fe^{2+}	2.81	0.25	4.05	0.20
t.i.c	0.04	0.04	0.04	0.03
$X_{Fe^{2+}}$	0.3	0.02	0.44	0.02
T(°C)	304	19	407	8

Figure 7.3C, however, clearly shows that the two groups of chlorites have different chemical substitution trends. Fabric-forming chlorites are tightly clustered on the line representing the direction of Tschermak (TM) substitution, with a small amount of di-octahedral (AM) substitution towards higher $Al^{(IV)}$ values. Gouge chlorites have a greater spread and show that di-octahedral substitution is also important (Figure 7.3C) occurring in the opposite direction, towards lower $Al^{(IV)}$ values. The chlorites in the fault gouge are therefore not likely

to be related to prograde metamorphic chlorite, and represent a later stage of chlorite growth that occurred under conditions of decreasing temperature and pressure. This is consistent with the petrographic observations, as these chlorites are extremely fine-grained and occur solely in seams that cut through earlier mylonitic fabrics (Chapter 6).

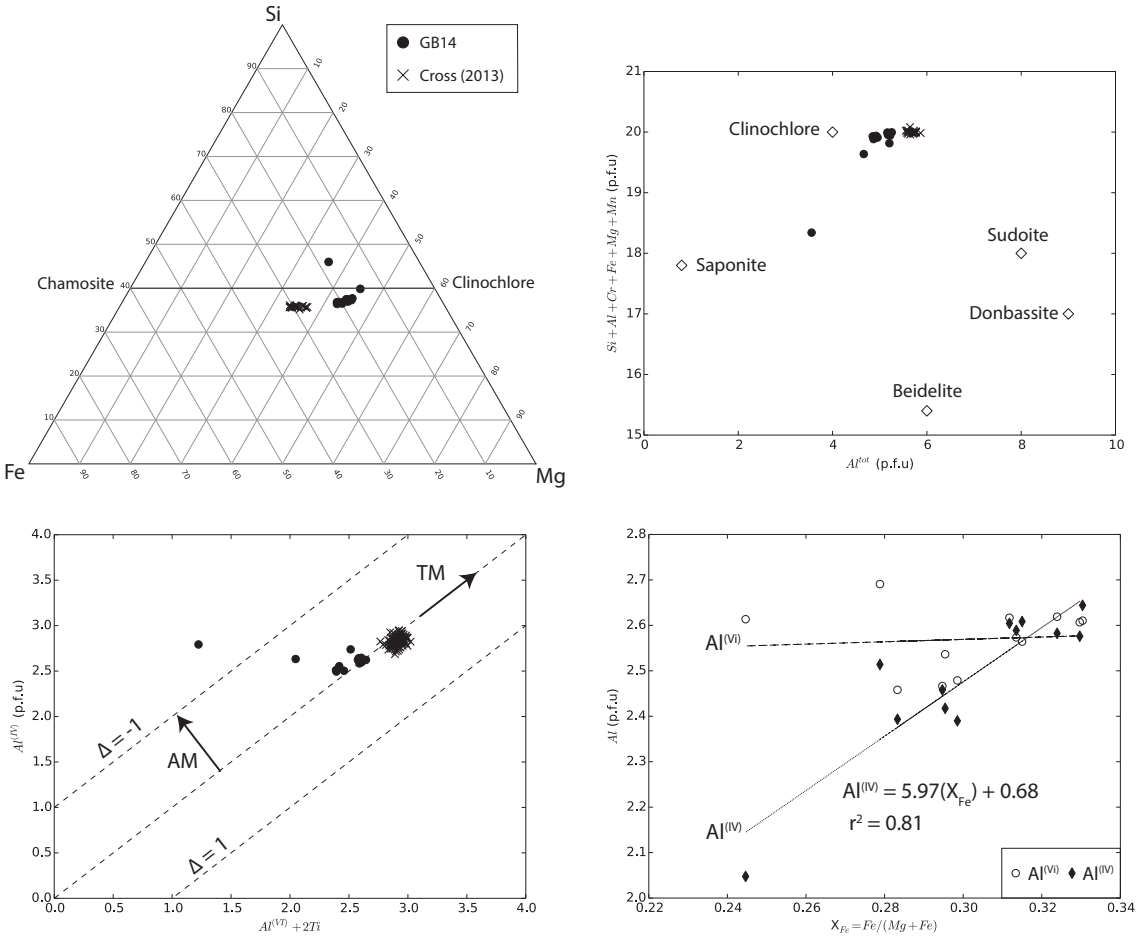

Figure 7.3: Chemical variations in chlorite from GB14. A) Si-Fe-Mg plot for chlorites from the fault gouge (GB14) along with fabric-forming chlorite from Cross (2013). Note that chlorites plot close to the straight line joining end-members clinochlore and chamosite, and that retrograde gouge chlorites are chemically distinct from the prograde fabric-forming chlorites. B) Total non-interlayer cations vs total Al (after Bailey, 1988). C) $Al^{(VI)}$ + 2Ti vs $Al^{(IV)}$ with arrows showing the direction of Tschermak (TM) and di-trioctahedral (AM) substitution (after Potel *et al.*, 2006). D) Plots showing a positive correlation between $Al^{(IV)}$ and X_{Fe}. $Al^{(VI)}$ is poorly correlated to X_{Fe} (after Kranidiotis & MacLean, 1987).

7.2 Chlorite Thermometry

The chemical variation observed in a chlorite is a result of three main substitution reactions (1) Tschermak exchange $Al^{(VI)}Al^{(IV)} \leftrightarrow Si(Mg,Fe^{2+})$; (2) $Fe^{2+} \leftrightarrow Mg$; and (3) di-trioctahedral exhange $3(Mg,Fe^{2+}) \leftrightarrow \square + 2Al^{(VI)}$, where $\square$ represents the octahedral vacancies. The degree to which these reactions occur is dependent on the physical and chemical conditions during crystallisation; chemical variation in chlorite is therefore related to factors such as pressure, temperature, bulk rock composition, as well as oxygen and sulphur fugacities and the pH of coexisting fluids (Walshe, 1986; Cathelineau, 1988; de Caritat & Walshe, 1993; Zang & Fyfe, 1995; Xie *et al.*, 1997; Frimmel, 1997; Bourdelle *et al.*, 2013), although the latter of these may only be important in hydrothermal systems and largely affects Fe-Mg exchange (Zang & Fyfe, 1995).

A number of empirical chlorite geothermometers relate $Al^{(IV)}$ contents directly to temperature conditions during crystallisation (c.f. Kranidiotis & MacLean (1987); Cathelineau (1988); Zang & Fyfe (1995)). The linear correlation (Equation 7.1) proposed by Cathelineau (1988) was calibrated using *in situ* temperature measurements and fluid inclusion data with chlorites from a variety of hydrothermally altered volcanic and sedimentary rocks, and is stated as being applicable to diagenetic, hydrothermal and metamorphic chlorites, as $Al^{(IV)}$ was virtually independent of rock type:

$$T(^{\circ}C) = -61.92 + 321.98(Al^{(IV)}). \tag{7.1}$$

Kranidiotis & MacLean (1987) point out that bulk rock composition effects are seen through the variation in $Al^{(IV)}$ with X_{Fe}, as increased Fe contents alter the chlorite crystal structure and enable incorporation of more $Al^{(IV)}$. The recalibration of Zang & Fyfe (1995) accounts for this by correcting for the relationship between $Al^{(IV)}$ and X_{Fe} (Figure 7.3D). This is done using a corrected $Al^{(IV)}$ value:

$$Al_c^{(IV)} = Al^{(IV)} - m(X_{Fe} - 0.34), \tag{7.2}$$

where m is the slope of the regression line in the plot of $Al^{(IV)}$ vs X_{Fe} (Figure 7.3D). This corrected value is then used in the geothermometer (Kranidiotis & MacLean, 1987):

$$T(^{\circ}C) = 106.2(Al_c^{(IV)}) + 17.5. \tag{7.3}$$

Frimmel (1997) states that these empirical calibrations should be applied only for uncontaminated tri-octahedral chlorites with Σ Na+K+Ca <0.2, and that temperatures calculated on sudoitic (di-trioctahedral chlorite) are generally underestimates. The chlorites in this study fulfil these requirements.

The calculated temperature data for gouge chlorites are summarised in Figure 7.4. Temperatures calculated using the thermometers of Kranidioitis and MacClean (1987) and Zang and Fyfe (1995) are in very good agreement, with a majority of the temperatures lying in the ranges 293-323°C and 295-312°C respectively. The Cathelineau (1988) calibration consistently gives higher temperatures, generally ranging from 323-368°C. Given the uncertainty of ±25°C (Zang & Fyfe, 1995) and the relatively close agreement of all calibrations, it is difficult to assess which of the thermometers is more accurate. Temperature data obtained using chlorites from Cross (2013) are also plotted (Figure 7.4). These temperatures are consistently ∼50°C higher than the GB14 chlorites with no overlap. The chlorites analysed in this study are therefore not believed to be genetically related to the prograde fabric-forming chlorites from Cross (2013), but grew later under retrograde conditions.

The chlorite chemistry in this study is similar to the chemistry of chlorites from which the Cathelineau (1988) thermometer was calibrated, and, given that the petrographic evidence suggests that they formed during cooling from high termperatures, the higher temperatures obtained from this thermometer are favoured. However, the fine-grained nature of the chlorites that occur solely in retrograde solution seams (Chapter 6) suggests that these crystals may have precipitated out of a hydrothermal fluid. The temperatures given here may thus reflect the temperature of the hydrothermal fluid, which is likely to be higher than the ambient rock temperature if the fluids are derived from depth. These temperatures are therefore likely to be overestimates and do not necessarily reflect the temperature conditions for the ceasation of exhumation of the fault zone.

7.3 Summary

The lack of pressure constraints for crystallisation of retrograde minerals means it is not possible to determine accurately the P-T path followed during retrograde deformation. The temperatures obtained from chlorite thermometry give a range in P-T space and only allow for construction of a P-T path if exhumation is assumed to occur along a stable geothermal gradient. However, the alteration of feldspars, and the differences in biotite and chlorite chemistry from those of known prograde minerals, are limited solely to the unit-bounding thrust structures. This is consistent with field and petrographic observations of highly localised retrograde, exhumation-related D_3 deformation in the SMZ.

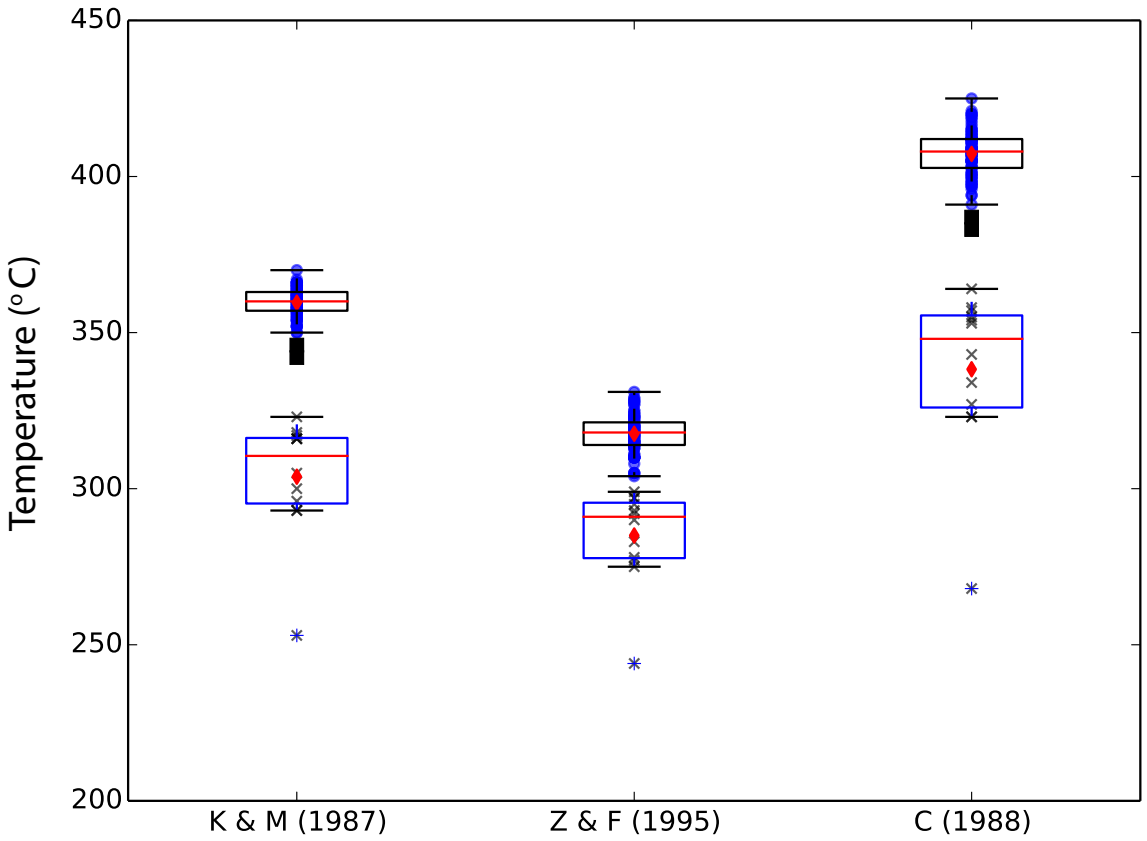

Figure 7.4: Summary of chlorite temperature data from this study (blue boxes) and Cross (2013, black boxes) for various empirical chlorite geothermometers. Black crosses and blue dots are individual measurements, the red diamonds are the mean temperatures, and the red line marks the position of the median. Black squares are statistical outliers. K&M = Kranidiotis & MacLean (1987), Z&F = Zang & Fyfe (1995) and C = Cathelineau (1988).

Chapter 8

Discussion

The structures described in Chapter 5 are believed to be the result of progressive deformation that initiated under low-grade metamorphic conditions (D_1). This evolved through prograde to peak amphibolite facies metamorphism (D_2) and ended in relatively low-temperature retrograde conditions (D_3). Each of the identified phases is characterised by a structural foliation, S_1, S_2 and S_3, respectively. D_1 is associated with layer-parallel extension and is characterised by a disrupted lithological layering and bedding-parallel foliation S_{0+1}. D_2 is defined as deformation related to the formation of the axial-planar S_2 foliation as a result of folding of the previously formed S_{0+1} fabric. Widespread isoclinal recumbent folding resulted in transposition of these fabrics, and the general foliation is thus termed S_{0+1+2}. Folding was contemporaneous with top-to-SE directed thrusting in D_2 faults and shear zones that are seen to cut D_1 fabric in places. D_3 is defined by a crenulation cleavage S_3, which forms at near right angles to S_{0+1+2} foliation. This phase of deformation may also, but not necessarily, be associated with retrograde, brittle reverse-faulting that occurs along a few of the unit-bounding D_2 shear zones. The presence of a sub-horizontal stretching lineation (L_3) is attributed to a strike-slip component during D_3 deformation.

8.1 Strain History: Kinematic Analysis

8.1.1 Episode D_1

Sub-horizontal layer parallel extension during D_1 resulted in the formation of boudinaged layers that lie parallel to S_1 (Figure 5.3D and 5.10A). In an accretionary environment this can occur in two settings: (1) gravity-driven olistostromes (sedimentary mélanges) on the wedge slope; or (2) vertical loading and layer-parallel shear of sediment below the décollement (Figure 3.2; Byrne & Fisher, 1990; Kusky & Bradley, 1999; Ujiie, 2002), where vertical loading occurs due to the weight of the overriding prism. The sediments in this study area are interpreted to be a mixture of hemipelagic and pelagic sediment with metamafic slivers and trench turbidites. These rock types are not typically found together in wedge-slope deposits (Ujiie, 2002), and are more characteristic of the incoming lower plate material (Underwood, 2007). Secondly, sub-vertical quartz veins developed in boudin necks show that, at least locally, pore pressures (P_f) exceeded the magnitude of sub-horizontally orientated local minimum compressive stress (σ_3) and the tensile strength of the rock ($T \geq 0$; rocks were consolidated). Therefore these early D_1 structures are interpreted to have formed below the décollement, as a result of flattening due to vertical loading during underthrusting (Chapter 3, Raimbourg *et al.*, 2009).

Anastomosing phacoidal cleavages and S-C type scaly fabrics (with C surfaces parallel to S_1) also developed locally during the late stages of D_1, and are preserved mesoscopically in the quartzitic unit (TS5) and microscopically in semi-pelitic and metamafic rocks (Figure 5.3D). The geometry of these fabrics indicates a general top-to-SE sense of shear. Similar fabrics have been reported to develop sporadically in other accretionary complexes in Alaska, Japan and New Zealand (c.f. Kusky & Bradley, 1999; Ujiie, 2002; Fagereng, 2011a), and are believed to be a result of localised layer-parallel shear, including volume loss if S_1 foliation forms part of the S-C structure (Fagereng, 2011a). Kusky & Bradley (1999) and Ujiie (2002) suggest that these structures indicate a change from layer-parallel extension to heterogeneous bulk shear, as underthrust sediment is progressively buried along the décollement. The D_1 deformation structures preserved in the SMZ therefore resemble structures associated with underthrusting in modern and ancient accretionary prisms. Specifically, they represent early homogeneous layer parallel extension followed by heterogeneous shear and volume loss. However, they may also have formed simultaneously at different stratigraphic levels in the underthrust sequence and therefore reflect proximity to the décollement (Ujiie, 2002). Their subsequent juxtaposition may thus be a result of D_2 deformation.

8.1.2 Episode D_2

On a map scale, D_2 is characterised by the abundance of top-to-SE reverse shear zones and thrust faults that locally cross-cut D_1 fabrics and reflect the overall dominance of localised strain during this phase of deformation. This cross-cutting relationship is best observed in

unit TS5, where thrust faults clearly transect the anastomosing D_1 fabric of the quartzite at acute angles that point up-dip and reveal the SE-directed shear sense (Figure 5.11A). The metamafic slivers exposed along these thrusts are composed of peak-metamorphic hornblende which defines the down-dip stretching lineation (L_2). These structures therefore most likely formed along the prograde path during D_2 as they do not show any evidence for retrogression. In other places, particularly in metapsammitic and metapelitic units, reverse ductile shear zones lie parallel to S_{0+1} and are identified by a significant increase in foliation intensity (Figure 5.9D); and locally by the presence of metamafic material (Figure 5.10B). The cross-cutting relationship between the D_1 fabric D_2 faults preserved in the quartzitic unit (TS5) indicates that the D_2 shear zones and faults probably initiated at steep angles to the S_{0+1}. In relatively incompetent rock types, progressive deformation has resulted in rotation of the D_1 fabric through time, also illustrated by the general upward steeping of the penetrative fabric in the tectonic stratigraphy on unit and map scales.

Cross-sections drawn perpendicular to the general strike of the penetrative fabric (Figure 5.2) also highlight the in-sequence imbricate geometry of these D_2 structures. Imbricate thrust geometry may represent emergent imbricate fans where faults terminate as blind thrusts, or, if the thrusts converge, duplex structures (Boyer & Elliott, 1982; Butler, 1987). A mesoscale imbricate stack of ductile shear zones in unit TS11 exhibits a somewhat sigmoidal shape (Figure 5.9C) indicating that they may converge, although the low-angle roof and floor thrusts are not observed owing to limited outcrop exposure. Duplexing has, however, been observed in a number of exhumed accretionary complexes (Sample & Fisher, 1986; Kimura & Mukai, 1991). It has also been inferred from seismic reflection data (Shipley *et al.*, 1992) to occur at depths correlated with a step down of the décollement towards (or into) the oceanic crust, and the onset of seismogenesis beneath the transition from outer- to inner-wedge segments (Kimura *et al.*, 2007).

Asymmetric SE-verging isoclinal recumbent folds are ubiquitously developed in metapelitic and metapsammitic rock types during D_2 deformation. Fold axial planes are parallel to S_{0+1} and hinge lines are sub-parallel to L_2, the down-dip stretching lineation. L_2 is also parallel to lineations measured on fault surfaces and shear zone foliation (Figures 5.7A and B, and Figure **??**F). Bedding-parallel quartz veins in unit TS8 are isoclinally and recumbently folded, and also appear to be dismembered through extension parallel to fold limbs (Figure 5.7B and D). S_{0+1+2} is warped towards boudin necks, indicating that extension of these veins occurred simultaneously with fabric reorientation and isoclinal recumbent folding of S_{0+1+2} and the foliation-parallel veins. This is interpreted to reflect the rotation of fold limbs into the extensional field of the finite strain ellipsoid through progressive non-coaxial shear, where SE fold vergence indicates top-to-SE shear sense. It is therefore suggested that asymmetrical folding was contemporaneous with SE-directed thrusting. In ideal simple shear, fold hinge lines will form perpendicular to the flow direction (indicated by L_2). F_2 is, however, parallel

to L_2 throughout the SMZ (Figure 5.4F, Figure 5.7C and Figure 5.8). This indicates that non-coaxial flow during this phase of deformation deviated from ideal simple shear, with a component of shear within the XY plane of the strain ellipse, resulting in rotation of fold hinges into parallelism with L_2 (e.g. Alsop & Holdsworth, 2004).

Peak-metamorphic biotite and staurolite locally define L_2 (Figure 5.3J), indicating that D_2 deformation occurred up until at least peak metamorphism. Staurolite is also, however, found locally to show no preferred orientation (Figure 5.3H), interpreted by Cross (2013) as an indication that peak metamorphism occurred in the absence of deformation. Biotite is also locally found to define a shallow sub-horizontal lineation (Figures 5.6A & 6.4D). That two mutually perpendicular lineations, which reflect different tectonic transport directions, are found on the same foliation surface, poses a kinematic conundrum. This apparent contradiction may be resolved by ductile strain localisation and kinematic partitioning of ductile flow resulting from transpressional shear of heterogeneous material (Goodwin & Tikoff, 2002; Druguet *et al.*, 2009) during prograde-to-peak metamorphism, thus indicating oblique convergence of the Kalahari and Congo Cratons. This will be discussed further in Section 8.3. This sub-horizontal lineation may also be related to a later deformation event (D_3).

The geometric and kinematic evidence from D_2 structures generally agrees with the duplex accretion or underplating model proposed by Sample & Fisher (1986), in which repetitive downward propagation of the décollement into flat-lying sediment on the subducting slab isolates thrust slices, coupling them to the prism. Subsequent bulk non-coaxial shear related to continued movement on the underlying décollement and fault ramps then results in the formation of asymmetric folds and steepening of thrust slices upon incorporation into the wedge (Figure 8.1). Similar geometries may also develop simply through imbrication of the underthrust sediment pile, as proposed by Meneghini *et al.* (2009) as a mechanism of mélange formation in poorly-sedimented accretionary margins.

The question therefore remains whether this tectonic imbrication is a result of duplex accretion and incorporation into the overriding wedge, or simply tectonic imbrication of the underthrust sediment pile. This also raises the question whether tectonic imbrication occurred at shallow structural levels or at depth, in the ductile regime; the implication being that, in the former case, earlier-formed brittle fractures will be overprinted by pervasive ductile deformation (Mancktelow & Pennacchioni, 2005). There is no apparent repetition of the typical ocean plate stratigraphy in the SMZ, as is observed for underplated units in the Franciscan Complex (Kimura *et al.*, 1996). It is, however, likely that in such a high strain environment, lithological coherence would be destroyed during progressive shearing. Slivers of metamafic rock are found along large brittle thrust faults observed in the quartzitic unit (TS5; Figure 5.11A) as well as many of the intra-unit ductile shear zones in more metapelitic units of the SMZ (Figure 5.10B). Brittle faults cross-cut disjunctive fabrics in the quartzites

and they are generally parallel to the ductile shear zones of the metapelites (Figure 5.2), indicating that they were formed by a similar, if not the same, mechanism. Duplex accretion decouples thrust slices of underthrust sediment from the subducting sediment pile (Sample & Fisher, 1986). Underplated units are therefore unlikely to undergo significant further burial upon incorporation into the overriding wedge (upper plate).

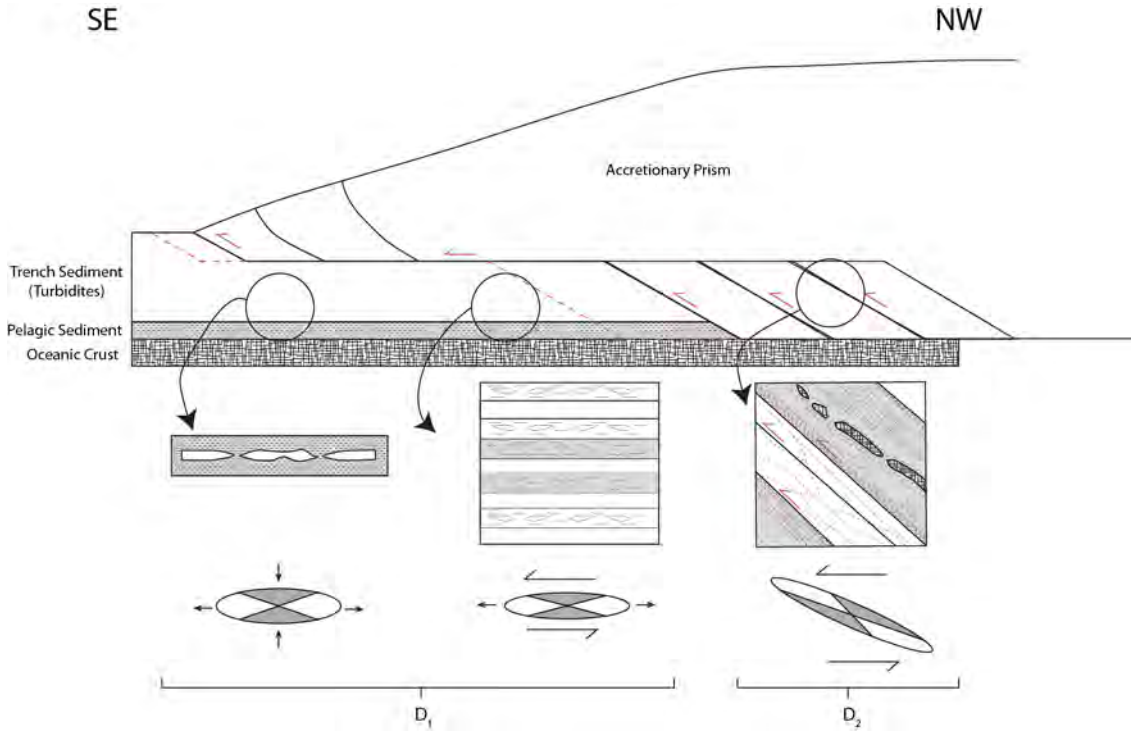

Figure 8.1: Schematic cross-section of an accretionary prism (not to scale), modified after Ujiie (2002), showing the progression of décollement-related deformation from underthrusting (D_1) to underplating (D_2) along with the orientations of the finite strain ellipses. This kinematic framework shows the progression from pure-shear-dominated to simple-shear-dominated deformation.

If the observed imbrication of the lithotectonic units of the SMZ occurred via imbrication of the underthrust sediment pile, and not duplex accretion, then the imbricate thrust stack remains confined within the subduction shear zone. In such a scenario, imbrication can occur at relatively shallow levels via brittle fracture, whereafter continued movement on the roof thrust (not observed) leads to further burial beneath the prism. This implies that, during burial and subsequent heating, the ductile shear zones were localised on these precursor brittle structures (Mancktelow & Pennacchioni, 2005). For this to occur, however, slip would have to be preferentially partitioned into the roof thrust, such that the imbricate stack could be buried as a coherent entity. Alternatively, duplex accretion at depth may also explain these observations. However, this argument is not favoured as it is unclear how in-sequence brittle faults would form at depths where pervasive ductile deformation is expected to dominate. A

reason why the brittle nature of these faults is still preserved within the quartzitic units is dealt with in Section 8.3.

8.1.3 Episode D_3

D_3 is characterised by a NE-SW striking S_3 crenulation cleavage approximately perpendicular to S_{0+1+2}, formed as a result of shortening sub-parallel to S_{0+1+2}. Ujiie (2002) proposes that similar structural relationships in the Mugi Mélange, on the exhumed portion of the Nankai prism, reflects deformation in the inner wedge, as maximum compressive stress is generally thought to be sub-horizontal within accretionary prisms. On the other hand, the Damara Belt is interpreted as an exhumed remnant of a Neoproterozoic collisional belt (Kasch, 1983a; Gray *et al.*, 2007). Slices of semipelitic and metamafic material intercalated with slices of sheared basement granite are found around the margin of the Rostock Inlier, just outside the eastern region map area, and are clear evidence that limited subduction of continental crust did occur. It is therefore also possible that D_3 structures formed during the change from accretion to collision after closure of the Khomas Sea (Adamastor Ocean; Hartnady *et al.*, 1985). The carbonate-bearing brittle faults that overprint a few of the D_2 shear zones are also evidence that these structures remained active during the retrograde cooling history of the SMZ. Retrograde mineral assemblages dominated by chlorite and amphibole indicate that faults remained active during cooling to at least (lower) greenschist facies conditions.

It is therefore proposed that D_3 deformation reflects the exhumation of the lower regions of the Khomas-Hochland accretionary prism during SE-directed overthrusting onto the Kalahari continental margin. The sub-horizontal stretching lineation L_3 is also rarely found on D_3 fault zones (Figure 5.11F), and can be interpreted in this setting as recording a strike-slip component associated with this phase of deformation. The Damara Belt may have evolved in a manner similar to that of the the indenter-escape tectonics currently observed in the Himalayan Orogenic Belt (e.g. Burke & Sengör, 1986). Because accretionary phase structures (D_1 and D_2) are remarkably well preserved, it is suggested that the collisional phase of deformation was rather short-lived and/or localised to major boundary structures of the SMZ and SZ (such as the Okahandja Lineament and the GRL etc.). Features characteristic of lateral extrusion have also been observed in the Central Zone of the Damara Belt (e.g. Kisters *et al.*, 2004) as well as other Pan-African aged orogenic belts (cf. The East African Orogen; Jacobs & Thomas, 2004).

There is a systematic spatial variation in the orientation of D_1, D_2 and D_3 structures across the map area from east to west. Both penetrative and non-penetrative fabrics are progressively rotated almost 90° from a W-E strike in the eastern regions to a NE-SW strike in the west, as shown by the foliation traces (Figure 5.5). The change in orientation of the main penetrative fabric is gradual, and occurs over a distance of approximately 8 km. This continuous change in orientation of S_{0+1+2} shows that re-orientation of the penetrative fabric and

finite strain in the eastern regions of the SMZ most likely occurred during high-temperature ductile deformation. This re-orientation of structures and fabrics is centred around the Rostock Inlier which lies just outside the NE corner of the map area, and is one of many Kalahari basement inliers that crop out within the SMZ (Miller, 1983). Earlier plate tectonic models for the Damara Belt proposed a stage of thermal relaxation, induced by delamination of the mantle lithosphere and a subsequent influx of asthenospheric mantle to the base of the crust as a means for emplacement of the post-tectonic granites that intrude along the Okahandja Lineament (Kasch, 1983a). It may be proposed then that such a later event (D_4) locally re-orientated D_1, D_2 and D_3 structures as a result of doming of the basement to the Damara Belt during this stage of thermal relaxation. However, passive doming of basement rock from below would be expected to cause local steepening of the penetrative fabrics. Since the opposite is observed, it is argued that the basement inliers represent palaeo-topographic highs or asperities on the subducting continental slab, around which the metasedimentary and metamafic sequence was deformed during subduction of continental crust and overthrusting onto the continental margin. Basement inliers in the Central Zone (CZ) of the Damara are, however, associated with large-scale fold structures (Miller, 1983) that may form via a passive doming mechanism or shortening perpendicular to the orogen (Kisters *et al.*, 2004). The strain pattern around the inliers of this section of the SMZ may therefore indicate that, at least in the SMZ, this doming was coincident with SE-directed overthrusting. This also suggests that the change from D_2 to D_3, representing the change from subduction to collision (Table 8.1), occurred close to or soon after peak metamorphism, after which deformation became more localised during exhumation and cooling.

8.2 Microstructural Evolution

In the deformation sequence inferred from the geometry and cross-cutting relationship of large-scale structures, the juxtaposition of the lithotectonic units occurred during the progressive large-scale imbricate thrusting and localisation of deformation on D_2 shear zones. During this stage of deformation the rocks of the SMZ were subjected to amphibolite facies metamorphism (Chapter 5; Cross (2013)). High-temperature ductile deformation of the rocks has therefore destroyed many of the early D_1 structures, which are locally preserved only in the more competent quartzitic units (TS5). The microstructures preserved in the shear zones and faults of the SMZ therefore track the evolution of deformation mechanisms from late-prograde and peak metamorphism (D_2) to retrogression and exhumation (D_3).

8.2.1 Ductile flow mechanisms of the internal shear zones

D_2 microstructures are preserved in the shear zones internal to the lithotectonic units of the SMZ. The earliest preserved ductile deformation is the strongly recrystallised mylonitic fabrics in these shear zones. The quartz mylonites in particular are characterised by uni-

modal grain size distributions and quartz fabrics similar to the high strain dislocation creep regime 3 of Hirth & Tullis (1992). Anisotropic grain fabrics, locally preserved core and mantle structures (Figure 6.1), and boudinaged ribbons with subgrains, indicate diclocation creep as the dominant deformation mechanism where recovery is accommodated by dislocation climb, and recrystallisation by progressive subgrain rotation (Hirth & Tullis, 1992; Stipp *et al.*, 2002). The average recrystallised grain size of approxiately 48 μm and high volume fraction of recrystallised grains-to-porphyroclasts ($> 85\%$) place temperature conditions during deformation between 550-600°C, near the transition from SGR to GBM recrystallisation mechanisms in quartz (Stipp *et al.*, 2002). These steady-state microstructures (White *et al.*, 1980) also indicate that crystal-plastic flow was active in the quartz matrix while porphyroclasts and ribbons acted as competent inclusions undergoing layer-parallel extension, which is a common feature in heterogeneous simple shear zones (White *et al.*, 1980; Fagereng, 2013).

Core-and-mantle structure is common in quartz-mica mylonites; thus there is a bimodal grain size distribution with a quartz texture resembling the bulging recrystallisation texture of Stipp *et al.* (2002), or the low-strain dislocation creep regime 3 of Hirth & Tullis (1992). A strong lattice preferred orientation (LPO) is observed in phyllosilicates, suggesting that dislocation creep in micas accommodated significant amounts of strain in these rocks. The average recrystallised quartz grain size is approximately 38 μm and the volume fraction of recrystallised grains is lower than that in quartz mylonites ($< 70\%$) reflecting deformation temperatures between 400-500°C, and spanning the transition from BLG to SGR recrystallisation mechanisms (Stipp *et al.*, 2002). The close spatial relationship between these rocks and uniform metamorphic grade across this part of the SMZ (Cross, 2013) means the different textures observed could not have resulted from differences in temperatures, but are rather a product of their rheologies and therefore differences in stress and strain rate (see Section 8.3).

D_2 deformation in micaceous shear zones is characterised by recrystallised quartz and mica fabrics with a strong LPO in mica. These fabrics have been modified in places by D_3 micro-faults and a weak crenulation cleavage, and are also overprinted by coarse-grained post-tectonic biotite (Figure 6.4D). Cosgrove (1976) notes that structures similar to these micro-faults may form by localised dissolution of the mica during foliation development. The association of these structures with coarse-grained biotite that overprints the recrystallised muscovite fabric, and weak crenulations, suggests instead that they represent a separate deformation event. Syn-tectonic quartz veins in these shear zones show coarse-grained quartz with irregular interfingering grain boundaries, a strong sweeping undulose extinction and subgrains (Figure 6.4A). In mixed quartz-mica domains grain-boundary pinning of quartz by mica is common (Figure 6.4B). These microstructures correlate to the lower temperature GBM(I) microstructure of Stipp *et al.* (2002), and are inferred to represent deformation temperatures in the range of 500 to 600°C.

Two generations of biotite overprint the mylonitic fabrics. The first stage of biotite growth is distinguished by biotites with long axes orientated down dip on micro-faults and crenulation axial planes as well as biotites with long axes parallel to crenulation hinge lines (L_3). In the second stage of biotite growth, biotites have a random fabric, and overprint both the earlier biotite and mylonitic fabrics. The association of the first generation of biotite with this reworking of the mylonitic fabric indicates that it occurred during the change from D_2 to D_3 deformation events and is therefore associated with the change from accretion to collision (Section 8.1; Table 8.1). The relative weakness of this biotite fabric compared with the dominant D_2 fabric, and its subsequent overprinting by static biotite growth, indicates that activity along these shear zones waned soon after collision occurred.

Progressive recrystallisation during simple shear generally results in the development of strong lattice preferred orientations (White *et al.*, 1980; Passchier & Trouw, 2005; Behr & Platt, 2013). This is observed for micas in phyllosilicate-bearing shear zones, but a lack of quartz c-axis fabrics (qualitatively analysed with a gypsum tint plate) and straight grain boundaries observed in quartz mylonites indicates that significant recovery has most likely occurred since deformation ceased. This is complemented by the evidence from the micaceous shear zones where static biotite overgrowths are common. The quartzitic shear zones internal to the lithotectonic units of the SMZ are therefore believed to have remained active until peak metamorphism, when mylonitic fabrics were progressively developed through climb-accommodated dislocation creep and SGR dynamic recrystallisation. This conclusion is also substantiated by the observation that the microstructures preserved in these shear zones give temperatures that correlate well with peak-metamorphic conditions for rocks in the Gaub Canyon (Cross, 2013). Micaceous shear zones, however, are interpreted to have remained active during peak metamorphism, as they record a weak overprinting of D_2 mylonitic fabrics; although static overprinting of peak-metamorphic biotite suggests that deformation in these shear zones ceased soon after peak metamorphism. Blastomylonitic textures of coarse-grained mica overgrowths indicate that static recrystallisation began close to peak metamorphism and then dominated microstructural development in all the intra-unit shear zones through retrogression and exhumation.

		Fabric Element	Deformation Mechanism	Orientation
Subduction	*D_1 Structures*			
	Early	Layer parallel extension	independent particulate flow & brittle fracture[a]	sub-horizontal
		Bedding-parallel foliation (S_{0+1})	dissolution-precipitation creep[a]	shallow NW dipping
	Late	Disjunctive/scaly fabric	dissolution-precipitation creep & brittle fracture	shallow NW dipping & anastamosing
	D2 Structures			
		Reverse shear zones	dislocation creep & dissolution-precipitation creep	low angle NW dipping
		Folding (F_2)	dislocation creep	hinge lines parallel to L_2
		Axial planar cleavage (S_2)	dislocation creep	parallel to S_{0+1}
		Penetrative composite fabric (S_{0+1+2})	dislocation creep	shallow NW dipping
		Stretching lineation (L_2)	dislocation creep	down dip on S_{0+1+2}
		Thrust faults	brittle fracture	NW dipping
Collision	*D_3 Structures*			
	Early	Crenulation cleavage (S_3)	dislocation creep	sub-vertical
		Stretching lineation (L_3)	dislocation creep	sub-horizontal on S_{0+1+2}
	Late	Thurst faults	dissolution-precipitation creep & frictional sliding	localised on D_2 shear zones

Table 8.1: Table of deformation fabrics with their respective deformation mechanisms and the inferred tectonic environment.[a] Early D_1 structures are not preserved in the SMZ, therefore deformation mechanism are inferred from other studies on low grade tectonic mélanges (e.g. Ujiie, 2002; Fagereng, 2011a).

8.2.2 Retrogression and Exhumation

A few of the faults bounding the lithotectonic units of the SMZ exhibit greenschist facies (or lower) mineral assemblages and brittle deformation structures that cross-cut earlier ductile fabrics (Chapter 6) and therefore preserve macro- and microstructure associated with D_3 retrograde exhumation-related deformation. Each has a unique macro- and micro-structure as a product of the wide range in mineralogy of these fault rocks (Table 8.2). A common feature of many of the structures that appear as tabular fault zones is the preservation of mylonitic textures in the hanging wall blocks. In these fault zones there is an increase in the intensity of brittle deformation as one gets closer to the basal fault surface, indicating that this phase of thrusting occurred during progressive cooling of the rocks in the SMZ, and was largely accommodated on unit-bounding viscous (at least initially) shear zones. A weak overprinting of D_2 mylonitic fabrics by coarse-grained biotite (Figure 6.4) and sub-horizontal stretching lineation (L_3) is found in the intra-unit micaceous shear zones. L_3 is also associated with lower temperature unit-bounding fault gouges (Figure 5.11F). This suggests that this phase of deformation began under high-temperature amphibolite facies conditions, while highly localised deformation continued down to low temperatures on a few unit-bounding fault structures. Chlorite thermometry performed on hydrothermal chlorites from the TS1-TS2 fault gouge indicates that D_3 deformation continued down to lower greenschist facies conditions (Chapter 7), and therefore into the brittle regime (Chapter 2). The presence of fine-grained dark material in microboudin necks in quartzitic D_3 fault structures (Figure 6.5A), coating fractures in dolomite in the TS5-TS6 structure (Figure 6.5C), and truncation of calcite grains in the GRL structure (Figure 6.7B), along with the general abundance of calcitic veins in many other D_3 fault zones (Figure 6.5E and 6.6D), indicate that dissolution-precipitation creep acted alongside both plastic and frictional mechanisms during the progressive development of these structures.

The intensity of brittle deformation that overprints earlier ductile fabrics is significantly higher in the carbonate-hosted fault zones that are characterised by breccia and cataclasitic textures (Chapter 5 and 6). In the silicate fault zones, evidence for dissolution-precipitation creep and static growth of greenschist facies minerals (Chapters 6 and Table 8.2) suggests that deformation ceased between 300-400°C. Burkhard (1990) studied the deformation microstructures in micritic limestones from the Helvetic nappes in western Switzerland. He concluded that the carbonate rocks this area deformed viscously down to temperatures of approximately 200°C, and that grain boundary sliding and dissolution-precipitation creep became important deformation mechanisms below this. Therefore, from a purely qualitative perspective, the carbonate-hosted fault zones appear to have remained active for longer than those hosted in silicate rocks, as the brittle textures would have developed only at temperatures below 200°C (Burkhard, 1990; Bestmann *et al.*, 2000; Passchier & Trouw, 2005).

Structure	Mineralogy	Microstructure/Deformation Mechanisms	Physical Conditions
TS1-TS2	quartz with retrograde chlorite and biotite	Mylonitic quartz fabric cut by solution seams indicating dissolution-precipitation creep as the dominant retrograde deformation mechanism	$250 < T < 350°C$ from chlorite geothermometry
TS5-TS6	Dolomite with minor plagioclase feldspar and quartz	Dolomite groundmass is extensively fractured with very little intracrystalline deformation. Quartz shows evidence only for intracrystalline deformation.	$T > 350°C$
TS12-TS13	Tremolite and quartz with retrograde tremolite, talc and calcite	Quartz deformed mainly by dislocation creep, while tremolite deformed by dissolution-precipitation creep and brittle fracture. Static growth of tremolite overprints this fabric.	$200 < T < 400°C$ from calcite twin morphology[a] and greenschist facies assemblage
GRL	Calcite and dolomite with quartz veins	Twinning common in recrystallised calcite matrix. Core and mantle structure, undulose extinction and subgrains in quartz veins indicative of dislocation creep. Cataclastic bands cut mylonitic fabric in Riedel shear network.	$T < 200°C$[b]

Table 8.2: Table summarising the deformation mechanisms and physical conditions of D_3 thrusting.[a] Type II twins form over the temperature range 150 to 300°C (Burkhard, 1993).[b] Approximate upper limit of brittle deformation in calcite (Burkhard, 1990; Bestmann *et al.*, 2000; Passchier & Trouw, 2005).

However, in the TS5-TS6 structure, fractured dolomite is observed with plastically deformed quartz (Figure 6.5C), suggesting that concomitant mixed-mode, brittle-viscous deformation could have occurred in this fault zone. The microstructures in the GRL may also be interpreted in this manner because, in places, plastically deformed quartz veins are found in a matrix of semi-brittle calcite (Figure 6.7A). Localised cataclasis in this fault zone does, however, affect both calcite and quartz indicating that it was active under conditions in which both minerals deform by pressure dependent deformation mechanisms (Figure 6.7B & D). Because of the heterogeneous nature of the D_3 fault rocks, an accurate assessment of the timing of activity of these faults is not possible without knowledge of their rheology. This is discussed in detail in the following section.

8.2.3 Rheological constraints on the lower temperature limit of D_3 deformation

Deformation of polymineralic rocks is complex and the microstructures that develop in such rocks are dependent on the relative strength of the constituent minerals (Handy, 1990, 1994; Blenkinsop, 2000; Passchier & Trouw, 2005). Handy (1990, 1994) states that, for a bimineralic rock composed of minerals of contrasting strength, the microstructure can be described by either a load-bearing framework (LBF) where the strong phase surrounds patches of the weaker phase, or an interconnected weak layer (IWL) if the weak mineral surrounds patches of the stronger phase. For an LBF microstructure, if the strong phase is present in proportions such that there is enough contact between adjacent grains to support an imposed differential stress (>70 to 80%), the mechanical behaviour of the aggregate should approach that of the strong phase as the model volume of the strong phase approaches 100% (Handy, 1994; Passchier & Trouw, 2005). The argument for the IWL microstructure is similar although, in this case, if the weak phase is suitably orientated, it need be present only in proportions high enough to form an interconnected network (> 20%).

The texture of the basal dolomite breccia in the TS5-TS6 structure corresponds the LBF microstructure of Handy (1994) with isolated pockets of quartz and feldspar (weak phase) in a groundmass of dolomite (strong phase), while the calc-mylonite in the GRL exhibits IWL microstructure with a weak calcite matrix enclosing veins of more competent quartz (Heard, 1976). The rheology of these aggregates should lie somewhere between the end-member rheologies of the constituent minerals, although Fagereng & Sibson (2010) point out that the bulk rheology of such a polyphase aggregate does not follow a simple linear mixing rule. Therefore, by comparing the microstructures preserved in these fault rocks with the exprimentally determined flow strengths of each mineral (e.g. Handy, 1994) one can determine the approximate conditions under which the microstructures developed, and more specifically, the approximate conditions of the change from viscous to brittle deformation.

There are a few simplifying assumptions that must be made first. The presence of retrograde assemblages on a number of the D_3 fault zones indicates that this phase of deformation occurred under conditions of decreasing temperature and pressure. Because of a lack of any pressure constraints (Chapter 7), however, it is not possible to determine an average geothermal gradient for this phase of deformation. Collisional environments are generally warmer than subduction environments, with average geothermal gradients in the range 20 to 30°C.km^{-1} (Brown, 1993, 2006). Field evidence (Chapter 5), suggests that D_3 deformation occurred during the collisional phase of the Damara Orogeny, while Cross (2013) proposed an average geothermal gradient of ∼18°C.km^{-1} for the prograde, subduction-related metamorphism. Therefore an average geothermal gradient of 25°C.km^{-1} is assumed during collision and exhumation. The second assumption is that deformation occurred at a constant bulk strain-rate. Implicit in this is that, for the largely polymineralic fault rocks, there was no strain-rate partitioning between the different constituent phases. This is unlikely to be the case; however, the modal abundance of carbonate minerals in the carbonate-hosted faults greatly outweighs that of the silicate minerals (Chapter 6). The rheology of these faults can be approximated by the rheology of the dominant carbonate mineral. Frictional strength is approximated by:

$$(\sigma_1 - \sigma_3) = K\rho g z(1 - \lambda_v), \tag{8.1}$$

where ρ is density, g gravitational acceleration, z is depth and λ_v is the pore fluid factor. K is a fault parameter that varies as a function of fault orientation (θ_r) and the static coefficient of friction (μ_s). K is commonly approximated as 1.6 for thrust faults; this assumes failure on pre-existing, optimally-orientated faults ($\theta_r = \theta^*$; Chapter 2) and an appropriate value for μ_s following Sibson (1974). Frictional strength is therefore calculated using a coefficient of friction of 0.6 at the low end of the Byerlee (1978) range, and an average density for quartzofeldspathic crust of 2650 kg.m^{-3}. Viscous strengths were calculated for the supposed thermal structure using material parameters for quartz (Jaoul *et al.*, 1984), dolomite (Delle Piane *et al.*, 2008) and calcite (Walker *et al.*, 1990). These flow laws were adjusted to simple shear where appropriate after Nye (1953):

$$\tau_v = \sqrt[n]{\frac{\dot{\gamma}}{\sqrt{3^{(n+1)}}Ae^{(-Q/RT)}}}, \tag{8.2}$$

where $\dot{\gamma}$ is the shear strain rate (s^{-1}), R is the universal gas constant (J.K^{-1}.mol^{-1}), and T is the absolute temperature (K). A, Q and n are material parameters (Table 2.1). The viscous flow laws for calcite and dolomite are sensitive to grain-size (Walker *et al.*, 1990; Davis *et al.*, 2008; Delle Piane *et al.*, 2008), and these rheologies are therefore modelled with grain sizes of 500 μm and 300 μm respectively, appropriate for the carbonate rocks in this study area (Chapter 6).

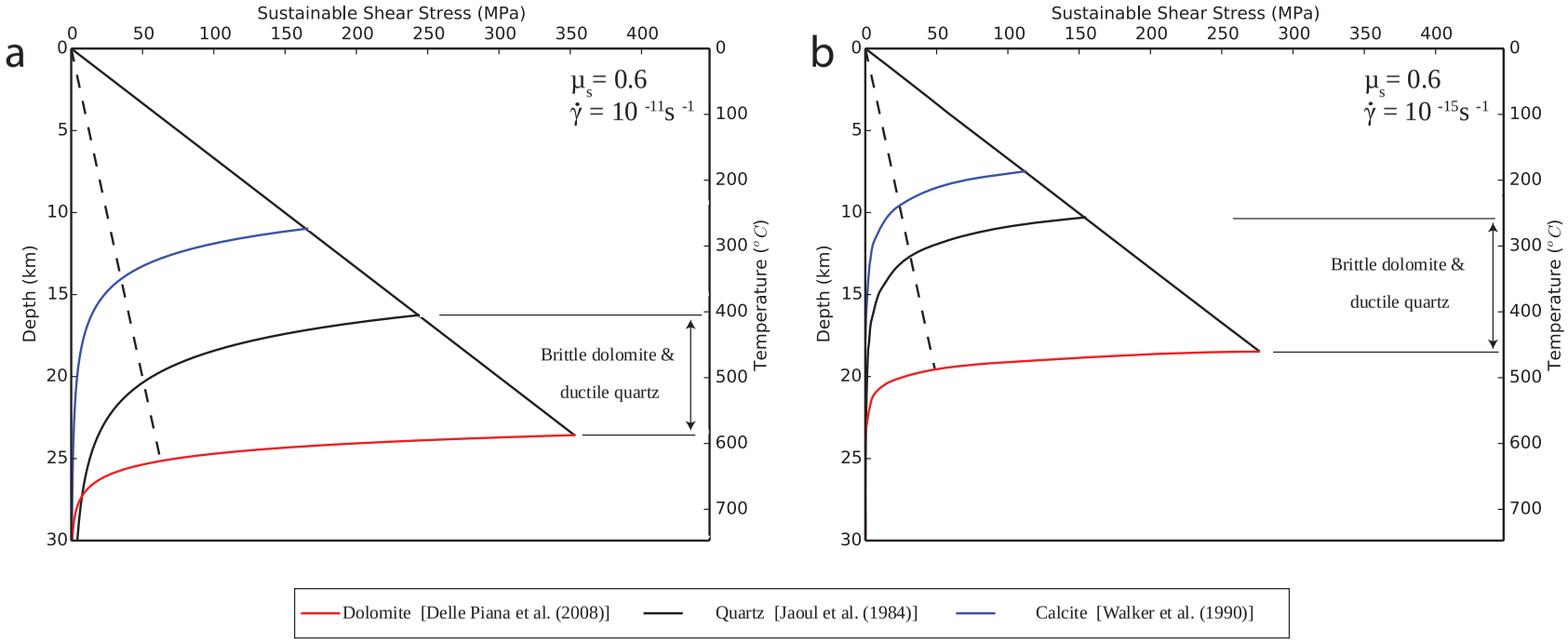

Figure 8.2: Crustal strength curves for quartz (black) and dolomite (red) and calcite (blue) with a geothermal gradient of 25°C.km^{-1} and strain rates of 10^{-11}s^{-1} (a) and 10^{-15}s^{-1} (b). Straight lines represent the frictional strength for a thrust fault with an average coefficient of friction of 0.6 (Byerlee, 1978). Solid line represents hydrostatic conditions ($\lambda_v = 0.4$), and dashed line represents overpressured conditions ($\lambda_v = 0.8$).

The crustal strength curves (Figure 8.2) show the predicted shear stress at failure (τ) plotted against depth. The changeover from brittle to viscous deformation occurs when the frictional strength exceeds the viscous strength. For a bulk shear strain rate of $10^{-11}s^{-1}$ and the supposed thermal structure, in a dolomite-dominated rock (e.g. TS5-TS6 fault rock) this transition is modelled to occur at ∼590°C, while in quartzitic and calcitic rocks it would occur at ∼400°C and ∼270°C respectively (Figure 8.2). This transition marks the depth (and temperature) where pressure-dependent, frictional deformation mechanisms give way to temperature-dependent plastic flow mechanisms (Chapter 2). Therefore, for a rock composed of dolomite and quartz deforming in the temparature range 400 to 590°C one would expect to observe brittle deformation in dolomite, while quartz should exhibit plastic deformation structures. This is observed in the TS5-TS6 structure (Chapter 6), and thus the lower temperature in this range is the imposed lower limit for deformation in this structure, i.e., this fault was not active at temperatures lower than 400°C as very little brittle deformation was observed in quartz. By similar argument, the abundant evidence for brittle deformation of calcite (and quartz) in the GRL suggests that this structure was active down to very low temperatures; brittle behaviour of calcite is modelled to occur only below temperatures of 190-270°C for geologically reasonable strain rates (Pfiffner & Ramsay, 1982). Increasing fluid pressure does not significantly affect the depth of the brittle-viscous transition in dolomite-dominated rocks (Figure 8.2). Its effect on the quartzitic and calcitic rocks is to deepen the brittle-viscous transition by ∼2 to 5 km and significantly reduce the magnitude of the applied shear stress required for frictional failure (Figure 8.2).

The retrograde evolution of major D_3 faults in the SMZ is therefore interpreted to be one of increasing localisation and partition of deformation into weaker material with decreasing temperature. In the dolomite-dominated structures (e.g. TS5-TS6), brittle deformation is likely to have begun soon after peak metamorphism. Decreasing the temperature from 600°C the strength of dolomite increases rapidly compared with that of quartz and calcite (Figure 8.2) and it is ∼12× stronger at 500°C. This may explain the partitioning of deformation, as viscous flow is concentrated in the weaker fault zones while the stronger faults would be expected to fracture episodically. This trend is accentuated upon cooling through the brittle-vicous transition in quartzitic fault zones (e.g. TS1-TS2 structure), as steady displacement on these structures is also expected to cease as strain is further concentrated in the weaker calcitic structures such as the GRL. The development, in this fault zone, of a localised cataclastic network that transects a recrystallised mylonitic fabric (Chapter 6) indicates that it was active beyond the brittle-viscous transition in calcite, and is therefore likely to have remained active longer than many of the other unit-bounding structures in the SMZ. The importance of the GRL as one of the major long-lived structures during exhumation of the Damara Orogen is also highlighted by its length, as it appears to run for >300 km along strike (Kasch, 1983b; Miller, 1983, 2008).

8.3 Strain Localisation and Partitioning of Deformation Modes

The strain distribution (Figures 5.1 and 5.5) clearly shows heterogeneous development of penetrative S_{0+1+2} fabric, localisation of shear strain along the boundaries of lithological domains in D_2 shears, and partitioning of continuous, discontinuous and mixed continuous-discontinuous deformation between these thrust sheets. Therefore, on a large-scale, deformation localises in two places: (1) in relatively incompetent metapelitic and metapsammitic rock; and (2) along the boundaries of lithological domains. The different mechanical behaviours are attributed primarily to the presence of lithological, and hence rheological, heterogeneities.

Strain localisation occurs as a result of local changes in the mode of deformation of a rock, so that deformation follows a path of minimum energy (Goodwin & Tikoff, 2002). It may occur for a number of reasons: rock/material anisotropy, pre-existing foliations, pre-existing brittle discontinuities, the presence of a fluid phase, and grain-size reduction during deformation (Goodwin & Tikoff, 2002; Mancktelow & Pennacchioni, 2005; Platt & Behr, 2011). The following discussion will evaluate the controls on strain localisation in the SMZ, where material anisotropy appears to play the most significant role.

8.3.1 Material Anisotropy

Semipelitic and pelitic units have a well-defined, closely-spaced, penetrative foliation whereas, in quartzitic and conglomeratic units, foliations are only weakly defined. The development of foliations and banding involves the partitioning and redistribution of weaker material (e.g. micas) into discrete domains. Therefore, the ability of a rock to form a foliation depends on the relative proportions of weak and competent material (the ratio of mica to quartz + feldspar; Goodwin & Tikoff, 2002). For this reason, more micaceous rocks develop more closely-spaced foliations than relatively mica-poor units, and the finite strains preserved in these rocks are greater than those in the more competent units (Ramsay & Graham, 1970). The lower regions of the metaturbidite (TS12) exemplify this on a small scale; metapelitic layers have a well-defined closely-spaced S_{0+1+2} tectonic foliation, whereas quartzitic layers preserve sedimentary bedding. Material anisotropy is therefore interpreted to be a major factor affecting strain localisation during D_1 and D_2 deformation. It results in the development of continuous fabrics in more micaceous metapsammitic and metapelitic rock types, while quartzites developed anastomosing, disjunctive fracture fabrics.

The compositional variability between lithotectonic units and subsequent strain partitioning is also a major factor affecting the observed differences in deformation mode. The rheological behaviour of crustal rocks is affected greatly by the modal proportions of quartz, feldspar and phyllosilicates (Handy *et al.*, 1999). Since feldspar behaves as a competent mineral relative to quartz at T >350°C, a rock unit with relatively high feldspar/quartz proportion behaves more competently in relation to its surroundings. Goodwin & Tikoff (2002) also noted that

strain will localise preferentially in rock units with an interconnected network of phyllosilicates. The formation of an interconnected phyllosilicate network is cited as a major factor contributing to weakening and strain localisation in polyphase rocks (Handy, 1990; Handy *et al.*, 1999; Holyoke & Tullis, 2006a). However, even for small differences in the magnitude of strain rate, the presence of mica-rich domains will only influence strain localisation if they constitute more than 10 to 20% (approximately) of the deforming material (Handy, 1990; Handy *et al.*, 1999; Goodwin & Tikoff, 2002).

During D_2 the whole system was experiencing bulk non-coaxial shear (Section 8.1.2). The difference in the degree of strain localisation (deformation mode) for each lithotectonic unit therefore indicates that shear strain was partitioned preferentially into units with an interconnected mica network and low proportions of feldspar, ultimately resulting in further disruption of these units by ductile shear zones (e.g. Units TS10, TS11 and TS14). However, in units with relatively low mica content (<10%) and higher proportions of feldspar (e.g. Unit TS8), strain was unable to localise effectively, and these units deformed fairly homogenously throughout, with no discontinuous deformation observed.

8.3.2 Palaeopiezometery

The effect of material anisotropy is semi-quantifiable, through the application of the palaeopiezometer of Stipp & Tullis (2003) and the dislocation-creep flow law for quartz of Hirth *et al.* (2001), to the quartz and quartz-mica mylonites described in Chapter 6. Both rock types are found in 1 to 2 m thick, lithologically-layered ductile shear zones internal to the quartzitic unit TS5, and are therefore likely to have deformed at the same pressure-temperature conditions. However, each lithology exhibits different quartz microstructures (Figure 6.2A and C) and grain sizes (Figure 6.3), which can therefore be attributed only to differences in strain rate.

The size of dynamically recrystallised grains is widely used as an indirect measurement of differential stress in the middle-to-lower-crust, where dislocation creep is the dominant deformation mechanism (Stipp & Tullis, 2003; Stipp *et al.*, 2010). This is done through the application of experimentally calibrated piezometers that relate the size of recrystallised grains directly to stress:

$$(\sigma_1 - \sigma_3) = exp(\frac{log(D/3631)}{-1.26}), \tag{8.3}$$

where $\sigma_1 - \sigma_3$ is the differential stress, and D is the recrystallised grain size, taken as the geometrical mean of a grain-size frequency plot (Figure 6.3) following Stipp & Tullis (2003). Substituting the stress value into the quartz flow law of Hirth *et al.* (2001) yields the strain rate ($\dot{\varepsilon}$):

$$\dot{\varepsilon} = A f_{\mathrm{H_2O}}^{m} (\sigma_1 - \sigma_3)^n exp(\frac{-Q}{RT}), \tag{8.4}$$

where A is a material parameter ($\log(\mathrm{A})$ = -11.2±0.6 $\mathrm{MPa}^{-n/s}$), $f_{\mathrm{H_2O}}$ is the water fugacity, m is the water fugacity exponent, σ is different stress, n is the stress exponent, Q is the activation energy (135±15 $\mathrm{kJ.mol}^{-1}$), R is the ideal gas constant (8.3145 $\mathrm{J.K}^{-1}\mathrm{.mol}^{-1}$) and T is the absolute temperature (K).

Methods of grain-size determination

Before stating the relevant assumptions and result of this analysis, it is important to outline briefly the methods by which D values were determined. 2D grain size measurements were performed on photomicrographs using ImageJ freeware applying the linear intercept method. Line-intercepts were counted both parallel and perpendicular to the mylonitic foliation, and averaged to account for the grain shape fabrics. The measurements were processed by a Python script (Appendix C) written specifically for this analysis, to perform the relevant calculations and publish the relevant figures. The estimated error of the grain size measurements is approximately ±2 μm. Since this analysis was performed solely for comparative reasons and the estimated error is small relative to the measured grain-sizes, it was not expected to be significant given the uncertainty associated with the other parameters. The major source of uncertainty with this type of point-counting approach is the human error in discerning between recrystallised and non-recrystallised grains. For this reason, grains were measured indiscriminately. A cut-off grain size was then chosen at 120 μm, as Stipp *et al.* (2010) point out that grain sizes greater than this fall outside the range from which the Stipp & Tullis (2003) palaeopiezometer was calibrated, and are therefore unlikely to yield reliable results.

Assumptions and Results

Field and petrographic observations indicate that deformation in this shear zone ceased close to peak metamorphism (Section 8.2). Peak metamorphic temperature and pressure are therefore used in this calculation (600°C and 10 kbar; Cross, 2013). $f_{\mathrm{H_2O}}$ was calculated for these conditions using the Tony Withers fugacity calculator, which applies the equation of state for water of Pitzer & Sterner (1994). It should also be noted that the microstructural evidence suggests that the mylonitic fabrics of the intra-unit shear zones have been modified by static recrystallisation (annealing) during post-peak metamorphism (Section 8.2). In this case the measured grain sizes are unlikely to be accurate representations of the true dynamically recrystallised grain sizes. The absolute values of the calculated stress and strain rates are therefore likely to be underestimates; however, they are of less importance than the relative difference in these values between the two rock types.

Sample	Microstructure	n	**D** (μm)	σ (MPa)	$\dot{\varepsilon}$ (s^{-1})
GB16	recrystallised quartz matrix	138	47.77±0.2	31.10	5.94×10^{-11}
GB17	recrystallised quartz matrix	136	51.67±0.3	29.22	4.63×10^{-11}
GB18	interconnected mica network	120	39.40±1	36.23	1.10×10^{-10}

Table 8.3: Results of quartz palaeo-piezometry. n is the number of measurements. Mean recrystallised grain-size (D) reported with standard error. Stresses in quartz mylonite (GB17) matrix are lower than those of quartz-mica mylonites (GB18). Higher strain rates calculated for the quartz-mica mylonites demonstrate the weakening effect of an interconnected phyllosilicate network. Shaded cells show samples from the same shear zone. GB16 shows data from a quartzitic lense in the TS1-TS2 fault gouge and is presented here for comparison. Shaded rows group rocks from the same shear zone.

In shear zones containing an interconnected phyllosilicate network, the dynamically recrystallised grain size is approximately 10 μm smaller than that in pure quartz mylonites (Figure 6.3 and Table 8.3). Palaeopiezometric calculations show that this may be due to elevated stresses in the quartz matrix of the phyllosilicate-bearing shear zones which deform at higher strain rates, approximately twice those of quartz-dominated shear zones (Table 8.3). The lower-strain microstructure preserved in the quartz matrix of the quartz-mica mylonites therefore indicates that these quartz domains, which are isolated by the through-going network of phyllosillicates, act as rigid lenses surrounded by an actively deforming weaker viscous phase, even though the phyllosillicates are by far the less dominant minerals. This has also been shown in experiments by Tullis & Wenk (1994) and Holyoke & Tullis (2006b) on mica-quartz aggregates. In both instances, the formation of interconnected mica networks leads to significant weakening and strain partitioning with stress concentrations in the quartz framework, which develops a lower strain or even semi-brittle microstructure. This outcome is also in line with the experimental observations of Niemeijer & Spiers (2005), who note that the presence of an interconnected phyllosilicate network significantly weakens a rock mass under mid- to lower-crustal conditions; although, in their experiment micas deformed by frictional-viscous flow rather than dislocation creep. For rock units of the SMZ containing enough phyllosilicate to form an interconnected network, the bulk rheology is effectively governed by the rheology of the weak phyllosilicate phase. Strain is partitioned preferrentially into these units which deform at higher strain rates relative to more competent rock types. Fagereng & Sibson (2010) note that, when there is a significant strength contrast between two actively deforming phases, bulk rheology can be approximated by that of the weak phase, even if it is present in relatively low proportions.

8.3.3 Coeval Brittle and Ductile Structures

A macro-scale manifestation of this strain partitioning is the apparent coeval nature of both brittle and ductile structures. In the SMZ, quartzites are clearly characterised by dominantly discontinuous brittle thrusting, while metapsammitic and metapelitic rock exhibit, predominantly, structures associated with ductile flow (Chapter 5). Some authors argue that coexisting brittle and ductile structures reflect temporal evolution from brittle to ductile regimes during prograde-to-peak metamorphism and deformation in which ductile shear strain is localised along pre-existing brittle fractures (Fusseis *et al.*, 2006; Mancktelow & Pennacchioni, 2005). Druguet *et al.* (2009) propose an alternative model, where deformation of a strongly rheologically layered rock results in partitioning of ductile flow into the incompetent layers while competent layers deform by brittle failure with faults and fracture boudins. If the first scenario is true, then the preservation of brittle structures in the lower regions of the quartzite unit (TS5) may result from strain-rate partitioning between the quartzites and metapelites during high-temperature viscous deformation. If the metapelites surrounding the quartzitic unit deform at higher strain rates, then differential stress in the quartzites will increase. A similar effect was demonstrated for the quartz-mica mylonites in the previous section (Table 8.3), and is also observed on a micro-scale in these rocks (Figure 6.2D). It is therefore suggested that such an increase in differential stress may induce friction reactivation of earlier-formed brittle structures in the quartzite during pervasive high-temperature viscous flow. The latter argument of Druguet *et al.* (2009) is also valid in this case, as very little penetrative ductile deformation was observed in quartzitic lithologies, even though the rocks experienced peak temperatures well above the onset of crystal plasticity in quartz (∼350°C). This line of argument implies that the quartzites remained intact during early brittle deformation. Such preservation of original bedding is observed in the lower regions of the turbidite unit (TS12), although in this region the interleaving metapelites are likely to have accommodated the bulk of the strain. Therefore the former argument is considered more likely as the magnitude of the increase in differential stress required to reactivate a pre-existing plane of weakness is lower than that required to form a new shear fracture (Figure 2.2; Chapter 2).

One could also argue that transient periods of high fluid pressure in the quartzitic units lowered effective normal stresses enough to promote brittle fracture (Hubbert & Rubey, 1959). There are two sources of fluid in the décollement: (1) fluid contained in the pore spaces of saturated unconsolidated sediment and hydrated oceanic crust; and (2) water that is structurally-bound in hydrous minerals (Saffer & Tobin, 2011). Moore & Saffer (2001) modelled fluid pressure variations along the subduction megathrust from the trench down to a depth of 12 km. Their study shows maximum fluid release at approximately 2 km and gradual decrease with depth down to 12 km, attributed to loss of pore water through compaction and lithification of sediment as it is underthrust beneath the wedge.

Structurally-bound water is released at various levels along the décollement; initially from clay minerals such as smectite, which undergo a change to illite over the temperature range 100 to 150°C (Moore & Saffer, 2001). At depths and temperatures greater than those modelled by Moore & Saffer (2001), dehydration reactions in zeolite to greenschist facies minerals are likely to be the main contributors to fluid production at temperatures from 150 to 400°C and above (Saffer & Tobin, 2011). D_2 deformation is therefore expected to have occurred during heating from 150 to 600°C as the cessation of the smectite-illite transition is widely cited as a marker for the onset of widespread brittle deformation and imbrication/underplating (Moore *et al.*, 2007; Kimura *et al.*, 2007). Fluid overpressuring in the SMZ during D_2 would therefore be a result of large scale fluid production upon intersection of major prograde metamorphic dehydration reactions. Fluid production is thus more likely to be concentrated in pelitic and mafic rock types, as these rocks have higher concentrations of minerals expected to be involved in major dehydration reactions during prograde metamorphism (e.g. chlorite and amphiboles; Connolly, 1997). Since these rock types show no evidence for large scale brittle reverse faulting, fluid overpressuring is not expected to have played a significant role. Vein (extension) fracturing is, however, abundant in these rock types, indicating that transient localised overpressuring did occur, while the quartzites were probably dehydrated at relatively shallow levels during initial compaction and lithification (Moore & Saffer, 2001; Saffer & Tobin, 2011).

The lack of penetrative ductile fabrics and dominance of discontinuous modes of deformation in the lower regions of the quartzite unit (TS5) and upper portion of the turbidite unit (TS12) are therefore interpreted to result from ductile strain partitioning during high-temperature viscous flow (D_2). Increased strain rate in the surrounding metapelites would result in stress concentration in the more competent rock units. This increase in differential stress may promote frictional reactivation of pre-existing fabrics with low cohesive strength, such as existing faults and fracture- or pressure-solution cleavages (Chapter 2). These are not believed to have been reactivated during D_3 as, at least in the TS5 quartzite, there is no evidence for retrogression of the metamafic rocks found along these structures.

8.3.4 The role of pre-existing D_2 Structures during D_3

Retrograde D_3 deformation is localised on a few of the major pre-existing D_2 structures in the form of reverse brittle fault zones. These are characterised by greenschist facies assemblages and carbonate-bearing breccias and fault gouges that overprint early ductile deformation (Section 8.2). A dip-frequency histogram of faults in the SMZ shows a peak in dip frequency occurring around the optimal reactivation angle, $\theta^* = 29.5$ (Chapter 2; Figure 8.3). The localisation of D_3 deformation of D_2 shear zones therefore most likely results from these structures, with dips in the range 15 to 51°, firstly being optimally orientated for reverse shear in a compressive regional stress regime (Figure 8.3a) where the greatest principal stress (σ_1) is subhorizontal (Davis *et al.*, 1983; Sibson, 1985); and secondly having lower cohesive strength than the surrounding intact wall rock due to finer grain-size and more closely-spaced foliations (Collettini *et al.*, 2009). Strength-dip plots in Figure 8.3 are contoured for fluid pressure given by λ_v. They demonstrate that increased fluid pressures significantly reduce the differential stress required to induce frictional failure; and also that as depth increases, exceedingly higher fluid pressures are required for reactivation (Figure 8.3).

Dissolution-precipitation creep is believed to be an important deformation mechanism operating simultaneously with dislocation creep in major unit-bounding shear zones (Section 8.2). Macroscopic solution cleavages are also observed in unit-bounding D_2 shear zones that show no evidence for retrograde deformation (Chapter 6, Figure 5.7D), and therefore are not likely to have experienced any D_3-related deformation. This indicates that solution-creep mechanisms were probably also active in these shear zones close to peak metamorphism. The microstructures preserved in the faults that reactivated these D_2 shear zones also show that dissolution-precipitation creep was an active deformation mechanism during retrograde deformation. Channellised fluid flow is also inferred for such structures, based on observations of localised fluid-seeps at the sea floor on actively accreting margins and high damage-zone permeability surrounding principal slip zones in other exhumed accretionary terranes (Saffer & Tobin, 2011, and references therein). These lines of evidence suggest high permeability for these structures which cannot implicitly sustain high fluid pressures. Moderately dipping faults of the SMZ, such as the GRL, which has a dip of ∼50°, are therefore believed to have been active under conditions of low fluid pressure, and were perhaps rotated into their current attitude during progressive sub-horizontal D_3 shortening.

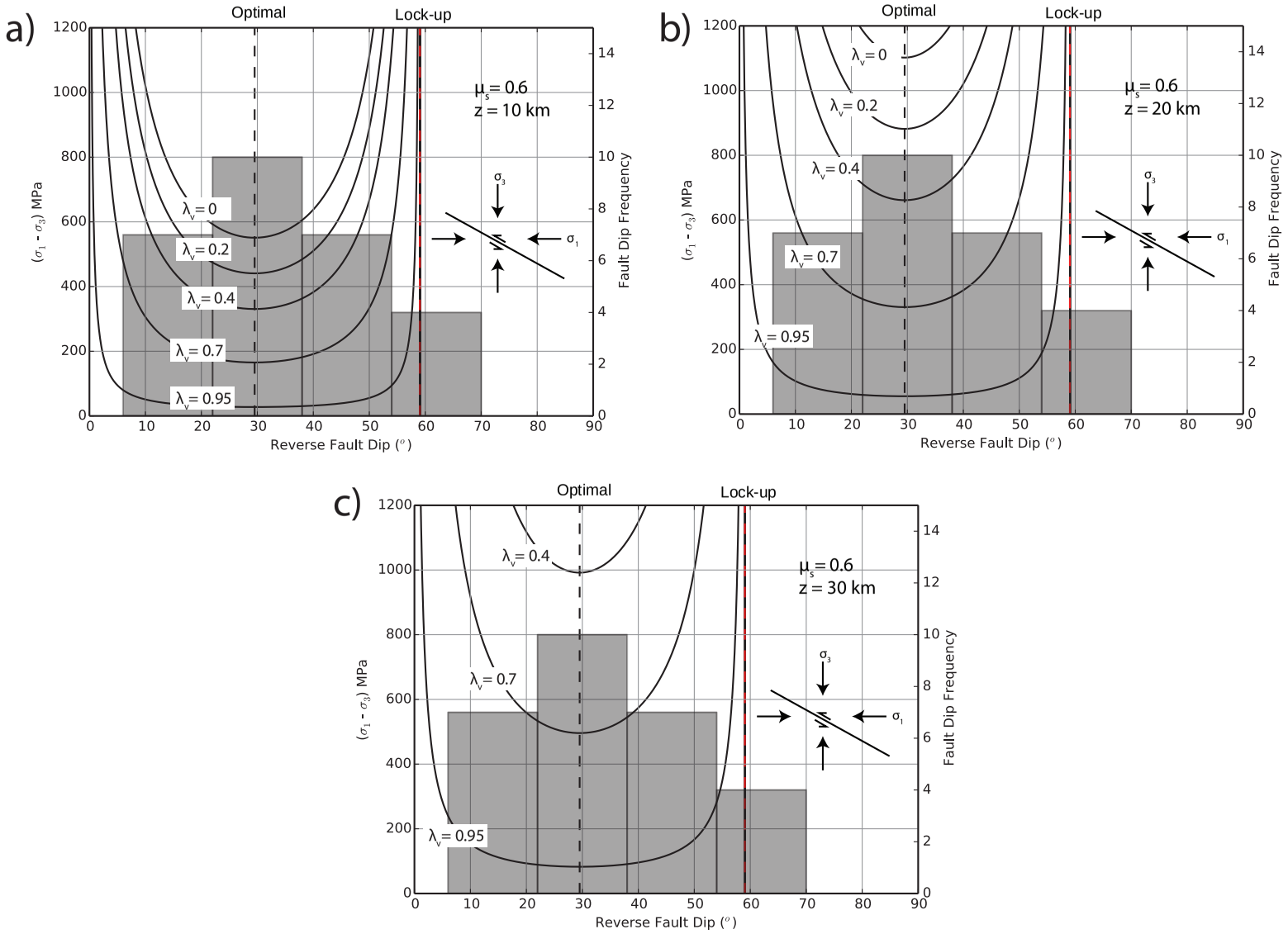

Figure 8.3: Plots showing the differential stress required for frictional reactivation of a cohensionless fault at depths of 10 km (a), 20 km (b) and 30 km(c) (Sibson, 2012), contoured for λ_v. Shaded gray bars show the dip frequency for faults in the SMZ with a distribution centred around the optimal reactivation angle, $\theta^* = 29.5$.

Work by Bachmann *et al.* (2009) on the South Penninic Mélange in the European Alps showed that collision and exhumation caused an overprinting of the subduction fabric geometry. While the subduction fabric was not completely destroyed, significant post-subduction shortening was still noticeable by large-scale folding and pervasive fracturing. This is not observed in the Gaub Canyon, where strain localisation on a few pre-existing D_2 structures exhumed the ancient décollement zone as relatively rigid blocks that only preserved D_3 deformation in the form of a comparatively weak (i.e. compared with the D_2 fabric) crenulation cleavage. This then suggests that orogenic deformation during the Damara Orogeny was probably short-lived and perhaps not on the scale of deformation observed in the Alps.

8.4 Implications

The overall style of deformation in the SMZ is much the same as described by previous workers in this region (Chapter 5; Miller, 1983, 2008). The overall geometry is characterised by D_2 deformation structures with shallowly-dipping, SE-verging isoclinally recumbent folds that transpose the main penetrative fabrics and top-to-SE thrusting. The rock assemblages of the SMZ represent a tectonically-imbricated mixture of upper- and lower-plate material, where lithologically homogeneous units are interspersed with block-in-matrix mélanges. The interpretation is, therefore, quite different, and is considered as a crustal-scale heterogeneous shear zone marking the position of the plate-boundary fault that was active during closure of the Khomas Sea. Because of this preservation of accretion-related deformation, and the metamorphic conditions under which these rocks were deformed (Cross, 2013), the deformation features recorded by the rocks in the Gaub Canyon offer valuable insight into the stress and strain conditions, as well as the deformation mechanisms operating, at depth in modern subduction margins. This study has shown that non-coaxial shear remains the dominant mode of strain, and that layer-parallel extension remains the major mode of stratal disruption to depths of 30 km and temperatures of ∼550°C. Pure shear is also likely to play a major role, as the great weight of the overlying prism would cause the décollement to experience vertical shortening. Dislocation creep is the dominant deformation mechanism under these conditions, although dissolution-precipitation creep is also likely to be an important mechanism contributing to material transfer and volume loss. Brittle deformation, in the form of extensional veining and micro-fracturing, may also make a minor contribution to strain accommodation.

8.4.1 Evolution of the Damara Orogen

D_2 deformation has been interpreted to record the process of imbrication of the underthrust sediment pile beneath an accretionary prism and, while D_3 is recognisable as a separate event, deformation related to it is localised along D_2 thrust structures with very little overprinting of penetrative D_2 fabrics outside of the reactivated D_2 shear zones. This localisation of deformation and retrogression related to collision-exhumation phases explains the general lack

of orogenic deformation and exhumation features observed in a recent metamorphic study of the same area by Cross (2013). There is evidence that subduction of continental crust did occur (Section 8.1); however, it is only present towards the structural base of the SMZ. Assuming in-sequence thrustiong, this indicates that there is a general younging direction towards SE in the SMZ, in constrast with older lithostratigraphic interpretations (Martin & Porada, 1977; Miller, 1983; Hoffmann, 1983). It also suggests that continental collision was probably short-lived, and therefore did not cause extensive overprinting of D_1 and D_2 structures (Meneghini *et al.*, 2014). Accordingly, the structures of the accretionary phases (D_1 and D_2) are remarkably well preserved. The Gomab River Line (GRL) may, in this case, represent a major out-of-sequences thrust (megasplay fault) that splayed off the décollement, similar to those found in modern accretionary prisms (e.g. Nankai; Strasser *et al.*, 2009) and may additionally be the roof thrust to which the other faults converge. The presence of intense localised cataclasis (Chapter 6) in this calcitic fault zone indicates that it was active down to low-grade conditions (Section 8.2), with its great length pointing to it being an important structure during exhumation of the rocks of the Southern Zone. It is therefore proposed that the boundary between the lower and upper plates is a broad structure essentially marked by the SMZ. However, the various tectonic components were not necessarily active simultaneously. The presence of a sub-horizontal stretching lineation (L_3) on many of the faults and shear zones that preserve evidence for D_3-related deformation points towards a strike-slip component during this phase of deformation suggesting that the collisional phase of the Damara Orogeny may have evolved in a manner similar to the indenter-escape tectonics currently observed in the Himalayan collisional front. This is not uncommon in other Pan African-aged orogenic belts and has also been documented in the Central Zone of the Damara Belt (Kisters *et al.*, 2004).

8.4.2 Thickness of the plate-boundary shear zone

While the thickness of each litho-tectonic unit is certainly not a constant in the SMZ, the seemingly regular spacing of major unit-bounding D_2 shear zones (occurring roughly every 750 to 1000 m) would indicate that these structures are geometrically controlled, and that large scale strain localisation during D_2 occurs along a stable geometrical framework that efficiently accommodates strain at this scale. If the tectonic stratigraphy of this section of the SMZ resulted from imbrication of the underthrust sediment layer, then each thrust slice represents the subduction megathrust at some point in time (Meneghini & Moore, 2007). Smaller scale, more localised thrusting in metapsammitic unit (TS10) and metapelitic units (TS11 and TS14) further divides these units into fairly consistent 100-200 m thick packages with even smaller scale thrusting being present at 5-30 m intervals (not mapped). These mesoscale ductile shear zones occur sporadicaly within the various lithotectonic units and tend to occur along boundaries of lithological domains (e.g.calc-silcate layers and metamafic lenses in the metapelites). The position of these mesoscale shears may therefore be controlled

by the presence of high strain-rate gradients across lithological domains, as a result of significant differences in rheological behaviour (Fagereng & Sibson, 2010).

A recent study by Rowe *et al.* (2013) investigated the thickness of subduction plate boundary faults from the trench to depths of approximately 15 km and temperature of ∼300°C. They noted that, down to depths of ∼2 km, the décollement thickness increases by an order of magnitude (Figure 8.4) and develops from a single 1-10 m fault strand into multiple fault strands, metres to tens of metres thick, that anastomose through zones with a consistent thickness of 100-350 m. This abrupt thickening correlates with the range of depths and temperatures over which clay mineral dehydration and dissolution-precipitation creep start to occur in underthrust sediments (Moore & Saffer, 2001; Moore *et al.*, 2007; Fagereng, 2011a; Rowe *et al.*, 2013). These processes act to increase the cohesion and rigidity of underthrust sediment in the décollement via cementation and vein precipitation, and are also regarded as important physical changes responsible for the onset of seismogenesis along the subduction megathrust (e.g. Hyndman *et al.*, 1997; Moore & Saffer, 2001; Moore *et al.*, 2007; Hyndman, 2007). The spacing observed by Rowe *et al.* (2013) does not, however, agree with the observed spacing of the unit-scale mappable faults, as shear zones in the metapsammitic and metapelitic rock types were only 1-2 m thick, occurring within packages with thicknesses of 750 to 1000 m. Peak-metamorphic pressure for the rocks in the Gaub Canyon was calculated to be approximately 10 kbar (Cross, 2013), equivalent to a depth of ∼30 km. It is therefore likely that the anastomosing fault strands may have narrowed with time, along the prograde path, as strain was continually localised through dynamic recrystallisation and grain size reduction (e.g. Platt & Behr, 2011). This is also suggested by the presence of strongly recrystallised quartz fabrics in the shear zones internal to the litho-tectonic units of the SMZ (Chapter 6). The fact that major lithotectonic units have average thickness of between 750 and 1000 m may thus reflect that, at depths greater than 15 km and temperatures >300°C, the overall thickness of the décollement zone may gradually increase over the brittle-viscous transition (dashed line in Figure 8.4) as distributed viscous strain predominates. In Section 8.3 it was argued that the intra-unit shear zones with spacing of 100 to 200 m may have localised on precursor brittle structures formed earlier during shallow imbrication of the underthrust sediment pile. Since this spacing agrees closely with the spacing observed by Rowe *et al.* (2013), it would suggest that widening of the shear zone with increasing depths is accommodated by concentration of strain on fewer larger structures; seemingly occurring, as has been mentioned frequently in this study, at the boundaries between different lithological and rheological domains.

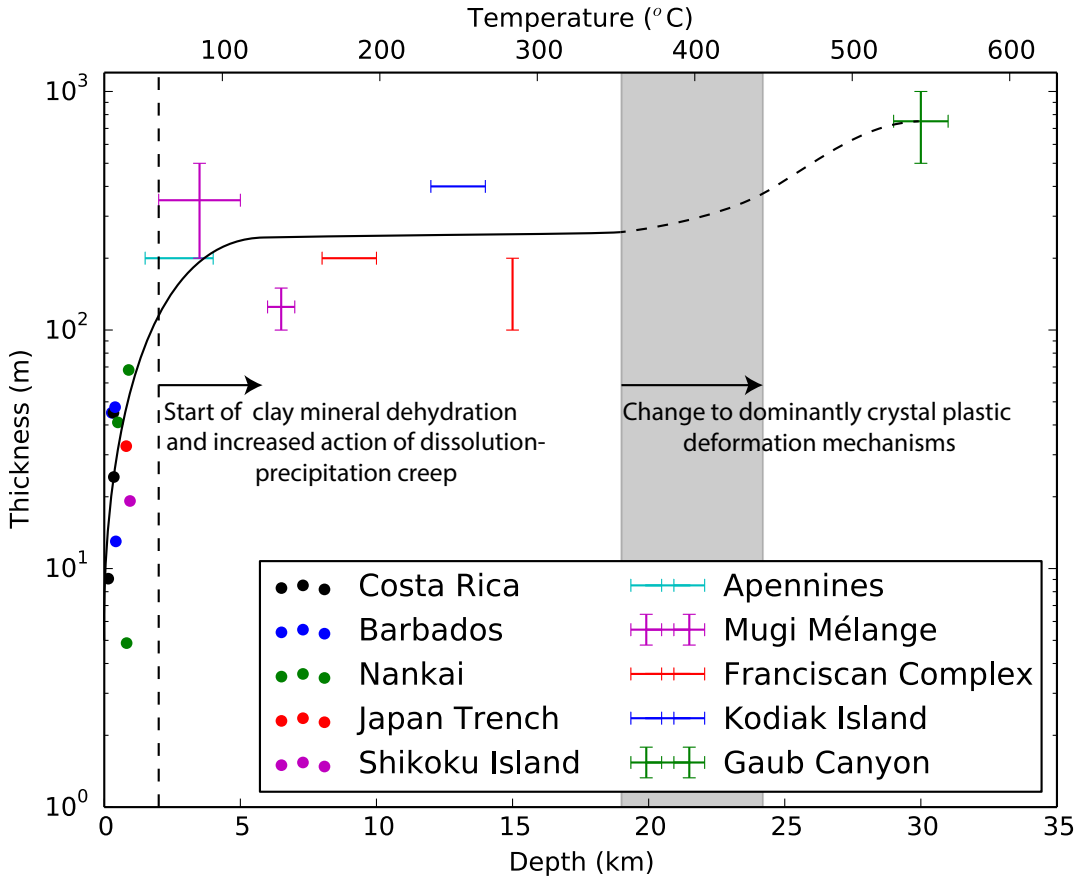

Figure 8.4: Plot of subduction zone megathrust thickness vs depth (adapted from Rowe *et al.*, 2013). Data from Rowe *et al.* (2013) are plotted along with data from the Gaub Canyon showing that the décollement zone may thicken gradually through the brittle-viscous transition.

8.4.3 Subduction Zone Seismicity

An ever-increasing amount of geodetic and seismic evidence (e.g. Obara, 2002; Obara *et al.*, 2004; Shelly *et al.*, 2007; Ito *et al.*, 2007; Beroza & Ide, 2011) has highlighted the close spatial and temporal relationships between the occurrence of non-volcanic tremor, and slow slip earthquakes around the down dip seismic-to-aseismic transition zone of the subduction plate boundary shear zone. However, the physical reasons for these observation are not well understood (Schwartz & Rokosky, 2007). Material heterogeneity and the resulting rheological constrast has been shown to exert crucial control on the distribution of strain at depths spanning (and below) the brittle-viscous transition along the subduction megathrust (Section 8.3). This manifests in a characteristic mixed-mode deformation regime. Considering this section of the SMZ as a crustal-scale hetereogeneous shear zone, it is clear that spatial distribution of deformation agrees with the model of Fagereng & Sibson (2010), whereby mixed-mode behaviour is characterised by brittle failure of competent rock while ductile flow dominates in

weaker rock types. In a cliff exposure in the centre of the map area (TS9; Figure 5.3A), fractured metamafic lenses are surrounded by a viscously-deformed phyllosilicate-rich metapelitic matrix (Figure 5.10C). Fagereng *et al.* (2014) suggest that such mixed-mode deformation may account for observations of slow-slip and tremor at these depths and temperatures, as, under these conditions, transiently elevated strain rates in the viscously deforming phyllosilicates may approach those observed during slow-slip events. They propose that elevated strain rates may be modulated by brittle failure of competent lenses and the resulting drop in fluid pressure and increase in effective shear stress. Similarly, elevated strain rates in the matrix increase the likelihood of brittle failure of competent lenses. This phenomenon is not limited to the outcrop studied by Fagereng *et al.* (2014) as similar mixed-mode deformation structures are found at various scales throughout the SMZ (e.g. Figure 6.2D & E). As Marone & Richardson (2010) point out, this mixed-mode behaviour highlights the complexity of the subduction megafault.

If the large-scale brittle thrusts observed in the quartizitic units (TS5 and TS12) are indeed earlier reactivated faults (Section 8.3), then they were seemingly active contemporaneously with the main phase of penetrative ductile deformation. This gives rise to some interesting implications for potentially deep seismogenesis in subduction zones. The presence of pseudotachylyte (frictional melt) is the only known conclusive evidence for seismic rupture on brittle faults (Sibson, 1975; Cowan, 1999; Ikesawa *et al.*, 2003) and, since no pseudotachylyte was found, the conclusion that these faults were seismically active cannot be drawn. However, brittle faulting is associated with seismic slip, and therefore this observation serves geological evidence that seismic rupture may occur at depths of >30 km and temperatures >500°C in subduction zones. Deep seismic rupture has been inferred previously from earthquake hypocentre calculations and modelled earthquake slip distributions (e.g. Byrne *et al.*, 1988; Tichelaar & Ruff, 1993; Hyndman & Wang, 1995), as well as from the presence of pseudotachylyte in eclogite (e.g. John & Schenk, 2006). These observation are nevertheless consistent with the observations of non-volcanic tremor and other low frequency earthquake signals with thrust fault focal mechanisms (e.g. Shelly *et al.*, 2007). The interpretation that reactivation of such structures can be modulated by varying strain rate in the surrounding viscously deforming material (Fagereng *et al.*, 2014) is also consistent with observations of coincident slow-slip and tremor/microseismicity at depths of 30-40 km along the Nankai, Cascadia and Hikurangi subduction zones (e.g. Ito *et al.*, 2007; Dragert & Wang, 2011; Wallace *et al.*, 2012).

Chapter 9

Conclusion

The SMZ is a tectono-stratigraphic terrane that runs in a NE-SW direction along the southern margin of the Neoproterozoic-Cambrian Damara Belt. The section of the SMZ exposed in the Gaub Canyon shows rather unique structural evidence for three phases of deformation associated with accretionary and collisional phases of the Wilson Cycle.

D_1 deformation is associated with underthrusting of hemipelagic, pelagic, and trench sediment beneath the Proterozoic accretionary prism, and is characterised by bedding parallel foliation S_1 and structures associated with layer-parallel extension.

D_2 deformation is attributed to imbrication of the underthrust sediment pile, possibly, but not necessarily, by underplating. Incorporation of underthrust sediment in thrust packages caused a re-orientation of S_{0+1}. Subsequent isoclinal recumbent folding during bulk non-coaxial shear of the thrust packages generated axial planar S_2 which was transposed with S_{0+1} through progressive deformation. S_{0+1+2} is therefore the major structural fabric. It has an average strike of 187° and dip 24° W, but shows systematic spatial variation ranging from an orientation of 113°/15° S in the southeastern regions to an orientation of 202°/33° NW in the northwestern parts of the map. The main tectonic transport direction is indicated by L_2, the down dip stretching lineation. It has an average trend of 278°, an average plunge of 27°, and shows the same systematic spatial variation as S_{0+1+2}.

D_3 structures appear to record the change from the accretionary to collision phases in the Damara Orogeny when exhumation-related deformation and retrogression of the Khomas accretionary prism were concentrated on discrete D_2 structures, as continental crust entered the subduction zone. As a result of this, the individual litho-tectonic units that make up the SMZ show very little evidence for the (seemingly short-lived) collision between the Kalahari and Congo Cratons, and deformation features related to the accretionary phases are remarkably well preserved between localised D_2 shear zones. A second, sub-horizontal stretching lineation is also found locally on S_{0+1+2}. It trends in two clusters in the NE and SW with

ranges of 168° to 252° and 002° to 51°, respectively, and plunges between 03° and 24°. Its apparent correlation with retrograde D_3 brittle reverse shears suggest that there was a component of lateral extrusion during collision and exhumation of the SMZ.

Strain was distributed heterogeneously throughout this section of the SMZ in both space and time. This strain localisation is largely a result of material anisotropy:

1. During D_1, strain localised preferentially in incompetent metapelitic rock types that formed finely-spaced continuous foliations and recorded greater finite-strain magnitudes than those of more competent quartzites and metapsammites.

2. During D_2, initial strain localisation appears to be geometrically controlled, and the juxtaposition of lithological domains and localisation of strain at their boundaries is a result of tectonic imbrication. During this time subsequent bulk shear strain is partitioned preferentially into incompetent lithological units which deform by ductile thrusting and folding, whereas competent lithological units deform largely by brittle fracture. Upon further burial and heating through the brittle-viscous transition, shear on the major unit-bounding D_2 structures and those within the litho-tectonic units occurred by climb-accommodated dislocation creep and dynamic recrystallisation. Continued localisation was probably assisted by the resulting grain size reduction. Dissolution-precipitation creep is also believed to be an important deformation mechanism operating under these conditions, as meso- and micro-structures preserved locally in the shear zones of the SMZ suggest that solution-transfer mechanisms acted alongside dislocation creep. This continued until amphibolite-facies conditions, after which deformation on the intra-unit shear zones ceased.

3. During D_3, shear strain was further localised on the pre-existing D_2 structures. The presence of a minor crenulation cleavage (S_3), sub-perpendicular to S_{0+1+2}, suggests that the lithotectonic units between these structures accommodate a relatively small fraction of this shortening. Early D_3 deformation on these unit-bounding structures occurred via dislocation- and solution-creep mechanisms. Frictional reactivation of these structures is believed to have resulted from these structures being optimally orientated for reshear in a compressive Andersonian stress field. This was also most likely aided by these structures having lower cohesive strength than the surrounding rock, resulting from the presence finer grain sizes and closely-spaced foliations formed during D_2 and early D_3 deformation. Microstructural observations and rheological modelling of these fault rocks indicate that, during the late stages of D_3 deformation, strain was increasingly concentrated into weaker fault zones. In particular, the calc-mylonitic GRL preserves a microstructure formed under very low grade conditions (<200°C), and is therefore a major long-lived structure responsible for the exhumation of the Southern Zone of the Damara Orogen.

The results of this study also have some wider implications concerning the nature of the subduction megathrust at depths and temperatures below the brittle-viscous transition. Dislocation creep has been observed as the dominant deformation mechanism operating at temperatures >500°C. Dissolution-precipitation creep is also believed to be an important deformation mechanism; however, its occurrence appears to be limited to the larger shear zones. A change from localised frictional, to distributed crystal-plastic deformation mechanisms, with increasing temperature (and depth), is proposed to result in widening of the subduction shear zone over the brittle-viscous transition. Both of these deformation mechanisms are also aseismic and these observations therefore generally agree with the observed decrease in seismic coupling below active seismogenic zones. Transient or episodic brittle failure, however, is inferred from the abundance of veins in metapelites, as well as the preservation of in-sequence brittle thrusts in more competent rock types. Thus, there is a predominance of mixed-mode, brittle-viscous deformation, with localised brittle deformation evident at micro- and meso-scales. This type of deformation regime has been suggested to account for the phenomenona of slow slip and episodic non-volcanic tremor observed at depths and temperatures spanning (and below) the seismic-to-aseismic transition in many contemporary subduction zones.

The rocks preserved in the Gaub Canyon offer a unique insight into the processes that occur at depth in modern subduction zones. It is particularly special because the scale of the exposed outcrop in the Gaub Canyon allows for examination of small-scale, high-resolution mechanistic behaviour within a broader context that is often only attainable through low-resolution geophysical studies. This thesis has attempted to draw parallels between the structures preserved in the rocks of the Gaub Canyon, and small- and large-scale processes known or inferred to be occurring at depths in modern accretionary margins. In doing so, it also attempts to account for some phenomena observed in active subduction zones. It has been demonstrated that meso-scale structures in the SMZ are adequately explained by the current theory on the mechanics of mixed-rheology heterogeneous shear zones. These concepts have been invoked to explain the larger-scale distribution of deformation within the SMZ; particularly the partitioning of brittle and viscous deformation between compentent and incompetent rock, respectively. The same physical factors that exert control over rock deformation processes on centimetre-to-metre scales may therefore be scaled up and used to model subduction zone deformation processes on hectometre-to-kilometre scales. However, a particular area of uncertainty still surrounds the processes of underplating at depth as the limited spatial dimensions of the Gaub Canyon do not allow for a full three-dimensional view of the larger-scale structure. Future research should therefore be directed at more widespread fieldwork throughout the SMZ and the rest of the Khomas accretionary prism. Such work should focus on tectonostratigraphic mapping, appropriate for such high-strain terranes. Determining the lateral extent of the larger-scale structures, and building of a three-dimensional geometrical model could possibly help a great deal to reduce the uncertainty surrounding the story of underplating at depth. Such a world-class exposure would have

much more to offer the field of subduction research.

References

Aki, K., 1967. Scaling law of seismic spectrum. *Journal of Geophysical Research*, **72**(4), 1217–1231.

Allmendinger, R. W., Cardozo, N. & Fisher, D. M., 2012. *Structural Geology Algorithms: Vectors and Tensors*, Cambridge University Press.

Alsop, G. & Holdsworth, R., 2004. Shear zone folds: records of flow perturbation or structural inheritance? *Geological Society, London, Special Publications*, **224**(1), 177–199.

Anderson, E. M., 1951. *The Dynamics of Faulting and Dyke Formations*, Oliver and Boyd.

Bachmann, R., Oncken, O., Glodny, J., Seifert, W., Georgieva, V. & Sudo, M., 2009. Exposed plate interface in the European Alps reveals fabric styles and gradients related to an ancient seismogenic coupling zone. *Journal of Geophysical Research: Solid Earth (1978–2012)*, **114**(B5).

Bailey, S. W., 1988. Chlorites; structures and crystal chemistry. *Reviews in Mineralogy and Geochemistry*, **19**(1), 347–403.

Behr, W. M. & Platt, J. P., 2013. Rheological evolution of a Mediterranean subduction complex. *Journal of Structural Geology*, **54**, 136–155.

Beroza, G. C. & Ide, S., 2011. Slow earthquakes and nonvolcanic tremor. *Annual review of Earth and planetary sciences*, **39**, 271–296.

Bestmann, M., Kunze, K. & Matthews, A., 2000. Evolution of a calcite marble shear zone complex on Thassos Island, Greece: microstructural and textural fabrics and their kinematic significance. *Journal of Structural Geology*, **22**(11), 1789–1807.

Blenkinsop, T., 2008. Relationships between faults, extension fractures and veins, and stress. *Journal of Structural Geology*, **30**(5), 622–632.

Blenkinsop, T. G., 2000. *Deformation microstructures and mechanisms in minerals and rocks*, Springer.

Blenkinsop, T. G. & Treloar, P. J., 1995. Geometry, classification and kinematics of S-C and S-C fabrics in the Mushandike area, Zimbabwe. *Journal of Structural Geology*, **17**(3), 397–408.

Bons, P. D., Elburg, M. A. & Gomez-Rivas, E., 2012. A review of the formation of tectonic veins and their microstructures. *Journal of Structural Geology*, **43**, 33–62.

Borradaile, G. J., 1981. Particulate flow of rock and the formation of cleavage. *Tectonophysics*, **72**(3), 305–321.

Bourdelle, F., Parra, T., Chopin, C. & Beyssac, O., 2013. A new chlorite geothermometer for diagenetic to low-grade metamorphic conditions. *Contributions to Mineralogy and Petrology*, **165**(4), 723–735.

Boyer, S. E. & Elliott, D., 1982. Thrust systems. *AAPG Bulletin*, **66**(9), 1196–1230.

Brace, W., 1960. An extension of the Griffith theory of fracture to rocks. *Journal of Geophysical Research*, **65**(10), 3477–3480.

Brown, M., 1993. P–T–t evolution of orogenic belts and the causes of regional metamorphism. *Journal of the Geological Society*, **150**(2), 227–241.

Brown, M., 2006. Duality of thermal regimes is the distinctive characteristic of plate tectonics since the Neoarchean. *Geology*, **34**(11), 961–964.

Burke, K. & Sengör, C., 1986. Tectonic escape in the evolution of the continental crust. *Reflection seismology: The continental crust*, pp. 41–53.

Burkhard, M., 1990. Ductile deformation mechanisms in micritic limestones naturally deformed at low temperatures (150–350 C). *Geological Society, London, Special Publications*, **54**(1), 241–257.

Burkhard, M., 1993. Calcite twins, their geometry, appearance and significance as stress-strain markers and indicators of tectonic regime: a review. *Journal of Structural Geology*, **15**(3), 351–368.

Butler, R., 1987. Thrust sequences. *Journal of the Geological Society*, **144**(4), 619–634.

Byerlee, J., 1978. Friction of rocks. *Pure and applied Geophysics*, **116**(4-5), 615–626.

Byrne, D. E., Davis, D. M. & Sykes, L. R., 1988. Loci and maximum size of thrust earthquakes and the mechanics of the shallow region of subduction zones. *Tectonics*, **7**(4), 833–857.

Byrne, T. & Fisher, D., 1990. Evidence for a weak and overpressured decollement beneath sediment-dominated accretionary prisms. *Journal of Geophysical Research: Solid Earth (1978–2012)*, **95**(B6), 9081–9097.

Cathelineau, M., 1988. Cation site occupancy in chlorites and illites as function of temperature. *Clay minerals*, **23**(4), 471–85.

Chester, F. M. & Chester, J. S., 1998. Ultracataclasite structure and friction processes of the Punchbowl fault, San Andreas system, California. *Tectonophysics*, **295**(1), 199–221.

Collettini, C., Niemeijer, A., Viti, C. & Marone, C., 2009. Fault zone fabric and fault weakness. *Nature*, **462**(7275), 907–910.

Coney, P. J., Jones, D. L. & Monger, J. W., 1980. Cordilleran suspect terranes. *Nature*, **288**(5789), 329–333.

Connolly, J., 1997. Devolatilization-generated fluid pressure and deformation-propagated fluid flow during prograde regional metamorphism. *Journal of Geophysical Research: Solid Earth (1978–2012)*, **102**(B8), 18149–18173.

Cosgrove, J., 1976. The formation of crenulation cleavage. *Journal of the Geological Society*, **132**(2), 155–178.

Cowan, D. S., 1985. Structural styles in Mesozoic and Cenozoic mélanges in the western Cordillera of North America. *Geological Society of America Bulletin*, **96**(4), 451–462.

Cowan, D. S., 1999. Do faults preserve a record of seismic slip? A field geologist's opinion. *Journal of Structural Geology*, **21**(8–9), 995.

Coward, M., 1983. The tectonic history of the Damara belt. *Evolution of the Damara Orogen. Special Publication of the Geological Society of South Africa*, **11**, 409–421.

Cross, C., (2013). *The metamorphic history of an ancient accretionary prism in the southern zone (sz) of the damara belt in namibia*, Master's thesis, University of Cape Town.

Dahlen, F., 1990. Critical taper model of fold-and-thrust belts and accretionary wedges. *Annual Review of Earth and Planetary Sciences*, **18**, 55.

Davis, D., Suppe, J. & Dahlen, F., 1983. Mechanics of fold-and-thrust belts and accretionary wedges. *Journal of Geophysical Research: Solid Earth (1978–2012)*, **88**(B2), 1153–1172.

Davis, N., Kronenberg, A. & Newman, J., 2008. Plasticity and diffusion creep of dolomite. *Tectonophysics*, **456**(3), 127–146.

de Caritat, P. & Walshe, J. L., 1993. Chlorite geothermometry: a review. *Clays and clay minerals*, **41**(2), 219–239.

Delle Piane, C., Burlini, L., Kunze, K., Brack, P. & Burg, J. P., 2008. Rheology of dolomite: large strain torsion experiments and natural examples. *Journal of Structural Geology*, **30**(6), 767–776.

Dragert, H. & Wang, K., 2011. Temporal evolution of an episodic tremor and slip event along the northern Cascadia margin. *Journal of Geophysical Research: Solid Earth (1978–2012)*, **116**(B12).

Druguet, E., Alsop, G. I. & Carreras, J., 2009. Coeval brittle and ductile structures associated with extreme deformation partitioning in a multilayer sequence. *Journal of Structural Geology*, **31**(5), 498–511.

Engelder, J. T., 1974. Cataclasis and the generation of fault gouge. *Geological Society of America Bulletin*, **85**(10), 1515–1522.

Evans, B. & Kohlstedt, D. L., 1995. Rheology of rocks. *Rock Physics & Phase Relations: A Handbook of Physical Constants*, pp. 148–165.

Fagereng, Å., 2011a. Geology of the seismogenic subduction thrust interface. *Geological Society, London, Special Publications*, **359**(1), 55–76.

Fagereng, Å., 2011b. Wedge geometry, mechanical strength, and interseismic coupling of the Hikurangi subduction thrust, New Zealand. *Tectonophysics*, **507**(1), 26–30.

Fagereng, Å., 2013. On stress and strain in a continuous-discontinuous shear zone undergoing simple shear and volume loss. *Journal of Structural Geology*, .

Fagereng, Å. & Sibson, R. H., 2010. Melange rheology and seismic style. *Geology*, **38**(8), 751–754.

Fagereng, Å. & Toy, V. G., 2011. Geology of the earthquake source: an introduction. *Geological Society, London, Special Publications*, **359**(1), 1–16.

Fagereng, Å., Hillary, G. W. & Diener, J. F., 2014. Brittle-viscous deformation, slow slip and tremor. *Geophysical Research Letters*, .

Fagereng, Å., Remitti, F. & Sibson, R. H., 2010. Shear veins observed within anisotropic fabric at high angles to the maximum compressive stress. *Nature Geoscience*, **3**(7), 482–485.

Festa, A., Dilek, Y., Pini, G., Codegone, G. & Ogata, K., 2012. Mechanisms and processes of stratal disruption and mixing in the development of mélanges and broken formations: Redefining and classifying mélanges. *Tectonophysics*, **568**, 7–24.

Fossen, H., 2010. *Structural geology*, Cambridge University Press.

Foster, D. A. & Goscombe, B. D., 2013. Continental Growth and Recycling in Convergent Orogens with Large Turbidite Fans on Oceanic Crust. *Geosciences*, **3**(3), 354–388.

Frimmel, H. E., 1997. Chlorite thermometry in the Witwatersrand Basin: constraints on the Paleoproterozoic geotherm in the Kaapvaal Craton, South Africa. *The Journal of Geology*, **105**(5), 601–616.

Fusseis, F., Handy, M. & Schrank, C., 2006. Networking of shear zones at the brittle-to-viscous transition (Cap de Creus, NE Spain). *Journal of Structural Geology*, **28**(7), 1228–1243.

Goodwin, L. B. & Tikoff, B., 2002. Competency contrast, kinematics, and the development of foliations and lineations in the crust. *Journal of Structural Geology*, **24**(6-7), 1065–1085.

Gratier, J.-P. & Gueydan, F., 2007. Effect of Fracturing and Fluid–Rock Interaction on Seismic Cycles. *Tectonic Faults: Agents of Change on a Dynamic Earth*, **95**, 319e356.

Gratier, J.-P., Guiguet, R., Renard, F., Jenatton, L. & Bernard, D., 2009. A pressure solution creep law for quartz from indentation experiments. *Journal of Geophysical Research: Solid Earth (1978–2012)*, **114**(B3).

Gray, D. R., Foster, D. A., Maas, R., Spaggiari, C. V., Gregory, R. T., Goscombe, B. & Hoffmann, K. C., 2007. Continental growth and recycling by accretion of deformed turbidite fans and remnant ocean basins: Examples from Neoproterozoic and Phanerozoic orogens. *Geological Society of America Memoirs*, **200**, 63–92.

Gudmundsson, A., 2011. *Rock fractures in geological processes*, Cambridge University Press.

Handy, M. R., 1990. The solid-state flow of polymineralic rocks. *Journal of Geophysical Research*, **95**(B6), 8647–8661.

Handy, M. R., 1994. Flow laws for rocks containing two non-linear viscous phases: a phenomenological approach. *Journal of Structural Geology*, **16**(3), 287–301.

Handy, M., Wissing, S. & Streit, L., 1999. Frictional–viscous flow in mylonite with varied bimineralic composition and its effect on lithospheric strength. *Tectonophysics*, **303**(1), 175–191.

Hartnady, C., Joubert, P. & Stowe, C., 1985. Proterozoic crustal evolution in southwestern Africa. *Episodes*, **8**(4), 236–244.

Heard, H., 1976. Comparison of the flow properties of rocks at crustal conditions. *Philosophical Transactions of the Royal Society of London. Series A, Mathematical and Physical Sciences*, **283**(1312), 173–186.

Hirth, G. & Tullis, J., 1992. Dislocation creep regimes in quartz aggregates. *Journal of Structural Geology*, **14**(2), 145–159.

Hirth, G., Teyssier, C. & Dunlap, J. W., 2001. An evaluation of quartzite flow laws based on comparisons between experimentally and naturally deformed rocks. *International Journal of Earth Sciences*, **90**(1), 77–87.

Hoffmann, K., 1983. Lithostratigraphy and facies of the swakop group of the southern damara belt, swa/namibia. *Special Publication-Geological Society of South Africa*, **11**, 43–63.

Holyoke, C. W. & Tullis, J., 2006a. Formation and maintenance of shear zones. *Geology*, **34**(2), 105–108.

Holyoke, C. W. & Tullis, J., 2006b. Mechanisms of weak phase interconnection and the effects of phase strength contrast on fabric development. *Journal of Structural Geology*, **28**(4), 621–640.

Hubbert, M. K. & Rubey, W. W., 1959. Role of fluid pressure in mechanics of overthrust faulting I. Mechanics of fluid-filled porous solids and its application to overthrust faulting. *Geological Society of America Bulletin*, **70**(2), 115–166.

Hyndman, R., 2007. The seismogenic zone of subduction thrust faults. *The seismogenic zone of subduction thrust faults*, pp. 15–40.

Hyndman, R., 2013. Downdip landward limit of Cascadia great earthquake rupture. *Journal of Geophysical Research: Solid Earth*, **118**(10), 5530–5549.

Hyndman, R. & Wang, K., 1993. Thermal constraints on the zone of major thrust earthquake failure: The Cascadia subduction zone. *Journal of Geophysical Research: Solid Earth (1978–2012)*, **98**(B2), 2039–2060.

Hyndman, R. & Wang, K., 1995. The rupture zone of Cascadia great earthquakes from current deformation and the thermal regime. *Journal of Geophysical Research: Solid Earth (1978–2012)*, **100**(B11), 22133–22154.

Hyndman, R., Wang, K. & Yamano, M., 1995. Thermal constraints on the seismogenic portion of the southwestern Japan subduction thrust. *Journal of Geophysical Research: Solid Earth (1978–2012)*, **100**(B8), 15373–15392.

Hyndman, R., Yamano, M. & Oleskevich, D., 1997. The seismogenic zone of subduction thrust faults. *Island Arc*, **6**(3), 244–260.

Ide, S., Baltay, A. & Beroza, G. C., 2011. Shallow dynamic overshoot and energetic deep rupture in the 2011 Mw 9.0 Tohoku-Oki earthquake. *Science*, **332**(6036), 1426–1429.

Ikesawa, E., Sakaguchi, A. & Kimura, G., 2003. Pseudotachylyte from an ancient accretionary complex: Evidence for melt generation during seismic slip along a master décollement? *Geology*, **31**(7), 637–640.

Ito, Y., Obara, K., Shiomi, K., Sekine, S. & Hirose, H., 2007. Slow earthquakes coincident with episodic tremors and slow slip events. *Science*, **315**(5811), 503–506.

Jacobs, J. & Thomas, R. J., 2004. Himalayan-type indenter-escape tectonics model for the southern part of the late Neoproterozoic–early Paleozoic East African–Antarctic orogen. *Geology*, **32**(8), 721–724.

Jaeger, J. & Cook, N., 1979. *Fundamentals of rock mechanics*, Chapman and Hall Ltd.

Jaoul, O., Tullis, J. & Kronenberg, A., 1984. The effect of varying water contents on the creep behavior of Heavitree quartzite. *Journal of Geophysical Research: Solid Earth (1978–2012)*, **89**(B6), 4298–4312.

John, T. & Schenk, V., 2006. Interrelations between intermediate-depth earthquakes and fluid flow within subducting oceanic plates: Constraints from eclogite facies pseudotachylytes. *Geology*, **34**(7), 557–560.

Jung, S. & Mezger, K., 2003. Petrology of basement-dominated terranes: I. Regional metamorphic T–t path from U–Pb monazite and Sm–Nd garnet geochronology (Central Damara orogen, Namibia). *Chemical Geology*, **198**(3), 223–247.

Kanamori, H. & Anderson, D. L., 1975. Theoretical basis of some empirical relations in seismology. *Bulletin of the Seismological Society of America*, **65**(5), 1073–1095.

Kasch, K., 1983a. Continental collision, suture progradation and thermal relaxation: a plate tectonic model for the Damara orogen in central Namibia. *Evolution of the Damara Orogen of South West Africa/Namibia: Geological Society of South Africa, Special Publication*, **11**, 423–429.

Kasch, K., 1983b. Regional PT variations in the Damara Orogen with particular reference to early high-pressure metamorphism along the southern margin. *Evolution of the Damara Orogen of South West Africa/Namibia*, **11**, 243–253.

Kimura, G. & Mukai, A., 1991. Underplated units in an accretionary complex: Melange of the Shimanto Belt of eastern Shikoku, southwest Japan. *Tectonics*, **10**(1), 31–50.

Kimura, G., Kitamura, Y., Hashimoto, Y., Yamaguchi, A., Shibata, T., Ujiie, K. & Okamoto, S., 2007. Transition of accretionary wedge structures around the up-dip limit of the seismogenic subduction zone. *Earth and Planetary Science Letters*, **255**(3), 471–484.

Kimura, G., Maruyama, S., Isozaki, Y. & Terabayashi, M., 1996. Well-preserved underplating structure of the jadeitized Franciscan complex, Pacheco Pass, California. *Geology*, **24**(1), 75–78.

Kimura, G., Yamaguchi, A., Hojo, M., Kitamura, Y., Kameda, J., Ujiie, K., Hamada, Y., Hamahashi, M. & Hina, S., 2012. Tectonic mélange as fault rock of subduction plate boundary. *Tectonophysics*, **568**, 25–38.

Kisters, A. F., Jordaan, L. S. & Neumaier, K., 2004. Thrust-related dome structures in the Karibib district and the origin of orthogonal fabric domains in the south Central Zone of the Pan-African Damara belt, Namibia. *Precambrian research*, **133**(3), 283–303.

Knipe, R., 1989. Deformation mechanismsrecognition from natural tectonites. *Journal of Structural Geology*, **11**(1), 127–146.

Kranidiotis, P. & MacLean, W., 1987. Systematics of chlorite alteration at the Phelps Dodge massive sulfide deposit, Matagami, Quebec. *Economic Geology*, **82**(7), 1898–1911.

Kronenberg, A. K., Kirby, S. H. & Pinkston, J., 1990. Basal slip and mechanical anisotropy of biotite. *Journal of Geophysical Research: Solid Earth (1978–2012)*, **95**(B12), 19257–19278.

Kukla, P. A. & Stanistreet, I. G., 1991. Record of the Damaran Khomas Hochland accretionary prism in central Namibia: Refutation of an" ensialic" origin of aLate Proterozoic orogenic belt. *Geology*, **19**(5), 473–476.

Kusky, T. M. & Bradley, D. C., 1999. Kinematic analysis of mélange fabrics: examples and applications from the McHugh Complex, Kenai Peninsula, Alaska. *Journal of Structural Geology*, **21**(12), 1773–1796.

Lay, T., Kanamori, H., Ammon, C. J., Nettles, M., Ward, S. N., Aster, R. C., Beck, S. L., Bilek, S. L., Brudzinski, M. R., Butler, R.et al., 2005. The great Sumatra-Andaman earthquake of 26 december 2004. *Science*, **308**(5725), 1127–1133.

Lister, G. & Snoke, A., 1984. SC mylonites. *Journal of Structural Geology*, **6**(6), 617–638.

Lockner, D. A., 1995. Rock failure. *AGU Reference Shelf*, **3**, 127–147.

Mancktelow, N. S. & Pennacchioni, G., 2005. The control of precursor brittle fracture and fluid–rock interaction on the development of single and paired ductile shear zones. *Journal of Structural Geology*, **27**(4), 645–661.

Marone, C. & Richardson, E., 2010. Learning to read fault-slip behavior from fault-zone structure. *Geology*, **38**(8), 767–768.

Marrett, R. & Peacock, D. C., 1999. Strain and stress. *Journal of structural geology*, **21**(8), 1057–1063.

Martin, H. & Porada, H., 1977. The intracratonic branch of the Damara Orogen in South West Africa I. Discussion of geodynamic models. *Precambrian Research*, **5**(4), 311–338.

Masberg, H., Hoffer, E. & Hoernes, S., 1992. Microfabrics indicating granulite-facies metamorphism in the low-pressure central Damara Orogen, Namibia. *Precambrian research*, **55**(1), 243–257.

McClay, K., 1977. Pressure solution and Coble creep in rocks and minerals: a review. *Journal of the Geological Society*, **134**(1), 57–70.

Meneghini, F. & Moore, J. C., 2007. Deformation and hydrofracture in a subduction thrust at seismogenic depths: The Rodeo Cove thrust zone, Marin Headlands, California. *Geological Society of America Bulletin*, **119**(1-2), 174–183.

Meneghini, F., Kisters, A., Buick, I. & Fagereng, Å., 2014. Fingerprints of late Neoproterozoic ridge subduction in the Pan–African Damara belt, Namibia. *Geology*, pp. G35932–1.

Meneghini, F., Marroni, M., Moore, J., Pandolfi, L. & Rowe, C., 2009. The processes of underthrusting and underplating in the geological record: structural diversity between the Franciscan Complex(California), the Kodiak Complex (Alaska) and the Internal Lingurian Units (Italy). *Geological Journal*, **44**, 126–152.

Miller, R., 1983. The Pan-African Damara Orogen of South West Africa/Namibia. *Evolution of the Damara orogen of South West Africa/Namibia: Geological Society of South Africa Special Publication*, **11**, 431–515.

Miller, R., 2008. Neoproterozoic and early Palaeozoic rocks of the Damara Orogen. *The Geology of Namibia. Geological Survey of Namibia, Windhoek*, pp. 13–11.

Miyashiro, A., 1973. Paired and unpaired metamorphic belts. *Tectonophysics*, **17**(3), 241–254.

Moore, G. F., Taira, A., Klaus, A., Becker, L., Boeckel, B., Cragg, B. A., Dean, A., Fergusson, C. L., Henry, P. & Hirano, S., 2001. New insights into deformation and fluid flow processes in the Nankai Trough accretionary prism: Results of Ocean Drilling Program Leg 190. *Geochemistry, Geophysics, Geosystems*, **2**(10).

Moore, J. C. & Byrne, T., 1987. Thickening of fault zones: A mechanism of melange formation in accreting sediments. *Geology*, **15**(11), 1040–1043.

Moore, J. C. & Saffer, D., 2001. Updip limit of the seismogenic zone beneath the accretionary prism of southwest Japan: An effect of diagenetic to low-grade metamorphic processes and increasing effective stress. *Geology*, **29**(2), 183–186.

Moore, J. C., Rowe, C. D. & Meneghini, F., 2007. How Accretionary Prisms Elucidate Seismogenesis in Subduction Zones. *The Seismogenic Zone of Subduction Thrust Faults*, 288.

Needham, D., 1995. Mechanisms of mélange formation: Examples from SW Japan and southern Scotland. *Journal of Structural Geology*, **17**(7), 971–985.

Nicolas, A. & Poirier, J.-P., 1976. *Crystalline plasticity and solid state flow in metamorphic rocks*, Wiley London.

Niemeijer, A. & Spiers, C., 2005. Influence of phyllosilicates on fault strength in the brittle-ductile transition: insights from rock analogue experiments. *Geological Society, London, Special Publications*, **245**, 303.

Nye, J. F., 1953. The flow law of ice from measurements in glacier tunnels, laboratory experiments and the Jungfraufirn borehole experiment. *Proceedings of the Royal Society of London. Series A. Mathematical and Physical Sciences*, **219**(1139), 477–489.

Obara, K., 2002. Nonvolcanic deep tremor associated with subduction in southwest Japan. *Science*, **296**(5573), 1679–1681.

Obara, K., Hirose, H., Yamamizu, F. & Kasahara, K., 2004. Episodic slow slip events accompanied by non-volcanic tremors in southwest Japan subduction zone. *Geophysical Research Letters*, **31**(23).

Oleskevich, D., Hyndman, R. & Wang, K., 1999. The updip and downdip limits to great subduction earthquakes: Thermal and structural models of Cascadia, south Alaska, SW Japan, and Chile. *Journal of Geophysical Research: Solid Earth (1978–2012)*, **104**(B7), 14965–14991.

Passchier, C. W. & Trouw, R. A., 2005. *Microtectonics*, Springer.

Peacock, S. M., 1996. Thermal and petrologic structure of subduction zones. *Subduction top to bottom*, pp. 119–133.

Petit, J., 1987. Criteria for the sense of movement on fault surfaces in brittle rocks. *Journal of Structural Geology*, **9**(5), 597–608.

Pfiffner, O. & Ramsay, J., 1982. Constraints on geological strain rates: arguments from finite strain states of naturally deformed rocks. *Journal of Geophysical Research: Solid Earth (1978–2012)*, **87**(B1), 311–321.

Pitzer, K. S. & Sterner, S. M., 1994. Equations of state valid continuously from zero to extreme pressures for H2O and CO2. *The Journal of chemical physics*, **101**(4), 3111–3116.

Platt, J. & Behr, W., 2011. Grainsize evolution in ductile shear zones: Implications for strain localization and the strength of the lithosphere. *Journal of Structural Geology*, **33**(4), 537–550.

Platt, J., Leggett, J., Young, J., Raza, H. & Alam, S., 1985. Large-scale sediment underplating in the Makran accretionary prism, southwest Pakistan. *Geology*, **13**(7), 507–511.

Ponce, C., Druguet, E. & Carreras, J., 2013. Development of shear zone-related lozenges in foliated rocks. *Journal of Structural Geology*, **50**, 176–186.

Potel, S., Mählmann, R. F., Stern, W., Mullis, J. & Frey, M., 2006. Very low-grade metamorphic evolution of pelitic rocks under high-pressure/low-temperature conditions, NW New Caledonia (SW Pacific). *Journal of Petrology*, **47**(5), 991–1015.

Raimbourg, H., Tadahiro, S., Asuka, Y., Haruka, Y. & Kimura, G., 2009. Horizontal shortening versus vertical loading in accretionary prisms. *Geochemistry Geophysics Geosystems*, **10**(4), Q04007.

Ramsay, J., 1980. Shear zone geometry: a review. *Journal of Structural Geology*, **2**(1), 83–99.

Ramsay, J. & Graham, R., 1970. Strain variation in shear belts. *Canadian Journal of Earth Sciences*, **7**(3), 786–813.

Ramsey, J. M. & Chester, F. M., 2004. Hybrid fracture and the transition from extension fracture to shear fracture. *Nature*, **428**(6978), 63–66.

Rice, J. R. & Cleary, M. P., 1976. Some basic stress diffusion solutions for fluid-saturated elastic porous media with compressible constituents. *Reviews of Geophysics*, **14**(2), 227–241.

Rowe, C. D., Moore, J. C., Remitti, F.et al., 2013. The thickness of subduction plate boundary faults from the seafloor into the seismogenic zone. *Geology*, **41**(9), 991–994.

Rutter, E., 1983. Pressure solution in nature, theory and experiment. *Journal of the Geological Society*, **140**(5), 725–740.

Saffer, D. M. & Tobin, H. J., 2011. Hydrogeology and mechanics of subduction zone forearcs: Fluid flow and pore pressure. *Annual Review of Earth and Planetary Sciences*, **39**, 157–186.

Sample, J. & Fisher, D., 1986. Duplex accretion and underplating in an ancient accretionary complex, Kodiak Islands, Alaska. *Geology*, **14**(2), 160–163.

Schermer, E. R., Howell, D. G. & Jones, D. L., 1984. The origin of allochthonous terranes: perspectives on the growth and shaping of continents. *Annual Review of Earth and Planetary Sciences*, **12**, 107.

Scholz, C., 1988. The brittle-plastic transition and the depth of seismic faulting. *Geologische Rundschau*, **77**(1), 319–328.

Scholz, C. H., 1989. Mechanics of faulting. *Annual Review of Earth and Planetary Sciences*, **17**, 309–334.

Scholz, C. H., 1998. Earthquakes and friction laws. *Nature*, **391**(6662), 37–42.

Scholz, C. H., 2002. *The mechanics of earthquakes and faulting*, Cambridge university press.

Schwartz, S. Y. & Rokosky, J. M., 2007. Slow slip events and seismic tremor at circum-Pacific subduction zones. *Reviews of Geophysics*, **45**(3).

Shelly, D. R., Beroza, G. C. & Ide, S., 2007. Non-volcanic tremor and low-frequency earthquake swarms. *Nature*, **446**(7133), 305–307.

Shimizu, I., 1995. Kinetics of pressure solution creep in quartz: theoretical considerations. *Tectonophysics*, **245**(3), 121–134.

Shipley, T. H., McIntosh, K. D., Silver, E. A. & Stoffa, P. L., 1992. Three-dimensional seismic imaging of the Costa Rica accretionary prism: Structural diversity in a small volume of the lower slope. *Journal of Geophysical Research: Solid Earth (1978–2012)*, **97**(B4), 4439–4459.

Sibson, R., 1977. Fault rocks and fault mechanisms. *Journal of the Geological Society*, **133**(3), 191–213.

Sibson, R., 2012. Reverse fault rupturing: competition between non-optimal and optimal fault orientations. *Geological Society, London, Special Publications*, **367**(1), 39–50.

Sibson, R. H., 1974. Frictional constraints on thrust, wrench and normal faults. , .

Sibson, R. H., 1975. Generation of pseudotachylyte by ancient seismic faulting. *Geophysical Journal International*, **43**(3), 775–794.

Sibson, R. H., 1982. Fault zone models, heat flow, and the depth distribution of earthquakes in the continental crust of the United States. *Bulletin of the Seismological Society of America*, **72**(1), 151–163.

Sibson, R. H., 1985. A note on fault reactivation. *Journal of Structural Geology*, **7**(6), 751–754.

Sibson, R. H., 1986. Earthquakes and rock deformation in crustal fault zones. *Annual Review of Earth and Planetary Sciences*, **14**, 149.

Sibson, R. H., 1998. Brittle failure mode plots for compressional and extensional tectonic regimes. *Journal of Structural Geology*, **20**(5), 655–660.

Sibson, R. H., 2003. Brittle-failure controls on maximum sustainable overpressure in different tectonic regimes. *AAPG bulletin*, **87**(6), 901–908.

Sibson, R. H., 2009. Rupturing in overpressured crust during compressional inversionthe case from NE Honshu, Japan. *Tectonophysics*, **473**(3), 404–416.

Stewart, M., Holdsworth, R. & Strachan, R., 2000. Deformation processes and weakening mechanisms within the frictional–viscous transition zone of major crustal-scale faults: insights from the Great Glen Fault Zone, Scotland. *Journal of Structural Geology*, **22**(5), 543–560.

Stipp, M. & Kunze, K., 2008. Dynamic recrystallization near the brittle-plastic transition in naturally and experimentally deformed quartz aggregates. *Tectonophysics*, **448**(1), 77–97.

Stipp, M. & Tullis, J., 2003. The recrystallized grain size piezometer for quartz. *Geophysical Research Letters*, **30**(21).

Stipp, M., StuÈnitz, H., Heilbronner, R. & Schmid, S. M., 2002. The eastern Tonale fault zone: a natural laboratoryfor crystal plastic deformation of quartz over a temperature range from 250 to 700 C. *Journal of Structural Geology*, **24**(12), 1861–1884.

Stipp, M., Tullis, J., Scherwath, M. & Behrmann, J. H., 2010. A new perspective on paleopiezometry: Dynamically recrystallized grain size distributions indicate mechanism changes. *Geology*, **38**(8), 759–762.

Strasser, M., Moore, G. F., Kimura, G., Kitamura, Y., Kopf, A. J., Lallemant, S., Park, J.-O., Screaton, E. J., Su, X., Underwood, M. B.et al., 2009. Origin and evolution of a splay fault in the Nankai accretionary wedge. *Nature Geoscience*, **2**(9), 648–652.

Suppe, J., 1983. Geometry and kinematics of fault-bend folding. *American Journal of science*, **283**(7), 684–721.

Tichelaar, B. W. & Ruff, L. J., 1993. Depth of seismic coupling along subduction zones. *Journal of Geophysical Research*, **98**(B2), 2017–2037.

Tullis, J. & Wenk, H.-R., 1994. Effect of muscovite on the strength and lattice preferred orientations of experimentally deformed quartz aggregates. *Materials Science and Engineering: A*, **175**(1), 209–220.

Twiss, R. & Moores, E., 1992. *Structural Geology*, Freeman, New York.

Ujiie, K., 2002. Evolution and kinematics of an ancient décollement zone, mélange in the Shimanto accretionary complex of Okinawa Island, Ryukyu Arc. *Journal of Structural Geology*, **24**(5), 937–952.

Underwood, M., 2007. Sediment inputs to subduction zones: Why lithostratigraphy and clay mineralogy matter. *The seismogenic zone of subduction thrust faults*, pp. 42–85.

Urai, J., Means, W. & Lister, G., 1986. Dynamic recrystallization of minerals. *Mineral and Rock Deformation: Laboratory Studies: The Paterson Volume*, pp. 161–199.

Van der Pluijm, B. A. & Marshak, S., 2004. *Earth structure: an introduction to structural geology and tectonics*, New York: WW Norton; 2nd ed.

Vannucchi, P. & Bettelli, G., 2002. Mechanisms of subduction accretion as implied from the broken formations in the Apennines, Italy. *Geology*, **30**(9), 835–838.

Walker, A., Rutter, E. & Brodie, K., 1990. Experimental study of grain-size sensitive flow of synthetic, hot-pressed calcite rocks. *Geological Society, London, Special Publications*, **54**(1), 259–284.

Wallace, L. M., Beavan, J., Bannister, S. & Williams, C., 2012. Simultaneous long-term and short-term slow slip events at the Hikurangi subduction margin, New Zealand: Implications for processes that control slow slip event occurrence, duration, and migration. *Journal of Geophysical Research: Solid Earth (1978–2012)*, **117**(B11).

Walshe, J. L., 1986. A six-component chlorite solid solution model and the conditions of chlorite formation in hydrothermal and geothermal systems. *Economic Geology*, **81**(3), 681–703.

Wang, K. & Hu, Y., 2006. Accretionary prisms in subduction earthquake cycles: The theory of dynamic Coulomb wedge. *Journal of Geophysical Research: Solid Earth (1978–2012)*, **111**(B6).

Ward, R., Stevens, G. & Kisters, A., 2008. Fluid and deformation induced partial melting and melt volumes in low-temperature granulite-facies metasediments, Damara Belt, Namibia. *Lithos*, **105**(3), 253–271.

Wernicke, B., 1995. Low-angle normal faults and seismicity: A review. *Journal of Geophysical Research: Solid Earth (1978–2012)*, **100**(B10), 20159–20174.

Westbrook, G., Ladd, J., Buhl, P., Bangs, N. & Tiley, G., 1988. Cross section of an accretionary wedge: Barbados Ridge complex. *Geology*, **16**(7), 631–635.

White, S., Burrows, S., Carreras, J., Shaw, N. & Humphreys, F., 1980. On mylonites in ductile shear zones. *Journal of Structural Geology*, **2**(1), 175–187.

Xie, X., Byerly, G. R. & Ferrell Jr, R. E., 1997. IIb trioctahedral chlorite from the Barberton greenstone belt: crystal structure and rock composition constraints with implications to geothermometry. *Contributions to Mineralogy and Petrology*, **126**(3), 275–291.

Zang, W. & Fyfe, W., 1995. Chloritization of the hydrothermally altered bedrock at the Igarapé Bahia gold deposit, Carajás, Brazil. *Mineralium Deposita*, **30**(1), 30–38.

Zoback, M. D., Zoback, M. L., Mount, V. S., Suppe, J., Eaton, J. P., Healy, J. H., Oppenheimer, D., Reasenberg, P., Jones, L., Raleigh, C. B.et al., 1987. New evidence on the state of stress of the San Andreas fault system. *Science*, **238**(4830), 1105–1111.

Appendix A

Geological Map of the Gaub Canyon

Geological map of the Gaub Canyon between the Rostock Mountain inlier and the Gomab River Line

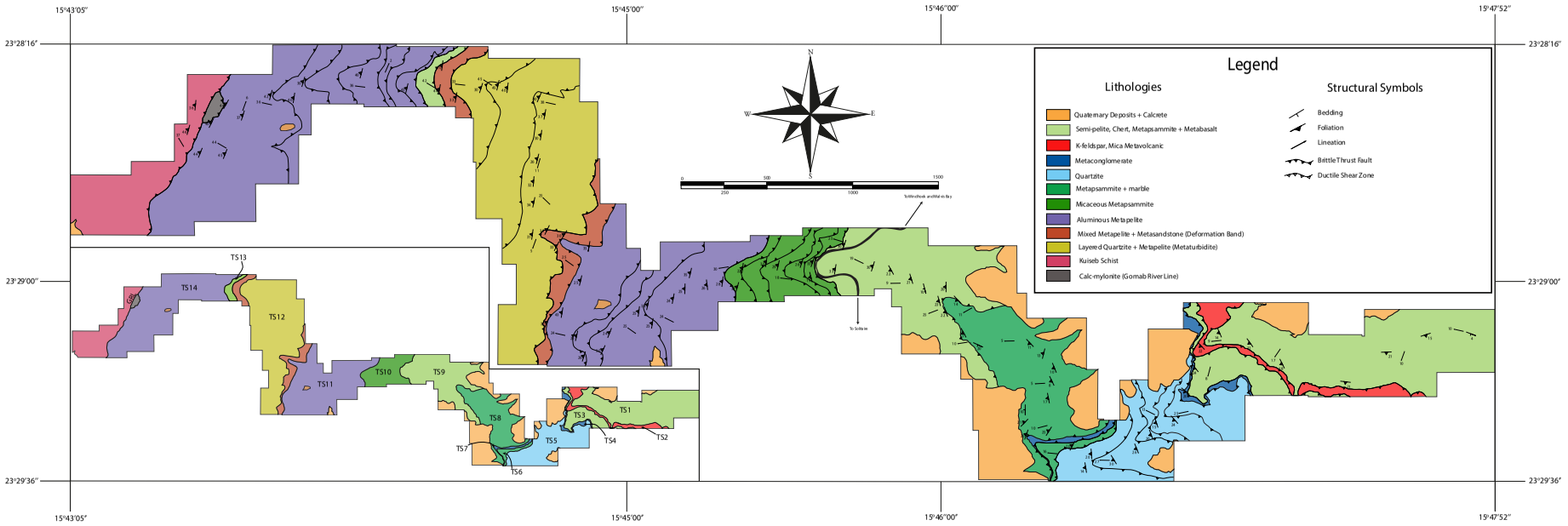

Figure A.1: Geological Map of the Gaub Canyon

Appendix B

Mineral Chemistry

B.1 Microprobe Data

Mineral chemistry analyses were discussed in Chapter 7 where average compositions and standard deviations are reported. The following tables contain the individual measurements. The data is presented for each mineral and sample, as stated in the captions.

Table B.1: Chemical compositions of chlorites in sample GB14. All Fe is taken as Fe^{2+}. Total interchange charge (t.i.c) = Na+K+2Ca. Temperature calculated using the chlorite thermometer of Kranidiotis and MacLean (1987).

Chlorite													
Sample	Gb14a	Gb14b	Gb14c	Gb14d	Gb14e	Gb14f	Gb14g	Gb14h	Gb14i	Gb14j	Gb14k	Gb14l	Gb14m
Al_2O_3	20.90	20.42	21.94	22.17	21.80	14.94	21.85	21.99	21.98	20.64	21.03	19.92	22.16
SiO_2	27.72	27.73	26.95	27.00	27.08	33.56	26.99	27.12	26.98	28.11	27.93	29.98	26.62
TiO_2	0.12	0.10	0.12	0.10	0.16	1.52	0.04	0.05	0.07	0.12	0.06	0.07	0.04
K_2O	0.02	0.02	0.03	0.02	0.13	4.43	0.02	0.00	0.03	0.00	0.02	0.07	0.02
MgO	22.35	21.76	21.48	21.42	21.66	17.68	21.53	20.94	20.98	22.72	22.06	22.93	20.86
Cr_2O_3	0.01	0.03	0.03	0.10	0.10	0.07	0.00	0.01	0.03	0.02	0.06	0.00	0.00
CaO	0.08	0.12	0.06	0.05	0.06	0.25	0.01	0.03	0.03	0.00	0.01	0.18	0.00
Na_2O	0.00	0.04	0.05	0.00	0.06	0.07	0.00	0.01	0.01	0.00	0.02	0.06	0.03
MnO	0.15	0.27	0.22	0.24	0.22	0.23	0.27	0.22	0.19	0.25	0.21	0.23	0.24
FeO	16.65	16.51	17.61	17.30	14.93	15.62	17.53	18.36	17.92	16.01	16.49	13.24	18.35
Total	88.00	87.00	88.48	88.39	86.19	88.37	88.23	88.73	88.22	87.87	87.88	86.68	88.32
Number of cations (p.f.u) on the basis of 28 oxygens													
Si	5.54	5.61	5.39	5.40	5.49	6.78	5.41	5.42	5.42	5.61	5.58	5.95	5.36
$Al^{(IV)}$	2.46	2.39	2.61	2.60	2.51	1.22	2.59	2.58	2.58	2.39	2.42	2.05	2.64
$Al^{(VI)}$	2.47	2.48	2.56	2.62	2.69	2.33	2.57	2.61	2.62	2.46	2.54	2.61	2.61
Ti	0.02	0.02	0.02	0.01	0.02	0.23	0.01	0.01	0.01	0.02	0.01	0.01	0.01
K	0.00	0.00	0.01	0.00	0.03	1.14	0.00	0.00	0.01	0.00	0.01	0.02	0.00
Mg	6.66	6.56	6.41	6.38	6.54	5.32	6.43	6.24	6.28	6.76	6.57	6.79	6.26
Cr	0.00	0.00	0.00	0.02	0.02	0.01	0.00	0.00	0.00	0.00	0.01	0.00	0.00
Ca	0.02	0.03	0.01	0.01	0.01	0.05	0.00	0.01	0.01	0.00	0.00	0.04	0.00
Na	0.00	0.02	0.02	0.00	0.02	0.03	0.00	0.01	0.01	0.00	0.01	0.02	0.01
Mn	0.03	0.05	0.04	0.04	0.04	0.04	0.05	0.04	0.03	0.04	0.04	0.04	0.04
Fe^{2+}	2.78	2.79	2.95	2.89	2.53	2.64	2.94	3.07	3.01	2.67	2.76	2.20	3.09
t.i.c	0.04	0.07	0.05	0.03	0.08	1.28	0.01	0.02	0.03	0.00	0.02	0.12	0.02
$X_{Fe^{2+}}$	0.29	0.30	0.31	0.31	0.28	0.33	0.31	0.33	0.32	0.28	0.30	0.24	0.33
(K&M) T(°C)	300	293	318	317	305	172	316	316	316	293	296	253	323
(Z&F) T(°C)	283	275	297	297	290	148	295	292	293	277	278	244	299
(C) T(°C)	334	323	358	357	343	135	355	353	354	323	327	268	364

Table B.2: Chemical compositions of biotite from sample GB14

Biotite											
Gb14											
SiO_2	38.43	36.98	38.00	37.96	37.97	38.50	38.12	36.23	38.18	37.91	38.13
Al_2O_3	16.03	15.55	16.19	15.46	15.53	15.92	15.83	15.58	16.40	16.15	15.89
TiO_2	1.24	1.32	1.29	1.28	1.36	1.37	1.28	1.23	1.31	1.31	1.17
K_2O	7.68	8.49	8.98	8.39	7.44	8.98	8.92	7.58	8.52	8.67	8.88
Na_2O	0.04	0.09	0.16	0.03	0.09	0.16	0.09	0.11	0.16	0.16	0.11
MnO	0.10	0.16	0.15	0.15	0.10	0.14	0.13	0.13	0.13	0.15	0.13
CaO	0.10	0.11	0.01	0.06	0.12	0.00	0.11	0.22	0.07	0.08	0.14
MgO	15.90	15.05	15.42	15.72	15.95	15.26	15.56	15.41	15.83	15.54	16.73
Cr_2O_3	0.10	0.03	0.08	0.03	0.08	0.11	0.10	0.09	0.07	0.09	0.03
FeO	13.95	14.36	14.64	13.46	13.82	14.19	14.54	13.61	13.51	13.77	13.64
Total	93.58	92.14	94.92	92.55	92.47	94.63	94.69	90.19	94.18	93.82	94.84
Number of cations (p.f.u) on the basis of 22 oxygens											
Si	5.72	5.66	5.65	5.74	5.72	5.72	5.68	5.63	5.67	5.67	5.65
$Al^{(IV)}$	2.28	2.34	2.35	2.26	2.28	2.28	2.32	2.37	2.33	2.33	2.35
$Al^{(VI)}$	0.54	0.47	0.49	0.50	0.48	0.51	0.46	0.48	0.54	0.52	0.42
Ti	0.14	0.15	0.14	0.15	0.15	0.15	0.14	0.14	0.15	0.15	0.13
K	1.46	1.66	1.70	1.62	1.43	1.70	1.70	1.50	1.61	1.65	1.68
Na	0.01	0.03	0.05	0.01	0.03	0.05	0.03	0.03	0.05	0.05	0.03
Mn	0.01	0.02	0.02	0.02	0.01	0.02	0.02	0.02	0.02	0.02	0.02
Ca	0.02	0.02	0.00	0.01	0.02	0.00	0.02	0.04	0.01	0.01	0.02
Mg	3.53	3.44	3.42	3.54	3.58	3.38	3.46	3.57	3.51	3.47	3.69
Cr	0.01	0.00	0.01	0.00	0.01	0.01	0.01	0.01	0.01	0.01	0.00
Fe^{2+}	1.74	1.84	1.82	1.70	1.74	1.76	1.81	1.77	1.68	1.72	1.69
$X_{Fe^{2+}}$	0.33	0.35	0.35	0.32	0.33	0.34	0.34	0.33	0.32	0.33	0.31
VI	5.97	5.92	5.90	5.91	5.99	5.85	5.90	5.99	5.90	5.89	5.96
A	1.49	1.70	1.75	1.64	1.48	1.75	1.74	1.57	1.67	1.71	1.73

Table B.3: Chemical compositions of biotite from sample GB17

Biotite											
Gb17											
SiO_2	39.86	40.32	40.14	40.29	40.61	39.72	40.31	39.85	40.48	40.59	40.02
Al_2O_3	17.55	17.14	17.26	16.55	16.81	16.99	16.86	17.26	16.79	16.68	17.25
TiO_2	0.86	0.74	0.79	0.77	0.76	0.85	0.79	0.85	0.84	0.87	0.80
K_2O	9.61	9.32	9.48	9.27	9.20	9.74	9.27	9.75	9.31	9.62	9.83
Na_2O	0.16	0.17	0.16	0.17	0.12	0.09	0.18	0.14	0.20	0.10	0.15
MnO	0.15	0.15	0.18	0.19	0.15	0.11	0.16	0.09	0.13	0.10	0.08
CaO	0.00	0.00	0.00	0.00	0.00	0.00	0.00	0.00	0.00	0.07	0.00
MgO	20.88	20.93	20.92	21.40	21.19	20.47	20.61	20.75	20.73	20.54	20.38
Cr_2O_3	0.03	0.00	0.01	0.01	0.06	0.03	0.01	0.00	0.00	0.00	0.00
FeO	5.95	5.89	5.83	5.91	5.74	5.91	5.94	6.04	5.98	5.94	5.89
Total	95.04	94.66	94.78	94.55	94.64	93.91	94.13	94.73	94.46	94.51	94.41
Number of cations (p.f.u) on the basis of 22 oxygens											
Si	5.67	5.74	5.72	5.75	5.78	5.72	5.78	5.70	5.78	5.80	5.73
$Al^{(IV)}$)	2.33	2.26	2.28	2.25	2.22	2.28	2.22	2.30	2.22	2.20	2.27
$Al^{(VI)}$	0.62	0.62	0.62	0.54	0.60	0.61	0.62	0.60	0.61	0.61	0.65
Ti	0.09	0.08	0.08	0.08	0.08	0.09	0.08	0.09	0.09	0.09	0.09
K	1.74	1.69	1.72	1.69	1.67	1.79	1.69	1.78	1.70	1.75	1.80
Na	0.04	0.05	0.05	0.05	0.03	0.02	0.05	0.04	0.05	0.03	0.04
Mn	0.02	0.02	0.02	0.02	0.02	0.01	0.02	0.01	0.02	0.01	0.01
Ca	0.00	0.00	0.00	0.00	0.00	0.00	0.00	0.00	0.00	0.01	0.00
Mg	4.43	4.45	4.44	4.56	4.49	4.40	4.40	4.42	4.41	4.38	4.35
Cr	0.00	0.00	0.00	0.00	0.01	0.00	0.00	0.00	0.00	0.00	0.00
Fe^{2+}	0.71	0.70	0.69	0.71	0.68	0.71	0.71	0.72	0.71	0.71	0.71
$X_{Fe^{2+}}$	0.14	0.14	0.14	0.13	0.13	0.14	0.14	0.14	0.14	0.14	0.14
VI	5.87	5.87	5.86	5.90	5.88	5.83	5.84	5.85	5.84	5.80	5.80
A	1.79	1.74	1.77	1.73	1.70	1.82	1.75	1.82	1.75	1.79	1.84

Table B.4: Chemical compositions of biotite from sample GB18

Biotite							
Gb18							
SiO_2	39.46	40.20	39.51	39.40	39.72	39.73	39.59
Al_2O_3	16.02	15.51	15.40	15.39	15.28	15.30	15.57
TiO_2	1.57	1.43	1.20	1.38	1.42	1.48	1.32
K_2O	10.33	9.50	8.87	9.15	8.91	8.97	9.60
Na_2O	0.05	0.13	0.09	0.27	0.09	0.05	0.08
MnO	0.27	0.18	0.23	0.25	0.26	0.21	0.26
CaO	0.00	0.20	0.25	1.57	0.22	0.07	0.00
MgO	20.06	20.37	20.95	19.77	19.92	19.58	20.79
Cr_2O_3	0.00	0.00	0.00	0.02	0.01	0.02	0.00
FeO	7.68	7.70	7.04	7.54	7.65	7.62	7.05
Total	95.45	95.22	93.55	94.76	93.47	93.04	94.25
Number of cations (p.f.u) on the basis on 22 oxygens							
Si	5.68	5.77	5.74	5.71	5.79	5.81	5.73
$Al^{(IV)}$	2.32	2.23	2.26	2.29	2.21	2.19	2.27
$Al^{(VI)})$	0.40	0.39	0.38	0.33	0.42	0.45	0.39
Ti	0.17	0.15	0.13	0.15	0.16	0.16	0.14
K	1.90	1.74	1.64	1.69	1.66	1.67	1.77
Na	0.01	0.04	0.03	0.08	0.02	0.02	0.02
Mn	0.03	0.02	0.03	0.03	0.03	0.03	0.03
Ca	0.00	0.03	0.04	0.24	0.03	0.01	0.00
Mg	4.31	4.36	4.54	4.27	4.33	4.27	4.49
Cr	0.00	0.00	0.00	0.00	0.00	0.00	0.00
Fe^{2+}	0.92	0.92	0.86	0.91	0.93	0.93	0.85
$X_{Fe^{2+}}$	0.18	0.17	0.16	0.18	0.18	0.18	0.16
VI	5.83	5.85	5.93	5.70	5.87	5.85	5.90
A	1.93	1.79	1.71	1.97	1.72	1.71	1.80

Table B.5: Chemical compositions of muscovites from sample GB18

Muscovite											
Gb18											
SiO_2	49.31	47.18	47.46	47.56	46.89	47.62	47.11	47.28	47.46	47.26	47.21
Al_2O_3	24.93	27.52	27.16	27.02	26.33	26.47	26.88	26.55	26.44	27.04	27.15
TiO_2	1.15	1.28	1.31	1.31	1.36	1.32	1.31	1.33	1.26	1.35	1.46
K_2O	10.13	10.40	10.03	10.28	9.92	10.37	10.29	10.03	10.22	10.39	10.12
Na_2O	0.08	0.21	0.19	0.12	0.13	0.12	0.18	0.09	0.17	0.16	0.17
MnO	0.07	0.01	0.05	0.02	0.03	0.08	0.06	0.02	0.05	0.05	0.06
CaO	0.03	0.00	0.00	0.00	0.00	0.02	0.00	0.02	0.00	0.03	0.00
MgO	3.76	2.80	2.93	3.02	2.80	2.88	2.87	2.89	2.95	2.81	2.86
Cr_2O_3	0.00	0.00	0.05	0.02	0.02	0.03	0.03	0.00	0.00	0.00	0.00
FeO	4.73	5.61	5.57	5.33	5.79	5.89	5.69	5.79	5.39	5.82	6.03
Total	94.19	95.01	94.75	94.67	93.26	94.81	94.42	94.00	93.94	94.91	95.06
Number of cations (p.f.u) on the basis of 22 oxygens											
Si	6.75	6.46	6.50	6.52	6.53	6.54	6.50	6.53	6.56	6.49	6.47
$Al^{(IV)}$	1.25	1.54	1.50	1.48	1.47	1.46	1.50	1.47	1.44	1.51	1.53
$Al^{(VI)}$	2.78	2.90	2.89	2.88	2.86	2.83	2.86	2.86	2.87	2.86	2.85
Ti	0.12	0.13	0.13	0.13	0.14	0.14	0.14	0.14	0.13	0.14	0.15
K	1.77	1.82	1.75	1.80	1.76	1.82	1.81	1.77	1.80	1.82	1.77
Na	0.02	0.06	0.05	0.03	0.04	0.03	0.05	0.02	0.04	0.04	0.04
Mn	0.01	0.00	0.01	0.00	0.00	0.01	0.01	0.00	0.01	0.01	0.01
Ca	0.00	0.00	0.00	0.00	0.00	0.00	0.00	0.00	0.00	0.00	0.00
Mg	0.77	0.57	0.60	0.62	0.58	0.59	0.59	0.60	0.61	0.58	0.58
Cr	0.00	0.00	0.01	0.00	0.00	0.00	0.00	0.00	0.00	0.00	0.00
Fe^{2+}	0.54	0.64	0.64	0.61	0.67	0.68	0.66	0.67	0.62	0.67	0.69
$X_{Fe^{2+}}$	0.41	0.53	0.52	0.50	0.54	0.53	0.53	0.53	0.51	0.54	0.54
VI	4.22	4.25	4.27	4.25	4.26	4.25	4.26	4.27	4.23	4.25	4.28
A	1.80	1.87	1.80	1.83	1.80	1.85	1.86	1.79	1.85	1.86	1.81

Table B.6: Chemical compositions of feldspars from sample GB14

Feldspar														
Gb14														
SiO_2	68.63	65.60	68.73	65.23	69.01	69.23	67.82	69.20	69.00	68.79	68.75	68.77	66.21	69.12
Al_2O_3	20.12	22.50	20.37	22.98	20.09	20.14	21.05	20.07	20.29	20.35	20.52	20.52	22.29	20.17
TiO_2	0.00	0.01	0.00	0.00	0.00	0.01	0.00	0.00	0.00	0.01	0.07	0.00	0.00	0.00
CaO	0.27	2.71	0.22	3.13	0.11	0.05	0.93	0.07	0.22	0.33	0.49	0.49	2.30	0.07
MgO	0.00	0.01	0.01	0.00	0.00	0.00	0.02	0.00	0.00	0.01	0.13	0.00	0.00	0.00
MnO	0.04	0.03	0.02	0.00	0.04	0.03	0.06	0.00	0.04	0.00	0.04	0.06	0.01	0.00
FeO	0.08	0.10	0.11	0.02	0.02	0.31	0.33	0.21	0.19	0.27	0.47	0.15	0.06	0.09
Na_2O	9.85	8.53	10.06	8.48	9.22	9.95	9.33	9.46	9.65	9.68	8.99	9.99	9.04	10.35
K_2O	0.09	0.10	0.10	0.07	0.07	0.06	0.02	0.08	0.05	0.05	0.06	0.02	0.07	0.06
Total	99.09	99.59	99.61	99.91	98.57	99.78	99.56	99.09	99.44	99.48	99.52	100.01	99.99	99.86
Number of cations (p.f.u) on the basis on 8 oxygens														
Si	3.00	2.88	2.99	2.86	3.02	3.01	2.96	3.02	3.01	3.00	3.00	2.99	2.89	3.00
Al	1.04	1.16	1.05	1.19	1.04	1.03	1.08	1.03	1.04	1.05	1.05	1.05	1.15	1.03
Ti	0.00	0.00	0.00	0.00	0.00	0.00	0.00	0.00	0.00	0.00	0.00	0.00	0.00	0.00
Ca	0.01	0.13	0.01	0.15	0.01	0.00	0.04	0.00	0.01	0.02	0.02	0.02	0.11	0.00
Mg	0.00	0.00	0.00	0.00	0.00	0.00	0.00	0.00	0.00	0.00	0.00	0.00	0.00	0.00
Mn	0.00	0.00	0.00	0.00	0.00	0.00	0.00	0.00	0.00	0.00	0.00	0.00	0.00	0.00
Fe^{2+}	0.00	0.00	0.00	0.00	0.00	0.01	0.01	0.01	0.01	0.01	0.02	0.01	0.00	0.00
Na	0.84	0.73	0.85	0.72	0.78	0.84	0.79	0.80	0.81	0.82	0.76	0.84	0.77	0.87
K	0.01	0.01	0.01	0.00	0.00	0.00	0.00	0.00	0.00	0.00	0.00	0.00	0.00	0.00

Table B.7: Chemical compositions of feldspars from sample GB17

Feldspar										
	Gb17									
SiO_2	68.63	69.18	68.42	68.57	69.05	68.48	68.80	68.68	68.96	69.12
Al_2O_3	20.15	20.34	20.27	20.01	20.21	19.95	20.04	20.43	20.38	20.25
TiO_2	0.00	0.01	0.00	0.00	0.05	0.04	0.00	0.01	0.01	0.03
CaO	0.15	0.35	0.52	0.08	0.17	0.09	0.08	0.26	0.17	0.24
MgO	0.00	0.00	0.01	0.00	0.00	0.00	0.00	0.01	0.00	0.01
MnO	0.00	0.03	0.04	0.06	0.02	0.03	0.00	0.01	0.03	0.03
FeO	0.13	0.07	0.07	0.00	0.06	0.00	0.11	0.04	0.15	0.07
Na_2O	9.79	9.72	8.72	8.82	9.18	9.09	9.95	9.76	9.49	9.22
K_2O	0.08	0.10	0.13	0.11	0.08	0.07	0.09	0.10	0.09	0.08
Total	98.94	99.80	98.19	97.66	98.81	97.75	99.06	99.30	99.28	99.06
Number of cations (p.f.u) on the basis of 8 oxygens										
Si	3.01	3.00	3.01	3.03	3.02	3.02	3.01	3.00	3.01	3.01
Al	1.04	1.04	1.05	1.04	1.04	1.04	1.03	1.05	1.05	1.04
Ti	0.00	0.00	0.00	0.00	0.00	0.00	0.00	0.00	0.00	0.00
Ca	0.01	0.02	0.02	0.00	0.01	0.00	0.00	0.01	0.01	0.01
Mg	0.00	0.00	0.00	0.00	0.00	0.00	0.00	0.00	0.00	0.00
Mn	0.00	0.00	0.00	0.00	0.00	0.00	0.00	0.00	0.00	0.00
Fe^{2+}	0.00	0.00	0.00	0.00	0.00	0.00	0.00	0.00	0.01	0.00
Na	0.83	0.82	0.74	0.75	0.78	0.78	0.84	0.83	0.80	0.78
K	0.00	0.01	0.01	0.01	0.00	0.00	0.00	0.01	0.00	0.00

Appendix C

Python Scripts

Python scripts written to perform various calculations for this thesis are attached in the pages that follow. The first script calculates frictional and viscous strengths of various minerals and was used to construct the crustal strength curves presented in Chapter 8 (Figure 8.2). The second script calculates stress and strain rates from recrystallised grain sizes (Figure 6.3) by applying the methods of Stipp & Tullis (2003).

C.1 Python script used in crustal strength calculations

```
import numpy as np
import matplotlib as mpl
import matplotlib.pyplot as plt
import math

c = 1.60 # Fault parameter = 1.60 for thrust faults following
    Sibson (1974)
#mu = 0.6 # static coefficient of friction
ro = 2650 # rock density in kg.m-3
g = 9.81 # gravitational acceleation m.s-2
#lv = 0.4 # pore-fluid factor 0.4 = hydrostatic

t6 = []  #hydrostatic
t4 = []  #hydrstaitc
t68 = [] # Overpressure
t48 = [] # overpressure
th = []
temp = []
tempC = []
flowsil = []
```

```
flowcar1 = []
flowcar2 = []
flowcar3 = []
flowcar4l = []
flowcar4h = []
gtest1 = []
gtest2 = []
dol1 = []
dol1g = []

#FUNCTIONS

def shear(z,mu,lv):
    tau = c*mu*(ro*g*z)*(1-lv)
    return tau/(10**3)

def flow_stress(e,T):
    s = (e/((np.sqrt(3**(2.4+1))*(10**-5))*math.exp((-163)
       /((8.31*(10**-3))*T))))**(1/2.4)
    return s

# CALCITE FLOW LAWS FROM SCHMID ET AL. 1980 ----------------------

def flow_calc1(e,T):
    s = 114*(np.log(e)-np.log((5.9*10**5))-(-62/(0.0019872041*T)))
    return s*0.1

def flow_calc2(e,T):
    s = (e/((10**(-4.5))*math.exp(-100/(0.0019872041*T))))**(1/7.6)
    return s*0.1

def flow_calc3(e,T):
    s = (e/((10**(3.9))*math.exp(-102/(0.0019872041*T))))**(1/4.2)
    return s*0.1

# CALCITE FLOW LAWS FROM WALKER ET AL. 1990 -----------------

def flow_calc4l(e,T,d):
    s = (e/((10**(4.9)*math.exp(-190/(0.008314*T))*(d**(-1.9)))))
       **(1/1.7)
```

```
    return s

def flow_calc4h(e,T,d):
    s = (e/(((np.sqrt(3**(3.3+1))*100)*math.exp(-190/(0.008314*T))
       *(d**(-1.3)))))**(1/3.3)
    return s

# Dolomite flow law from Piana et al. 2008 ----------------------

def flow_dol(e,T,d):
     s = (e/((10**(15))*math.exp(-368/(0.008314*T))*(d**(-2.6))))
        **(1/1.3)
     return s

#Calculations

for i in np.arange(0,30, 0.1): #Calculates frictional shear
   strength at various depths
    t6.append(shear(i,0.6,0.4))
    t68.append(shear(i,0.6,0.9))
    t4.append(shear(i, 0.4,0.4))
    t48.append(shear(i,0.4,0.8))
    th.append(shear(i,0.6,0.98))
    temp.append((i*25)+273)
    tempC.append((i*25))

for i in temp:  # Calculates viscous flow stress at temperatures
   calculated from depths using assumed geothermal gradient
    if  i > 0:
        flowsil.append(flow_stress((10**-11),i))
        flowcar1.append(flow_calc1((10**-11),i))
        flowcar2.append(flow_calc2((10**-11),i))
        flowcar3.append(flow_calc3((10**-11),i))
        flowcar4l.append(flow_calc4l((10**-11),i,300))
        flowcar4h.append(flow_calc4h((10**-11),i,300))
        gtest1.append(flow_calc4l((10**-11),i,300))
        gtest2.append(flow_calc4h((10**-11),i,300))
        dol1.append(flow_dol(10**-11,i,500))
        dol1g.append(flow_dol(10**-11,i,1000))
```

```
#GRAPHS

fig, ax1 = plt.subplots()
ax1.plot(t6, np.arange(0,30, 0.1), color = 'k', label = '$\mu_{s}$
    = 0.6')
ax1.plot(t68, np.arange(0,30, 0.1), color = 'k', ls = '--')
#ax1.plot(th, np.arange(0,30,0.1), color = 'k', ls = ':')
#ax1.plot(t4, np.arange(0,40,0.1), color = 'b', label = '$\mu_{s}$
    = 0.4')
#ax1.plot(t48, np.arange(0,40, 0.1), color = 'b', ls = '--')
ax1.plot(flowsil, np.arange(0,30,0.1) , color = 'k')
#ax1.plot(flowcar1, np.arange(0,40,0.1), color ='b')
#ax1.plot(flowcar2, np.arange(0,30,0.1), color ='y')
#ax1.plot(flowcar3, np.arange(0,30,0.1), color ='r')
#ax1.plot(flowcar4l, np.arange(0,30,0.1), color = 'g')
ax1.plot(flowcar4h, np.arange(0,30,0.1), color = 'b')
#ax1.plot(gtest1, np.arange(0,30,0.1), color = 'g', ls = '--')
#ax1.plot(gtest2, np.arange(0,30,0.1), color = 'b', ls = '--')
ax1.plot(dol1, np.arange(0,30,0.1), color = 'red')
#ax1.plot(dol1g, np.arange(0,30,0.1), color = 'red', ls = '--')
ax1.set_xlim(0, t6[len(t6)-1])
ax1.set_ylim(30, 0)
ax1.set_ylabel('Depth (km)')
ax1.set_xlabel('Sustainable Shear Stress (MPa)')
ax1.xaxis.set_label_position('top')
ax1 = plt.gca() # Get current axes object
ax1.xaxis.set_ticks_position('top')
#ax1.yaxis.set_ticks_position('right')

ax2 = ax1.twinx()
#ax2.plot(flowsil, tempC , color = 'k')
#ax2.axhspan(160,200, alpha =0.5)
ax2.set_ylim(0,tempC[len(tempC)-1])
ax2.set_ylabel('Temperature ($^{o}C$)')
ax2 = plt.gca().invert_yaxis()

#ax1.legend()
plt.show()
```

C.2 Python script used for palaeopiezometry

```
import math
import numpy as np
import matplotlib as mpl
import matplotlib.pyplot as plt
import csv

##Data

#Import data from CSV Files & Append to python readable format

datafile16 = open('C:\Users\Michael\Documents\MSc\Piezometry\Data\
    Grain_measurements_IJ_GB16.csv', 'r')
data_gb16 = csv.reader(datafile16)
data_gb16 =[eval(row[0]) for row in data_gb16]

datafile17 = open('C:\Users\Michael\Documents\MSc\Piezometry\Data\
    Grain_measurements_IJ_GB17.csv', 'r')
data_gb17 = csv.reader(datafile17)
data_gb17 =[eval(row[0]) for row in data_gb17]

datafile18 = open('C:\Users\Michael\Documents\MSc\Piezometry\Data\
    Grain_measurements_IJ_GB18.csv', 'r')
data_gb18 = csv.reader(datafile18)
data_gb18 =[eval(row[0]) for row in data_gb18]

num_16 = len(data_gb16)
num_17 = len(data_gb17)
num_18 = len(data_gb18)

recryst16 = []
recryst17 = []
recryst18 = []


# Apply recrystallised grain size cut-off

for i in data_gb16:
    if i < 120:
```

```
        recryst16.append(i)

for i in data_gb17:
    if i < 120:
        recryst17.append(i)

for i in data_gb18:
    if i < 120:
        recryst18.append(i)

num_16r = len(recryst16)
num_17r = len(recryst17)
num_18r = len(recryst18)


#FUNCTIONS

# Fuction to calculate the geometrical mean of the data

def geomean(numbers):
    product = 1
    for n in numbers:
        product *= n
    return product ** (1.0/len(numbers))

# Function converts decimal value to scientific notation

def format_e(n):
    a = '%E' % n
    return a.split('E')[0].rstrip('0').rstrip('.') + 'E' + a.split
       ('E')[1]

#Paleopiezometery - Flow Stress Piezometers of Stipp et al. (2003)
   and Shimizu (2008)

def stress_stipp(D):
    difstress = math.exp(((math.log(D/3631)/(-1.26))))
    return difstress

def stress_shim(D,T):
```

```
    flowstress = ((3.52*(10**2))*(D**(-0.8))*math.exp((6.98*(10**2)
        )/T))
    return flowstress

#Strain Rates: Using Stipp & Tullis (2003) Flow Stress & Quartz
    Flow Law - Hirth et al.(2001)

def strainrate(f, sig, T):
    sr = (((10**(-11.2))*(f**1)*(sig**4))*(math.exp((-135*(10**3))
        /((8.3145)*(T)))))
    return sr

# Mean Grain-Size Used for Stress Calculations

D16 = geomean(recryst16)
D17 = geomean(recryst17)
D18 = geomean(recryst18)


# Conversion of Stipp & Tullis (2003) stresses for plotting

S16 = int(stress_stipp(D16))
S17 = int(stress_stipp(D17))
S18 = int(stress_stipp(D18))

#Graphs

fig1,ax1 = plt.subplots()
ax1.hist(data_gb16,30, histtype='bar', color='black', alpha =
    0.6)
#ax1.hist(data_gb17, 30, histtype = 'bar', color = 'red', alpha =
    0.4)
#ax1.hist(data_gb18, 30, histtype = 'bar', color = 'blue', alpha =
    0.4)
ax1.set_title('GB16')
ax1.set_xlabel('Grain-Size($\mu$m)')
ax1.set_ylabel('Frequency')
ax1.set_xlim(0,800)
ax1.set_ylim(0,60)
#ax1.annotate(51,22, 'n=' + str(num_16))
```

```
#ax1.text(51,21, '$\sigma$='+ str(S16) + 'MPa')
ax1.grid(True)
ax1.axvline(geomean(recryst16), color = 'black', linestyle = '
    dashed', linewidth = 2, label = 'Geometrical Mean')
ax1.axvline(120, color = 'red', linestyle = '-', linewidth = 2,
    label = 'Cut-off recrystallised grain-size')
ax1.legend()

fig2,ax1 = plt.subplots()
ax1.hist(data_gb17,30, histtype ='bar', color ='black', alpha =
    0.6)
#plt.hist(data_gb17, 25, histtype = 'bar', color = 'red', alpha =
    0.4)
#plt.hist(data_gb18, 25, histtype = 'bar', color = 'blue', alpha =
    0.4)
ax1.set_title('GB17')
ax1.set_xlabel('Grain-Size($\mu$m)')
ax1.set_ylabel('Frequency')
ax1.set_xlim(0,800)
ax1.set_ylim(0,60)
#ax1.annotate('n= + str(num_16)', xytext = (51,22))
#ax1.text(51,21, '$\sigma$='+ str(S16) + 'MPa')
ax1.grid(True)
ax1.axvline(geomean(recryst17), color = 'black', linestyle = '
    dashed', linewidth = 2, label = 'Geometrical Mean')
ax1.axvline(120, color = 'red', linestyle = '-', linewidth = 2,
    label = 'Cut-off recrystallised grain-size')
ax1.legend()

fig2,ax1 = plt.subplots()
ax1.hist(data_gb18,30, histtype ='bar', color ='black', alpha =
    0.6)
#plt.hist(data_gb17, 25, histtype = 'bar', color = 'red', alpha =
    0.4)
#plt.hist(data_gb18, 25, histtype = 'bar', color = 'blue', alpha =
    0.4)
ax1.set_title('GB18')
ax1.set_xlabel('Grain-Size($\mu$m)')
ax1.set_ylabel('Frequency')
ax1.set_xlim(0,800)
```

```
ax1.set_ylim(0,60)
#ax1.annotate(51,22, 'n=' + str(num_16))
#ax1.text(51,21, '$\sigma$='+ str(S16) + 'MPa')
ax1.grid(True)
ax1.axvline(geomean(recryst18), color = 'black', linestyle = '
    dashed', linewidth = 2, label = 'Geometrical Mean')
ax1.axvline(120, color = 'red', linestyle = '-', linewidth = 2,
    label = 'Cut-off recrystallised grain-size')
ax1.legend()


#Numbers

print 'Total grains measured and total recrystallised grains'
print num_16
print num_16r
print num_17
print num_17r
print num_18
print num_18r

print 'Arithmetic Means'
print np.mean(data_gb16)

print 'Geometrical Means'
print geomean(recryst16)
print geomean(recryst17)
print geomean(recryst18)

print 'Standard Deviations'
print np.std(data_gb16)
print np.std(data_gb17)
print np.std(data_gb18)



print 'Flow Stresses'
print  'Stipp et al.' + ' ' + str(stress_stipp(D16)) + ' ' + str(
    stress_stipp(D17)) + ' ' + str(stress_stipp(D18))
print 'Shimizu' + ' ' +  str(stress_shim(D16, 873)) + ' ' +  str(
    stress_shim(D17, 873)) + ' ' +  str(stress_shim(D18, 873))
```

```
print 'Strain Rates assuming P = 10kbar and T = 600 degrees C'
print format_e(strainrate(1.203*(10**3), stress_stipp(D16), 873))
print format_e(strainrate(1.203*(10**3), stress_stipp(D17), 873))
print format_e(strainrate(1.203*(10**3), stress_stipp(D18), 873))



plt.show()
```